UNIVERSITÀ DEGLI STUDI DI NAPOLI "FEDERICO II"

DEPARTMENT OF CHEMICAL, MATERIALS AND PRODUCTION ENGINEERING
(DICMAPI)

PHD IN "INDUSTRIAL PRODUCT AND PROCESS ENGINEERING"

XXXVI CYCLE

ENGINEERED ARTIFICIAL NICHES FOR SKELETAL MUSCLE REGENERATION *IN VITRO*.

Supervisor
Prof. Paolo A. Netti
Prof. Maurizio Ventre

PhD Student
Sarah Willems

Coordinator
Prof. Andrea D'Anna

January 2021 – December 2023

ACKNOWLEDGEMENTS

I want to start this work by thanking a few people whose involvement made this whole project possible. First and foremost, I want express my gratitude to my supervisors Prof. Paolo Antonio Netti and Prof. Maurizio Ventre, for their support, their input and their patience throughout these three years. This journey was made possible by the Horizon2020 fund program under the Marie Sklodowska-Curie grant agreement No 860034. Therefore I would like to profoundly thank everyone involved in the RENOIR-ITN project, as the collaborations and scientific trainings that were provided, have been invaluable to improve my research training and skills. Collaborating with different partners of the project and participating in all the conferences have been truly treasured experiences. A special thanks also goes out to Dr. Carlo Fortunato Natale, whose research input, ideas, and spirit have been of tremendous help for the project and myself. I am eternally grateful to have been able to partake in this experience of moving abroad to study and train in research, which would not have been possible without the support of the before mentioned people. I would be remiss in not mentioning the support of my family and partner throughout these years. A big thank you to my parents, for giving me all their support and encouraging me to take these crazy opportunities abroad. Last but not least, I want to express my gratitude as well to my partner, whose patience, belief, love and cheerleading have been fundamental in this adventure.

From the bottom of my heart, I am grateful to all of you.

ABSTRACT

Skeletal muscle tissue engineering aims to provide a model of the muscle for regenerative medicine applications. In this work, the aim was to replicate the intricate microenvironment of the muscle tissue, using an engineered artificial *in vitro* niche. The dissertation delves into the characterisation of nanogrooved substrates for skeletal muscle tissue niches, as a foundation for cultivating the cells. The study progresses from an initial material characterisation to the formation of a three-dimensional (3D) skeletal muscle tissue construct *in vitro*, by using the microenvironmental cues within an artificial niche.

In the first phase, nanogrooved substrates are thoroughly investigated to characterise their suitability for skeletal muscle tissue cultures. This investigation involves topographical analysis of the nanogrooves using atomic force microscopy (AFM), followed by an analysis of the adhesive and elastic properties of the surface. The biocompatibility of these substrates was assessed using C2C12 murine myoblast cells.

Subsequently, the microenvironmental cues of the artificial niche are harnessed to guide the cells into a self-assembled 3D muscle construct. The resulting constructs are extensively characterised using immunofluorescence and focused ion beam scanning electron microscopy (FIB SEM).

A third part of the dissertation explores the mechanical identity of cells cultivated on the engineered niche. This evaluation encompasses the assessment of actinin tension within the cells and the determination of the Young's Modulus of the cell using AFM measurements. Considering this mechanical evaluation at the construct formation stage, revealed that the muscle constructs exhibit a Young's Modulus comparable to that of native skeletal muscle, highlighting the success of the self-organisation approach in recapitulating the structural and mechanical characteristics for skeletal muscle tissue.

This dissertation contributes valuable insights into the complex cell-material crosstalk, by using nanotopographical cues, mechanical properties and biochemical signals in skeletal muscle tissue engineering. The findings in this study provide a foundation for the development of advanced strategies in regenerative medicine and hold promise for applications in tissue repair and regeneration studies.

TABLE OF CONTENTS

LIST OF FIGURES

LIST OF TABLES

AIMS AND RESEARCH QUESTIONS

In this thesis the interest goes out to the biointerface between skeletal muscle cells and their surrounding artificial niche. By manipulating the (mechanical) microenvironment of the cells using biochemical and biophysical cues, it was hypothesised that the substrate could guide skeletal muscle cell differentiation and the formation of a three-dimensional (3D) muscle structure. This structure is of interest for the skeletal muscle tissue engineering field as it could present a model for the study of 3D *in vitro* cultures that aides in the assessment of disease models and drug efficacy. Furthermore, the formed 3D structure could provide extra information on the behaviour of skeletal muscle stem cells *in vitro* and their interaction with the surrounding microenvironment.

The cues necessary for the formation of a 3D skeletal muscle construct were assessed and the skeletal muscle construct was evaluated using mechanical and structural characterisation methods, specifically for the set-up.

This thesis starts by evaluating different substrates and their properties, comparing alternative materials, and highlighting the nano-topographical features. In the second chapter, the formation of the tissue construct is discussed in detail, exploring different important parameters for the formation of the construct, such as the size, the extracellular matrix and the myosin content. The third chapter explores the mechanical identity of single cells and multicellular layers on the used substrates by evaluating the tension and elasticity/compressibility of the cells and tissues.

I. SUBSTRATE EVALUATION FOR SKELETAL MUSCLE TISSUE ENGINEERING

This chapter discusses the different materials used and focusses on the literature of the biological use of these materials. Polydimethylsiloxane, FlexDym™ and were chosen to build a nanogrooved platform for muscle cell cultures due to their biological compatibility and favourable mechanical characteristics. In the introduction, attention is given to the already evaluated material properties found in literature, with a focus on those properties useful for the development of the nanogrooved platform. Furthermore, the platform was characterised using atomic force microscopy and scanning electron microscopy to visualise the topography. Lastly, initial experiments with skeletal muscle myoblasts on the different substrates demonstrated their compatibility and effects on muscle cell culture.

1. INTRODUCTION

This introduction discusses the three different materials used with a focus on their surface properties, mechanical properties, and biocompatibility. Here a large and important part of the substrate evaluation is presented, as numerous characterisation methods have already been carried out in the past. Nevertheless, these will be discussed to create an understanding of the substrate and its properties useful for cell culture.

1.1 Polycarbonate

Polycarbonate (PC) is a transparent, thermoplastic polyester, most commonly formed in a reaction of bis-phenol A and carbonyl chloride. It is used in baby feeding bottles, safety helmets and bullet-proof glass, for instance.

1.1.1 Composition and surface modification of polycarbonate

PC is manufactured by the condensation polymerization of bisphenol A and phosgene as seen in Figure 1 below.

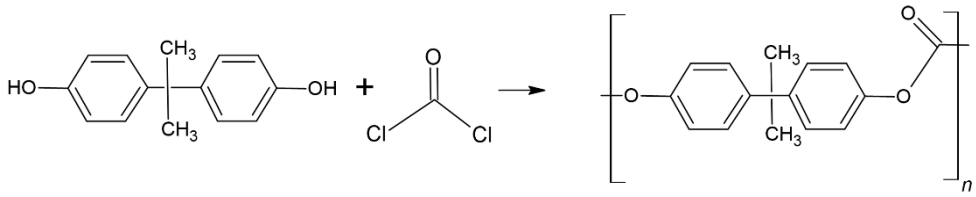

Figure 1: Condensation polymerisation of PC, drawn in ChemSketch.

PC has low surface free energy, causing it to be evaluated for plasma treatments to enhance the adhesion on the surface for different applications [1]. Without any

surface treatment, PC has a contact angle of around 70.18 ± 0.47°. The contact angle decreases down to 25.36 ± 0.95° with the repeated use of oxygen plasma cycles thanks to the generation of high energy surface groups to increase wettability [2]. It has furthermore been shown that the contact angle of PC increases up to 109.00 ± 0.35° using tetrafluoromethane plasma thanks to the fluorination process, where hydrogen atoms are replaced with fluorine atoms [3]. PC based implants, for instance, have been treated to prevent bacterial adhesion or enhance the compatibility with the tissue [4]. Plasma treatment of PC increases the hardness and surface roughness [1].

1.1.2 Mechanical properties of polycarbonate

PC in its standard form offers good thermal resistance, high impact resistance and high stiffness [5]. A drawback of the material, however, is that it scratches easily, which is important to consider in nano-topographical applications. Other interesting mechanical properties of PC are given in Table 1 [6]–[8].

Table 1: Material properties of PC.

Material properties	
Property (unit)	**Result**
Hardness Shore D	80-95
Specific gravity	1.2
Refraction index	1.58
Thermal conductivity (W/m*K)	0.2
Tensile strength (MPa)	60
Young's Modulus (GPa)	2.3

1.1.3 Biocompatibility of polycarbonate

PC is mostly used in engineering applications but has found its purpose in medical applications as well. PC-ISO is used to manufacture medical devices and food packaging and can be sterilised using gamma radiation. PC meets the ISO 10993 and USP Class VI standards used for assessing biocompatibility [9].

Applications of PC include filter cartridges used for haemodialysis in patients with renal disease. As PC is clear, the dialysis technician can observe the blood sample through the procedure [10]. PC has also been used in blood oxygenators and blood reservoirs used during invasive cardiac surgeries where the heart is stopped, and a blood oxygenator takes over its function [11]. Another application includes surgical equipment where the rigidity and toughness of PC are relevant material properties [11].

1.2 Polydimethylsiloxane

Polydimethylsiloxane (PDMS) shows advantages for cell culture-based applications and organ-on-chip projects due to its resolution, low-cost [12], flexibility [13], and biocompatibility [14], [15]. It is a silicon-based organic polymer, which has a glass transition temperature of -120°C, leading to a rubber state at room temperature. It is often used as a polymer in science and engineering applications thanks to the possibility to recreate micrometric dimensions [16].

1.2.1 Composition of PDMS

The polymer comes as a prepolymer and a curing agent and can be cured with a variety of different ratios, using a variety of temperatures and conditions each resulting in unique mechanical properties. The high tuneability of PDMS allows it to mimic different mechanical properties of tissues, advantageous for its use in cell culture experiments.

The individual components and curing mechanism of PDMS provided by Dow Corning is shown in Figure 2. Panel A of the figure contains the siloxane oligomer, also called prepolymer while panel B contains the chemical composition of the crosslinker. In panel C, the curing reaction is demonstrated. The reaction does not create any waste product and alternative ratios of crosslinker and PDMS will result in a difference in elasticity of the resulting elastomeric polymer.

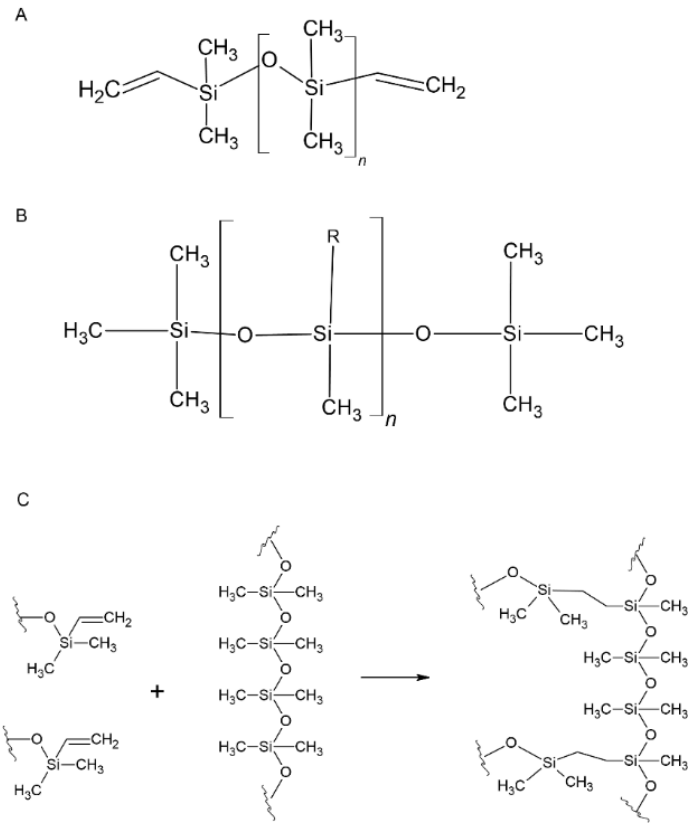

Figure 2: Components of Dow Corning Sylgard 184 PDMS and curing process.
A. Siloxane oligomer, also named prepolymer, where n is equal to ± 60. B. Siloxane cross-linkers, where n is equal to ± 10. R is typically CH_3 or occasionally H. C. The curing reaction of the prepolymer and crosslinker for the formation of the elastic polymer. The reaction is organometallic and generates no waste products. An alternative ratio of crosslinker and prepolymer will result in a stiffer or less stiff PDMS. Figure based on [17] created using ChemSketch.

The elastic properties of the polymer can thus be tuned using alternative ratios of prepolymer and crosslinker, resulting in Young's moduli from a few kPa to around 5 MPa [18], [19] in literature. These different values are used to mimic the elastic modulus of the native extracellular matrix (ECM) in cell culture studies, as a way to mimic its properties *in vitro*.

1.2.2 Surface modification of PDMS

Because PDMS is a hydrophobic material, in some applications, there is the necessity to alter this surface property. PDMS has a contact angle of 107°-120° [20], [21] when untreated, whereas a hydrophilic material is characterised by a contact angle of less than 90° [22]. Reduction of hydrophobicity can be attained by treating the surface with ultraviolet (UV) radiation, corona dischargers or oxidizing plasmas [23]–[25]. UV/Ozone-treated PDMS showed mostly silanol

groups on the surface, of which the concentration increased with increasing treatment time [26].

Studies have shown the creation of a super-hydrophilic surface when working with low pressure oxygen plasma treatments [22]. The oxygen plasma treatment introduces polar functional groups on the surface with mainly silanol (SiOH) groups being formed [27], [28]. The presence of the silanol groups changes the surfaces from hydrophobic to hydrophilic [22]. This process does lead to hydrophobic recovery, an effect well studied where the contact angle increases already minutes after plasma treatment [29], [30]. Hydrophobic recovery is caused by condensation of the hydroxyl groups and re-orientation of the polar groups from the surface of the PDMS to the bulk of the material [30], [31]. The speed with which this phenomenon takes place depends, for instance, on the humidity and temperature in which the PDMS substrates are stored [32], [33]. For instance, in a microfluidic chip, the contact angle immediately after a 200 second treatment duration decreases to 21°, but when leaving the substrate in air for six hours, it increased back up to 115°. Increasing the treatment duration to 300 seconds and longer let to an initial angle of 17° that remained between 50 and 60° after six hours of air exposure [21]. Another consequence of the oxygen plasma treatment are nano cracks in the surface of the PDMS layer. These cracks are caused by extended plasma treatment times and affect the roughness of the substrate [20]. A study by Zhu *et al.* in 2005 has shown the effects of these cracks on the adhesion of proteins to support the growth of biological cells [34].

1.2.3 Mechanical Characterisation of PDMS

As the Young's Modulus of PDMS is tuneable, depending upon the choice of crosslinker ratio and curing conditions, PDMS is suitable for a variety of applications. There is the ability to create either a very soft or very stiff environment for biological cells for example. Table 2 presents an overview of the different Young's moduli, resulting from different ratios of prepolymer to curing agent at different curing conditions taken from a study by Kim et al. in 2013 [35].

Table 2: Young's Modulus of PDMS with different curing conditions

Mixing ratio	Curing T (°C)	Curing time (h)	Thermal aging		E (MPa)
			T (°C)	Time (h)	
5:1	85	0.5	-	-	1.61
		1	-	-	1.57
			85	18	1.93
		0.5	250	0.5	2.39
				1	2.56
				2	2.46
10:1	85	0.5	-	-	1.35
		1	-	-	1.39
			85	18	1.75
				72	2.01

Another study by Iturri *et al.* in 2022 [18] compared PDMS membranes before and after plasma treatment and demonstrated an increase in stiffness with plasma treatment regardless of the curing ratio. These results are given in Table 3.

Table 3: Calculated Young's Modulus values for PDMS substrates with different crosslinker ratios and environmental conditions.

Young's Modulus (MPa)				
	Hydrophobic		**Hydrophilic**	
Sample	**Dry**	**Wet**	**Dry**	**Wet**
5:1	2.0 ± 0.2	2.4 ± 0.2	43.2 ± 0.7	44 ± 2
10:1	1.4 ± 0.1	2.0 ± 0.7	35.3 ± 5.2	31.6 ± 9.1
20:1	0.7 ± 0.1	0.9 ± 0.1	30.9 ± 3	25 ± 1.5
30:1	0.4 ± 0.1	0.7 ± 0.1	20.8 ± 2.1	14.4 ± 3
50:1	0.4 ± 0.1	0.7 ± 0.1	24.4 ± 1.1	18.3 ± 2.8

Both of these tables demonstrate the large variety of Young's Moduli for the same material, depending on the manufacturing conditions and surface modification techniques. These values are useful for experiments in cell culture where the surface is often modified using oxygen plasma and used in a wet environment for cells to be able to survive. Oxygen plasma treatment for 20 s at 60 W of the membrane led to 20-to-60-fold increases in the original values of the Young's Moduli, an effect confirmed by other studies as well [36], [37].

Other interesting material characteristics for cell culture are given in the Table 4 with data summarised from [38]–[43].

Table 4: Material properties of PDMS.

Material properties	
Property (unit)	**Result**
Hardness Shore A	37-43
Specific gravity – cured	1.03
Refraction index	1.4
Thermal conductivity (W/m*K)	0.2 – 0.27
Tensile strength (MPa)	2.24-6.7

1.2.4 Biocompatibility of PDMS

There have been plenty of research group evaluating the biocompatibility of PDMS for different cell types and applications, with examples of applications and challenges given in the following paragraphs.

For some *in vitro* cell culture systems, the hydrophobic character of PDMS can present an issue to the long-term viability of cells cultured on PDMS chips. For instance, P19 cells on PDMS show very little attachment and growth on untreated PDMS [44]. This results in limitations for long-term experiments in neural aging and death, synaptic plasticity and in synaptogenesis on PDMS chips. However, this was solved by using chemical surface modification with (3-aminopropyl)triethoxysilane (APTES) based cross-linking of ECM proteins to enhance the growth and attachment of rat cortical primary cells [45]. This technique showed stable protein attachment and improved the cell adhesion, the morphology, and the growth of the cells up until three weeks *in vitro* [45].

Another study compared four types of cells (HUAECs, 3T3 fibroblasts, osteoblast-like MC3T3-E1 cells, and HeLa (epithelial cells) on different PDMS substrates. All growth rates were comparable on PDMS and on polystyrene culture dishes and different PDMS stiffnesses did not alter the attachment and proliferation for these cell types [46].

Furthermore, PDMS has been studied as a coating for medical implants, as the original material can present some limitations regarding bioactivity, bone conductivity and blood compatibility [47], [48]. Usually, the body reacts using an inflammatory response to foreign objects inserted, encapsulating implants, and damaging them. This caused the need to look for alternatives with a decreased impact on the tissues. Because PDMS presents the option to fabricate smooth and hydrophobic surfaces, the material has aided in coatings for the osseointegration of implants [47], [49]–[51]. Moreover, the hydrophobic nature has been shown to prevent bacterial adhesion to the coated implants [47], [52].

A micro-device designed to monitor bladder volume was coated with PDMS and implanted in rats to evaluate cell viability and cytotoxicity. The cell viability of

the experimental group at 24 hours and 72 hours was 84.6 % and 82.3 % respectively. The formation of the granulation layer and neovascularization showed that after two weeks, the thickness of the layer peaked but stabilised back to the thickness of the control group at four weeks. This study concluded that the coating made the micro-device a reliable biomedical device [53].

1.3 FlexDym™

FlexDym™ is a soft thermoplastic elastomer designed by Eden Tech Paris for the rapid fabrication of microfluidic chips. The polymer has similar characteristics as PDMS in terms of flexibility and biocompatibility but has a more optimized production process that allows the material to be used for high throughput production. The chips are made out of the polymer material using hot embossing applications that press the pattern on the flex in 30 seconds at about 165°C.

1.3.1 Surface modification of FlexDym™

Like PDMS, FlexDym™ is hydrophobic in its original state. To use the polymer in biological applications it may be necessary to treat the surface with oxygen plasma in order to decrease the contact angle. Table 5 contains the surface properties of FlexDym™ before and after plasma treatment as well as its bonding behaviour to different materials [54].

Table 5: Surface properties of FlexDym™ as determined by Eden Tech.

Surface properties	
Dynamic contact angles (CA)	
Advancing CA	105° ± 4°
Receding CA	88° ± 4°
Static contact angle (plasma treatment)	
2 minutes	34.0° ± 2.8°
5 minutes	32.3° ± 5.3°
10 minutes	22.0° ± 1.8°
Sticking behaviour (thermal aid adhesion)	
Strong bonding	Flexdym™, PS, COC
Moderate bonding	PC, PMMA, Glass
Bonding behaviour varies by material grade	
Bonding strength can be enhanced by using a coating agent on the substrate	

Properties shown in Table 5 are reported as part of the brochure for the FlexDym™ acquisition [54].

Table 5, furthermore, shows the possibility to use plasma treatment for the hydrophilization of the surfaces by incorporating -OH groups. Lachaux et al demonstrated that a plasma treatment of 100 W - 200 W - 300 W for 5 minutes

was able to reduce the static contact angle to 20°. This hydrophilization effect remained for 7 days, at which point the measurements were stopped [55].

1.3.2 Physical properties of FlexDym™

The soft thermoplastic elastomer has been reported to reproduce features from 10 µm with a high reproducibility. Furthermore, tests by the company show that the absorption of Rhodamine B inside the polymer is lower for FlexDym™ when compared with PDMS, and thus a smaller amount of the fluorophore is absorbed and lost to the material.

Other physical properties are shown in Table 6 below [54].

Table 6: Mechanical properties of FlexDym™ as determined by Eden Tech.

Physical properties	
Property (unit)	**Result**
Hardness Shore A	35
Specific gravity	0.9
Tear strength (kN/m)	15
Elongation (%)	720
Tensile strength (MPa)	7.6
Young's Modulus (MPa)	1.15
Melt Flow Rate (g/min)	2

The polymer comes as pellets or sheets leading to fixed material properties, unlike PDMS, where the Young's Modulus can be altered depending on the prepolymer to crosslinker ratio.

1.3.3 Biocompatibility of FlexDym™

As PDMS remains the golden standard for fabrication of microfluidic chips and cell culture applications, only a limited number of studies have been performed evaluating FlexDym™ for cell culture. McMillan et al recently evaluated a chip fabricated out of FlexDym™ for adhesion of cells using human dermal fibroblasts [56], while Lachaux et al assessed the use of progenitor endothelial cells [57]. Endothelial cells were observed for four days and confirmed to have adhered within the first 24 hours of seeding. Cells were proliferating within 72 hours and reached confluence around 96 hours after seeding [57]. Fibroblasts were cultured within microfluidic channels for 7 days and showed good initial adhesion but were not evaluated more in detail [56].

2. MATERIALS AND METHODS

2.1 Fabrication of grooved substrates

The patterned substrates were fabricated using a commercially available polycarbonate (PC) master, polydimethylsiloxane (PDMS, Sylgard 184, Dow Corning) [58] or FlexDym™ (EdenTech Microfluidics) [54].

The PC template was used both as a master for replica molding of the PDMS and hot embossing of FlexDym™ but also as a substrate itself. The PDMS was prepared by mixing the prepolymer and crosslinker in weight ratios of 10:1 (medium hard PDMS) and 5:1 (hard PDMS) and degassed before pouring on the master. Curing of PDMS took place at different temperatures and times to evaluate the resulting nano-topography. The evaluated conditions evaluated are shown in Table 7 where the temperature and time indicate the settings of the oven. Moreover, degassing with a vacuum pump for 20 minutes before curing was evaluated. All PDMS substrates were left on a flat surface for two hours before initiating the curing, so that the polymer had a chance to spread out evenly.

Table 7: Curing conditions of PDMS.

Temperature (°C)	Time (hours)	Vacuum
60	2	YES
		NO
80	1	YES
		NO

PDMS substrates were sterilised using UV treatment inside a sterile culture hood, before proceeding with surface treatments.

The FlexDym™ comes in a solid polymer form of 1.2 mm thickness. The PC was placed on top of the polymer inside the hot embossing device at 130°C for 5 minutes resulting in a replica of the pattern present on the PC. Resulting FlexDym™ surfaces were sterilized using 70 % ethanol.

The substrates were prepared for cell culture after sterilisation with UV or ethanol washing. The PC, PDMS and the FlexDym™ underwent oxygen plasma treatment (Pfeiffer Vacuum Single Gauge – Cesar RF Power Generator) at 50 W for 3 minutes before incubation with coating solution to prepare for cell culture.

To control the seeding of the cells, PDMS boundaries were designed to attach to the nanogrooved substrates after the oxygen plasma treatment. These borders have a thickness of 1 mm and an inner size of 18 mm by 18 mm.

2.2 Scanning electron microscopy characterisation of the PDMS and FlexDym™

Surface morphology of nanogrooved PDMS and FlexDym™ was visualised for impurities by scanning electron microscope (LEO1550). The polymers were coated with a gold layer (10 nm thickness) using a HR208 Cressington sputter coater. Afterwards, surfaces were analysed by FESEM ULTRA-PLUS (Zeiss) with the SE2 detector.

2.3 Atomic force microscopy characterisation of the substrates

Evaluation of the depth and width of the topographical cues was conducted using an atomic force microscope (AFM) JPK Nanowizard II (JPK Instruments). The AFM module was combined with an LSM 700 Zeiss confocal microscope to control the tip and sample position. For topography mapping of the substrate, silicon nitride probes (MLCT, Bruker) were used, with a spring constant of 0.01 N/m. The cantilevers have a triangular shape and a pyramidical tip. The evaluation was conducted in contact mode, in air at room temperature. The resulting images were revised in the JPK data processing software by using a standardized procedure that flattens the curve and separates the artifact lines caused by the tip extension and retraction.

Indentation Young's Moduli were measured using the 0.6 N/m triangular cantilever of the MLCT probes with pyramidical tips before and after the oxygen plasma treatment. These measurements were conducted in Milli-Q water at room temperature. An area of 10 x 10 µm was scanned in 64 force curves with an indentation speed of 1 µm/s. The samples were scanned immediately after the plasma treatment and after four days in the Milli-Q water. Young's Moduli were determined using the Hertz/Sneddon adjusted model for pyramidical tips in JPK imaging software, by analysing the force curves.

From the force curves of the AFM the adhesive force can also be determined using the JPK data processing software. It is an indicator of the stickiness of the surface, brought by the minimum value of force recorded when retracting the cantilever.

Due to the fundamental nature of AFM for Chapter III, a more detailed review of the working principle and applications for material and biological sciences is given in III.1.2.2

2.4 Indentation elasticity using PIUMA

To determine elastic properties using a tip in a micrometre size (~ 50 µm), the PIUMA displacement-controlled nanoindenter was used (Optics11). The device uses a cantilever with a spherical tip to apply load and measure indentation depth simultaneously. The tip used for PDMS measurements had a stiffness of 44.6 N/m and radius of 50 µm. Before measurements, the tip was calibrated on a glass petri

dish in water, to equate the bending of the cantilever to the probe displacement. Each polymer was indented 9 times using a combination of single indentations and matrix indentations.

The applied indentation protocol was composed of a loading phase for 2 s at 10 000 nm indentation depth, which was held for three seconds, and then an unloading phase for 2 seconds. All single indentation values were calculated by Piuma Dataviewer version 3.5.0 using the Hertz model (Piuma; Optics11).

2.5 Cell culture on the substrates

Immediately after the oxygen plasma treatment, coating of the substrates was conducted by incubating the surfaces 10 µg/mL of Fibronectin (Merck) in phosphate buffered saline (PBS, Sigma-Aldrich) for 1 hour at room temperature. Excess coating was taken off before seeding the cells.

C2C12 skeletal muscle mouse myoblast cells (CRL-1772™, ATCC) were used for evaluation of the surfaces. C2C12 cells were cultivated in Dulbecco's minimum essential medium with high glucose (DMEM-HG, Sigma-Aldrich), supplemented with 10 % foetal bovine serum (FBS, Sigma-Aldrich), 1 % L-glutamine (Gibco) and 100 U/mL penicillin-streptomycin (PenStrep, Gibco). The cells were incubated at 37°C and 5 % CO_2 in a cell culture incubator. Medium was changed every 2 – 3 days and before reaching 70 % confluence the cells were passaged using Trypsin/Ethylenediaminetetraacetic acid (EDTA) (0.25 % w/v trypsin/0.02 mM EDTA; Gibco) for seeding on the substrates. C2C12 cells for experimental use were kept below passage 9. The seeding density of cells on the surfaces was 3100 cells/cm² and cells were kept in culture for as long as they adhered to the substrates.

2.6 Characterisation of the cells on the substrates

Cells were evaluated in culture for their attachment to the surface, their morphology, and their directionality. This was done by fixing the cells at 14 days in culture using 4 % paraformaldehyde (Electron Microscopy Sciences USA) for 20 minutes at room temperature. Cells were afterwards stained using Phalloidin 647 (Abnova) and Sytox Green (Thermo Fisher Scientific). Visualisation was carried out using confocal microscopes (Inverted LEICA TCS SP5 II or upright Zeiss LSM 900). Images were analysed for the direction of cells in ImageJ using the Directionality plugin.

2.7 Statistical analysis

All statistical analyses were carried out in MATLAB (version R2022a) using either Wilcoxon rank-sum test or Kruskal Wallis test. Statistical relevant differences were defined as having a p-value below 0.05.

3. RESULTS

3.1 Nanogroove depth and definition depend on the moulding technique

A scanning electron microscopy overview of the substrates was carried out for polydimethylsiloxane (PDMS) and FlexDym™ to identify impurities on the surface and get an overview of the topography. At a zoom of 2 KX, using a SE2 detector, the resulting topography is represented in Figure 3. Panel A contains the topography for a hard PDMS substrate, panel B for a medium stiff substrate and panel C for a FlexDym™ substrate. The difference in fabrication techniques might cause the perturbations in the surface seen in panel C, due to the detachment method of FlexDym™. Either these perturbations were already present in the surface before molding, or they were caused by the hot embossing and consequent detachment from the PC master.

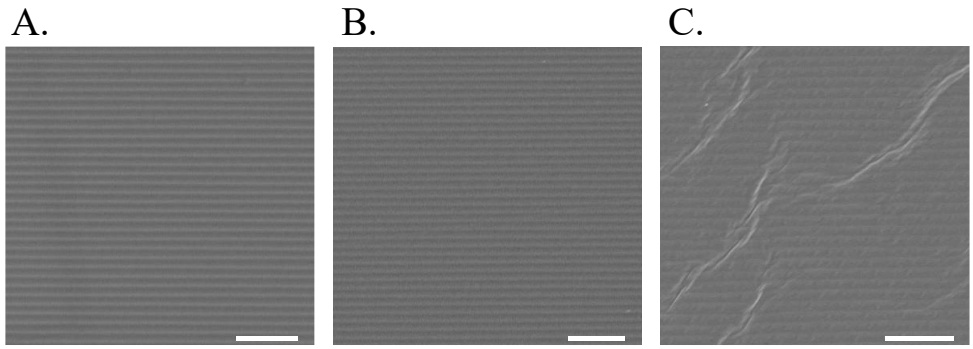

Figure 3: Scanning electron microscopy of the topography on different substrate materials.
A. Hard PDMS with horizontal grooves. B. Medium PDMS with horizontal grooves. C. FlexDym™ with horizontal grooves. Scalebars = 10 µm

To further investigate these findings, the topography was characterised using AFM indentation to refine the depth of the grooves on each of the substrates. Considering that the original PC master has a depth of 250 nm [58], AFM was used to clarify if this depth was replicated. As demonstrated in Figure 4 the topography was characterised per fabrication method, per type of polymer. Hard and medium PDMS but also FlexDym™ were all three suited for replicating the grooved pattern. The depth however, of FlexDym™ samples was significantly lower than that of PDMS, ranging around 160.63 ± 11.52 nm.

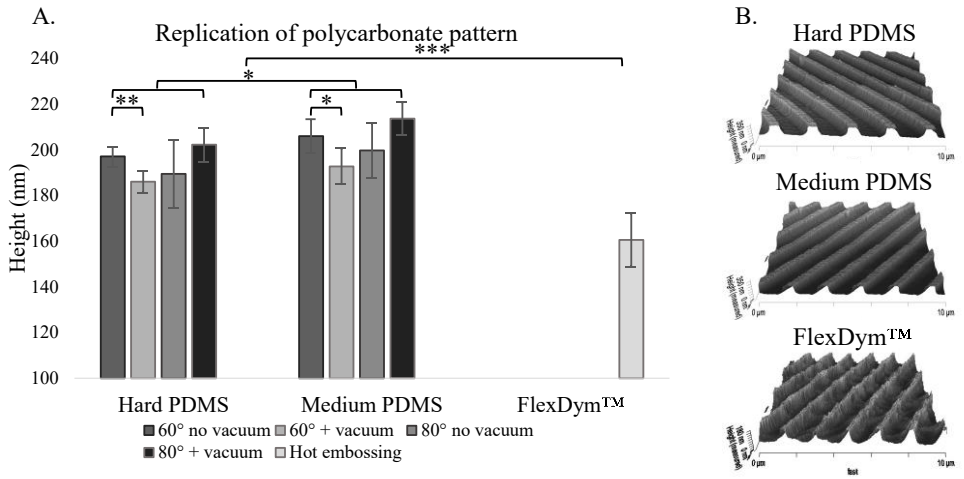

Figure 4: Atomic force microscopy of the depth of the topography on different substrate materials.
A. Overview of average nanogroove depth in relation to the polymer and the fabrication method, measured using AFM. B. Representative 3D-renderings of AFM topography maps to indicate the nanogroove replication on different polymers. * $p < 0.05$, ** $p < 0.01$, *** $p < 0.001$.

Furthermore, Panel B Figure 4 shows representative 3D renderings of the resulting AFM topography map for each of the polymers, as an indicator of nanogroove shape and size.

3.2 Young's Modulus of the used substrates in medium and surface treated conditions

To evaluate the Young's Modulus of the surface in contact with cells, the indentation elasticity of the substrates was determined using AFM and PIUMA.

3.2.1 Indentation Young's Modulus of substrates in the nanoscale

As there is a lot of research into AFM for PDMS substrates in air, a comparison was made between the three types of substrates in cell culture settings. To measure the indentation Young's Modulus that the cells experience *in vitro*, measurements were carried out in liquid instead of in air. Furthermore, a comparison was made for the different types of materials, before and after surface treatment using oxygen plasma. As it was shown that for PDMS the Young's Modulus might increase on the surface after treatment, an experiment was set up to compare FlexDym™ in similar settings.

Two categories of substrates were considered, those immersed in Milli-Q water without oxygen plasma treatment, and those immersed in Milli-Q water after the treatment. Measurements were then carried out immediately after immersing the samples in water with and without plasma treatment, and at a time point of four days after immersing them in water and after the treatment to verify any longer lasting effects.

The overview in Figure 5 presents the Young's Moduli measured using the AFM immediately after immersion in water or after oxygen plasma treatment. After adding water to the PDMS without treatment, the values for hard PDMS and medium PDMS are 3.55 ± 0.15 MPa and 1.29 ± 0.15 MPa respectively, close to indentation values in literature [18]. Measuring the same PDMS with a nanogroove topography instead, results in values of 2.96 ± 0.55 MPa and 2.8 ± 0.2 MPa for hard and medium PDMS, respectively.

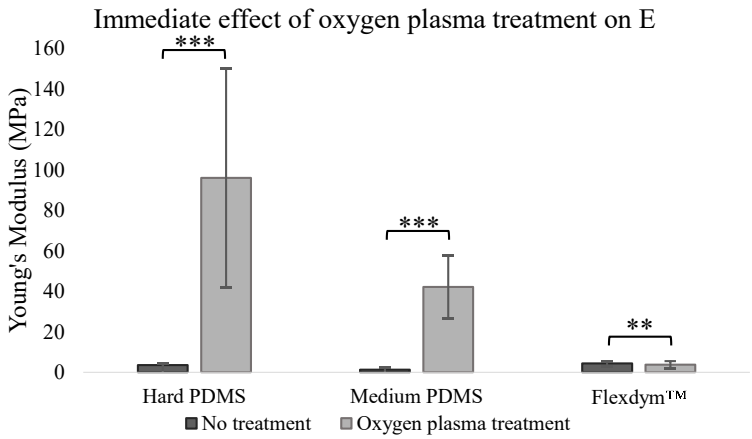

Figure 5: Effect of oxygen plasma treatment on the indentation Young's Modulus of substrates, immediately after treatment.
Side by side comparison of Young's Modulus determined by using 64 force curves measured by AFM for each substrate before and after oxygen plasma treatment. Non treated samples were submerged in water right before the measurement, and treated samples were treated using oxygen plasma before submerging them into water for the measurements. ** $p < 0.01$, *** $p < 0.001$.

However, after oxygen plasma treatment, indentation using AFM demonstrated increased Young's Moduli. On flat PDMS substrates, increased Young's Moduli of 96.06 ± 53.91 MPa and 42.19 ± 15.39 MPa were observed for hard and medium PDMS. Taking these values into account, the substrates demonstrated a 27x and a 32x increase in their Young's Moduli upon nanoindentation. Repeating this experiment using patterned PDMS lead to values 36x times higher than before the plasma treatment.

Indentation Young's modulus values for FlexDym™ immediately before and immediately after the plasma treatment were 4.39 ± 0.8 and 3.3 ± 1.56 MPa respectively. Comparisons between 64 points on the surface lead to the observation that FlexDym™ substrates after plasma treatment had a significantly lower Young's Modulus ($p < 0.01$).

These same measurements were carried out on substrates 4 days after the initial measurements as well, to evaluate the effect of the stiffening on a larger timescale. Resulting values for the Young's Modulus are shown in Figure 6.

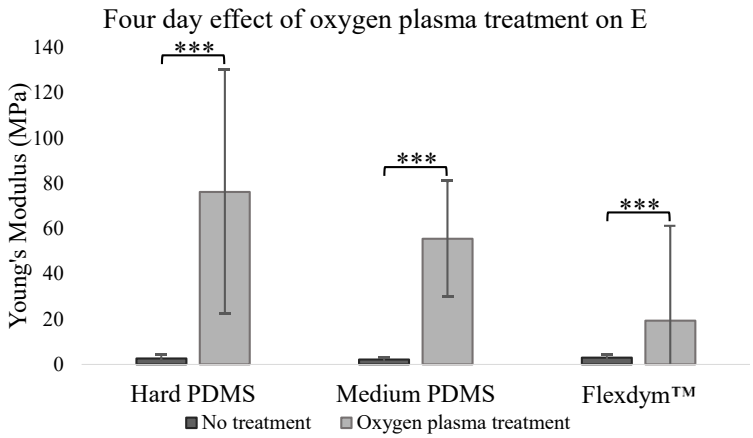

Figure 6: Effect of oxygen plasma treatment on the indentation Young's Modulus of substrates, four days after treatment.
Side by side comparison of Young's Modulus determined by using 64 force curves measured by AFM for each substrate before and after oxygen plasma treatment. All measurements were carried out four days after treatment and submerging them in water. ** $p < 0.01$, *** $p < 0.001$.

A similar trend is seen after four days as well, where the difference between non treated and treated PDMS results in a 25 – 28 times higher Young's Modulus. Indenting the Flexdym™ four days after the oxygen plasma treatment, resulted in an observed Young's Modulus that was 6 times higher than for non-treated substrates.

At both timepoints, measurements of PC demonstrated large Young's Moduli (>500 MPa) corresponding to values found in literature, but values found had large standard deviations and are thus not shown in comparative graphs. Moreover, due to the larger standard deviations, no comparisons were made between plasma treated and non-treated PC.

3.2.2 Indentation Young's Modulus of substrates in the microscale

As AFM for material stiffness can result in low signal-to-noise-ratio due to adhesive forces on the surface, a second technique was used to evaluate the same experimental set up as discussed in 3.2.1. Using the PIUMA instrumentation provided by Optics11life, a micro-sized tip (50 µm) can be used to indent the surface for distances up to 10 µm. The increased distance is an important parameter when comparing results obtained using the AFM but allows to evaluate the material in greater depth. When setting the indentation depth to 10 µm for 2 seconds, the actual depth reached ranged between 1.27 and 3 µm using the current tip and measurement methods. The Young's Modulus is fitted directly in the Piuma Dataviewer, using a Hertzian Model, and fitting range of 20 % of the maximum load at the contact point. These parameters resulted in a fit where $R^2 > 0.95$.

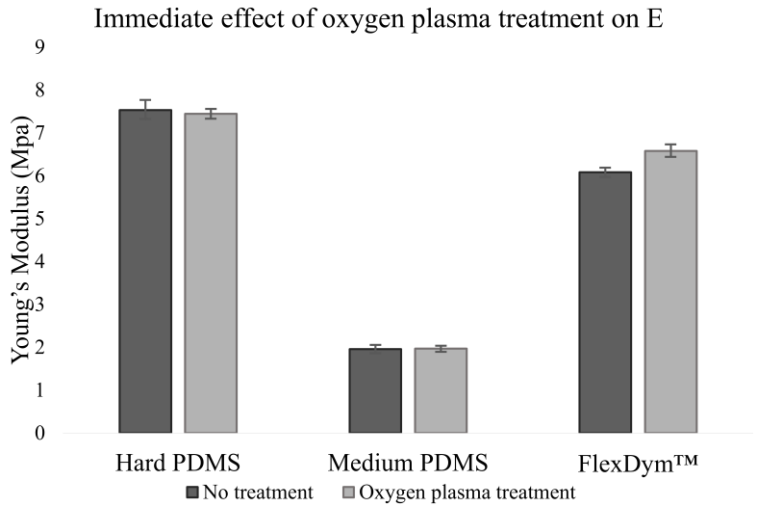

Figure 7: Effect of oxygen plasma treatment on the indentation Young's Modulus of substrates, immediately after treatment, measured using a 50 µm spherical tip.

The difference before and after the treatment seen in AFM measurements, was not seen using the PIUMA indentation (Figure 7). The indentation Young's Modulus of medium PDMS did not differ depending on the type of measurement, while the hard PDMS and FlexDym™ showed increased values compared to AFM measurements and values found in literature [18].

3.3 Adhesive properties of the substrates

Adhesion forces were determined from the force curves of the AFM measurements. Demonstrated in Figure 8, the adhesion expressed in nN is shown for substrates immediately before and after plasma treatment, and four days after the treatment. At both time points, a lower adhesive force between the substrate and the AFM tip, was observed on plasma treated PDMS and FlexDym™. This effect was observed on PC only after four days immersed in water. Hydrophilized surfaces thus demonstrated lower adhesive forces, which can affect protein adsorption and cell adhesion in future cell culture experiments.

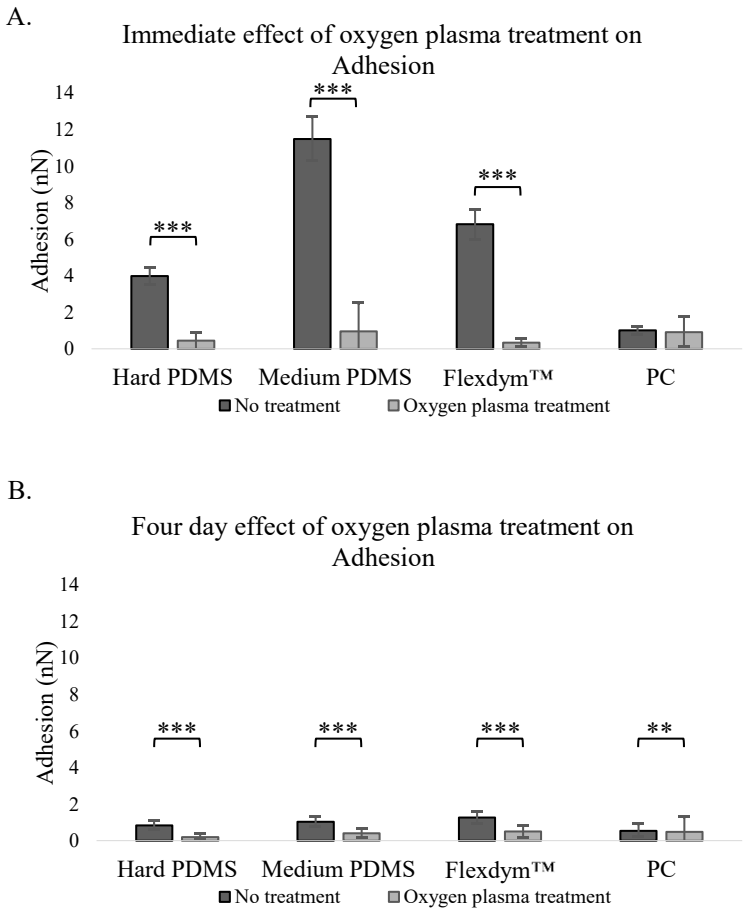

Figure 8: Effect of oxygen plasma treatment on the adhesive forces of the surfaces.
A. Adhesive force measurements immediately after plasma treatment or immersion in Milli-Q water. B. Adhesive force measurements four days after plasma treatment or immersion in Milli-Q water. ** $p < 0.01$, *** $p < 0.001$.

Examples of representative force curves on medium hard PDMS are illustrated in Figure 9 with the corresponding explanation of the force curve. Using the retraction curve in dark red, the adhesion can be calculated in the JPK data processing software. Additional force curves for all materials can be found in the supplementary materials.

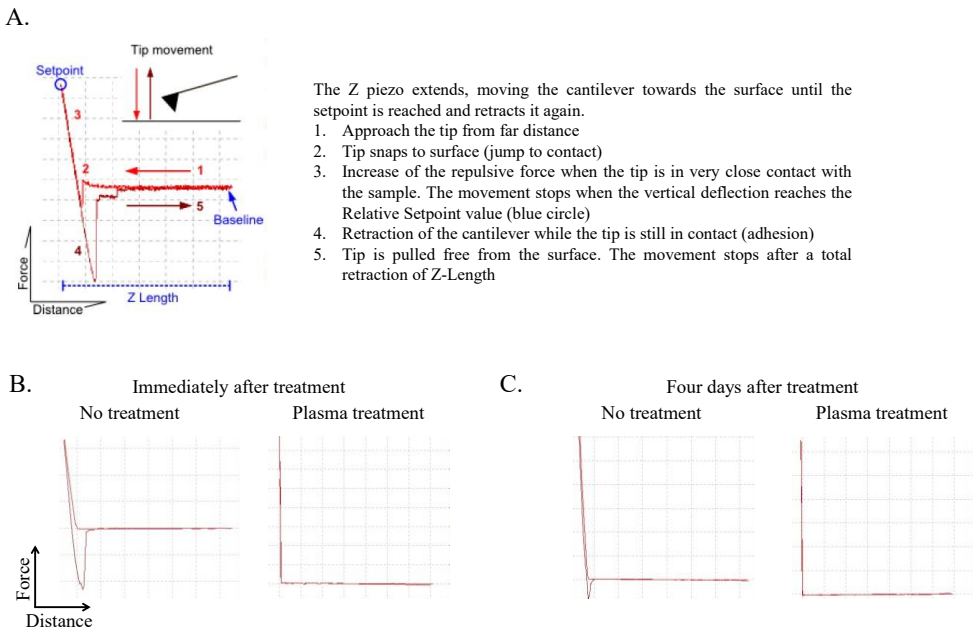

Figure 9: Adhesion identification on force curves of medium-hard PDMS.
A. Explanation of force curve meaning as given by JPK Nanowizard Manual [59] for the determination of the adhesion in the retraction curve of the AFM. B. Examples of medium hard PDMS force curves to visualise the adhesion component in the retraction curve, either immediately after submerging the sample in water without treatment, or after treating the sample with oxygen plasma and submerging the PDMS then in water. C. The same samples were also analysed after four days, to determine if the effect was solely observed immediately after treatment.

As observed in panel B and C of Figure 9, the oxygen plasma treatment decreases the adhesive effect on the AFM tip both immediately after and four days after the treatment. Furthermore, storing the PDMS in water for longer times decreases the adhesion between the AFM tip and the surface of non-treated samples.

3.4 Biocompatibility of the substrates

Apart from the ability to replicate the nanogrooves and maintain elastic properties, the substrates were also evaluated for their biocompatibility. To this end, C2C12 cells were used, which are a mouse myoblast cell line, able to differentiate into long, multinucleated myotubes.

3.4.1 Biocompatibility of polycarbonate for skeletal muscle cell culture

The first substrate evaluated is the PC master, where both the grooved and flat side of the master were used to evaluate cell culture. To unify the process across all substrates, the PC was cut in 18 mm x 18 mm squares to fit in a culture dish, sterilized, treated with oxygen plasma, and coated with fibronectin before cell culture. Cells adhered well and proliferated on the PC substrates to form a mostly confluent layer on day 4 in culture. By day 8, myotubes were visible that

maintained a stable layer on the surface until day 14 when they were fixed for imaging. Panel A of Figure 10 shows this evolution for cells on the flat PC surfaces, where the corresponding directionality of the cells is given in the spider plot. On day 1 and day 4 the direction in which the cells grow and adhere is mostly random, as can be seen by the large distribution of angles in the corresponding spider plots. When myotubes start forming, this direction becomes more uniform in a random angle. Patches of cells start to align, in the direction of the myotube formation, leading to a locally aligned cell layer.

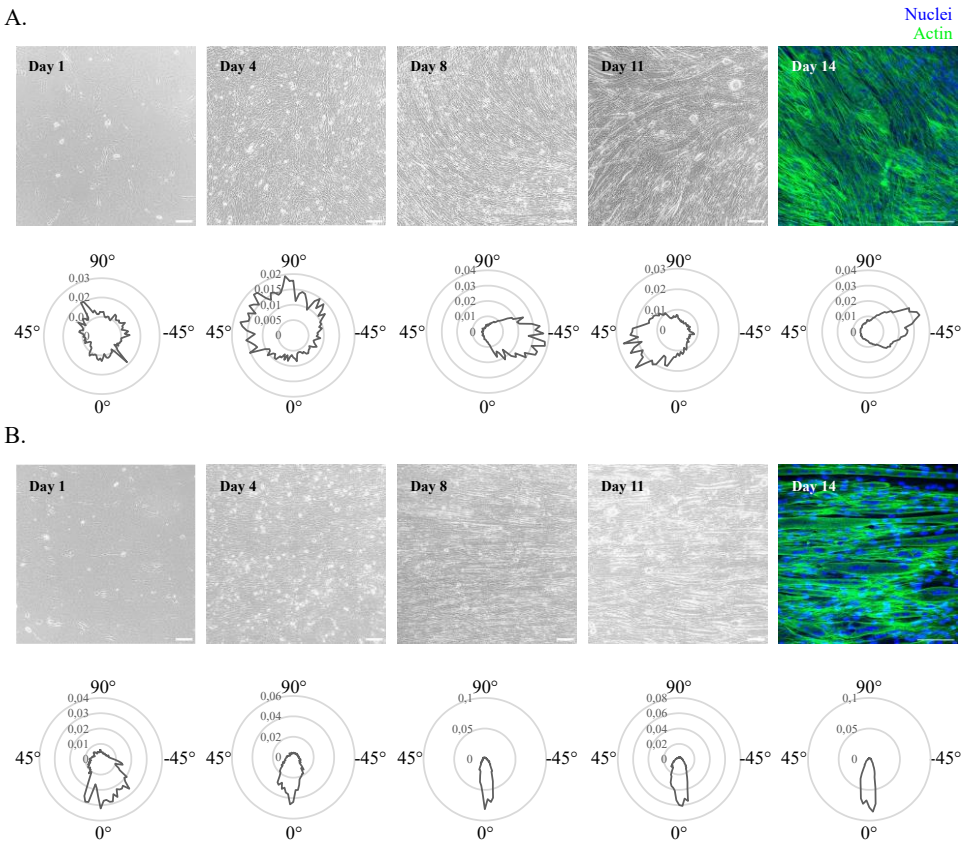

Figure 10: Biocompatibility of oxygen plasma treated PC substrates in time.
A. Flat PC substrates evaluated using C2C12 cells, with the corresponding directionality overview in time. B. Horizontally patterned PC substrates evaluated using C2C12 cells with the corresponding directionality overview in time. All spider plots show the frequency of cell aligning according to an angle between -90° and 90° where 0° equals horizontal alignment. Scalebars = 100 µm; Green = Actin; Blue = Nuclei

In panel B of Figure 10, these same plots and regions of interest are shown for cells cultured on patterned PC substrates. The direction of the pattern in all images, is horizontally aligned for a better comparison. On day 1 in culture, the majority of cells already aligns in the direction of the grooves, with some cells aligned

randomly, leading to a slightly wider corresponding spider plot. From day 4, when there is a confluent layer, all cells are mostly aligned in the direction of the grooves. Myotubes start forming parallel to the direction of the grooves as can be seen in the plot of day 8. These myotubes keep growing and maturing in the direction of the grooves, demonstrated in the figure on day 11 and day 14 in culture. Instead of a local alignment as seen on the flat substrates, on the patterned PC all the cells are collective aligned along the grooves. Both flat and patterned substrates sustained cell culture until day 14

3.4.2 Biocompatibility of polydimethylsiloxane for skeletal muscle cell culture

Similar as for PC substrates, for PDMS both grooved and flat surfaces were used to evaluate cell culture. All PDMS substrates were sterilized, treated with oxygen plasma, and coated with fibronectin before cell culture. Cells adhered well and proliferated on the PDMS to form a mostly confluent layer on day 4 in culture. By day 8, myotubes were visible on the flat surfaces but less on the patterned substrates. Panel A of Figure 11 shows this evolution for cells on the flat PDMS, where the corresponding directionality of the cells is given in the spider plot. On day 1 to 11 the direction in which the cells grow and adhere is mostly random, as can be seen by the large distribution of angles in the corresponding spider plots. When myotubes start forming and maturing, this direction becomes more uniform in a random angle as demonstrated in the spider plot of day 14.

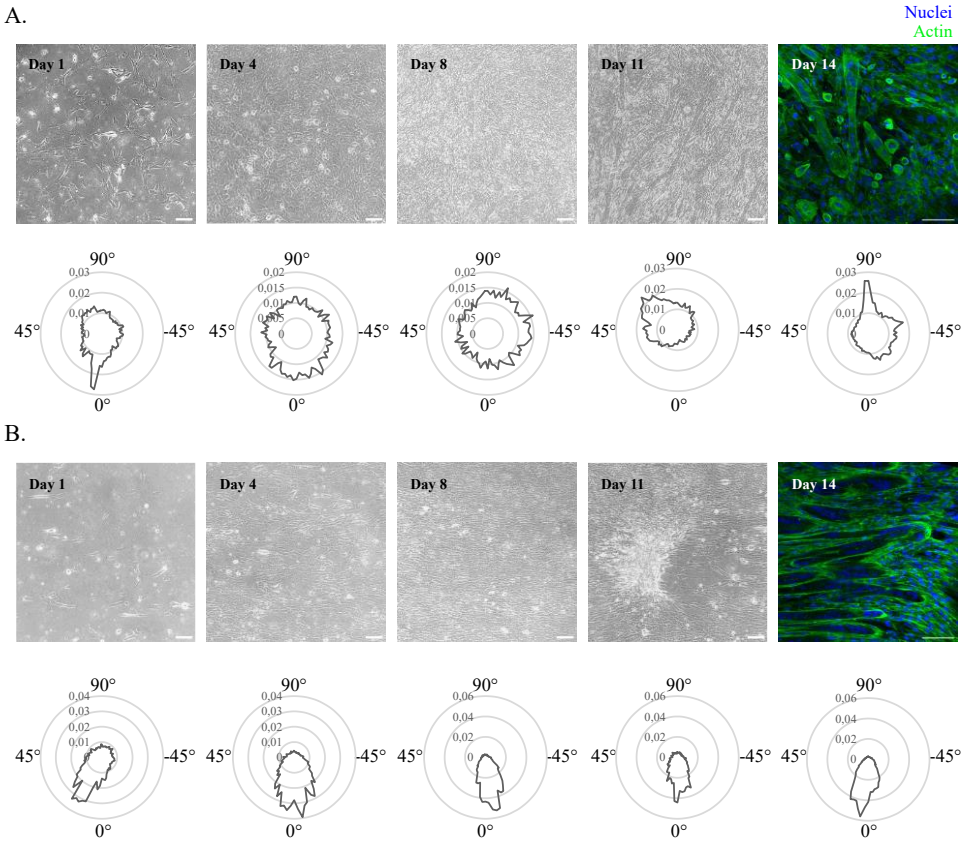

Figure 11: Biocompatibility of oxygen plasma treated, medium hard PDMS substrates in time.
A. Flat, medium-hard, oxygen plasma treated PDMS substrates evaluated using C2C12 cells, with the corresponding directionality overview in time. B. Horizontally patterned, medium-stiff, oxygen plasma treated PDMS substrates evaluated using C2C12 cells with the corresponding directionality overview in time. All spider plots show the frequency of cell aligning according to an angle between -90° and 90° where 0° equals horizontal alignment. Scalebars = 100 µm; Green = Actin; Blue = Nuclei.

In panel B of Figure 11, these same plots and regions of interest are shown for cells cultured on patterned PDMS substrates. The direction of the pattern in all images, is horizontally aligned for a better comparison. On day 1 in culture, the majority of cells already aligns in the direction of the grooves, with some cells aligned randomly, leading to a slightly wider corresponding spider plot. From day 8, all cells are mostly aligned in the direction of the grooves. Myotubes start forming parallel to the direction of the grooves as can be seen in the plot of day 11. These myotubes keep growing and maturing in the direction of the grooves, demonstrated in the figure on day 14 in culture. Instead of a local alignment as seen on the flat substrates, on the patterned PDMS all the cells are collective aligned along the grooves. Both flat and patterned substrates sustained cell culture until day 14.

Oxygen plasma treatment is used often on polymers like PDMS due to their hydrophobic nature. Cell culture of skeletal muscle myoblast cells on coated PDMS without oxygen plasma, was used to verify the necessity of the treatment for this material. As seen in Figure 12, cells grew on both substrates, with a similar density at the time of fixation. Patterned substrates with oxygen plasma treatment led to more myotubes compared to non-treated substrates but on flat substrates, no visual differences are observed.

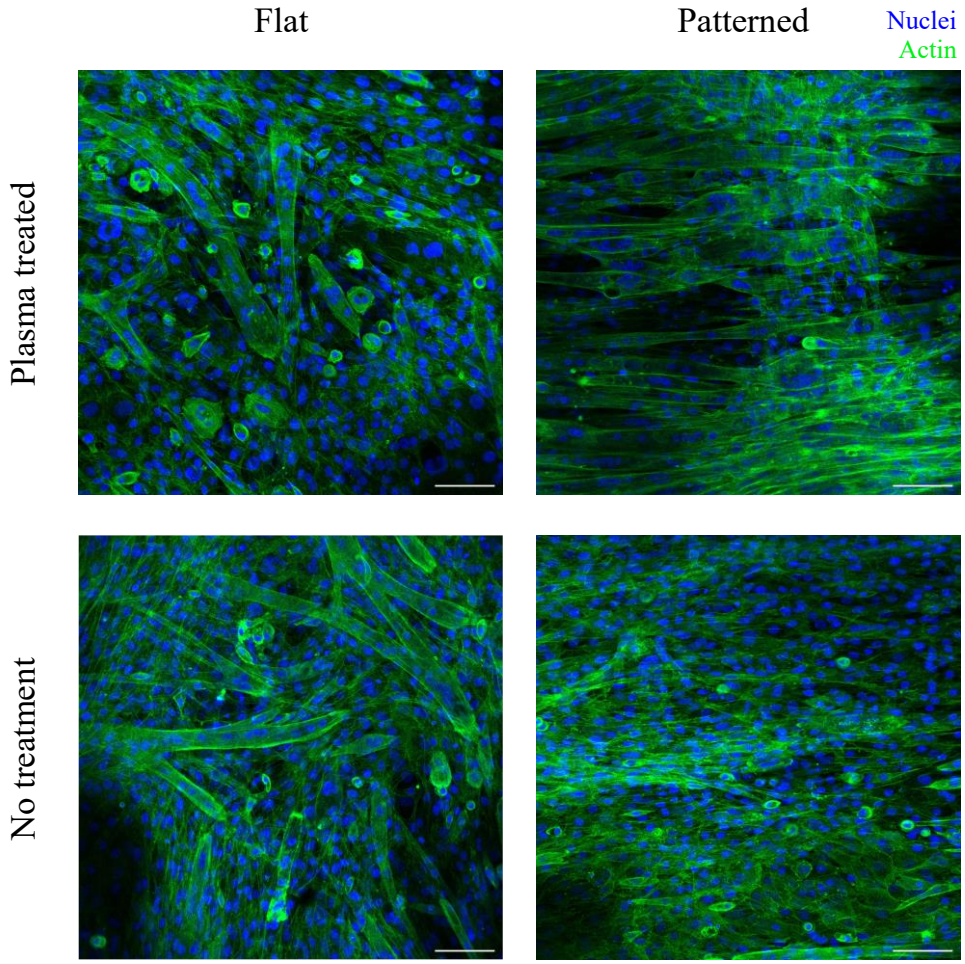

Figure 12: Comparison of oxygen plasma treated and non-treated, medium PDMS substrates for cell culture at 14 days in culture.
Comparison between cell seeded on oxygen plasma treated surfaces and non -treated surfaces both for flat and patterned substrates. Scalebars = 100 µm; Green = Actin; Blue = Nuclei.

Despite all surfaces supporting cell culture until day 14, later timepoints show less maturity and more detachment on non-treated PDMS compared to their oxygen

plasma treated counterpart. As an example, Figure 13 displays an example of substrates without oxygen plasma, fixed around day 21.

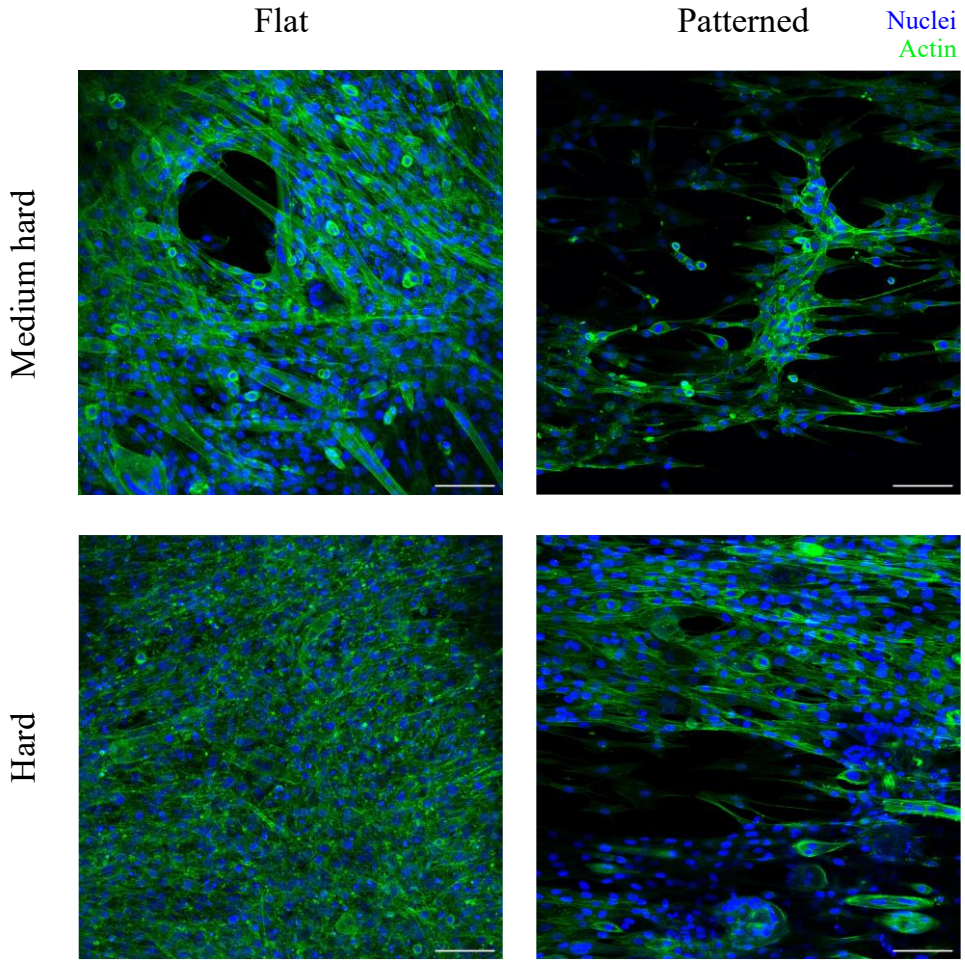

Figure 13: Non-oxygen plasma treated PDMS after three weeks in culture.
Longer culture time experiments using non-treated PDMS and fibronectin coating. Comparison between flat and patterned substrates for PDMS substrates with two different stiffnesses. Scalebars = 100 µm; Green = Actin; Blue = Nuclei

Both on flat and patterned substrates, the cells start to detach more and less thick myotubes appear on the substrates. Compared to oxygen plasma treated substrates, the non-treated substrates also fail to induce maturation of cells and eventual formation of a supracellular layer, as will be discussed in Chapter II. Increasing the stiffness of the substrates led to less myotube formation on non-treated flat substrates. No visual difference is observed on the patterned substrates, as both types present an equal portion of cells detaching of the substrate. Therefore,

increasing the substrate stiffness did not improve the adhesion of cells on substrates without oxygen plasma treatment.

3.4.3 Biocompatibility of FlexDym™ for skeletal muscle cell culture

Lastly, patterned FlexDym™ surfaces were used to evaluate cell culture. All FlexDym™ substrates were sterilized, treated with oxygen plasma, and coated with fibronectin before cell culture. Cells adhered well and proliferated on the FlexDym™ to form a mostly confluent layer on day 4 in culture. Figure 14 contains an overview of cell proliferation and direction at different points in time. For a better comparison, the direction of the pattern in all images is horizontally aligned. On day 1 in culture, the majority of cells already aligns in the direction of the grooves, with some cells aligned randomly, leading to a slightly wider corresponding spider plot. This trend continues until day 14 in culture, with the formation of myotubes in the direction of the grooves. Patterned FlexDym™ substrates sustained cell culture until day 14.

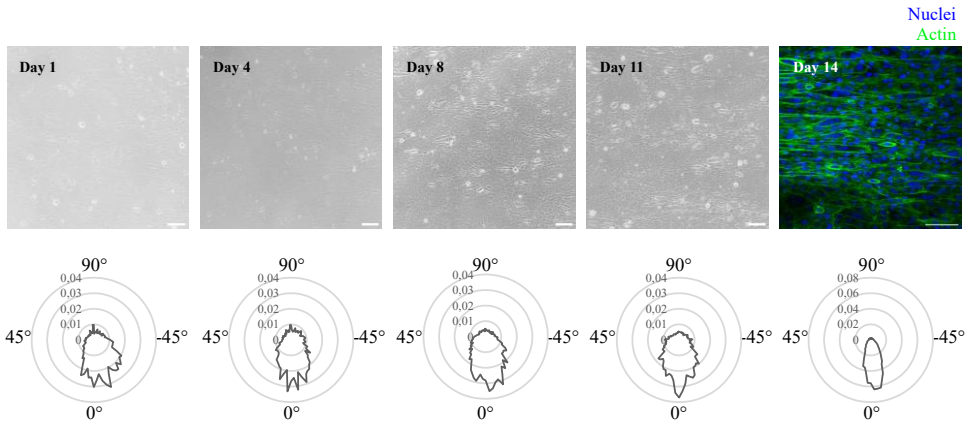

Figure 14: Biocompatibility of oxygen plasma treated, FlexDym™ substrates in time.
Horizontally patterned, oxygen plasma treated FlexDym™ substrates evaluated using C2C12 cells with the corresponding directionality overview in time. All spider plots show the frequency of cell aligning according to an angle between -90° and 90° where 0° equals horizontal alignment. Scalebars = 100 µm; Green = Actin; Blue = Nuclei.

Compared to the differentiation seen on PC and PDMS, myotubes seem to form later on the FlexDym™ substrates. Substrates on day 11 still consist largely of non-differentiated cells, compared to other substrates, indicating that FlexDym™ is less suitable for spontaneous skeletal muscle differentiation than PC and PDMS. Nevertheless, cells adhered and proliferated until day 14, indicating no observed impedance of cell viability.

4. DISCUSSION AND CONCLUSIONS

In this chapter, a comparison was made between different fabrication methods and substrates for a nanogrooved substrate to culture skeletal muscle cells. Polycarbonate (PC), polydimethylsiloxane (PDMS) and FlexDym™ were compared in their ability to recreate the grooves and maintain stable cell culture for at least two weeks. Furthermore, as PDMS and FlexDym™ are considered flexible materials with a Young's Modulus around 1-3 MPa, indentation Young's Moduli were determined for these materials before and after oxygen plasma treatment, to evaluate the effect of the treatment on the stiffness of the top layer. Cell culture experiments evaluated the biocompatibility, and the capacity of the grooves on each material to align the cells into forming an anisotropic cell layer.

4.1 Groove replication on PDMS and FlexDym™ substrates

A nanogrooved surface was replicated on PDMS using different curing temperatures and different vacuum treatments to compare the effectiveness of replicating the depth of the original pattern. Comparing hard and medium hard PDMS with nanogrooved FlexDym™ using SEM highlighted some macroscopic structures on top of the grooved surface for the case of FlexDym™. This additional topography might be caused by the detachment of the Flexdym™ from the master after the hot embossing step, or this phenomenon could be due to damage in of the layer before patterning. The nanogrooves were observed on all three types of polymers. PDMS replicated solely the grooves, with no additional microtopography, in contrast to the FlexDym™.

The fabrication methods for all three substrates were evaluated with AFM to measure the depth of the replicated grooves. Comparisons between vacuum treated and non-treated substrates revealed that curing the PDMS at 60°C, followed by vacuum treatment decreased the depth of the nanogrooves significantly for both hard and medium PDMS. When increasing the temperature from 60°C to 80°C, this effect of the vacuum treatment became negligible. Furthermore, medium stiff PDMS was able to recreate a higher depth of grooves than stiff PDMS.

When comparing PDMS and FlexDym™, both PDMS subtypes replicated deeper grooves than FlexDym™, with an average depth of 160.63 ± 11.52 nm.

Thanks to its liquid precuring form, PDMS is capable to more easily fill the grooves of the PC master compared to the solid Flexdym™ polymer sheets, leading to a more effective replication. Nevertheless, such small replication dimensions as the nanometric wide grooves, for Flexdym™ are useful when aligning cells and have not yet been reported in literature, where the smallest replicated feature was 10 µm [54].

4.2 Surface stiffness of PDMS and FlexDym™

Indentation of the surfaces, using a nanometric sized tip with AFM, resulted in observed Young's Moduli of the surface for PDMS and FlexDym™, both in line with reports in literature for non-plasma treated surfaces [18], [35], [36], [54], [60]. Treating the surface with plasma and consecutively measuring the Young's Modulus again, resulted in an increased value for the Young's Modulus for both types of PDMS immediately after treatment. When later measuring these values at 4 days after treatment, the treated PDMS continues to show an increase in the Young's Modulus. FlexDym™ values immediately after treatment first decreased, while showing an increase in Young's Modulus 4 days after treating the surface with oxygen plasma.

It is important to emphasize that these results are measured using AFM measurements, leading to small indentations only on top of the surface, with a nanometric sized tip. The tips used in this study had a force constant of 0.6 N/m and a radius of 20 nm. The indentation into the surfaces in these cases is dependent on the force with the vertical deflection limited to 20-50 nanometres. Resulting Young's Moduli thus represent only information about the surface layer of the substrate and not the bulk of the material. The choice of the tip for AFM measurements is influenced by the expected stiffness of the substrate. Because the substrates were found to have Young's Moduli in the MPa size in literature [18], [35], [36], [54], [60], the 0.6 N/m stiff AFM tip was chosen, in line with findings from Suriano *et al.* [61].

A potential cause of this stiffened surface can be the formation of a silica-like surface layer, thanks to the oxidation of the surface. This layer might be more rigid than untreated elastomeric surfaces [18], [62].

To get a deeper measurement of the indentations Young's Modulus, the PIUMA nanoindenter (Optics11) was used, where no difference was observed between samples before and after oxygen plasma treatment. However, the observed Young's Moduli for hard PDMS and FlexDym™ were 3 times as high as reported elsewhere in literature [18], [35], [36], [54], [60]. Values determined using this tool, are measured using a spherical tip, in contrast to the quadratic pyramid tip of the AFM. In literature, measurements with the pyramidal tip have been shown to be influenced by the depth of the measurement, with decreasing depths causing larger Young's Moduli [63]. This in contrast to spherical tips, which have been demonstrated to yield constant values [63].

Comparing both of these indentation experiments leads to the observation that the Young's Modulus of the substrates is solely increased on the upper layer of the substrate, with the effect disappearing when indenting at a micrometre scale.

Both measurements are valuable for the effect of the surface stiffness on cells. Cells, however, cannot feel the elasticity of the bulk of the material but rather detect the surface layer to which they adhere [64]. Experiments using thin 1 kPa gels with underlying glass substrates, demonstrated that cells were able to respond to the rigidity of an underlying surface on gels with a 5 µm thickness. The measurements carried out for FlexDym™ and PDMS indicate that cells initially might feel a stiffer substrate than expected, due to the oxygen plasma treatment used for cell culture experiments. Due to the materials used being in a much higher stiffness range, and the upper layer of the substrate having an even higher stiffness, it is not clear how deep the cells can feel on these surfaces and finite element modelling could provide some useful information with respect to this cellular property.

4.3 Adhesion forces of substrates decreased after oxygen plasma treatment

As demonstrated on Figure 8, adhesion of the substrate surface as measured using AFM decreased for PDMS and Flexdym™ immediately after oxygen plasma treatment to hydrophilize the surfaces. This effect was continued four days after treatment as well and measured for PC too at this timepoint. The decrease in adhesive force is in line with what was shown by Iturri *et al.*, for PDMS [18], where the adhesiveness of soft PDMS surfaces decreases when the surfaces became more hydrophilic.

The behaviour of cells differs depending on the used substrate, where studies have demonstrated differences between hydrophily and hydrophobic substrates when comparing, for instance, osteoblast (MC3T3-E1) attachment on UV treated and non-treated PDMS. Fibronectin coating revealed that on hydrophobic surfaces, the surface density of fibronectin was higher than on hydrophilic surfaces. However, cell adhesion and spreading on the treated surfaces was increased, regardless of the surface density of fibronectin, compared to non-treated, hydrophobic PDMS [65], [66]. Activating the PDMS surfaces was hypothesized to cause a favourable fibronectin conformation, leading to improved cellular function [65]. Another study stated that adsorption of fibronectin on hydrophobic and hydrophilic substrates leads to a conformational change, which is more drastic on hydrophobic surfaces [67], [68]. Some proteins denature to allow the protein to bind on the hydrophobic surface, by exposing the internal hydrophobic residues [69]. Increasing the surface energy of superhydrophobic layers with polydopamine provided a solution to increase cell adhesion [70]. These studies confirm the importance of hydrophilizing or chemically modifying the hydrophobic surfaces for cell culture, despite the observation of a decrease in adhesive force on all substrates.

Adsorption of the proteins on the different substrates is just the first step in a longer process where cells require modifications of the proteins for better cell function. It is suggested that surfaces on which the ECM proteins as fibronectin are adsorbed loosely, will result in better substrates for cell growth due to the cells being able to remove and organize the fibronectin, similar to physiological FN fibrillogenesis [71].

4.4 Substrates are able to maintain C2C12 culture for 14 days and align cells

Samples cultured on the three different substrate materials were all able to maintain cell culture for 14 days until fixation. In the presence of nanogrooves, the cells aligned in the direction of the grooves for the formation of an anisotropic layer. Cells are sensitive to a variety of cues, and the surface topography at the nanoscale has a particular effect on cellular behaviour through the mechanism of contact guidance [72], [73]. Features on this scale are much smaller than the cell size, but guide the growth in a specific way, with a unique cellular response for different cell types. In literature, evaluated materials include, for instance, grated Polystyrene [74] or PDMS [75] and aligned electrospun nanofibers of PMMA [76]. As previously reported, nano-topographical alignment was induced above a specific dimension for skeletal muscle cells and deemed effective on a variety of materials [77]. Different sizes of grooves previously used, range from 100 nm to 1.5 µm, with all studies showing enhanced alignment and formation of longer myotubes than on a flat culture dish [78], [79]. Most studies switch to differentiation medium after forming a confluent cell layer, to optimize differentiation efficiency and speed.

A recent study of Wu *et al.*, in 2021 [80], indicated suitability for C2C12 culture and alignment of the cells in the presence of grooves ranging from 100 to 900 nm width, with depts of maximally 100 nm. Grooved PC demonstrated a larger degree of differentiation than flat PC, assessed by the fusion index of myoblasts into multinucleated myotubes. Myoblasts did proliferate faster on a flat surface, while C2C12 cells on grooved topographies showed 19% slower proliferation [80]. C2C12 cells grown on nanogrooved PC, furthermore, showed a 40% increase in elongation compared to flat substrates. Differentiated myotubes were shown to be 34% longer on patterned PC compared to myotubes formed on flat PC. Moreover, said myotubes, showed better maturity on nanogrooved substrates, indicating significant improvement of the maturation under the guidance of topographical cues [80].

PDMS has, in the past, been shown to be able to support skeletal muscle cell culture. C2C12 cells cultured on flat PDMS substrates proliferate more rapidly than on grooved PDMS substrates, similar to PC substrates. One study compared

three different types of grooves on PDMS to flat PDMS. Included sizes were i) 890 nm groove width, 520 nm ridge width and 110 nm groove depth, ii) 420 nm groove width, 320 ridge width and 110 nm groove height, iii) 190 nm groove width, 120 nm ridge width and 17 nm groove depth. For PDMS, the presence of a pattern of any of these sizes resulted in a 15% slower growth rate when compared to flat substrates. On all patterned substrates, the cells showed a 74% increase in elongation and formation of 45% longer myotubes compared to flat PDMS [80].

Experiments on PC, with topography of 700 nm wide ridges and grooves with a ~ 250 nm depth carried out for comparison with PDMS and FlexDym™, demonstrated similar findings; the grooved substrates aligned the cells collectively in the direction of the grooves, with myotube formation starting from day 8 on both flat and patterned substrates. For flat substrates, a random direction of cell alignment was observed on day 1 and day 4, with a random global orientation from day 8. Cells cultured on patterned substrates show mostly uniform alignments from day 1, in the direction of the grooves. This trend was continued up until day 14 in culture, when the cells were fixed. On both flat and patterned PDMS, it was possible to culture and adhere cells for two weeks.

The observations showed the ability of both flat and patterned PDMS to maintain C2C12 for 14 days. By day 8 myotubes spontaneously formed on flat PDMS, while forming fewer myotubes on patterned PDMS at that time. Up until day 11 the direction of the cells was mostly random on flat substrates, and highly aligned along the direction of the grooves on patterned substrates. These results indicate that both types of PDMS sustain cell culture, with ~ 700 nm wide ridges and grooves of ~ 200 nm depth influencing cell alignment and directionality.

As FlexDym™ is a relatively new player on the market, no previous studies were conducted using C2C12 for cell culture on the polymer. As demonstrated in this work, the replication of the grooves is slightly less deep compared to PDMS substrates, for instance. However, the substrates were still able to align the cells and maintain longer cultures. On FlexDym™ surfaces the differentiation and maturation of myotubes was slightly impeded, resulting in shorter myotubes. Spontaneous differentiation was thus less effective on FlexDym™ substrates than on PDMS and PC, even though the substrate stiffness was similar to that of PDMS.

A possible cause might be the altered reaction to oxygen plasma treatment compared to PDMS, where the Young's Modulus of the surface increases not immediately after the treatment but over the course of 4 days. This in contrast to PDMS surfaces where this increase was observed immediately. As this is the first reported study using FlexDym™ for muscle cell culture experiments, there is no validation of these observations in literature. Further analysis to understand why

this difference occurs, even though PDMS possesses similar mechanical properties, is necessary.

4.5 Conclusion and future perspectives

This chapter has demonstrated that all introduced materials can be used to replicate the groove definition and provide depth to the grooves and ridges. When evaluating the Young's Modulus of the surface, AFM measurements showed a large increase in Young's Modulus after plasma treatment for the upper layer of the surface. The use of deeper and wider measurements with PIUMA, did not lead to similar observations and the Young's Modulus of the materials before and after treatment was considered constant. Moreover, the three materials supported cell culture and cell alignment of C2C12 cells up until 14 days in culture. On FlexDym™ myotube formation was less effective but cells adhered and proliferated.

Next steps include the evaluation of the nanogrooved substrates for 3D tissue construct formation and an evaluation of the mechanical identity of cells cultured on the grooved substrates. As there is a large variability in Young's Modulus and adhesion on the surfaces, further effort should be made to explore the effects on gene expression of the muscle cells and pinpoint the causes for the differences of cells seeded on PDMS and FlexDym™.

II. THE FORMATION OF *IN VITRO* 3D SKELETAL MUSCLE TISSUE CONSTRUCTS

1. INTRODUCTION

Skeletal muscle is an aligned, organised, and contractile tissue responsible for movements and the posture of the human body. It encompasses about 40% of the total body weight [81]. To understand the choices made for the design of an engineered niche, some knowledge of the skeletal muscle formation, system and regeneration is necessary. This chapter of the introduction will treat those subjects starting from the developmental origin to the adult skeletal muscle, with the regeneration of the tissue, its mechanobiological potential and its natural niche as important pillars for engineered muscles and muscle niches. In a second part, an overview is given of the currently used techniques and models in skeletal muscle tissue engineering.

1.1 Skeletal muscle biology

To understand choices made in the skeletal muscle tissue engineering approach, it is important to first demonstrate the formation, structure, and function of skeletal muscles briefly. This section highlights myogenesis, skeletal muscle structures, the known mechanobiology of the skeletal muscles and the skeletal muscle microenvironment.

The primary function of muscle is to generate movement or force upon a physiological stimulus. Skeletal muscle is responsible for the both the posture, voluntary movement of bones and the breathing cycle of the lungs, via the contraction of the diaphragm [81].

1.1.1 Skeletal muscle structure and function

Skeletal muscle tissue consists of bundles of fascicles, which each consist of bundles of myofibres (muscle cells) that in their turn consist out of myofibrils [82]. These myofibrils are composed of an array of contractile modules, called the sarcomeres, demonstrated in Figure 15.

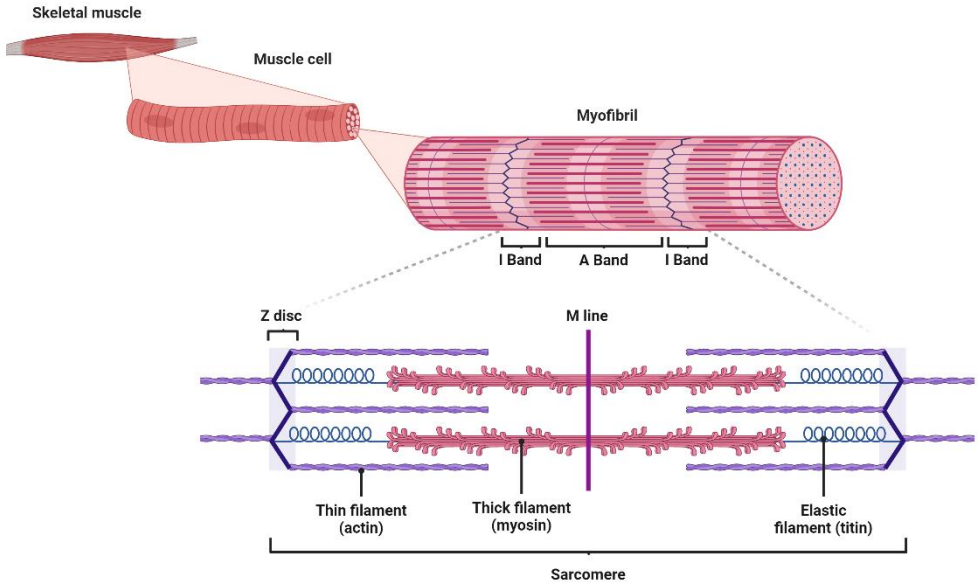

Figure 15: Overview of skeletal muscle tissue organisation from tissue structure to contractile unit. Created using Biorender.com.

Each myofibre is encapsulated by a specialized basal lamina, the endomysium [83], [84], while the fascicle bundles are encapsulated in the perimysium and the bundle of fascicles is enveloped by a thick collagenous sheet called the epimysium [81]. Beneath the endomysium lies the sarcolemma, which is a specialised plasma membrane, which provides structural stability. The sarcolemma anchors to the basal lamina through the dystrophin-associated glycoprotein complex [85], that connects the cytoskeleton of the fibre to the extracellular matrix (ECM).

The sarcomere can be divided into even smaller units called the myofilaments, which exist in two types, the thick filaments consisting mostly of myosin, and the thin filaments, consisting of actin [81]. The organisation of these filaments within sarcomeres, and the organisation of sarcomeres linked in series in the muscle cells, are responsible for the striated microscopic appearance of skeletal and cardiac muscles [86]. The organized structure of the skeletal muscle fibres and its connective tissues allow the generation of mechanical force. The process of muscle contraction is called the cross-bridge cycle, which is activated by adenosine triphosphate hydrolysis, causing the myosin and actin to bind. The filaments slide over each other and the contractile unit contracts. Force generation is influenced by the sarcomere length [81], [87].

1.1.2 Myogenesis and regeneration

Understanding how muscle is formed *in vivo*, will improve the techniques and understanding of creating muscle tissue *in vitro*. Therefore, the developmental origin will be briefly discussed, as to give an essential insight into this complicated process.

1.1.2.1 Myogenesis

Myogenesis is a multifaceted process that involves a number of precisely coordinated events. Skeletal muscles originate from progenitors in the somites [88], an embryonic structure originating from the paraxial mesoderm [88], [89]. In chicken and mouse embryos, myogenesis is initiated by myogenic factor Myf5, causing the progenitors specify and become myoblasts, which subsequently differentiate into post-mitotic mononuclear myocytes. Myocytes express slow and embryonic myosin heavy chains (MyHC), α-actins, and desmin [90]–[93]. These precursors further undergo fusion, resulting in the formation of multinucleated myotubes [88], [94].

Myogenesis during development is separated into two distinct phases, with the first one being an early embryonic (or primary) phase, followed by a later foetal (or secondary) phase. The early embryonic phase results in primary myofibres, providing the templates upon which adults muscles will be build [88]. During the foetal phase, a subset of myogenic progenitors begins to express Pax7. Precursor cells fuse either to themselves, or to primary fibres, resulting in secondary foetal fibres [89]. In this second phase, growth of the muscle is sustained by cell fusion and the addition of myonuclear derived from Pax7 positive progenitors [95]. This is in contrast to postnatal muscle growth, which results primarily from individual fibre hypertrophy. A subdivision of Pax7 positive cells will form the pool of adult stem cells known as satellite cells [96]–[98].

The mechanical microenvironment and mechanical cues are fundamental in different steps of the process of myogenesis. During the fusion of two cells, invasive protrusion of the “attacking cell” appear to inflict a mechanical force on the receiving fusion partner in Drosophila embryos [99], [100]. MyoII senses the mechanical cues in the receiving cells and accumulates as a response to the invasive force of the attacking cells. To promote cell-cell fusion, the accumulated MyoII increases cortical stiffness and tension of the receiving cells at the fusogenic synapse [101]. Pushing against a stiff cortex of the receiving myoblast, increases the stiffness of the invasive cell protrusions. The establishment of positive feedback mechanisms involving the mechanical forces, may facilitate overcoming the energy barrier to bring apposing cell membranes into close proximity, ultimately promoting fusion of the myoblasts [101], [102].

Mature skeletal myofibres possess an organized cytoskeletal structure consisting of aligned myofibrils. These fibrils are the result of fusion of the myocytes, for the formation of myotubes, that further mature into myofibres [103]. The fusion and its mechanisms are less well understood in vertebrates [104], but in fruit flies, two populations of progenitor cells were distinguished. The first population is a group of initiating founder cells, that fuse with adjacent fusion-competent myoblasts [105]. The fusion-competent cells produce actin-based podosome-like structures, which infiltrate the muscle founder cell, creating pores that facilitate the transfer of the cytoplasm and nuclei from the myoblast to the founder cell [101]. In vertebrates, fusion commences with a recognition and an adhesion phase, mediated by surface receptors. Evidence suggest that actin dynamics might be a key aspect [106].

The main skeletal muscle stem cell population is called satellite cells, which can be traced by to the Pax7 positive progenitors in the embryonic myogenesis [96]–[98]. The embryonic progenitors become the source of adult stem cells in the muscle [96], [107], [108]. Notch signalling maintains the pool of progenitor cells [98], [109] . In mice, satellite cells are enclosed under the basal lamina of myofibres.

In vitro formation of myofibres using pluripotent stem cells has presented a significant challenge, often resulting in differentiated cells retaining a foetal-like phenotype. Mature striated myotubes were successfully generated *in vitro* using murine embryonic stem cells [110], [111], and myotubes with mature characteristics have also been obtained from human pluripotent stem with Pax7 reprogramming [112]. Myotube formation using the latter technology, resulted in a slower maturation rate. Furthermore, millimetre-long myofibres were achieved, in serum-free conditions presenting MyHC positive striations from both human and mouse pluripotent stem cells [113].

Adult myofibres express specific MyHC isoforms, associated with different electrophysiological properties and metabolisms. Glycolytic fast twitch fibres express fast MyHC, whereas oxidated slow twitch fibres express slow MyHC [114].

1.1.2.2 Skeletal muscle regeneration

After damage, skeletal muscle fibres can repair themselves efficiently in healthy tissues thanks to its large regenerative capacity. In healthy tissue, this process is divided into three stages: i) the inflammatory phase, ii) the phase of satellite cell activation, differentiation and fusion and iii) the maturation phase [115]. Necrosis of myofibres triggers the immune response by recruiting circulating leukocytes and neutrophils followed by macrophages [116]. During the next step, the

normally quiescent satellite cells are activated and initiate to differentiate into myoblasts that fuse with the damaged muscle fibres [117]. Other cells with myogenic potential such as mesoangioblasts have been demonstrated to target the damaged site and fuse with the fibres as well [118]. During the third and final step, the newly regenerated myofibres mature, and their nuclei migrate towards the periphery of the cell [119].

In chronic injury and diseases, the myofibres are continuously damaged and the satellite cells are constantly activated [120]–[122]. For instance, in age-related muscle mass loss, a decreased number of satellite cells has been reported. Together with the continuous activation, this leads to a depletion of the stem cell pool. Diseases such as Cerebral Palsy, show a similar behaviour, leading to impaired muscle regeneration [123].

1.1.3 Skeletal muscle mechanobiology

Skeletal muscle exhibits a remarkable capacity for adaptation and regeneration, with its structural and functional attributes intricately shaped by the mechanical and physical surroundings [124]. Processing intra- and extracellular mechanical signals, contributes to the regulation of processes such as cell growth, viability, migration, and differentiation [125]. The tissue has a fundamental mechanical role and is equipped with various structures involved in detecting mechanical forces [126]. Muscle activity and exercise are recognized regulators of skeletal muscle mass. Increased mechanical loading leads to muscle hypertrophy, while reduced mechanical loading and inactivity lead to muscle atrophy [127]. Numerous signalling molecules have been identified, associated with this process [128], [129], such as, the rapamycin-sensitive complex mTORC1. An increase in activity of mTORC1 is observed in response to increased muscle loading [129]. Both in cell culture experiments and *in vivo* model systems mTORC1 has shown to be activated by a wide range of mechanical stimuli [128].

Stretching C2C12 myotubes activated different types of anabolic pathways depending on the type of stretch (uniaxial or multiaxial). Using uniaxial stretch an increase in activity levels of protein kinase B (AKT) and extracellular signal-regulated kinases were observed, while activity of mTORC1 did not change. On the contrary, multiaxial stretch of myotubes triggered the mTORC1 activity [130].

Nuclear mechanotransduction is likely of importance to skeletal muscle physiology. Force transmission from the cell periphery to the nucleus involves intricate interplays between the cytoskeleton, the Linker of Nucleoskeleton and Cytoskeleton (LINC) complex and nuclear envelope associated proteins such as lamins. Mechanical forces exerted can induce alterations in nuclear lamina polymerisation, efficiency, nuclear elasticity, and deformability. Alterations in

nuclear mechanotransduction are likely to impact the architecture of the nuclei and the response, contributing to muscle dysfunction in diseases. Perturbations of the LINC complex have been demonstrated to cause, for instance, Emery-Dreifuss muscular dystrophy, when Nesprins1-and -2 are mutated [131]–[134]. Furthermore, laminopathies include skeletal muscle dystrophies and are characterised by an A-type lamins mutation [135]. These examples show the importance of the nuclear environment and mechanotransduction and are reviewed in more detail, elsewhere [136]–[138]. Mutations specifically in the LMNA gene impair the YAP regulation by increasing nuclear import [139].

YAP/TAZ and the Hippo signalling pathway have emerged as pivotal components in mechanotransduction processes of the skeletal muscle tissue. It exerts influence over myogenic activities and the regenerative capabilities of muscle tissue, with abnormal YAP activity being implicated in conditions such as muscular dystrophy [140]. It has been recognised for its role in muscle mass regulation, with YAP overexpression leading to skeletal muscle hypertrophy, and an increase in YAP observed in skeletal muscle cells following mechanical overloading [141]. YAP is involved in cell fate decision in different stem cell pools but in the skeletal muscle, since YAP activity promotes proliferation of satellite cells, while blocking differentiation [142]–[145]. It influences migration, which is crucial for activated satellite cells to migrate to the site of injury in skeletal muscle regeneration processes [140].

Mechanosensitive calcium channels and titin (a structural sarcomeric protein) have been identified as mechanosensors within skeletal muscle [126], [146], [147]. These elements undergo conformational changes in response to mechanical loading, thus leading to skeletal muscle mass regulation [148]–[150]. Calcium channels, for instance, can be activated in response to mechanical stress, due to interactions with the lipids surrounding the channel, proteins of the ECM or with another primary mechanosensor such as angiotensin II receptor type I [126].

A better understanding of all processes surrounding the mechanobiology of muscle, will likely provide interesting knowledge for therapeutic strategies for the treatment of muscular dystrophy or muscle atrophy, for instance [151], [152].

1.1.4 Skeletal muscle microenvironment

Inside skeletal muscles, the residing stem cells (or satellite cells) are localised in a specialised niche between the sarcolemma and the basal lamina that surrounds the muscle [153], [154]. Inside this niche, the ECM components are mostly fibronectin, laminin and collagen, and satellite cells are able to interact with them through a7- and B1 integrin and dystroglycan interactions [84], [155]. A variety

of muscle disorders are caused by defects of the ECM, leading to altered interactions and behaviour of satellite cells [156].

The skeletal muscle ECM is composed of three distinct layers called the epimysium, perimysium, and endomysium, as discussed in section II.1.1.1. The three layers contain specific ECM molecules such as collagen-I and fibronectin in the epimysium, collagen-I, -III and -IV and fibronectin in the perimysium and collagen-IV, laminin, and fibronectin in the endomysium [157]–[165] .

In the skeletal muscle tissue, collagen is the most abundant component of the ECM [160]. Fibroblasts, fibro/adipogenic progenitor cells and skeletal muscle progenitor cells are able to and responsible for producing collagen within the tissue [166]. Increases in collagen content of the muscle has been shown to contribute to muscle stiffness and decreased mechanical performance [167]. Type I collagen, for instance, has been shown to significantly impede myogenic differentiation [168], but can contribute to migration and proliferation of myoblasts [169], [170]. Type IV collagen is important in the basal lamina where it promotes Insulin-like growth factor I (IGF1) mediated processes such as migration, differentiation, and fusion [171].

Laminin is located in the basal lamina of the muscles, where it promotes both expression and activation of integrin [157], [172]. Laminin enhances the proliferation, differentiation, and adhesion of muscle cells [173], [174]. The inherent expression profiles of different subtypes of laminin protein chains are valuable for the regeneration of damaged skeletal muscles. Laminin-1 plays a pivotal role in the adhesion of muscle fibres to the basal lamina and improves muscle performance of mdx mice [160]. Injection of Laminin-111 in dystrophic mice contributes to the stabilization of the basal lamina and provides protection of the muscle in sports related injuries [175]. Furthermore, the activation of satellite cells during the regeneration process is accompanied by an upregulated of Laminin expression [176].

Fibronectin is localised within the epimysium, perimysium, and endomysium of the skeletal muscle. It is secreted by fibroblasts and activates integrin proteins through the focal adhesion kinase pathway [177]. Fibronectin has a dual role in myoblast behaviour, where it promotes the adhesion and differentiation of myoblasts, but inhibits their migration and division [173], [178]. Moreover, fibronectin facilitates the fusion and linear alignment of myotubes during differentiation [179]. The expression level of fibronectin has been demonstrated to influence the remodelling of the niche, affecting satellite cell behaviour [180]. Loss of fibronectin in aged niches, affects the regenerative capacity of skeletal muscles and lead to a loss of satellite cells present in the tissue [181]. Fibronectin

has been demonstrated to be the preferred adhesion substrate for muscle stem cells, and cell culture on fibronectin coated substrates was shown to alter the activity a number of signalling pathways involved in adhesion and cell matrix interactions [181]. Further cell culture experiments on fibronectin coated substrates demonstrated that fibronectin induces a collective migratory behaviour [179].

1.2 Skeletal muscle tissue engineering

Tissue engineering stands as a multidisciplinary field where biology, engineering, and medicine are combined to address the need for functional tissue generation and models [182]. The field represents a promising pathway to tackle the challenges posed by organ dysfunction, degenerative diseases, and the replacing of animal studies. Central to the idea of tissue engineering, is the idea to mimic the architectural and structural precision of natural tissues [183]. Native tissues exhibit complex structures, hierarchical compositions, and biomechanical properties that showcase optimal functions [184], [185]. Tissue engineering tries to replicate these attributes *in vitro* by developing and utilizing biomaterial scaffolds, cellular constituents, and regulatory cues. The fusion of these elements orchestrates the correct assembly, growth, and differentiation of cells into functional tissue constructs [186].

Many innovative strategies have been developed to tackle the challenges posed by tissue engineering. For instance, techniques such as 3D bioprinting enable the precise deposition of cells and biomaterials to recreate tissue-like structures. Hydrogel matrices, sourced from biological tissues, offer an ECM-like framework that promotes cellular adhesion, migration, and differentiation [187]. Moreover, recent advancements in stem cell technologies empower the cultivation of specialized cell populations, which can be made responsive to specific biochemical and mechanical stimuli, enabling desired cellular fates.

Skeletal muscle tissue engineering is useful to study the dynamic interactions between skeletal muscle cells and ECM components. The created models offer insights into muscle development and function and can improve the understanding of muscle dystrophies. The following section highlights different strategies used for the generation of skeletal muscle models and demonstrates their importance in the understanding of muscle biology and associated diseases.

1.2.1 Hydrogel based approaches in Tissue Engineering

Hydrogels consist of a 3D polymer network, which retains its structure in aqueous phase, without dissolving. They provide mechanical support and, for some tissues, mimic the native extracellular environment [188].

1.2.1.1 General principles and applications of hydrogels

Hydrogels are pivotal materials in tissue engineering and offer a versatile platform for constructing functional tissues. These 3D hydrophilic polymer networks showcase exceptional biocompatibility and tuneable physical properties, making them ideal candidates for mimicking the ECM and supporting cellular processes [186].

Hydrogels can be categorized based on the materials used, identifying three main groups: natural, synthetic and hybrid or combination hydrogels [186]. Natural hydrogels like collagen, gelatine, and fibrinogen are derived from ECM components and offer biocompatible environments enriched with cell-adhesive motifs. They facilitate cell growth and resemble the native tissue environment. Naturally derived hydrogels are characterized by high biocompatibility, biodegradability, and low inflammatory response [189]. However, while these natural hydrogels provide valuable biological cues, their limitations in precise control over the various mechanical properties and their high variability have led to exploration of synthetic or hybrid hydrogels [189], [190]. Synthetic hydrogels, typified by materials like polyethylene glycol (PEG) [191] and polyacrylamide [192], provide tunability in mechanical and physical properties, addressing the shortcomings of natural counterparts. Even though these synthetic hydrogels are inherently resistant to protein adsorption, they can be chemically modified and cross-linked to enhance cell adhesion and mimic biological functionalities [193], [194]. Techniques such as photo-cross-linking allow precise modifications of these hydrogels, tailoring them for applications in tissue engineering applications [193]. The combination of natural and synthetic hydrogels, along with advanced fabrication techniques, is being studied to address the limitations of current clinical treatments for extensive muscle damage. Hybrid hydrogels offer a high degree of diversity in materials and components, with advantages depending on the chosen combination. Their creation is more time consuming and appears to have a higher cost associated with the fabrication and use [195], [196].

1.2.1.2 Applications of hydrogels for skeletal muscle tissue engineering

Examples of the use of hydrogels for skeletal muscle fabrication include, for instance, Collagen since it is a major component of the ECM [197]. Other natural polymers include alginate, fibrin, and agarose. One study compared these different polymers and discovered that fibrin had the highest myogenic potential, followed by collagen [198]. Fibrin hydrogels have been implanted in mouse models with a muscle defect, where they showed the capacity to form myotubes and withstand tension application [199]–[201]. Another example using natural hydrogels incorporated laminin within fibrinogen gels. Increases in myoblast proliferation and secretion of growth factors were observed, while addition of tensile and

electrical stimulation improved the alignment of the cells within the scaffold [202].

Synthetic hydrogels like polyurethane-, polylactic acid-, or polyethylene glycol-based scaffolds have been suggested for skeletal muscle formation, however, they are less favoured compared to natural scaffolds [197], [203]. A self-folding system using PEG diacrylate was designed to mimic muscle fascicles to control cell adhesion and spatial alignment [193]. A synthetic PEG based hydrogel was used for the delivery of satellite cells and myogenic factors for skeletal muscle regeneration [204].

Using hybrid hydrogels, scaffolds with improved regeneration capacity are created [205], [206]. Efficient myotube formation was demonstrated using a PEG-fibrinogen hydrogel. The scaffold with cells was later implanted into mice, where the presence of mature myofibres and blood vessels was shown [207]. Using protein-PEG hydrogels to liver induced pluripotent stem cells after ischemic injury in mice demonstrated reduced necrosis and a high number of myofibres compared to non-cell-laden hydrogels [208].

1.2.2 Bioprinting approaches in Tissue Engineering

Bioprinting for tissue engineering describes the field where additive manufacturing using biocompatible materials and cell-laden materials are used for tissue engineering. The following sections briefly describe advancements and the state-of-the-art in this field of tissue engineering for skeletal muscle tissues.

1.2.2.1 General principles of bioprinting in tissue engineering

3D bioprinting uses layer-by-layer printing of biological materials and living cells. With 3D bioprinting, constructs and tissue layers are built with spatial control using ECM elements, biomaterials and living cells [209], [210]. Most 3D bioprinting approaches have some steps in common such as i) the creation of a computer model, ii) processing of this model to create a real-life 3D model iii) post-processing to improve the tissue or organ development [211]. Techniques used are, for instance, micro extrusions, inkjets and laser-assisted bioprinting platforms [212]. With micro extrusions, a precise amount of bioink is guided through a needle, using pneumatic pressure. Micro extrusions work with sticky liquids and recent reviews indicated a 100 µm resolution [213]–[215]. Inkjet offers low-cost and high resolution, but was recently reviewed as unable to offer a continuous flow or a good vertical structural functionality [213], [215]. In laser assisted bioprinters, high energy lasers can be used to create the pressure system that excretes the biomaterial [216]. The drawbacks of this method are high cost and possible thermal damages due to the lasers. However, the resolution of 10 µm might be necessary for specific tissue applications [212]–[214].

3D bioprinting offers advantages such as simplicity of models, precise deposition, and controllable cell dispersion, but extensive research remains necessary to find novel bioinks suitable for different types of tissue [214]. Optimizing the bioink composition (balancing biocompatibility, mechanical strength, and degradation kinetics) poses a substantial challenge. This challenge necessitates continuous refinement to mimic, for instance, the native muscle microenvironment faithfully [214].

1.2.2.2 Applications of bioprinting for skeletal muscle tissue engineering

Within skeletal muscle tissue engineering, diverse bioprinting strategies exist, including, for instance; i) cell-based approaches, ii) construction of parallel aligned muscle fibres, iii) vascularized construction, and iv) neural construction [217].

The cell-based strategy focuses on using myoblasts, like C2C12 cells, encapsulated within specific hydrogels for 3D muscle tissue models [218], [219]. The aim is to create suitable bioinks that allow cell proliferation, alignment, and differentiation. For instance, a study by Alheib *et al.* [220] combined gellan gum with laminin-derived peptides to form hydrogels that exhibited favourable properties for bioprinting, including shear-thinning behaviour. Another approach introduces a coaxial nozzle system enabling the deposition of multiple materials and cells, either at the same time or consecutively, improving complex tissue structures [219], [221].

Achieving alignment in muscle fibres is important for mimicking natural muscle structures. Various approaches, like using oxidized alginate-gelatine hydrogels or thermally responsive block copolymers, have demonstrated successes in inducing cell alignment [222]. Researchers have manipulated extrusion parameters, such as nozzle size and pressure, to achieve higher directional arrangement of myoblasts within the printed structures [223]. Additionally, pre-culturing bioinks or introducing specific peptides or hydrogels has shown promise in promoting myoblast alignment and subsequent differentiation [223]–[225].

Furthermore, creating a vascular construction system within the bioprinted muscle tissue is crucial for ensuring nutrient and oxygen supply. Studies have explored using acellular matrix components, including tissue-specific vascular network skeletons and active cytokines, to encourage endothelial cell growth and formation of functional vascular channels [226]. Sacrificial support materials, such as gelatine, have been utilized to generate hollow structures resembling blood vessels within the printed tissues. Incorporating growth factors and specific bioinks has been effective in promoting angiogenesis and vascularization within the printed muscle structures [227].

Lastly, the integration of neural components, especially neuromuscular junctions (NMJs), is essential for regenerating functional muscle tissues. Researchers have used various bioink compositions, including those containing neural cells like mouse embryonic motor neuron-enriched spinal cord cells, to form structured NMJ models [228]. Additionally, introducing neurotrophic factors (NFs) has shown promise in promoting nerve regeneration and NMJ formation within bioprinted muscle structures. The sustained release of NFs through microsphere-based delivery systems has been explored to enhance neural integration within the printed tissues [229].

Despite the various advances made in the last years, significant challenges remain present. Developing bioinks that closely mimic the native microenvironment of skeletal muscle tissue stands as a crucial goal in 3D bioprinting. While combining various hydrogels enhances functionality, challenges persist due to material limitations and the need for optimal biological and mechanical properties [221]. Advancements are required in hydrogel performance, new cross-linking processes, and enhancing differentiation efficiency of available cell sources like mesenchymal stem cells (MSCs). Moving towards 4D bioprinting [230], characterized by stimuli-responsive bioinks [231], represents a promising direction. Yet, challenges regarding understanding mechanisms and improving smart hydrogels' performance remain [205], [232].

Furthermore, vascularization is critical for the viability and maturation of large engineered muscles [227]. Methods utilizing sacrificial materials show promise in fabricating vasculature, but replicating complex vascular networks matching host tissues remains a significant challenge. Achieving precise micro-to-large vascular networks remains a hurdle, necessitating a deeper understanding of vascularization mechanisms, efficient growth factor utilization, and risk assessments for materials and strategies [233].

Efforts in bioprinting have the goal to replicate the native structure of skeletal muscle, emphasizing uniaxial muscle cell alignment [219]. Cellular function, orientation, and differentiation significantly rely on biochemical and biophysical cues within bioinks. The establishment of neuromuscular junctions (NMJs) and the integration of host nerves into bioengineered skeletal muscle structures are crucial for functional recovery. Despite promising results, the full potential of bioprinting in achieving innervation capacity remains untapped [234].

1.2.3 Microfluidic approaches in Tissue Engineering

Microfluidics, using both micro-electromechanical systems and fluidic mechanics, presents a versatile platform for handling fluids with exceptional precision in both spatial and temporal dimensions [235]. This technology enables

careful control over fluid volumes ranging from nanolitres to picolitres [236]. Its applications span across a manifold of fields including environmental, manufacturing, and biological sciences. In biotechnological domains, microfluidics has made substantial progress, particularly in creating lab-on-a-chip platforms [237]–[240], water quality control [241]–[243], biomolecular analysis [244], [245], and personalized medicine [246]–[248].

1.2.3.1 General principles of microfluidics in tissue engineering

The unique behaviours of fluids in the micro-domain, governed by surface tension and energy dissipation, have paved the way for miniaturization of systems, including lab-on-a-chip technologies. Microfluidics facilitates the growth of cells in diverse configurations, from adherent monolayers to complex 3D tissue models created through self-assembled cell aggregates or seeded onto scaffolds [249], [250]. The limitations of conventional static culture methods have driven the emergence of microfluidic cell cultures, which employ controlled fluid flows on a micrometre scale to generate more *in vivo*-like environments [249]. Organ-on-a-chip systems developed through microfluidic technologies have gained traction, mimicking specific aspects of human physiology *in vitro* across various organs such as liver, lung, gut, skin, kidney, brain, bone, eye, heart, and muscle [238]–[240], [251]–[257].

Microfluidic devices allow the growth of cells in hydrogel-based microenvironments, enabling the replication of physiologically relevant 3D cellular structures [258]. These devices also offer the capability to engineer perfusion systems that sustain cell survival within large tissue constructs. The integration of microfluidics in tissue engineering benefits spatial control of fluids in micrometre-sized channels, co-culture system engineering, signalling gradient control, and perfusion/flow regulation for cells. Additionally, microfluidic approaches support the evolution of biological constructs and the production of micro-engineered units necessary for tissues with elevated complexity such as skeletal muscles [259].

Hydrogel-based microfluidic systems offer promising prospects in tissue engineering by providing a biocompatible environment. Despite challenges in their fabrication, the potential for hydrogel integration in microfluidic systems garners significant interest due to their enhanced bio-integrability compared to conventional chip materials like PDMS [260].

1.2.3.2 Applications of microfluidics for skeletal muscle tissue engineering

Microfluidic platforms offer a unique opportunity to dissect muscle functionality at various levels, from observing single-cell behaviour to exploring complex interactions with diverse cell types, such as motoneurons [261]. These

microfluidic systems allow real-time monitoring within precisely controlled microenvironments, facilitating in-depth investigations into skeletal muscle biology [262].

At the cellular level, microfluidic tools allow to unravel the mysteries of myoblast migration and their responses to a multitude of molecular factors and ECM stimuli [263], [264]. Traditional 2D cultures have limitations in assessing cell migration responses accurately for dynamic 3D regeneration processes [265]. Researchers have harnessed microfluidic approaches to bridge the gaps, enabling longitudinal, quantitative, single-cell migration analyses. For instance, Ferreira *et al.* [266] highlighted the shortcomings of traditional transwell assays in producing stable gradient concentrations required for precise quantification of chemotaxis phenomena. Their microfluidic setup facilitated extensive analyses of primary human myoblasts, delivering crucial insights into the impact of ECM alterations due to ageing or diseases on muscle fibre regeneration, migration, and proliferation dynamics [266].

Moving into the functional unit level, microfluidic chips have been designed to create cell-laden fibre-shaped constructs [262]. These constructs, like building blocks, play a vital role in assembling higher-level structures that resemble the complex hierarchical architecture of human organs. Interestingly, this approach showcased the gradual dispersion of cells within ECM-protein/Ca-alginate microfibers, replicating fundamental living tissue functions [262], [267].

On the tissue level, microfluidic systems have been utilized to expand the understanding of muscle contraction dynamics. For instance, Shimizu *et al*., [268] developed a 3D contractile skeletal muscle tissue cultured within microfluidic channels. This model successfully demonstrated tissue contraction upon electrical stimulation, offering valuable insights into muscle physiology [268]. The interaction between muscle cells and motoneurons, essential for coordinated muscle contraction, has been thoroughly studied using microfluidic models. These studies resulted in the creation of artificially functional neuromuscular junctions and provided a robust platform to model degenerative processes [269].

While these advancements mark significant strides in skeletal muscle tissue engineering, a multitude of challenges persist in replicating the complex characteristics of *in vivo* muscle fibres using microfluidics. Some of the key considerations include metabolic activity, oxygen consumption, and nutrient delivery. More physiologically relevant models are needed for future application such as comprehensive drug screening and toxicological assessments in a controlled environment [270], [271].

1.2.4 Engineering artificial niches for Tissue Engineering

A promising novel approach in tissue engineering are stem cell niches, which play a pivotal role in tissue development, regeneration, and maintenance. These niches serve as crucial microenvironments that regulate the transition of progenitors into adult cells. The niches develop initially in embryogenesis and can undergo changes throughout its lifespan, impacting their regenerative potential [272]. Across various tissue systems, these niches share common features, orchestrating the maturation, self-renewal, and activation of cells during regeneration processes [273].

To this end, designing (bio)materials that mimic the complex, nanoscale features of the local environment, presents a valuable approach to expend *in vitro* models [274].

Approaches specifically to mimic the niche of cells or tissues, include a variety of techniques, comprising the aforementioned techniques as well. The importance of the extracellular environment has already been highlighted in hydrogel, 3D bioprinting and microfluidic strategies. The focus of this particular branch is based on the engineering of *in vitro* model environments for tissues and cells, to mimic their natural niches [275]. The following section, therefore, focuses on different aspects of the extracellular environment that have been suggested in literature to improve artificial niches. These aspects can also be implemented in the aforementioned strategies.

1.2.4.1 General principles and applications of engineered artificial niches.

The cellular environment *in vivo* is involved in the modulation of cell fate, therefore, mimicking this environment *in vitro* could present the possibility to regulate cell behaviour and tissue formation in a controlled environment [276]. Cell-matrix interactions are crucial for cellular behaviour and constructing an *in vitro* environment to regulate this behaviour is an important application tissue engineering [275].

An example of the value of engineered artificial niches is found in the central nervous system (CNS), to treat the lack of regeneration from spinal cord injuries [277], [278]. Nanostructured scaffolds to mimic the native ECM can be employed for the investigation of unknown mechanisms, substrates for nervous fibre migration and carriers for cell transplantation [274]. In the CNS, a number of diseases are caused by injuries to fibres, altered extracellular environments or degeneration of the ECM [279]. Differences in the mechanical properties of the tissues are a hallmark of altered tissue development or diseases, and the development of suitable materials thus helps in uncovering mechanisms responsible and targeted treatments [274].

To preserve stem cell properties *in vitro,* artificial niches from the anterior ocular segment have been designed as a way to control stem cell phenotype. Furthermore, in corneal transplantation, the design of substitutes could create problems with the current strategies such as donor tissue shortage and immune rejection [280]. Equivalents of the epithelium, stroma and endothelium layers have been the focus of research in this particular field of artificial niches [281], [282].

Approaches to mimic the microenvironment, include designing materials with a tuneable rigidity, as to replicate the mechanical properties of the native tissues [283]. Methods using spatial patterning, have been developed to better approach the dynamic nature of the surrounding matrix [284], [285]. Improving the mechanical complexity of the platform has a number of benefits compared to standard culture dishes, including the fact that they can provide information about the cellular responses to mechanical stimuli [283].

1.2.4.2 Applications of artificial niches for skeletal muscle tissue engineering

Finding a suitable *in vitro* niche for skeletal muscle would allow the satellite cells to retain their stemness or to include desirable cytokines and growth factors for *in vivo* delivery [286], [287]. Furthermore, creating a specialised support could improve current *in vitro* models of skeletal muscle regeneration and tissue formation by incorporating aspects of the niche and mechanical microenvironment. One of those aspects, is the organisation of skeletal muscle tissue. As skeletal muscle is a highly organised tissue, with long aligned fibres [288], approaches to align the cells *in vitro* have been considered as well. The proper alignment of scaffolds profoundly dictates cellular behaviours, orchestrating the complex cellular responses which are crucial for tissue regeneration. Such topographical cues have an undeniable influence over cell morphology, distribution, adhesion, proliferation, and migration [289], [290].

Various different cell shapes and orientations have been observed dependent upon the scaffold's structural coherence or alignment. Aligned scaffolds orchestrate elongated cell shapes, inducing cell alignment along fibre directions. This effect creates alterations in nuclear aspect ratios and instigates a higher order of ECM organisation [289], [290]. Different cell types, such as fibroblasts, osteoblasts, endothelial cells, Schwann cells, and others, showcase distinctive behavioural responses dictated by scaffold topographic variations [290]–[293]. The phenomenon of contact guidance underscores the adaptiveness of cells in detecting and interpreting substrate physicality, thereby modulating cytoskeletal and musculoskeletal dynamics to organize alterations in cell morphology and functional activities. This complex mechanobiological process of mechanosensing varies across various tissue types, where further studies are needed to find the nuanced mechanisms [294]–[297].

Alignment of skeletal muscle myoblasts and myotubes can be achieved through cultivation on substrates with micro-or nanometre scale patterns [298]. Improved neuromuscular junction was observed when using linearly aligned culture surfaces to organise skeletal muscle myotubes [299], [300]. C2C12 cells have been cultured on a wide range of topographies in order to align them *in vitro*. Not only the width, but also the depth of the grooves in the microscale influences alignment, with 7 µm deep grooves aligning the cells better than 2 µm grooves [298]. Myoblasts were also aligned on wave patterns with 3 to 12 µm sized periodicities, to form aligned myotubes [301]. Nanofibres with a 500 nm diameter were used for the same goal, assessing the alignment of myoblasts and myotubes on even smaller topographical cues [302]. Cellulose scaffolds naturally have a topography, with decellularized green onions providing grooves of 20 µm wide and 10 µm deep as a biodegradable alternative [303].

As shown in the section on the mechanobiology of skeletal muscles, the tissue is highly dynamic and stretchable. Subjecting the designed niches to stretch, has been shown to cause different types of alignment depending on the stretch, where uniaxial strain aligned C2C12 cells perpendicular to the direction of the strain [304]. Myogenic differentiation was enhanced both in uniaxial and biaxial strain [304], [305], however, some studies have also reported an inhibition of differentiation upon strain [306], leading to the need for better comparisons of strain inducing protocols.

The stiffness of the environment has been well known to influence skeletal muscle stem cells behaviour; increasing stiffness has been demonstrated in injured or diseased muscle. Skeletal muscle satellite cells, cultured on stiffnesses close to the stiffness of the tissue, have been shown to self-renew *in vitro*. Moreover, those cells could be transplanted into mice and contribute to muscle regeneration *in vivo* [307]. When increasing the stiffness to match that of injured muscle, enhanced proliferation and migration were observed for C2C12 cells, together with YAP/TAZ localisation to the nucleus [308], [309].

The mechanical properties of the skeletal muscle provide interesting signals as well when designing an *in vitro* platform serving as a niche or microenvironment. Skeletal muscle is flexible and stiffening of the tissue is related to a variety of diseases such as Duchenne Muscular Dystrophy or Cerebral Palsy [310].

1.2.5 Self-organisation approaches for Tissue Engineering

An alternative to approaches using hydrogels or bioprinting, is the self-organisation and self-assembly of tissues, where cells are allowed to secrete their own ECM for the formation of tissues.

1.2.5.1 General principles of self-organisation

Within this section, two distinct processes are merged to form one overview of organised tissue approaches. The first process is that of self-organisation, where cultures of cells are transformed into a tissue structure by applying an external force, such as adding gelling components, rotating the cultures, pelleting cells or rolling the cell sheets. Fundamental in these tissue engineering approaches, is the application of external energy. Self-assembly processes on the other hand, rely on the cells to form tissue, without the need for external force application [311].

Self-organisation approaches have been successfully used in cardiovascular, musculoskeletal, and corneal tissues, for instance [311], [312]. By pelleting the cells for instance, cartilage and bone tissues were formed with the production of relevant ECM proteins [313]. These cultures however, had fewer clinical applications as their mechanical properties were less relevant in real life situations [311]. Cellular aggregates or spheroids can be formed using self-organisation processes by pelleting or rotating the cultures, or by hanging-drop culture methods. Small spheroids are produced that provide relevant information about the phenotypic maintenance of various cell types [311], [314]. Cells cultured in monolayer sheets, were instructed to form 3D tissues by employing functionalized substrates or thermoresponsive polymers. A change in temperature could change the confirmation of the polymer and induce detachment of the monolayer of cells on the surface, to then be moulded into a 3D structure [315]. An example of such a process used corneal stem cells for the formation of corneal epithelial sheets [315].

Self-assembling approaches have been demonstrated for instance in cartilage tissue engineering, where functional biomimetic tissues were created without any external energy, by using nonadherent culture substrates. By preventing attachment in these cultures, the cell-cell interactions were enhanced, and cartilage like tissue constructs were formed [316]. In vascular tissue, self-assembling rings of smooth muscle cells were formed and assessed for their mechanical properties, indicating tensile strengths between 100 and 500 kPa [317]. The driving force behind these formations was previously described in two hypotheses: the differential adhesion and differential interfacial tension hypothesis. The differential adhesion theory hypothesis that tissues minimize the free energy via cell-cell binding [311]. In the cartilage example on nonadherent surfaces, the free energy is minimised via cell-cell binding due to increased levels of N-cadherin [318], [319]. On the other hand, the differential interfacial tension hypothesis stipulates that the free energy is minimised by forming aggregates of cells with similar tensions [320].

1.2.5.2 Applications of self-organisation for skeletal muscle

One of the first approaches to self-organising muscle, was carried out using a combination of muscle cells and fibroblast for ECM deposition on saran wrap substrates [321]. Replacing the saran wrap with laminin coated PDMS reduced the need for fibroblast dependent ECM [322], [323]. The laminin supported cell adhesion for tissue formation in combination with fibroblast derived ECM [322]. Further advancements were made by micropatterning the PDMS substrates for myoblast fusion and myotube alignment and adding a fibrin gel afterwards to force the tissues into a contractile 3D structure [324]. Moreover, self-organizing muscle cell sheets were created on a thermoresponsive polymer that allows controlled detachment from the culture plates by lowering the temperature [325], [326]. The sheets were then used in a multi-layered tissue comprised of neuronal, vascular and muscle cells [326]–[329]. Recently, self-organising skeletal muscle microtissues were even generated using healthy and Duchenne muscular Dystrophic phenotype cells. In this case, however, cells were embedded in a Thrombin/fibrinogen gel before placing them into their system, as to create a 3D microtissue [330], [331].

Self-organising tissues can solve some of the problems faced using current hydrogel models, for instance, since the cells excrete their own matrix instead of relying on commercially available polymers with high variability [332]. The self-organising tissues do require a longer culture time before formation compared to hydrogels, which is why, for some short-term applications, hydrogels remain the method of choice [332]. As demonstrated, this sometimes results in combined approaches, as for the microtissues embedded in fibrinogen [327], or the sheets with added fibrin, where the cells together with the hydrogel are considered a self-organizing system [324].

These self-organising approaches still leave some room for spontaneous self-assembling processes, where fewer intervention remains necessary by addition of hydrogels, or ECM production by other cells.

2. MATERIALS AND METHODS

2.1 Fabrication of grooved substrates

Artificial niches using the substrates described in Chapter I were designed for the formation of skeletal muscle tissue constructs *in vitro*. These substrates were fabricated using grooves and ridges and extended with a variety of fabrication techniques to optimise the formation of the tissue constructs. Tissue constructs were then characterized with immunofluorescence and electron microscopy to observe the construct properties.

2.1.1 Base protocol for grooved substrate fabrication

The patterned substrates were fabricated out of polydimethylsiloxane (PDMS, Sylgard 184, Dow Corning) and FlexDym™ (Eden Tech) using the protocols discussed in I.2.1. The PDMS was prepared by mixing the prepolymer and crosslinker in weight ratios of 20:1 (soft), 10:1 (medium hard) and 5:1 (hard) and degassed before pouring onto the master.

To control the seeding of the cells, PDMS boundaries were designed to attach to the nanogrooved substrates after the oxygen plasma treatment. These borders have a thickness of 1 mm and an inner size of 18 mm by 18 mm.

The substrates were prepared for cell culture after sterilisation with ultraviolet radiation (UV) or ethanol washing. Both the PDMS and the FlexDym™ underwent oxygen plasma treatment (Pfeiffer Vacuum Single Gauge – Cesar RF Power Generator) at 50 W for 3 minutes before incubation with coating solution.

Surfaces used for primary muscle stem cells experiments were treated using plasma for 3 minutes at 50 W with a PDC Harrick Expanded Plasma Cleaner, during the secondment in Paris (Université Paris-Est Créteil).

Coating of the substrates was either carried out by incubating the surfaces 10 µg/mL of Fibronectin (Merck) or Laminin (Sigma-Aldrich) in phosphate buffered saline (PBS, Sigma-Aldrich) for 1 hour at room temperature or by incubating using serum rich growth medium, overnight at 37°C and 5 % CO_2. Excess coating was taken off before seeding the cells.

2.1.2 Extension of the patterns using micropillars

Variations of this set-up were designed by addition of pillars in different set-ups, and millipatterned masks. The pillars were created by micromilling directly on the grooved polycarbonate (PC) using MiniTech Micromilling, to create pillars of 100 µm in diameter and 150 µm in height. Spacing between the pillars was varied between 1 mm and 2 mm in the parallel and orthogonal directions of the grooves. The design and spacing of the pillars are given in Figure 16.

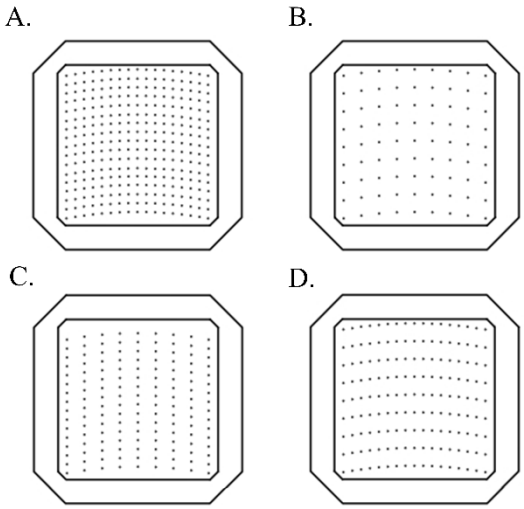

Figure 16: Pillar design for PDMS substrates.
A. Pillar design with 1 mm x 1 mm distances in both orthogonal and parallel directions to the grooves. B. Pillar design with 2 mm x 2 mm distances in both orthogonal and parallel directions to the grooves. C. Pillar design with 1 mm orthogonal x 2 mm distances parallel directions to the grooves. D. Pillar design with 2 mm orthogonal x 1 mm distances parallel directions to the grooves. Groove direction is presented horizontally.

2.1.3 Extension of the patterns using micropatterned coating

In experiments with micropatterned coating, the samples were not immediately treated with an adhesive coating after oxygen plasma treatment but were coated with poly(L-lysine) graft polyethylene glycol (PLL-g-PEG) for 3 hours at room temperature. Following the incubation, samples were placed in the UV/Ozone ProCleaner™ under Photomask (4DCell, Figure 17) to remove the PLL-g-PEG coating in the patterned spaces. For the current experiments, solely region R1 was used and considered, for individual cell seeding and control of the distribution. Samples were detached from the mask with distilled water and coated in a 10 µg/mL fibronectin solution overnight at 4°C. The next day, before cell seeding, the samples were washed with PBS.

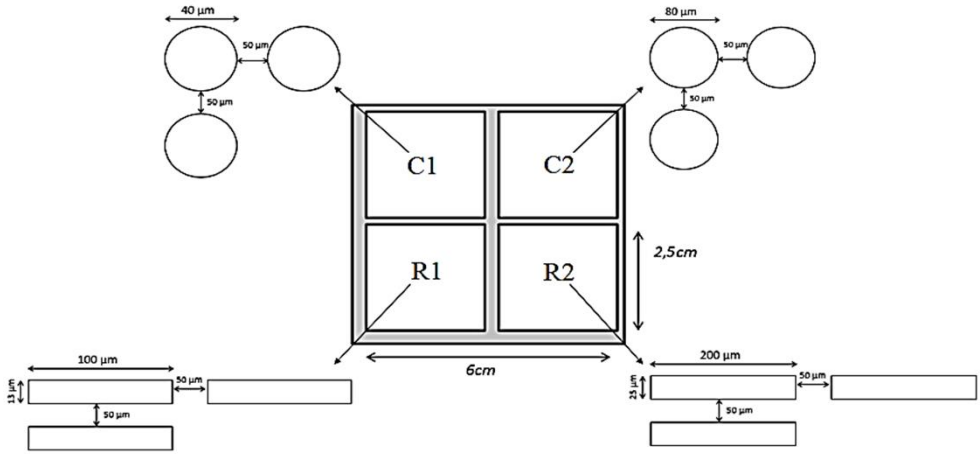

Figure 17: Photomask used for micropatterning from 4D Cell.
The photomask is divided into four different regions: Two circular patters with a diameter of 40 µm (C1) and 80 µm (C2) and two rectangular patterns namely R1 with length 100 µm and width 13µm and R2 with length 200µm and width 25 µm. Region R1 was used for the micropatterning of PDMS substrates for C2C12 culture. Figure from [333]

2.1.4 Extension of the patterns using millipatterned coating

In experiments with larger patterning samples, a PDMS mask was designed with rectangles of 1-2-3 mm wide and 20 mm long, for selective patterning of the ECM coating (Figure 18). The mask was placed on top of the nanogrooved PDMS before oxygen plasma treatment, to selectively treat the surface. ECM coating was also carried out with the PDMS mask attached; this mask was removed right before cell seeding.

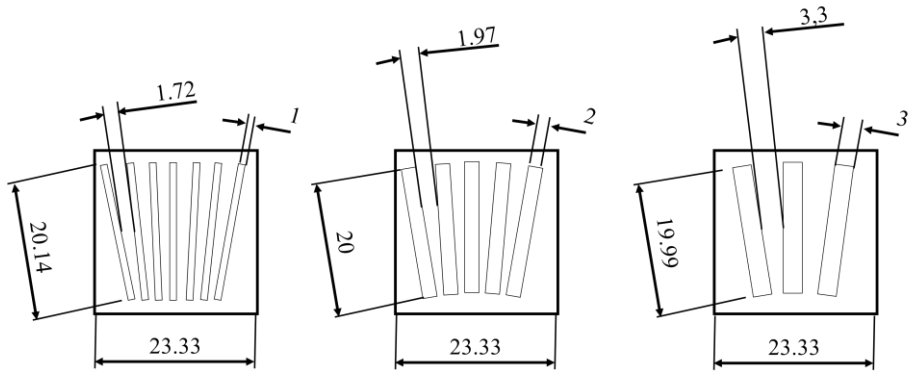

Figure 18: Custom mask created for millipatterning experiments.
Custom mask used for millipatterning experiments with spacing 1 mm, 2 mm, and 3 mm wide rectangular stripes. Masks were used for oxygen plasma treatment and fibronectin coating before removal to proceed with cell culture. All sizes on the figure are given in mm.

2.2 Cell seeding and culture

2.2.1 Protocol for C2C12 cell line

C2C12 cells and primary mouse muscle stem cells (pMuSCs) were used for evaluation of the surfaces. C2C12 (CRL-1772™, ATCC) cells were cultivated in Dulbecco's minimum essential medium with high glucose (DMEM-HG, Sigma-Aldrich), supplemented with 10 % foetal bovine serum (FBS, Sigma-Aldrich), 1 % L-glutamine (Gibco) and 100 U/mL penicillin-streptomycin (PenStrep, Gibco). The cells were incubated at 37°C and 5 % CO_2 in a cell culture incubator. Medium was changed every 2 – 3 days and before reaching 70 % confluence the cells were passaged using Trypsin/Ethylenediaminetetraacetic acid (EDTA) (0.25 % w/v trypsin/0.02 mM EDTA; Gibco) for seeding on the substrates. C2C12 cells for experimental use were kept below passage 9.

2.2.2 Protocol for primary cells

Primary Muscle Satellite Cells (pMuSCs) were isolated from C57BL/6 wild type mice, 7-15 days postnatal by digesting the limb muscles of the mouse. Muscles were minced using surgical scissors and the resulting slurry was digested using a digest solution containing Dispase II (3 mg/mL, Roche), Collagenase A (2 µg/µL, Roche), $CaCl_2$ (8 mM, Sigma-Aldrich), $MgCl_2$ (5 mM, Sigma-Aldrich), DNase I (10 µg/mL, Roche) in Hanks' balanced salt solution (HBSS, Gibco) supplemented with 0.2 % bovine serum albumin (BSA, Sigma-Aldrich) and 0.1 % Ciflox (Bayer Pharma) to create HBSS+. Digestion was continued for a maximal duration of 1 hour and 30 minutes at 37°C while resuspending and isolating cells every 20 minutes. Once the digestion was finished, cells were filtered through a 40 µm filter (Corning® Cell strainer, Merck), and the filter was rinsed using HBSS+. Filtered cells were centrifuged for 10 minutes at 1400 revolutions per minute (rpm). The filtered solution was cleared of red blood cells using lysis buffer diluted in water (10X, BD Pharm Lyse™, BD biosciences) for 10 minutes at room temperature, then centrifuged for 10 minutes at 1400 rpm. The pellet contains cells ready for preplating. All cells were preplated in coating-free, polystyrene culture flasks for the sedimentation and adherence of fibroblasts and epithelial cells. After 4 hours at 37°C and 5 % CO_2, the supernatant containing pMuSCs, was recuperated and replated in a gelatine (0.1 %, Sigma-Aldrich) coated culture flask. pMuSCs were cultured in growth medium consisting of DMEM-HG supplemented with 20 % FBS (Merck), 10 % horse serum (HS, Gibco), 1 % HEPES buffer (Gibco), 1 % Sodium Pyruvate (Gibco) and 0.5 % Ciflox. pMuSCs were passaged using TrypZean® (Merck) before being seeded on the substrates. pMuSCs for experimental use were kept below passage 3.

2.2.3 Cell seeding on grooved substrates.

Seeding of the cells on the substrates was carried out by incubating a droplet of 300 µL containing 10^4 cells for 2-4 hours on the surfaces, before covering the whole culture dish with medium for a 3000 cells/cm² density.

2.3 Immunofluorescence and visualisation

Depending on the experiment, cells were fixed and stained at different timepoints, indicated with their respective results. The fixation was performed by incubation the constructs in a 4 % paraformaldehyde (Electron Microscopy Sciences USA) in phosphate buffered saline (PBS, Sigma Aldrich) solution for 20 minutes.

After fixation, the cells were either stored at 4°C for later immunostainings, or immediately permeabilised with 0.1% Triton X-100 (Sigma Aldrich) in PBS for 15 minutes at room temperature.

Two types of staining were performed, one where solely Phalloidin and Sytox Green were used, for directionality of the cells, and another where primary antibodies were involved to stain for specific proteins. In the former case, blocking was not necessary. For experiments with primary antibodies, the blocking was carried out with 3 % Bovine Serum Albumin (BSA, Sigma Aldrich) in PBS for 1 hour at room temperature to avoid non-specific binding of the antibodies.

The primary antibodies used are given in the Table 8, as well as their respective incubation times.

Table 8: Primary antibodies used for muscle visualisation.

Primary antibody	Code	Incubation	Concentration	Supplier
Anti-Myosin Heavy chain	M4276	Overnight at 4°C	1:400	Sigma Aldrich
Anti-Laminin	L9393	1 hour at room temperature	1:1000	Sigma Aldrich
Anti-Fibronectin	F0791	1 hour at room temperature	1:300	Sigma Aldrich

After incubation with primary antibodies, the cells were washed with the 0.1 % Triton PBS solution and incubated with their respective secondary antibodies, given in Table 9. Table 9 also shows the excitation and emission wavelengths of the used secondary antibodies and stains.

Table 9: Secondary antibodies used for muscle visualisation.

Secondary antibody	Code	Incubation	Concentration	Supplier
Phalloidin 647	ab176759/ U0298	1 hour at room temperature	1:400 / 1:100	iFluor / Abnova
Mouse 546	A11030	1 hour at room temperature	1:200	Thermo Fisher scientific
Rabbit 488	A11034	1 hour at room temperature	1:200	Thermo Fisher scientific
Hoechst	62249	15 minutes	1:10 000	Thermo Fisher scientific
Sytox™ Green	S34860	15 minutes	1:10 000	Thermo Fisher scientific

Lastly, the cultures were incubated with Hoechst or Sytox Green (1:10 000 dilution, Thermo Fisher Scientific) for 15 minutes at room temperature for nuclear staining. Samples were washed and stored in 4°C before visualisation with an Upright LSM 900 confocal Microscope (Zeiss).

2.4 Transmission Electron Microscopy of the cultures

Samples were fixed with a 2.5 % glutaraldehyde in 0.1 M sodium cacodylate buffer at 4°C overnight, followed by three ten-minute washes in the same buffer. Post fixation, samples were incubated in the dark, in a solution of 1 % osmium tetroxide/ 1 % potassium ferrocyanide in sodium cacodylate for 1 hour at 4°C. After a wash with the buffer, specimens were incubated with 0.15 % tannic acid aqueous solution for 3 minutes then rinsed again in chilled distilled water before dehydration. The dehydration was carried out by using ascending series of ethanol (30° 50° 70° 95° (two times) 100° (three times)), incubating the samples in each step for 15 minutes on ice. The last step in ethanol was performed at room temperature before overnight infiltration in 1:1 epoxy resin/ethanol mixing. Samples were embedded in fresh Spurr's resin for 2 days before polymerization at 70°C. Each sample was cut with a diamond knife at an ultramicrotome FC7-UC5 Leica (thickness 60 nm), collected on 200 mesh thin bar copper grid and stained with 1 % uranyl acetate for 12 minutes in the dark. The imaging was performed by using TEM Tecnai G2, 20_Thermofisher Company equipped by Veleta side-view camera, at 120 KV. Chemicals were purchased from Electron Microscopy Sciences USA.

2.5 Focused Ion Beam Scanning Electron Microscopy

Samples with cells were prepared for Focused Ion Beam Scanning Electron Microscopy (FIBSEM) imaging using the ROTO and ultra-thin plasticization protocol [334]. Briefly, samples were fixed in 2.5 % glutaraldehyde in 0.1 M sodium cacodylate buffer at 4°C overnight. After rinsing in sodium cacodylate samples were quenched in a chilled solution of 20 mM glycine, then rinsed again in the washing buffer. A RO step was carried out by using of 1 % osmium tetroxide and 1 % potassium ferrocyanide for 1 hour in the dark on ice. After washing three times in sodium cacodylate, samples were incubated with 1 % thiocarbohydrazide at room temperature for 20 minutes (T step), washed (3 × 5 minutes) in distilled water and post fixed in 2 % osmium tetroxide aqueous solution for 1 h at room temperature (O step). After rinsing with distilled water, specimens were incubated overnight in a solution of 1 % uranyl acetate at 4°C. then washed in chilled water and stained with 0.15 % acid tannic aqueous solution for three minutes. Samples were dehydrated by increasing concentration of ethanol (30 %, 50 %, 70 %, 90 %, 100 %) each step, incubating the samples for 15 minutes on ice. The last step using absolute ethanol was performed at room temperature. Specimens were infiltrated with increasing concentration of Spurr's resin in absolute ethanol at a room temperature using these ratios: 1:3 (2 × 3 hour), 1:2 (2 × 3 hour), 1:1 (overnight), 1:2 (2 × 3 hour), 2:1 (2 × 3 hour), 3:1 (2 × 3 hour). Finally, samples were embedded in absolute resin overnight. Excess of resin was removed by ethanol washing after vertically mounting the samples for 3 hours, and afterwards put in an oven at 70°C. After 24 hours of polymerization samples were mounted on 12 mm aluminium pin stub by using silver paste and sputtered (sputter coater 208HR Cressington) with a layer of 20 nm of gold before FIBSEM imaging. For the imaging the Helios CX 5 (Thermo Fisher) was used at 3 KV in a range of magnification between 5 KX and 80 KX. Chemicals were purchased from Electron Microscopy Sciences USA.

3. RESULTS

3.1 Parallel and orthogonal cell growth

As seen in the previous chapters, the nanotopography of the substrates caused cellular alignment on PDMS substrates for C2C12 culture. This model was expanded by letting the cells over-proliferate past the confluent layer. Once the cells reached confluence, little cracks in the confluent monolayers start to appear, where the direction of the cells starts to shift in a 90° angle compared to the topographical cues. Figure 19 demonstrates an initial confluent layer, as seen before, on day 7 in culture. However, on day 10 in culture on the Medium PDMS, a crack becomes noticeable, demonstrated in panel B of Figure 19.

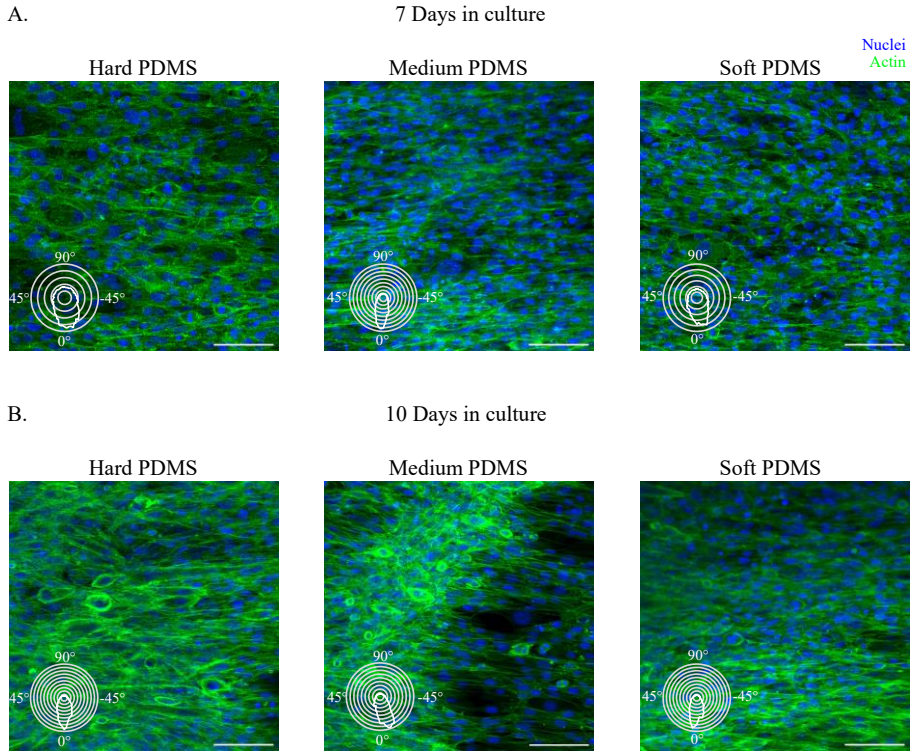

Figure 19: Side by side comparison of cellular organisation on different PDMS types at seven and ten days in culture on fibronectin coated substrates.
A. Patterned substrates with their corresponding directionality and stiffness after seven days in culture. B. Patterned substrates with their corresponding directionality and stiffness after ten days in culture. All spider plots show the frequency of cell aligning according to an angle between -90° and 90° where 0° equals horizontal alignment. The pattern was levelled horizontally for all images. Scalebars = 100 µm; Green = actin; Blue = nuclei.

At the ten-day timepoint, the directionality of the cells remains largely unchanged, but the confocal images shown, demonstrate a difference between the original confluent layer and the 3D layer of the cells.

Z-stacks from an area on each of the materials were taken to demonstrate the initial thickness of the orthogonal layer, starting from the 2D aligned layer on the pattern. Representative samples are shown in Figure 20.

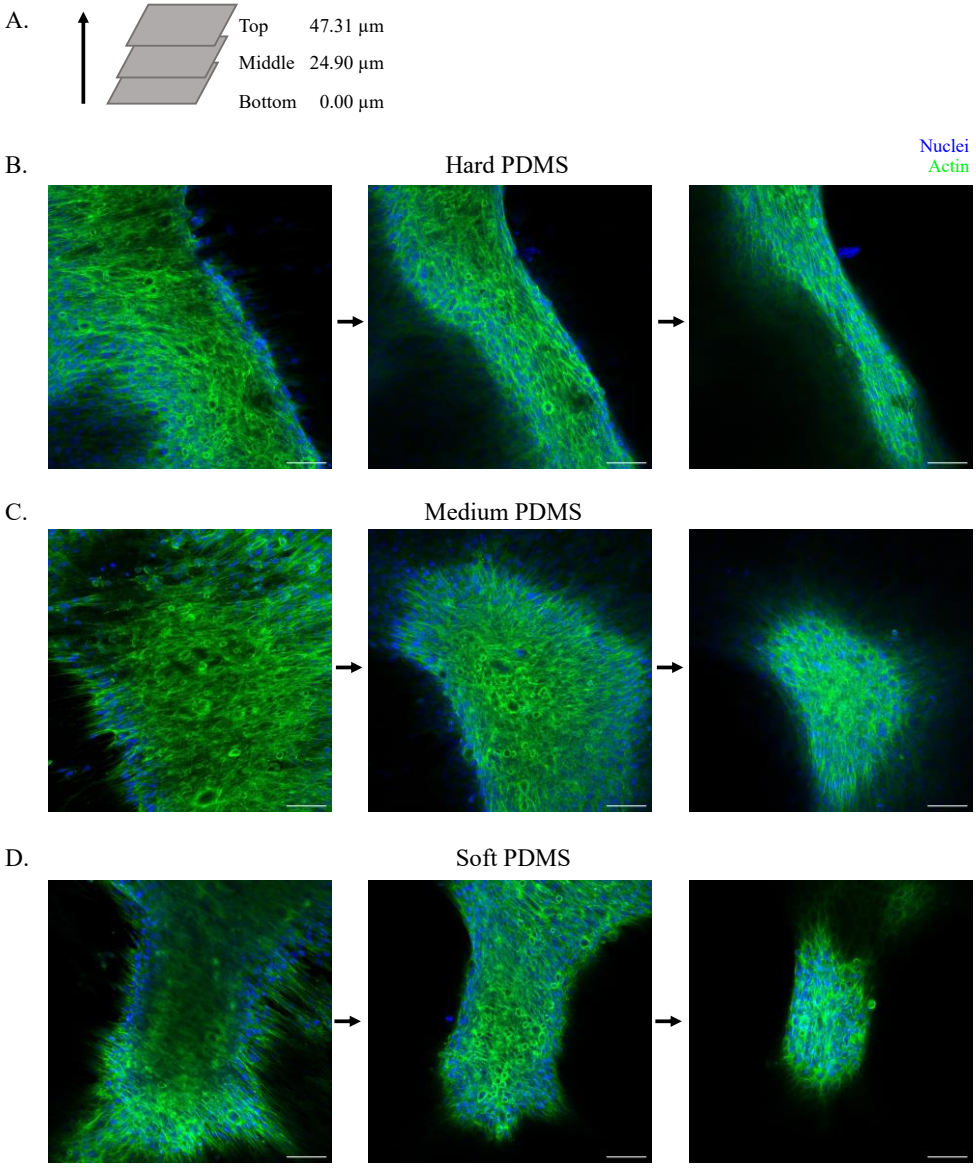

Figure 20: Z-stacks of the initiation of orthogonally formed constructs on different types of fibronectin coated PDMS.
A. Overview of thickness of demonstrated Z-stack and the position of each of the layers. B. Hard, patterned substrates forming an orthogonal supracellular layer after ten days in culture. C. Medium, patterned substrates forming an orthogonal supracellular layer after ten days in culture. D. Soft, patterned substrates forming an orthogonal supracellular layer after ten days in culture. The pattern was levelled horizontally for all images. Scalebars = 100 µm; Green = actin; Blue = nuclei.

On all of the different PDMS substrates, orthogonal structures started forming around day 10, with an increase in thickness compared to the monolayer of cells. These constructs formed at random locations and regardless of PDMS stiffness.

Figure 21 demonstrates the progress through time of constructs on medium hard substrates as an example of their growth and development in time. The thickness of each construct was determined using Z-stacks starting from the nanopatterned confluent layer to the top of the constructs.

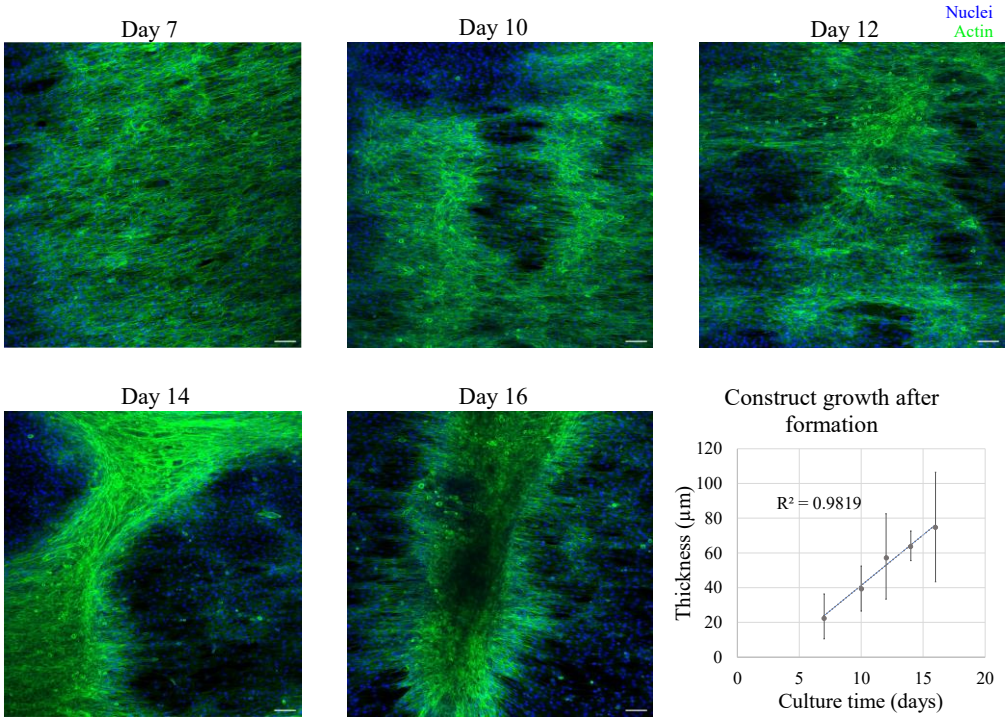

Figure 21: Growth of the constructs through time on fibronectin coated, medium hard surfaces. Fibronectin coated, medium hard, patterned substrates forming an orthogonal supracellular layer at different timepoints. The pattern was levelled horizontally for all images. Scalebars = 100 µm; Green = actin; Blue = nuclei.

The thickness of the substrates increases linearly with an R^2 value of 0.9819 as seen on Figure 21.

Monitoring these constructs over time in culture demonstrated that they increased in frequency and thickness until day 16 in culture. Structures on soft PDMS were able to attach to the substrates until day 19-21 in culture, while a considerable fraction (~ 66%) of the muscle constructs on stiffer PDMS detached earlier, around day 19. Figure 22 demonstrates how the constructs looked after 19 days in culture. Hard PDMS substrates showed a large detachment of the muscles and on medium hard PDMS the muscles demonstrated initial signs of premature

detachment. On soft PDMS the constructs never reached a larger thickness, but the cells remained stable even after 19 days in culture, with continued orthogonal construct formation.

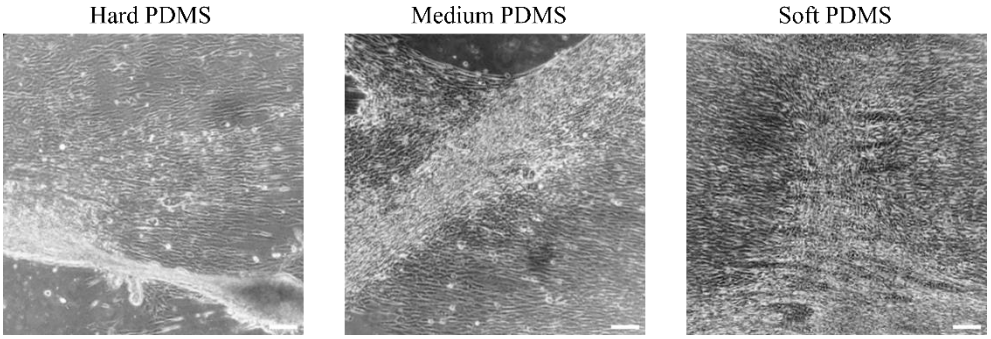

Figure 22: Comparison of different fibronectin coated PDMS substrates after nineteen days in culture. Patterned substrates with their corresponding stiffness after nineteen days in culture. The pattern was levelled horizontally for all images. Scalebars = 100 µm.

Changing the coating of the substrates to laminin or growth medium demonstrated fewer myotubes and no signs of orthogonal construct formation around day 10 in culture, whereas longer culture times allowed formation of these constructs as well (Figure 23).

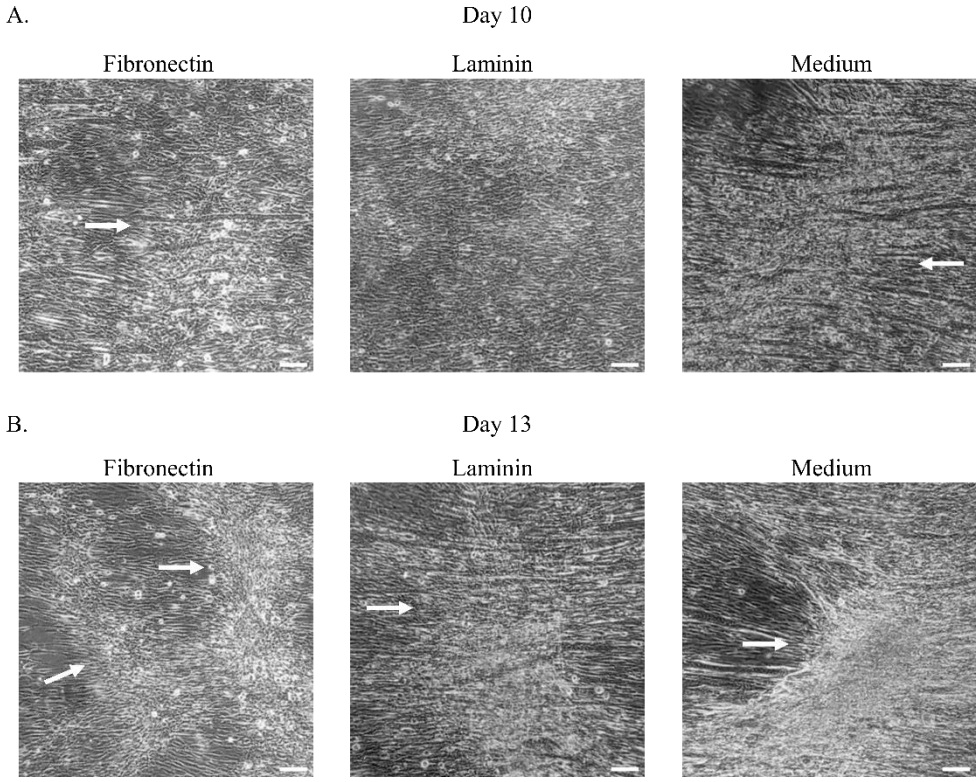

Figure 23: Side by side comparison of cellular organisation on different types of ECM coating.
A. Patterned substrates with their corresponding coating after ten days in culture. B. Patterned substrates with their corresponding coating after thirteen days in culture. Arrows indicate the initiation of orthogonal construct formation. The pattern was levelled horizontally for all images. Scalebars = 100 µm.

Fibronectin and growth medium coating proved to be most efficient for the formation of tissue constructs early in the cell culture process.

Further staining of Z-stacks, using a Myosin Heavy Chain antibody, demonstrated both Myosin presence inside and on the outside of the structures. Figure 24 contains a 3D rendering of two Z-stacks taken at fourteen days in culture. The panels on the side demonstrate the thickness of the constructs.

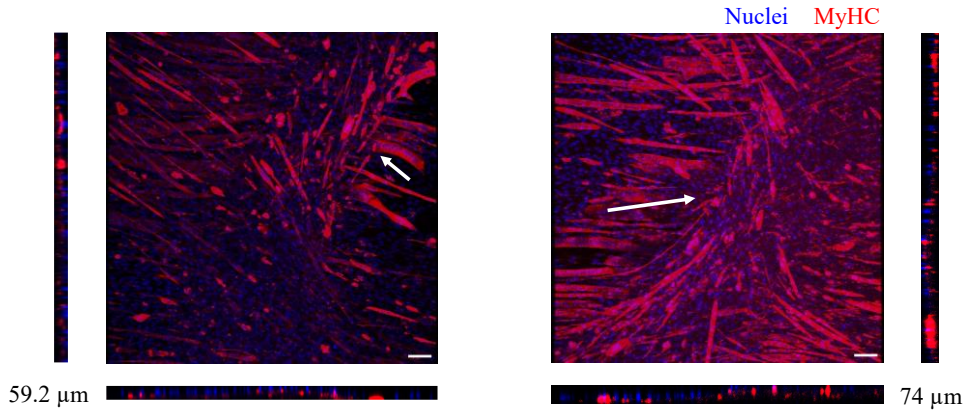

Figure 24: 3D rendering of Z-stacks after fourteen days in culture, stained for Myosin Heavy Chain. Fibronectin coated, patterned substrates forming an orthogonal supracellular layer in a 3D rendering by ImageJ. Side panels demonstrate the thickness of the constructs. The pattern was levelled horizontally for all images. Scalebars = 100 µm; Red = Myosin Heavy Chain; Blue = nuclei.

Staining of the substrates was impaired by the penetration of the antibodies within the constructs and fluorescent signal blocking, leading to difficulties visualising the contents of the muscles properly. To this end, a FIB-SEM protocol was designed, discussed in section 3.7.

3.2 Inclusion of micropatterns for construct formation

Original seeding density and distribution are important in any kind of set-up to minimise the effects of clusters at early timepoints. It was hypothesized that an equal spreading of the cells on the substrate, would create more homogeneous cell growth and an equal chance on the formation of tissue constructs. Therefore, a set-up was designed where cells are seeded in a controlled pattern using a photomask and adhesive versus anti-adhesive coatings.

The biochemical micropattern was applied over the topographical grooves, in a perpendicular fashion to the underlying nanogrooves. The idea was to both control the original distribution of the cells on the substrates, while also forcing them from the beginning to take this orthogonal formation. As demonstrated in Figure 25, the cells originally aligned mostly according to the chemical micropattern immediately after seeding, while recovering their horizontal alignment at later phases in culture. Two weeks after seeding, a large portion of the cells either adhered according to the grooves and not orthogonally or detached from the substrates. Possibly, the continued presence of the anti-adhesive of the PLL-PEG hindered the culture stability as compared to the standard grooved substrates of section 3.1.

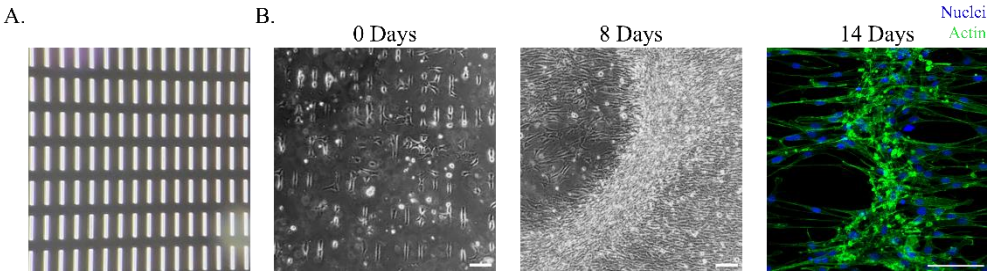

Figure 25: Overview of micropatterned and cells on micropatterned substrates in time.
A. Image of the photomask taken with rectangles of 100 µm in length. B. Overview of cells on the micro- and nanopatterned substrates over time. The grooves are aligned horizontally while the micropattern was aligned vertically on all images. Scalebars = 100 µm; Green = actin; Blue = nuclei.

3.3 Inclusion of millipatterns for construct formation

The inclusion of the micropattern confirmed the possibility of additionally patterning the cells on top of the microgrooves. Even though the outcome was suboptimal, the principle remained intriguing, and a larger mask was designed. This time the goal was not to separate the cells individually immediately after seeding, but to determine where the construct would be formed. To this end, a mask with 1 – 2 – 3 mm wide and 20 mm long spacing was designed as demonstrated in Figure 18. Initially cells collect within the patterns to adhere to the fibronectin present, leading to cells aligned in the direction of the nanogrooves, but collected in the direction of the millimetre sized pattern. Figure 26 presents the progress in time of cells on these millipatterns, with the grooves oriented horizontally. On day seven and fourteen, both hard and medium PDMS demonstrate the initiation and formation of orthogonal cell alignment.

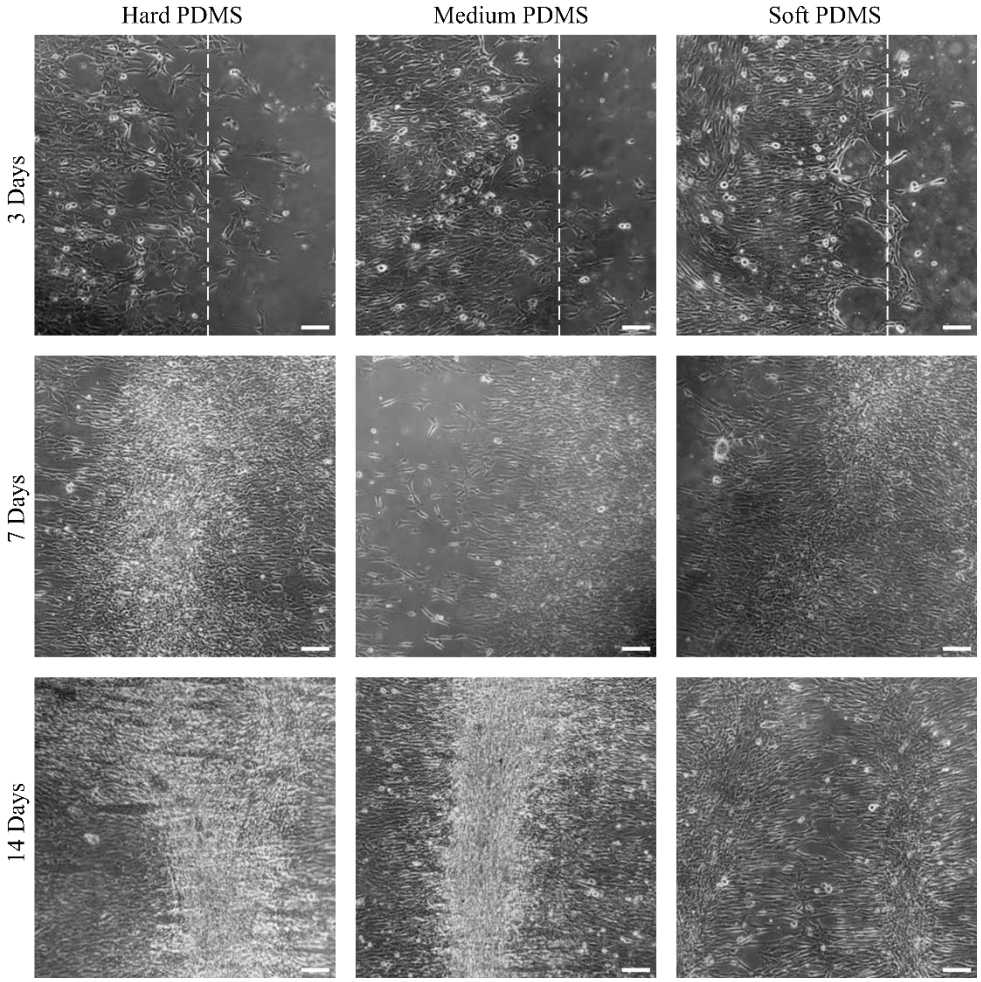

Figure 26: Comparison of millipatterned substrates with varying stiffness values.
Comparison of patterned substrates with their corresponding stiffness at different timepoints. All substrates had a millipattern orthogonal to the groove direction. The nanopattern was levelled horizontally for all images. At the three-day timepoint, dashed lines indicate the section where the millipattern stops, indicating oxygen plasma treated and fibronectin coated PDMS on the left of the line and non-treated PDMS on the right of the line. Scalebars = 100 µm.

Muscle constructs formed using the millipatterns were stable in culture up until 18 days after seeding, when they were fixed and stained for muscle construct visualisation as shown in Figure 27. Using this approach, fibre formation was constrained to the areas coated in fibronectin. Forcing the fibres to form in one area, led to muscle constructs growing over the whole length of the substrate, reaching a maximal length of 18 mm.

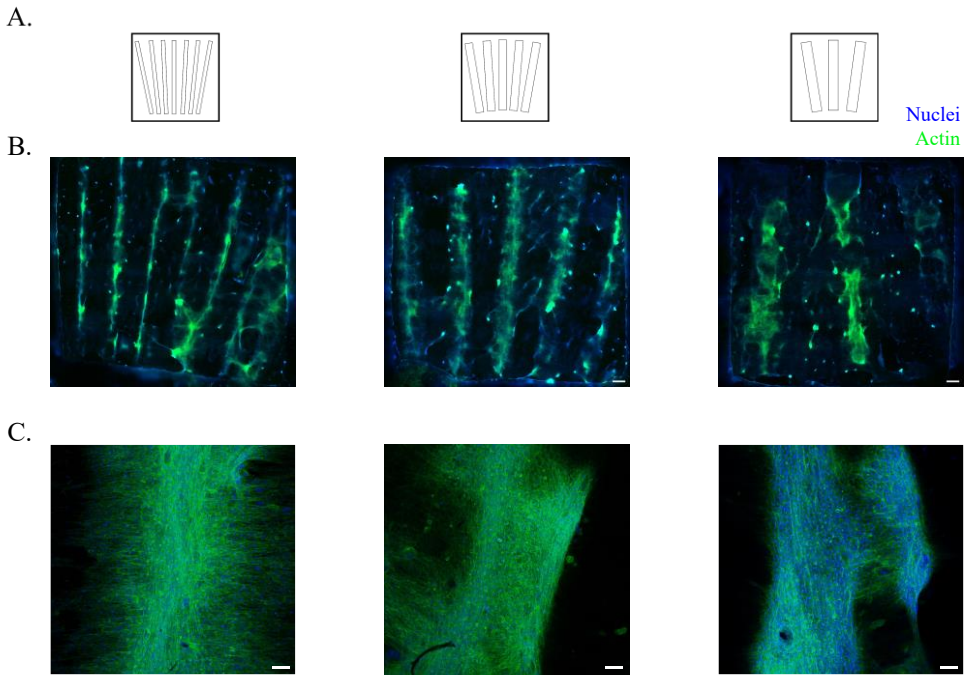

Figure 27: The three different spacing set ups demonstrated with cells for adherence to the millipattern. A. Overview of the size and spacing of the 1 mm, 2 mm, and 3 mm wide patterns respectively. B. Cell culture on day 18 in culture, with a full view of the whole plate per spacing type. Scalebars = 1000 µm. C. Zoom of the muscle construct formation for each of the millipatterns. Scalebars = 100 µm. Green = actin; Blue = nuclei.

The average thickness of constructs formed using the millipattern was 77.76 ± 17.75 µm as determined by Z-stack evaluation after 18 days in culture.

3.4 Inclusion of pillars for construct formation

An alternative substrate was designed with pillars of 100 µm in diameter and 150 µm in height to determine the effect of pillars both on the formation and the attachment of muscle constructs. The idea behind the pillar designs is that the protrusion in the confluent monolayer can create openings for the constructs to start forming at an earlier stage, all while catching the constructs when the grow larger.

Muscle tissue formation on these surfaces is represented in Figure 28.

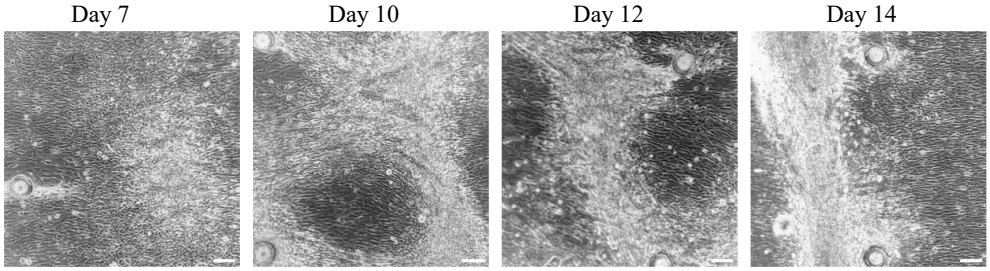

Figure 28: Muscle tissue formation on substrates with 1 mm spaced orthogonally and 2 mm parallel to the grooves.
Patterned substrates with pillars spaced 1 mm x 2 mm at different timepoints in culture. The pattern was levelled horizontally for all images. Scalebars = 100 µm.

Four designs were originally considered, with variations of 1 mm and 2 mm spacing between pillars in the orthogonal and parallel direction of the grooves, demonstrated in Figure 16 in the materials and methods section Figure 29.

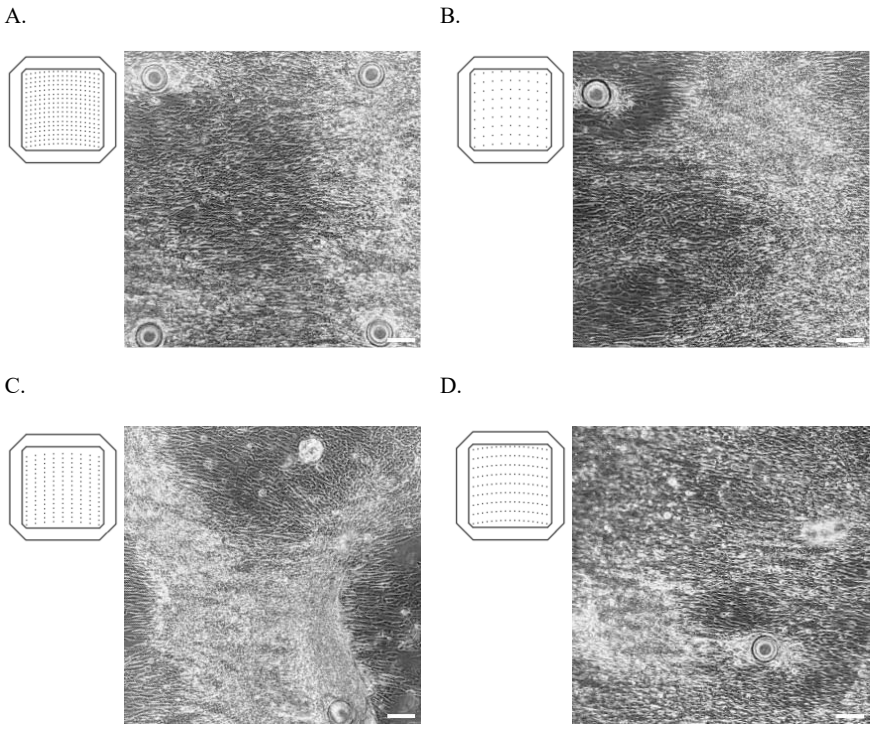

Figure 29: Pillar design and set-up with corresponding cell surfaces after eleven days in culture.
A. Pillar design with 1 mm x 1 mm distances in both orthogonal and parallel directions to the grooves, with corresponding cell layer after eleven days in culture. B. Pillar design with 2 mm x 2 mm distances in both orthogonal and parallel directions to the grooves, with corresponding cell layer after eleven days in culture. C. Pillar design with 1 mm orthogonal x 2 mm distances parallel directions to the grooves, with corresponding cell layer after eleven days in culture. D. Pillar design with 2 mm orthogonal x 1 mm distances parallel directions to the grooves, with corresponding cell layer after eleven days in culture. Groove direction is presented horizontally. Scalebars = 100 µm.

All pillar designs demonstrated muscle construct formation at some point during culture, but the set-up shown in Figure 29 panel C demonstrated the most consistent tissue formation at day 14 over all carried out experiments on hard and medium hard PDMS. Figure 30 shows the constructs on day 12 and day 14 of experiments carried out at different moments, in brightfield and in fluorescence.

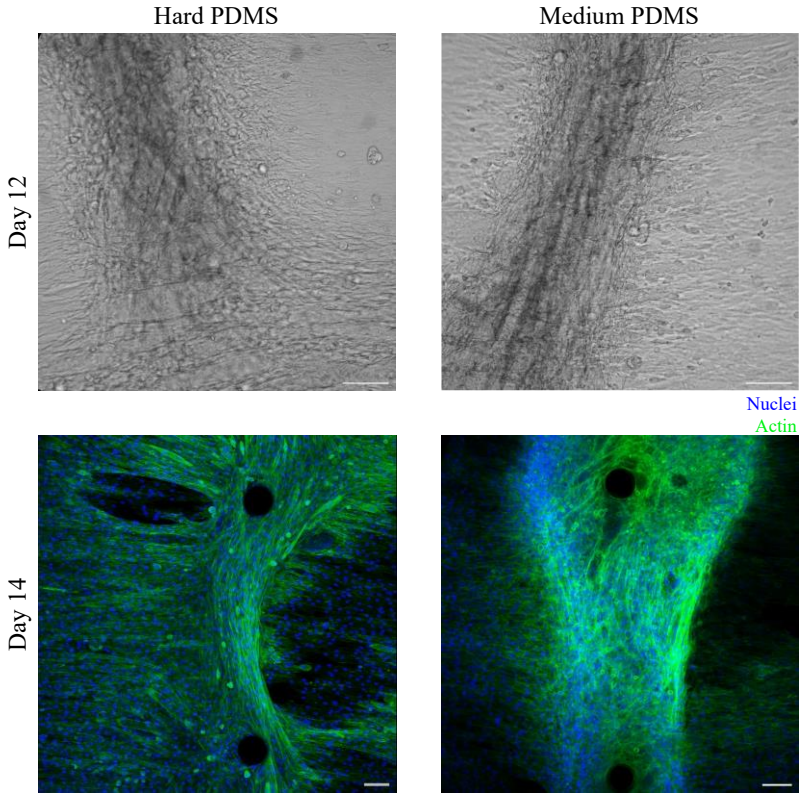

Figure 30: Hard and medium hard PDMS substrates with pillars generating muscle tissues at twelve and fourteen days in culture.
The formation of muscle constructs on fibronectin coated, hard and medium hard patterned substrates with pillars spaced 1 mm orthogonal and 2 mm parallel to the grooves at twelve and fourteen days in culture. The pattern was levelled horizontally for all images. Scalebars = 100 µm; Green = actin; Blue = nuclei.

Figure 30 contains three different experiments, carried out independently to evaluate the consistency of the tissue formation as well. Both brightfield images were part of the same experiment on different substrates, but the two confocal images represent experiments carried out at a different timepoint, with a different passage of C2C12 cells, as an indicator of the reproducibility of the tissue construct formation on pillared substrates. Tissue constructs on these pillared layers with a hard PDMS substrate had an average thickness of 96.73 ± 32.00 µm compared to 85.52 ± 40.18 µm. On the pillared substrates the maximal thickness

reached were 162.8 µm and 139.44 µm for hard and medium hard PDMS respectively.

Substrates of soft PDMS showed in some cases formation of orthogonal constructs, but less than the other substrates. The cells on the soft substrates with pillars presented as shown in Figure 31.

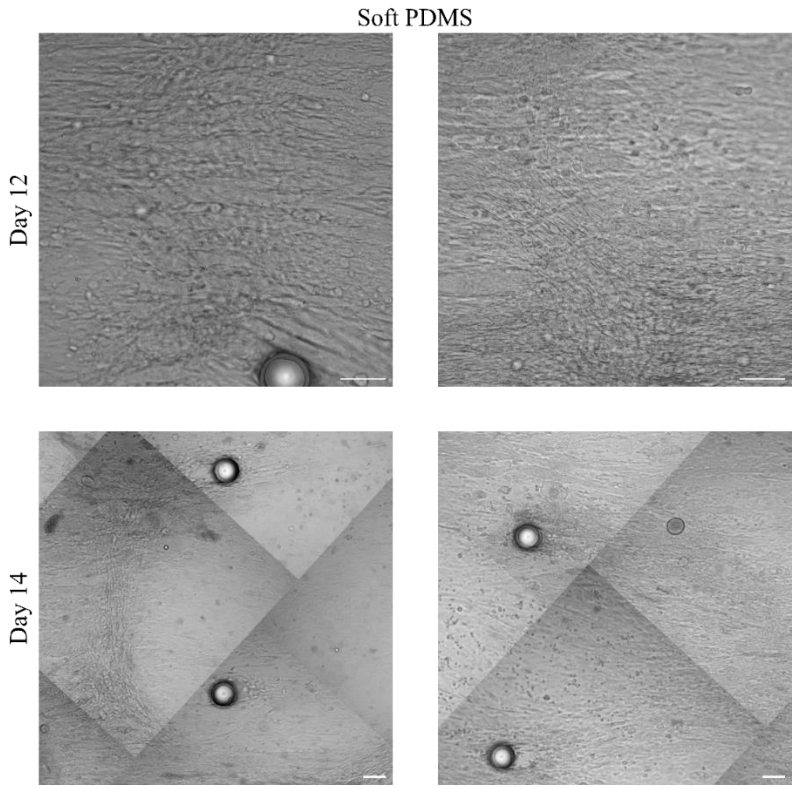

Figure 31: Soft PDMS substrates with pillars generating minimal muscle tissues at twelve and fourteen days in culture.
Cellular growth on fibronectin coated, soft, patterned substrates with pillars spaced 1 mm orthogonal and 2 mm parallel to the grooves at twelve and fourteen days in culture. The pattern was levelled horizontally for all images. Scalebars = 100 µm.

Muscle constructs formed both between and outside of the pillars, always in the orthogonal direction of the grooves, but never in the parallel direction. Even when providing a single line of pillars, in the parallel direction of the grooves, constructs were formed orthogonal to the groove direction. Examples of this are depicted in Figure 32 with examples of respective pillar organisations. Both substrates only had one single file of pillars present.

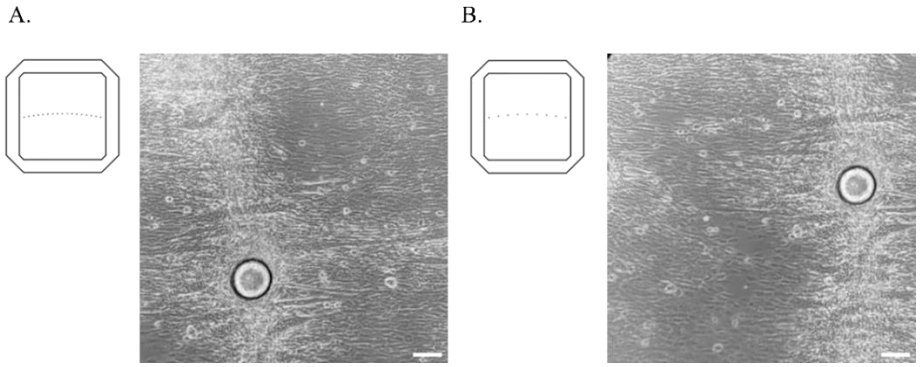

Figure 32: Construct formation on patterned substrates with a single line of pillars parallel to the grooves.
Cellular growth on fibronectin coated, patterned substrates with a single line of pillars, parallel to the grooves at two weeks in culture. The pattern was levelled horizontally for all images. Scalebars = 100 µm.

3.5 Extracellular matrix components of the constructs

The most efficient substrates were coated with fibronectin as discussed in 3.1. To evaluate why these constructs, form, a possible factor of interest was the ECM remodelling that cells perform on substrates with adsorbed proteins. The remodelling of the ECM was both evaluated in time, and compared to the substrates demonstrated in Chapter I, where no supracellular layer formation was observed. Figure 33 contains the fibronectin organisation on the surfaces in function of time. As the cells start forming an orthogonally oriented construct to the grooves, the fibronectin is remodelled as well.

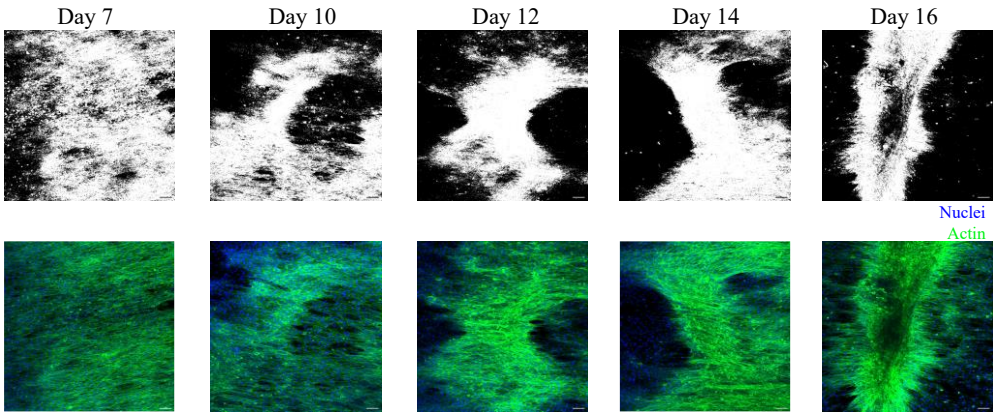

Figure 33: Remodelling of the fibronectin coating during tissue construct formation.
Binary masks of fibronectin present on the substrates with the corresponding cellular organisation at different timepoints. The mask was created in ImageJ for an overview of fibronectin organisation. Scalebars = 100 µm; Green = Actin; Blue = Nuclei.

Figure 33 demonstrates that during the tissue formation, the fibronectin layer on the surface does not remain a constant and flat attached layer but experiences a dynamic remodelling process.

These same samples were evaluated for their laminin production and remodelling as well. Laminin was not used as a coating for the substrates but is formed during the growth of the layers and tissue constructs and present in the growth medium. Laminin was found mostly within and close to the cells, as seen utilising immunofluorescence where the laminin is visualised in cyan and the actin in grey to enhance the contrast given in Figure 34.

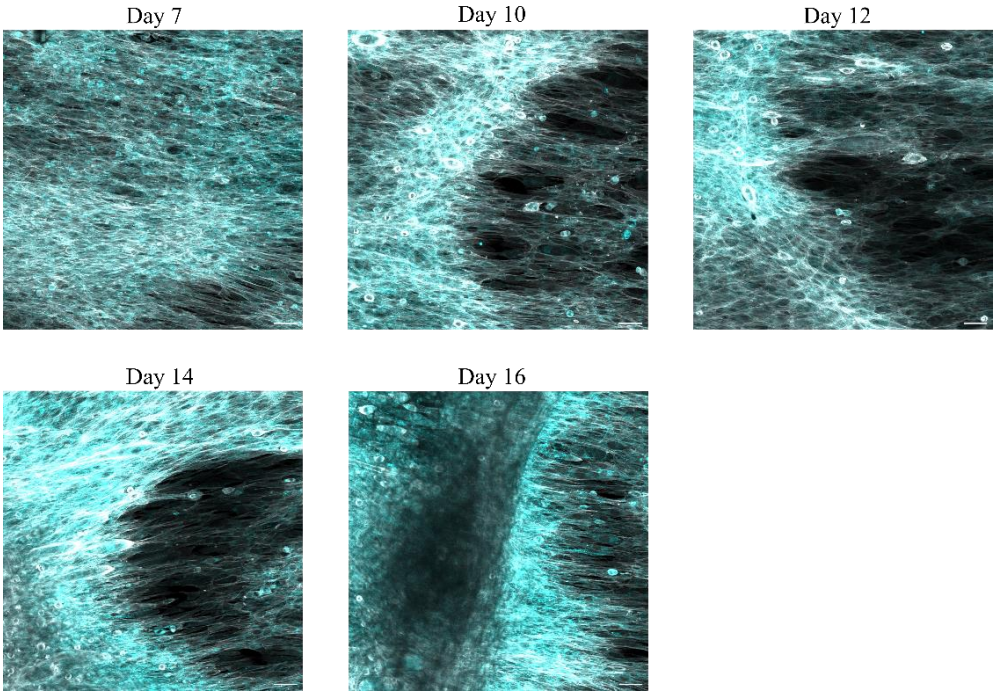

Figure 34: Laminin production by the muscle cells at different points in time.
Laminin present on the substrates with the corresponding cellular organisation at different timepoints. Scalebars = 50 µm; White = Actin; Cyan = Laminin.

Comparing these observations to 3D models of the cells, confirmed the presence of ECM compounds within the constructs. However, due to the visualisation of the antibody, this method provides no certainty about the presence of these components at the bottom of the structure, as demonstrated in Figure 35. The fact that the signal is lower at these positions, could be due to the limited penetration of the primary or secondary antibody, or due to the compound not being found there. A way to improve these findings was by electron microscopy, demonstrated in point 3.7.

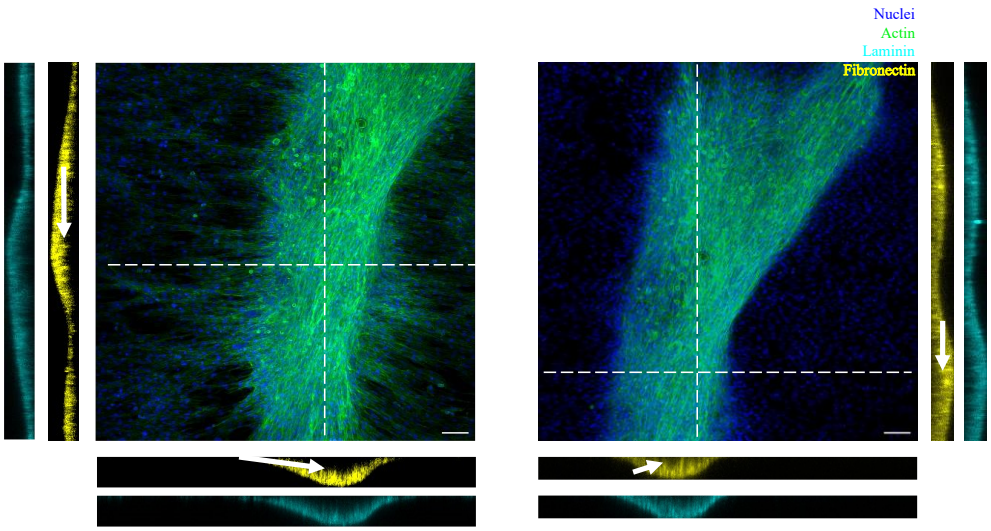

Figure 35: Sections of two representative constructs formed to visualise the depth and the ECM.
Cross section of two representative muscle constructs at sixteen days after seeding to visualise the shape and depth of the ECM. Cross-sections are taken along the white axes, for both laminin and fibronectin. Arrows indicate the depths at which no fluorescence was detected for the ECM proteins. Scalebars = 100 µm; Green = Actin; Blue = Nuclei; Cyan = Laminin; Yellow = Fibronectin.

As the PC and FlexDym™ used in Chapter I did not result in tissue formation, a possible explanation was sought in the remodelling of the ECM on those substrates. Since the FlexDym™ is similar to PDMS in a lot of mechanical characteristics, but consists of a different chemical composition, the fibronectin adsorption on the substrate might have been affected. PC on the other hand, is a much stiffer substrate with a lower contact angle, leading to a comparison of a vastly different substrate, with the same topography, to investigate whether topography is the decisive factor.

Figure 36 demonstrates the difference between the fibronectin remodelling on PDMS, FlexDym™ and PC after fourteen days in culture. The binary mask filter is applied to have clear image of the fibronectin-rich areas of the images. For the PDMS, most of the fibronectin is observed at the orthogonal muscle construct region, whereas for the FlexDym™ and PC the fibronectin is spread out over the whole region of interest. This observation indicates that the fibronectin was more effectively remodelled by the cells on PDMS rather than on FlexDym™ or PC.

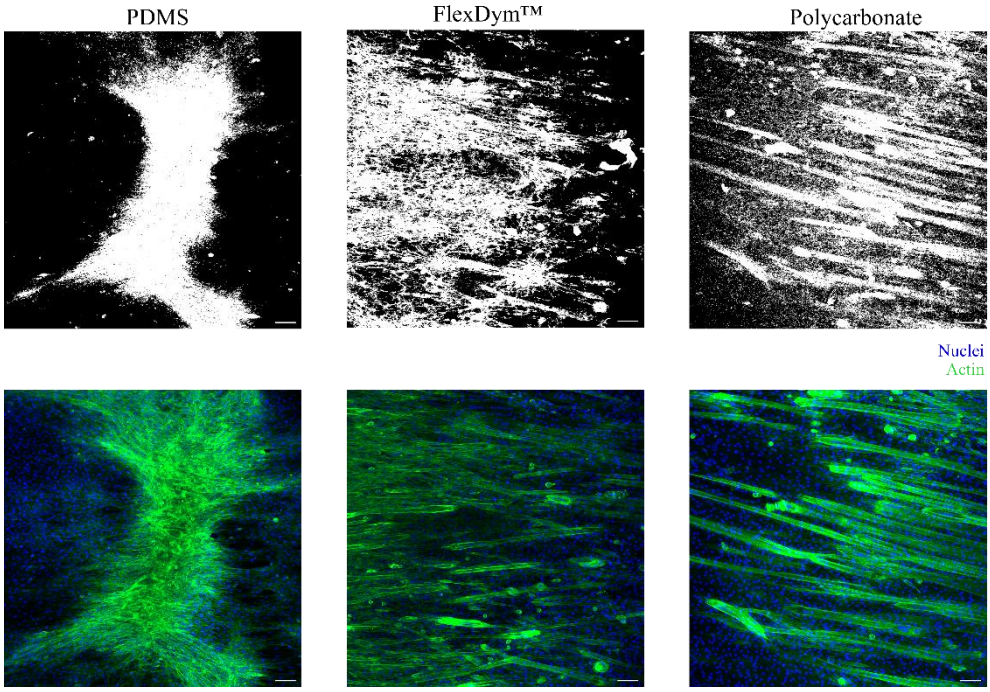

Figure 36: Remodelling of the fibronectin coating after fourteen days in culture on different substrate materials.
Binary masks of fibronectin present on the substrates with the corresponding cellular organisation at fourteen days in culture for PDMS, FlexDym™ and PC. The mask was created in ImageJ for an overview of fibronectin organisation. Scalebars = 100 µm; Green = Actin; Blue = Nuclei.

3.6 Transmission Electron Microscopy characterisation of the constructs

With the help of Dr. Mollo, Transmission Electron Microscopy (TEM) imaging was carried out to section the constructs parallel to their length. Visualising the cells in this manner, presents some information about the space in between cells and about the intracellular organisation. In Figure 37 three different views of cells within the construct are shown to get a view on the intracellular organisation. Panel A demonstrates side by side cells with elongated nuclei, while panel B contains a multinucleated cell, with a high density of mitochondria surrounding the nuclei. In panel C, a zoom is taken on the mitochondria organisation and fibre formation within the cells is found.

Intracellular organisation

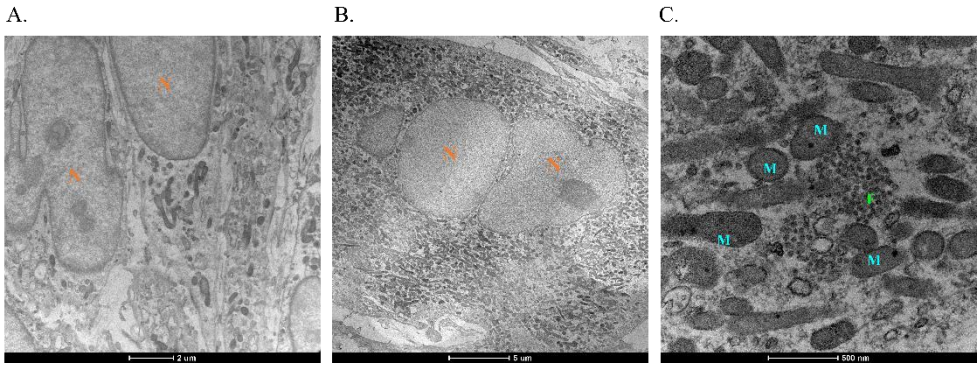

Figure 37: Intracellular organisation of cells within a construct at sixteen days in culture.
A. Focus on two nuclei of two cells, with elongated shapes. B. Focus on a high energy cell with at least two nuclei. C. Focus in the intracellular space with mitochondria and fibre production. N = nuclei; M = mitochondria; F = fibres.

These images show a high number of mitochondria within the cells, indicating a high energy cell phenotype.

Intercellular organisation

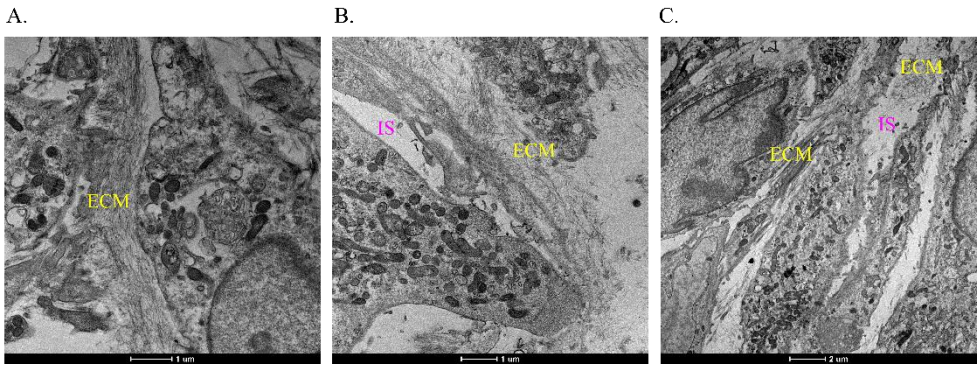

Figure 38: Intercellular organisation of cells within a construct at sixteen days in culture.
A.-C. focus on different regions of interest within the construct to demonstrate the space between cells and the ECM formation. ECM = extracellular matrix; IS = intercellular space.

Another way of using the TEM sectioning, is for the visualisation of the intercellular space, to indicate within the construct the interactions of the cells with their surrounding environment. Sectioning the tissue constructs gave a view on the ECM within the construct and indicated a large fibre formation as can be seen in Figure 38A. Other sections highlighted the elongated shape of the cells and the space between each cell (Figure 38).

3.7 Focused Ion Beam Scanning Electron Microscopy characterisation of the constructs

With the help of Dr. Mollo, Focused Ion Beam Scanning Electron Microscopy (FIB SEM) imaging was carried out on the constructs to visualise the depth and the attachment to the pattern. As the constructs at later culture times were very thick, some orthogonal formation on earlier timepoints were chosen to cut the structures using the FIB. Figure 39 demonstrates a SEM visualisation of a construct after ten days. Due to the sample preparation of the SEM images, the constructs slightly detach from the surface leading to a sort of elevated image. Due to the storage of the samples in PBS, there are some bacteria visible on the SEM images, but the general organisation of the orthogonal construct is highlighted in these images. Moreover, the construct visualised highlights the branches on the side of the construct parallel to the grooves, as some sort of little muscle constructs either feeding or stabilizing the main orthogonal structure.

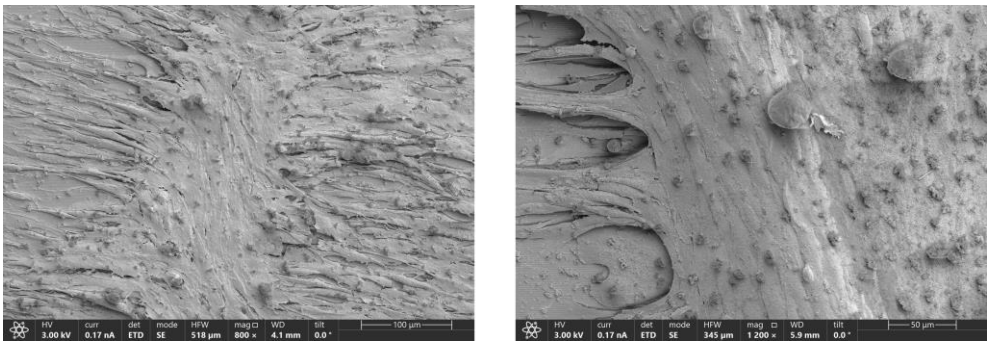

Figure 39: SEM imaging of an orthogonal construct after ten days in culture.
Construct formation as visualised by SEM after 10 days in culture, with the construct on the right being a zoom of the visualisation on the left.

Figure 40, Figure 41 and Figure 42 show the cross-sections of cells on the substrates after 10 and 12 days in culture. These FIB SEM images demonstrate that at these timepoints, the cells are still attached to the surface, and no detachment has yet occurred, as hypothesised by the gap in fluorescence in Figure 35. It is important to note that these sections represent just one area of the construct, and that thicker constructs might behave differently. However, using the FIB SEM it was not possible to cut large distances like 100 µm seen for the thickness of the constructs on day 16.

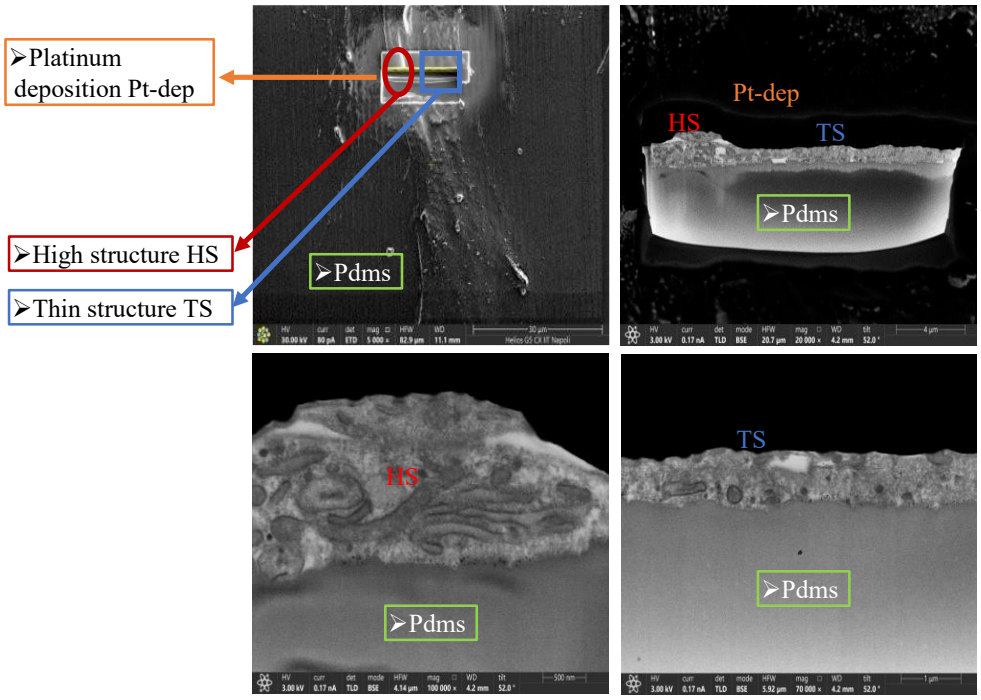

Figure 40: FIB SEM cross sectioning of muscle cells after ten days on the grooved substrates. Cross-section of the cells in the upper left panel using FIB SEM to identify the attachment of the cells to the PDMS substrates. Pattern direction is vertical in this instance. HS indicates the thicker part of the structure and TS indicates the thinner part of the structure.

Both the thick and thin layers on Figure 40 still indicate attachment of the cells to the substrate. However, these cells are not part of a larger construct and are aligned in the direction of the pattern.

A secondary sample was visualised after ten days in culture and a structure was observed to be attached to the PDMS as can be seen in Figure 41.

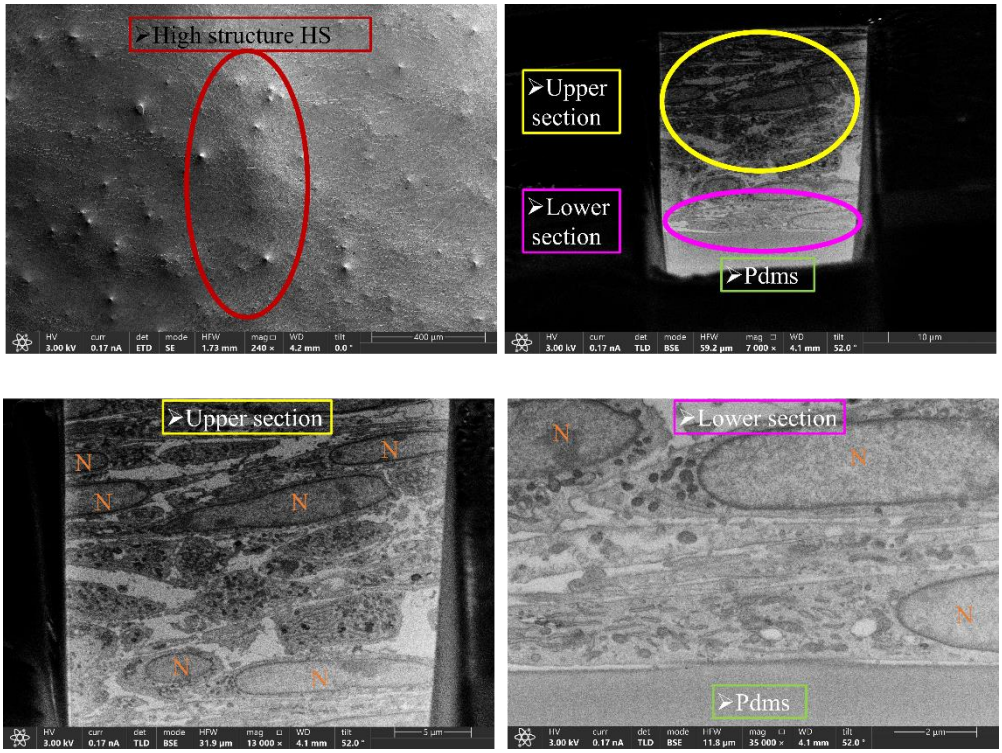

Figure 41: FIB SEM cross sectioning of a muscle construct after ten days on the grooved substrates. Cross-section of the high structure in the upper left panel using FIB SEM to identify the attachment of the cells to the PDMS substrates. Pattern direction is horizontal in this instance. A first section in the upper right panel was split into an upper section (yellow) and lower section (magenta). The upper section demonstrates the thickness of the construct after ten days in culture and the lower section indicates the attachment of the construct to the PDMS after ten days in culture. N indicates nuclei in the multicellular structure.

Figure 41 demonstrates a construct consisting of multiple layers of cells, as can be observed in the upper section of the FIB SEM cut, while still attached to the PDMS, clear from the lower section.

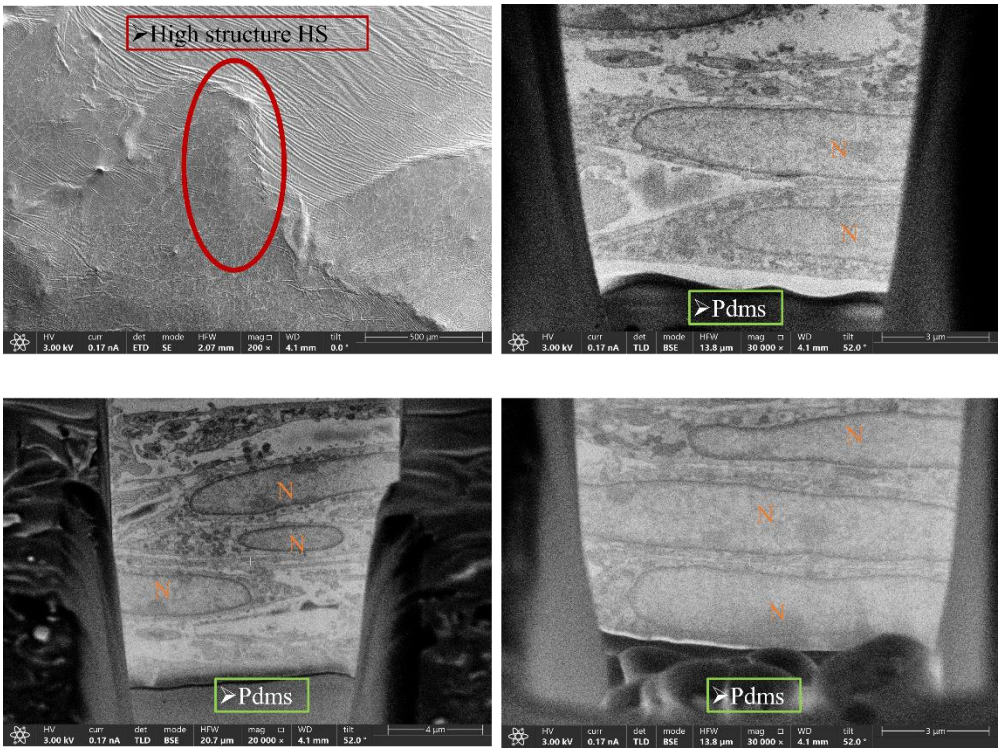

Figure 42: FIB SEM cross sectioning of muscle cells after twelve days on the grooved substrates. Cross-section of the cells in the upper left panel using FIB SEM to identify the attachment of the cells to the PDMS substrates with three representative sections. HS indicates the thicker part of the structure and N indicates nuclei in the multicellular structure.

FIB SEM sections of a high structure after twelve days in culture demonstrate that the cells are still adhering to the surface at this timepoint (Figure 42). Both right panels show the topography of the pattern in the PDMS layer, indicating that the cells shown are part of an orthogonal structure with multiple cells.

3.8 Introduction of primary cells to the model

Initial experiments using primary mouse muscle stem cells (MuSCs) isolated from mice fifteen days postnatal were used for the validation of the substrates.

MuSCs are activated upon isolation from the mouse and require growth factors and complex medium compositions to initiate myoblast formation and eventual differentiation. The protocol used for isolation of the cells was first described by Relaix in 2005 and allows the primary cell population to be a mix of satellite cell derived myoblasts and fibroblasts.

Primary cells are more variable and more sensitive to cell culture conditions compared to C2C12 cells. Therefore, the protocols used in previous set-ups were altered. Initially cells were seeded on surfaces without plasma treatment to verify

the need also in this set-up. Other conditions tested include: (1) no surface treatment with growth medium coating, (2) no surface treatment with gelatine coating, (3) air plasma treatment with growth medium coating, (4) air plasma treatment with fibronectin coating, all on nanogrooved surfaces of 700 nm width in hard PDMS, medium hard PDMS and FlexDym™. As an example, experiments with only growth medium coating of FlexDym™, without additional surface treatments showed adherence of the cells to the surface and morphologies aligned with the grooves. Cells proliferated until confluence but detached around day 10. Gelatine coating of these surfaces did not improve the adherence and cells did not proliferate until confluence. Representative examples of cultures on different timepoints are demonstrated in Figure 43. From day 8, also directionality plots are shown, to demonstrate the mostly horizontal localisation on the FlexDym™ surfaces.

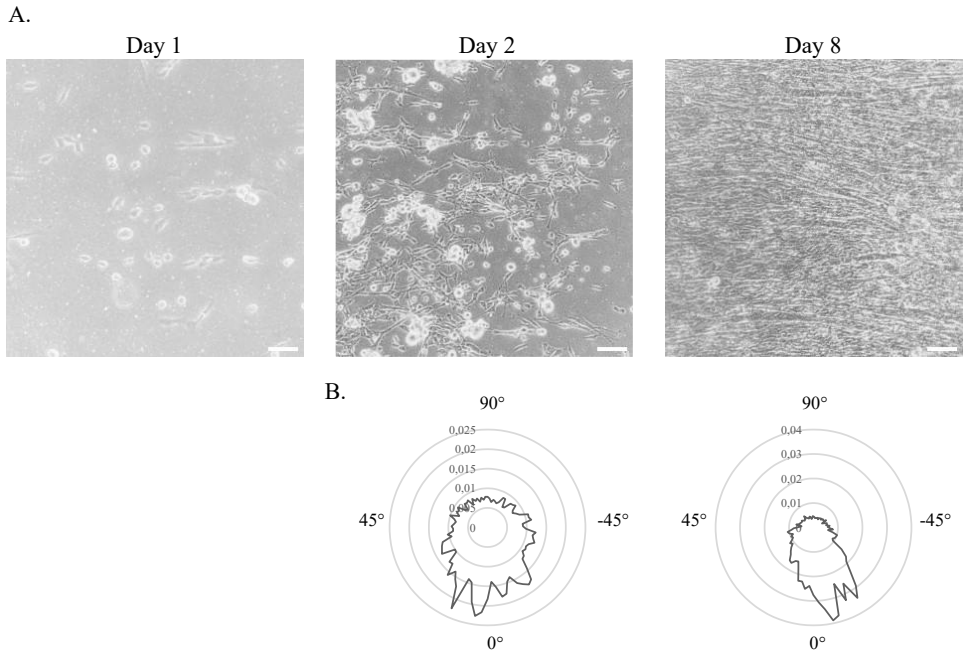

Figure 43: Primary cells on grooved FlexDym™ with overnight growth medium coating, without surface treatment.
A. Brightfield FlexDym™ substrates evaluated using primary satellite cells, at day one, day two and day eight in culture. B. The corresponding directionality overview in time. All spider plots show the frequency of cell aligning according to an angle between -90° and 90° where 0° equals horizontal alignment. The pattern was levelled horizontally for all images. All scalebars indicate 100 µm.

For experiments including air plasma treatments, the primary cells demonstrated less adhesion on fibronectin coated surfaces than on growth medium coated surfaces. On fibronectin coated PDMS surfaces, the cells showed initial alignment to the grooves, followed by a large portion of the samples prematurely detaching.

Surviving samples were fixed and stained at three weeks and examples are given in Figure 44. Primary muscle cells seeded on FlexDym™ formed aligned myotubes in the direction of the pattern, but no orthogonal muscles were observed at this timepoint using fibronectin coating.

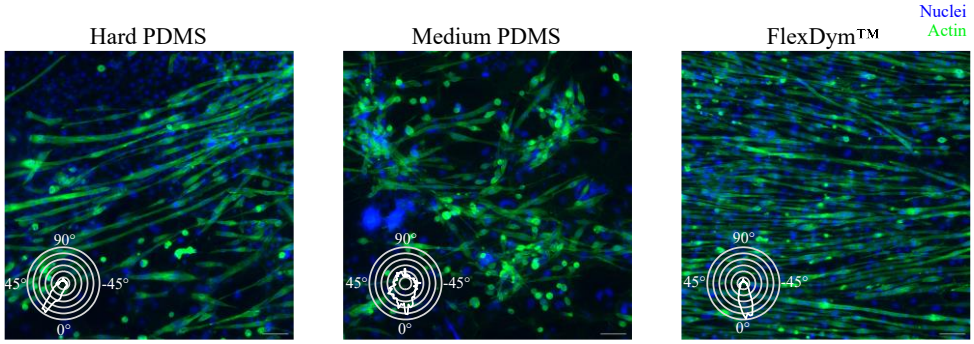

Figure 44: Primary myoblasts after three weeks in culture on fibronectin coated hard PDMS, medium PDMS and FlexDym™ substrates.
Patterned substrates with the corresponding directionality. All spider plots show the frequency of cell aligning according to an angle between -90° and 90° where 0° equals horizontal alignment. The pattern was levelled horizontally for all images. Scalebars = 100 µm; Green = actin; Blue = nuclei.

Growth medium coated PDMS with medium hard stiffness, and FlexDym™ surfaces demonstrated the possibility of prolonged MuSCs culture on the grooves with contraction of the cells starting on day 10. In initial experiments, samples were all switched to differentiation medium (DM) on day 8 to evaluate the possibility of myotube formation in these mixed cell culture populations. Samples cultured in DM on FlexDym™ started contracting on day 10 of culture and continued to contract up until day 21, when the cells were fixed. Orthogonal cell migration was postponed until day 20 in these samples, as the switch to differentiation medium hindered the proliferation of the cells in favour of the differentiation into myotubes. Nevertheless, on a confluently filled myotube surface, myoblasts were able to start migrating orthogonally to the pattern of the grooves as demonstrated by the orientation analysis in Figure 45.

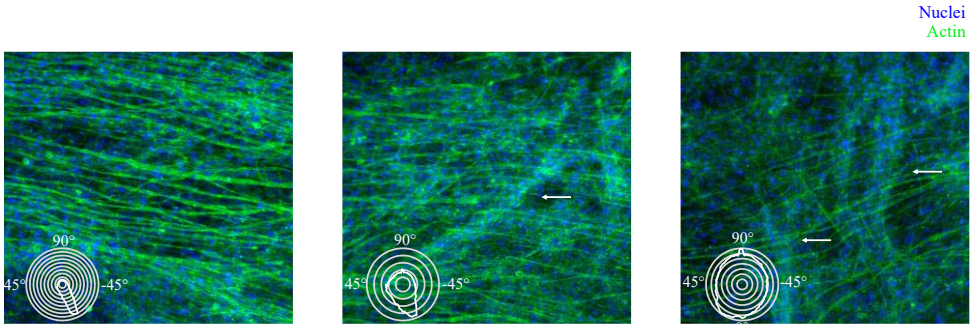

Figure 45: Primary myoblasts after three weeks in culture on growth medium coated FlexDym™ substrates, with orthogonally migrating myoblasts.
Patterned FlexDym™ substrates with the corresponding directionality. Arrows indicate orthogonally migrating cells. All spider plots show the frequency of cell aligning according to an angle between -90° and 90° where 0° equals horizontal alignment. The pattern was levelled horizontally for all images. Scalebars = 100 µm; Green = actin; Blue = nuclei.

On medium coated 1-5 PDMS all cells detached before reaching confluence, while on medium coated 1-10 PDMS, cells were able to cover the surface of the substrate. The sample that was switched to differentiation medium on day 8 demonstrated contraction and orthogonal migration of myoblasts on day 10 and day 13. The sample contracted in large movements and detached before the next timepoint on day 14. A video can be found in the supplementary materials for the visualisation of the contraction on the substrates.

Unfortunately, a limiting factor is the availability and quality of the primary cells, as they were directly isolated from mice. Repeating some of the experiments resulted in contradictory observations, where cells did not adhere in setups that worked for another batch of cells.

4. DISCUSSION AND CONCLUSIONS

Skeletal muscle tissue engineering is a field that aims to develop methods to regenerate, repair and study tissues in an *in vitro* setting. This to both reduce the need for animal studies and design patient specific strategies with, for instance, patient derived stem cells. *In vitro* tissue formation has been a point of focus for a variety of tissues, including skeletal muscle, cardiac muscle, tendons, and cartilage, for instance. A variety of approaches for this goal was discussed in the introduction of this chapter. The formation of tissues from single cells *in vitro*, remains an important topic with respect to the tissue formation *in vitro*, but also to study cell-cell interactions in specific set-ups. Driven by intracellular interactions and cell-matrix interactions, it has been hypothesized that for certain tissues, initial cues on the surface allow for self-organisation of supracellular structures and tissue constructs [335], [336]. With this chapter, this process was evaluated for skeletal muscles, to assess the ability of C2C12 cells to form skeletal muscle tissue constructs *in vitro*.

4.1 C2C12 cells on parallel grooves form orthogonal muscle constructs

This chapter highlights the formation of a 3D muscle tissue construct when growing the cells on PDMS substrates. In literature, plenty of examples were designed where cells, grown on a ridge and groove substrate align and form myotubes parallel to the grooves. Using a specific 700 nm wide ridge and groove substrate with a depth of 200 nm, it was observed that after 10 days in culture, cells start to aggregate in an orthogonal construct. This was not a singular observation where cells detached and cluster, but rather a replicable process with an organisation the cells in a 3D tissue like construct. Characterising this construct revealed information about the thickness of the constructs and the organisation within, as well as the preferred circumstances for the constructs to grow.

Different stiffnesses of PDMS were compared to pinpoint the effects of substrate stiffness on the construct formation, but the orthogonal movement was observed on all types of PDMS substrates tested. The only observed difference occurred at later timepoints when hard PDMS proved to promote early detachment, and when comparing the thickness of the substrate. Soft PDMS sustained orthogonal formation, but the constructs were less pronounced at any given timepoint as could be seen on Figure 19, Figure 20, Figure 22 and Figure 31, for instance.

The best constructs were formed using fibronectin or overnight medium coating, while laminin did not generate muscle constructs to the same level as the former two. However, medium contains serum that has a variable ECM protein content. Studies have demonstrated in the past, that serum contains mostly fibronectin and vitronectin [337]. Although, due to the Vroman effect [338], it is not as clear how much of which protein has been adsorbed, along with the localization on the

surface. Using a Myosin Heavy Chain staining, the presence of myotubes within the construct was verified and indicates the differentiation of the C2C12 cells.

Skeletal muscle is a dynamic tissue, sensitive to mechanical cues in the environment, and approaches using soft hydrogels [339], or nanotopography [80] are well considered in the field of skeletal muscle tissue engineering. Moreover, skeletal muscle tissue consists of a highly organised structure with long aligned fibres, approaches to align the cells *in vitro* are being considered as well [340]. These approaches include ridges and grooves of nanometre to micrometre sizes, but in all of the past approaches, the goal was to create a flat layer, aligned to the pattern. The pattern and protocols used in this work confirm this type of alignment at early stages of the protocol but report a self-assembled tissue in the orthogonal direction after prolonged culture times. The capacity of the cells to form a small tissue construct by themselves is the key point of this protocol, implying the formation of tissue constructs without forcing the cells in artificial 3D environments. The constructs were formed on surfaces coated with fibronectin containing agents, but not on laminin coated surfaces, implying a role for the initial cell adhesion in the later construct formation. Furthermore, changing the substrate to a softer stiffness or a different material with a similar topography, inhibited the tissue construct formation. This indicates a role of the material adhesion and surface energy in the formation of the constructs.

The formation of the orthogonal tissue construct is an important observation for other *in vitro* protocols, as the materials used are more influential than expected when using them solely for aligning the cells. Grooved PDMS has been used in microfluidic organ-on-a-chip platforms [341]–[343] or cell culture approaches [80], [340] for aligned myotube formation, and the cell-material interactions were here shown to have an additional impact the cultures. Highlighting the additional effects the material can have on a cell culture platform, is important to consider in these other setups as well.

4.2 Alterations in the substrate architecture improve the architecture of the C2C12 based muscle constructs

Expanding the substrates using micropatterning proved to be ineffective to create long term cell culture, due to the presence of the anti-adhesive agent PLL-PEG. In millipatterning, on the other hand, the mask is used to create alternating zones that were oxygen plasma treated and fibronectin coated and zones without coating or treatment. The mask was shown to be an effective way to force the origin of the construct formation in a particular area of the substrates. Using 20 mm long adhesive areas and forcing the cells from the cell seeding to adhere to those zones, lead to the formation of long, continuous muscle constructs on both hard and medium PDMS. Another approach was to expand the substrates with pillars, to

increase the formation rate of construct formation. Secondly, the pillars enhance the stability of the formed constructs, by hopefully catching them between the pillars. Again, in this case, the construct formation was improved compared to the standard grooved PDMS, for both hard and medium substrates, whereas for soft PDMS the constructs formed but remained less pronounced.

Patterning the substrates forces the cells to initially adhere in specific regions. As Chapter I discussed, the C2C12 cells were able to adhere to any type of PDMS, but preferred plasma treated and coated PDMS, at later timepoints. Using the millipatterned mask to trap the cells in long orthogonal regions to the nanogrooves provides a type of boundary condition that seems counterintuitive to the spontaneous formation of tissue constructs. However, cells originally did align in the direction of the nanogrooves and not along the direction of the orthogonally placed adhesive pattern, stipulating also here a role for the cell driven assembly. The addition of this adhesive pattern is simply an extension of the whole nanogrooved surface, where instead of regions of 18 x 18 mm to adhere and form tissue constructs randomly, the cells have a 1-2-3 mm x 18 mm area to adhere to instead.

The inclusion of small pillars on the substrate was considered to increase the mechanical stability of the formed tissue constructs [344]. The pillars, however, also disrupt the confluent cell layer and caused the formation of earlier orthogonal growth in the middle between four pillars instead or attached to them. These constructs then migrated and moved, and were sometimes caught between the pillars, for enhanced mechanical stability. Including pillars in, for instance, hydrogel structures has been considered as an approach to align cells within a hydrogel, but also allows the study of the movement of pillars to relate the stress of the formed constructs [345]. Expanding the current substrates monitoring the movement of the pillars after stabilising the tissue constructs, could lead to improved knowledge of the mechanics of the formed tissue.

4.3 The fibronectin coating is remodelled in time and becomes a part of the muscle constructs

Since the cells start remodelling and forming orthogonal constructs, a point of interest was to determine the faith of the fibronectin on the surface. Using an immunofluorescence staining for the fibronectin at different timepoints, the remodelling of the fibronectin coating was accentuated. When the constructs were forming, the monolayer of fibronectin was relocated and reshaped to support the muscle constructs. Immunofluorescent staining demonstrated a gap between the surface and the fibronectin with cells, once the constructs were formed, but FIB SEM imaging confirmed that the cells were still attached to the surface. This gap is shown in Figure 35 and was caused by the fluorescence and antibody

penetration within the tissue. Furthermore, both cells on the surfaces and within the constructs were surrounded by their own secreted laminin layer.

In vitro tissue formation is influenced by the ECM present, as it provides an additional level of topography, and cell-matrix interactions on the substrates. Furthermore, the ECM provides adhesion points for the cells on the surface through well-known interactions (e.g. Focal adhesions). The results shown in this chapter suggest that cells seeded on laminin coated substrates were not able to create muscle tissue constructs, whereas cells on fibronectin containing substrates formed a 3D layer orthogonal layer.

The substrates were treated with oxygen plasma and afterwards coated with either laminin, fibronectin or growth medium to increase the cell adhesion and proliferation on the substrates [65], [346].

Physically adsorbing the proteins to the substrate in static cultures, has resulted in, for instance, fibronectin desorption after seven days in culture in past research [347]. Coating the surfaces with laminin or fibronectin has been shown to result in a similar protein distribution and adhesion capacity of smooth muscle cells [348]. However, on the proposed skeletal muscle platform, differences in long term culture are observed with respect to the cellular behaviour in 3D, where the coating is incorporated into the 3D structure. These clusters in the fibronectin distribution were not observed on FlexDym™ or PC substrates, suggesting an altered capacity of the cells on those surfaces to remodel the fibronectin. As suggested in Chapter I, the fibronectin coating on oxygen plasma treated PDMS is less effective, but results in a better cellular adhesion than on non-treated PDMS. A possible explanation for the difference between the fibronectin layers on the different materials could be the surface energy of the FlexDym™ and PC, resulting in an altered binding of the fibronectin. Even though no differences in adhesion were shown in chapter one, when comparing the plasma treated materials, the surface composition and energy might influence the fibronectin modelling.

Skeletal muscle cells grow and fuse more on fibronectin coated substrates than laminin or gelatine coated substrates. The fibronectin influences the collective migration favouring cell-cell alignment and fusion with a contribution of N-Cadherin [179]. Furthermore, the collective cellular behaviour seen on fibronectin is mediated by $\alpha 5\beta 1$ and $\alpha v\beta 1/\alpha v\beta 3$ RGD binding integrins at the surface of the cell. It is exactly this type of behaviour that could be responsible for the improved tissue construct formation on fibronectin containing substrates over laminin containing substrates.

The skeletal muscle artificial niche platform here described, provides a basis that aligns the cells first in an organised monolayer, on loosely adhered fibronectin that has been demonstrated as a better environment for cells to adhere and remodel their environment [65], [71]. On this substrate, cells are demonstrated to align according to the grooved pattern [349] until the formation of an anisotropic monolayer of cells. The fibronectin present has encourages collective cell migration in C2C12 cells and this may result in global movements of the cells [179], according to the direction of the pattern as it may impact how the leading edge of the cells is oriented, in cellular migration. In the case that the movement of the cells is indeed global or collective, in the direction of the grooves upon monolayer formation, there might be groups of migrating cells that collide and cause the formation of the orthogonal construct.

As discussed, the fibronectin present can be used by the cells for remodelling, and their original monolayer organisation and migration are impacted due to the grooves and coating. This results in the hypothesis, that the combination of nanogrooves, formation of a monolayer, and collective movement due to the presence of fibronectin, are factors that once combined, cause the formation of the orthogonal construct. In Chapter III, a section about the collective movement of the cells around the constructs is included, to finetune this hypothesis.

4.4 Further research is necessary to improve the model for primary cell applications

The experiments using primary cells serve as preliminary assessments to improve the relevance of the model. Future research would allow the model to be applied to more relevant cell sources such as primary human cells of both healthy and diseased donors, but also to induced pluripotent stem cells. These preliminary tests show great potential for the use of the bio instructive surfaces in the guidance of myogenic cells towards three-dimensional tissue constructs, but as already done for C2C12 cells, require more effort into the maturation of the constructs to represent a better 3D entity. Current experiments demonstrate that FlexDym™ with plasma treatment and growth medium coating provides a possible candidate for orthogonal tissue formation of nanogrooves. In this case, improved growth/differentiation medium conditions and growth factors might be necessary, as primary cells are much more sensitive than cell lines as C2C12. With the air plasma limitation of the lab in this case, the FlexDym™ provided a better substrate than PDMS. A comparison of the primary cells on oxygen plasma treated PDMS instead of air plasma treated PDMS, could increase the efficacy of the substrates, since the efficacy of the hydrophilization is improved. Experiments in this section were limited by the materials present in a purely biological laboratory, without access to microfabrication and surface treatment facilities. Another limiting factor

is the availability and quality of the primary cells, as they were directly isolated from mice. Repeats of some experiments lead to contradictory results, where cells did not adhere in setups that worked for another batch of cells.

4.5 Conclusion and future perspectives

This work presents a unique way to create small muscle constructs *in vitro*, by providing the cells with a set of cues in the beginning of the cell culture process. No intervention at later timepoints was necessary to get the layers of cells to go from 2D to 3D, unlike previous studies using alignment strategies for skeletal muscle tissue engineering. This substrate can be considered as an artificial microenvironment for the muscle cells, which guides the formation of a construct thanks to the adsorbed proteins, the stiffness, and the presence of a topography. The muscle constructs present an easy to implement platform to study muscle behaviour *in vitro*, with a high replicability and a minimal manual involvement in the 3D formation. It further sheds a light on the importance of cell-material interactions in any kind of *in vitro* set-up. Simply using a material, with a topography, particular substate stiffness and protein coating, the cells were guided from a low-density environment to the formation of a microtissue *in vitro*.

Additional efforts should be given to implementing this platform in a co-culture with vasculature or neurons, to further mature the muscle and mimic biological processes. Adding blood vessels to the muscle increases the oxygen perfusion of the tissue and improves the capacity of the constructs to become larger, without forming necrotic cores in the middle of the construct. For the same reason, implementing a dynamic culturing condition, such as in a microfluidic chip, could improve the model. Co-culture with motor neurons, for instance, would allow the formation of neuromuscular junctions, and the consequent study of the formation of these junctions in health and disease on chip. The current model was designed using a mouse myoblast immortal cell line and initial experiments were carried out using primary mouse myoblasts. To improve the relevance of the model for *in vitro* drug testing, it would be interesting to use either primary cells from a mouse with a dystrophic phenotype, for instance, or induced pluripotent stem cells, to model their behaviour on the chip.

III. EVALUATION OF THE MECHANICAL PROPERTIES OF CELLS ON NANOGROOVED SUBSTRATES

As the techniques seen in Chapter II focus developing a muscle starting from a set of initial cues, the initial conditions of the cells on the different substrates were evaluated with respect to their effect on the mechanical identity of cells. Because the cells experience an altered morphology and alignment on flat and patterned substrates, an evaluation was carried out of the tension in the cells and the elasticity of the cells in the initial phases of the muscle cultures. This chapter focusses on two methods two evaluate cellular mechanical identity, namely actin tension using a fluorescent biosensor and elasticity determined by atomic force microscopy. Additionally, migration experiments at the construct formation stage were included in this section, to shine light on the migratory behaviour of cells on the substrates.

1. INTRODUCTION

This section reviews some important aspects of the cell and its interactions with the environment for a better understanding of cell mechanical identity, and the rationale behind the carried-out experiments. A second section discusses the techniques used, with a focus on their function for assessing cellular mechanical identity. Lastly, mechanisms of cellular migration are reviewed for an understanding of this process.

1.1 Introduction into the mechanical identity of a cell

Both factors inside and outside the cells influence their behaviour and function. Some important intracellular and extracellular interactions are briefly described to get a better comprehension of cell mechanics.

1.1.1 Important cytoskeleton components

The cytoskeleton is a voluminous network of protein filaments essential to maintain the mechanical integrity and the cellular shape [350]. It provides resilience to external mechanical forces and exhibits dynamic properties that enable it to undergo self-deformation. In mammalian cells, the cytoskeleton consists primary of three categories of protein filaments: microtubules, actin, and intermediate filaments [351]. The actin and microtubules are polar filaments, capable of generating forces in opposite directions by coupling their polymerization with nucleotide hydrolysis [352]. Intermediate filaments on the contrary are nonpolar and exhibit a higher degree of stability [353]. All three types

of filaments are semiflexible polymers, indicating their ability to maintain a linear conformation in the presence of thermal fluctuations [351]. Actin and intermediate filaments are typically regarded as the primary contributors to cellular stiffness [354], with the comparatively rigid microtubules participating in the resistance to compressive forces [355], [356]. When subjected to mechanical forces such as shear or stretching, actin and intermediate filaments exhibit an increase in stiffness [357]–[359]. This property allows cells to actively reinforce their actin skeleton when interacting with more rigid substrates, though a contraction that is facilitated by myosin motors [360]. In intermediate filaments this property is believed to serve as a protection against excessive deformation of the cells [358], [359].

1.1.1.1 Actin

Cells in a 2D culture typically demonstrate the presence of stress fibres within cells, which are contractile structures composed of acting and myosin II proteins [361]. There are several distinct categories of such fibres: ventral fibres, dorsal fibres, transverse arcs, and actin-cap fibres [361]–[363]. Ventral fibres are stress fibres that typically extend nearly the entire length of the cell, anchoring at both ends to focal adhesions (FAs) [364]. Dorsal stress fibres are linked to FAs at one end and link to transverse arcs [365]. They are assembled independently of myosin and regarded as non-contractile [366]. Transverse arcs are curved actomyosin fibres that emerge predominantly at the leading-edge during cell migration and are not associated with FAs [364]. Actin-cap stress fibres extend over the cell nucleus and remain tethered to it. The extend of actin crosslinking and bundling increases with increasing substrate stiffness [351].

Actomyosin contractility plays a pivotal role in the maturation process of nascent FAs, facilitating their growth into larger FAs [367]. It furthermore reinforces the anchoring of actin filaments through interactions with vinculin and talin [368]. In motile cells, nascent adhesions form in the lamellipodium, independent of myosin II activity [369]. However, these nascent adhesions fail to mature and instead undergo a rapid turnover in the absence of actin-myosin contractility [367]. Actin polymerization is critical factor for the formation of nascent adhesions [369].

In 3D extracellular matrix (ECM) networks, stress fibres tend to be less numerous and thinner in comparison to 2D environments [370]. However, in both conditions, the development of stress fibres remains dependent on the stiffness of the matrix [371]. For stem cells, for instance, a higher stiffness of the matrix leads to a higher concentration of actin near the cell cortex [372]. In dynamic 3D compression scenarios in collagen gels, actin protrusions are correlated with matrix remodelling [373].

Non muscle Myosin II (MyoII) is a part of the actomyosin complex and generates force to regulate cellular behaviours, like adhesion and migration [101]. MyoII can be repositioned by externally applied forces and directly senses mechanical tension [374]–[377].

Specifically in skeletal muscle, actin is the primary component of the sarcomeric thin filament, as highlighted in section II.1.1.1. It accounts for 20 % of the total striated muscle mass [378], with the primary isoform being α-Skeletal actin [379]. Upon α-Skeletal actin knockout in a mouse model, α-Cardiac actin is upregulated to restore the thin filaments, but a decrease in muscle strength is observed [380]. This upregulation has proved to be insufficient and without α-Skeletal actin, the mice died in the neonatal period [380], indicating the necessity of proper actin expression for the functionality of the muscle. Several myopathies are caused by mutations in straited muscle actin, with muscle weakness and decreased muscle tone as indicators of these diseases.

Other isoforms of actin present include β-cytoplasmic and γ-cytoplasmic actin, and are expressed in cardiac, skeletal and smooth muscle tissues [378]. A fraction of the β-cytoplasmic actin can be found at the leading edge in motile cells [381], and is specifically required for cell migration and proliferation [382], [383]. γ-Cytoplasmic actin is found in the filamentous structures surrounding the mitochondria, in proximity of the sarcolemma and at the costameres of the muscle [384]. The costameres are structures that bridge the sarcomere to the sarcolemma and ECM, and play an important role in the maintenance of the mechanical integrity of the muscle [385].

1.1.1.2 Microtubules

Microtubules (MTs) are built out of α-tubulin and β-tubulin for the formation of long cytoskeletal tubes, extending tens to hundreds of micrometres [386]. The structure is primarily known for its role in protein transport and chromosome segregation during mitosis. However, MTs are not only important in cell polarity and migration, but they also play a role in mechanosensation [387]. In endothelial cells, MTs are necessary for cell alignment in response to shear stress [388]. MTs in fibroblasts were shown to have a specific role in nuclear localisation [389], important for cell function in, for instance, neurons, cochlear hair cells and skeletal muscle cells [390]–[393]. On 2D substrates, the presence of MTs does not appear to exert a discernible influence on the degree of cell spreading for fibroblasts, for instance. However, absence of MTs resulted in cells incapable of polarization of 2D coverslips [387]. In a soft 3D environment, interfering with MTs resulted in round cells, unable to form extensions seen in normal fibroblasts [387]. MT acetylation promotes the disassembly of FAs [394], to improve cell migration by preventing excessive FA adhesion [395].

While centrosomal microtubule organising complexes can be found in any proliferating cell, a transition to non-centrosomal microtubules is observed in differentiating epithelial cells, skeletal myotubes or cardiomyocytes, for instance [396]. In myofibres, microtubules form a grid with longitudinal unites, parallel to the long axis of the fibre and perpendicular units, transverse across the fibre [397].

Moreover, in fused myotubes, nuclei move to the periphery, with mis-localised nuclei being featured in muscle diseases with impaired muscle function [398]. Connecting the nucleus to the microtubule cytoskeleton, via the LINC complex for example, is imperative to proper nuclear positioning in striated muscle [138]. Even though the microtubules are important for proper positioning in skeletal muscle, mutation in the microtubule organising complex are seldomly responsible for striated muscle diseases [399]. Emery-Dreifuss muscular dystrophy, for instance, presents altered nuclear positioning due to mutations in Nesprin-1 and Nesprin-2, but it is not clear whether the nuclear position is the cause of the dysfunction in these patients, or a combination of the position, as well as epigenetic regulation [138]. Microtubules and the LINC complex are furthermore important in the protection of the muscle nuclei during muscle contraction [396].

1.1.1.3 Intermediate filaments

Intermediate filaments (IFs) constitute a family of proteins categorized into five different types based on their self-assembly properties [400]. Acidic and epidermal keratins represent two out of five types, type 3 contains desmin, vimentin, peripherin and glial filament acidic protein. The fourth type are proteins mainly expressed in nerve cells, such as α-internexin and the fifth type includes nuclear lamins [400].

IFs have unique mechanical features and are important for cellular resistance to mechanical stresses. They are flexible thanks to their short persistence length, and highly stretchable both in nuclear and cytoskeletal domains, resisting stretches up to 300 % before breakage [401]. They are loading-rate dependent, indicating that for example fast stretching can induce stiffening of the filaments at a lower strain percentage than slow stiffening [402].

Single cell experiments of keratinocytes furthermore demonstrated that upon type I or type II keratins deletion, the Young's Modulus of the cells decreased by more than 50 % [403], [404]. Cell stiffening on the other hand, was caused when overexpressing either desmin or vimentin [405]. The wide variety of IF protein compositions, provides a spectrum of mechanical properties. IFs appear to be the main components responsible for cytoplasm elasticity [406]. Depletion leads to reduced FA turnover, altered direction of collective migration and a reduction in migration speed [407], [408].

In skeletal muscle cells, desmin has both a structural and a regulatory role, in the conservation of myofibrillar alignment, stress production and nuclear deformation [409]. Desmin is localised to the muscle Z-disk, where it connects the myofibrils laterally [410]. Desmin is one of the first muscle-specific genes expressed during muscle development, and can be found in high concentrations around the mitochondria and nuclei [411]. Desmin is involved in both the mechanical stress transmission and transduction in muscles [409]. Vimentin in skeletal muscles is associated with the cellular architecture and motility. Both desmin and vimentin, interact with the mitochondria and are primary factors in facilitating the mechanotransduction in muscle [412].

1.1.2 Extracellular signals influencing the mechanical identity of cells

The ECM is a complex network of proteins that presents the main acellular microenvironment of cells [413]. It is the mechanical support of cells and tissues, and additionally serves as a reservoir for enzymes, cytokines, and growth factors [414].

Important categorizations of the ECM are the connective tissue and basement membranes [415]. Connective tissues create a three-dimensional (3D) fibrous scaffold, primarily composed of proteoglycans, glycosaminoglycans and fibrillar collagens [416]. Proteoglycans and glycosaminoglycans are hydrophilic macromolecules that aide in water retention and influence the ECM deposition and cell movement [417]. The organisation and diameter of collagen fibres are unique to the specific biomechanical function of tissues [418]. Basement membranes on the other hand are thin sheets of ECM, to separate tissues and protect them from mechanical stress [419]. Laminin, collagen IV, heparan sulphate proteoglycans and nidogen are examples of key components of a basement membrane [419]. Functions that are dependent on basement membranes include strong (epi-)dermal attachment, selectivity of glomerular filtration and stabilization of the skeletal muscle sarcolemma [420]–[422].

The ECM furthermore contains non-structural components, that can regulate interactions between the ECM and cells [423]. When subjected to mechanical forces, the ECM proteins can also act as mechano-transducers to expose growth factors and cryptic sites [424]. During wound healing, cells encounter a temporary ECM that is formed as the result of blood clotting. This temporary ECM is formed of fibres composed of plasma proteins fibronectin and fibrin [425]. The stiffness, composition and architecture of the ECM can change during, for instance, disease progression and aging [426]. As the cells are highly responsive to extracellular cues, the ECM is seen as an active participant and even potential therapeutic target in diseases such as cancer and fibrosis [427], [428].

In the next paragraphs, some of the ECM properties that influence the cellular mechanical identity are briefly described.

1.1.2.1 Stiffness of the extracellular matrix

The mechanical properties of the ECM are critical in biological processes. ECM stiffness marks the resistance to tissue deformation and induces a shift in tissue elasticity [429]. Cells cultured on 2D substrates can actively sense and respond to the stiffness of the substrate material [360]. Various fundamental processes in cell behaviour are known to be mechanosensitive, including adhesion, migration, apoptosis, cell-cell interactions, and gene expression [430]. Substrate stiffness can furthermore modulate stem cell differentiation and interact with biochemical cues [351], [360]. Furthermore, ECM stiffness is involved in pathophysiological processes, such as in the case of tumour development, benign pancreatic diseases and multiple organ fibrosis [431]–[435].

In vitro experiments using 2D substrates frequently utilise nonadhesive materials such as polyacrylamide (PAA) or polydimethylsiloxane (PDMS), that are then coated with ECM proteins or ligands [351]. Systematic investigations have demonstrated that cells cultured on PAA gels, can perceive mechanical cues over tens of microns [64]. This range can be extended to approximately 200 µm when cells encounter fibrous networks of fibrin or collagen [436], [437]. This exceptionally long-range force transmission observed in these ECM networks, can be attributed to the fibrous nature of the ECM itself as has been supported by finite element simulations modelling traction force transmission in collagen and fibrin. They revealed that cell tractions predominantly concentrate in the relatively stiff ECM fibres, thus allowing for a grater propagation distance compared to a homogenous elastic medium [436], [438].

Unlike synthetic PAA and PDMS substrates who present a constant stiffness, fibrin and collagen networks undergo a strain-stiffening response as soon as strain levels reach just a few percent [359], [439], [440]. Their nonlinear elastic response significantly influences cellular behaviour. Studies with fibroblasts and stem cells demonstrated that cell spreading was independent of the linear elastic modulus of the gels, and resembled spreading on stiff PAA substrates [437]. These observations suggest that cells perceive this environment as stiff, because they actively reinforce the fibrin network though traction forces. Atomic force microscopy experiments demonstrated that cells cultured within or on top of fibrin gels induced network stiffening [437], [441]. In the case of collagen-based gels, evidence indicates that the accumulation of stresses resulting from cellular traction forces can influence fibroblast motility and morphology [442]. As the stiffness of the matrix or substrate increases, cells align their actin stress fibres to sustain the constant substrate strain [443].

1.1.2.2 Nanotopography of the extracellular matrix

Structural components of the ECM such as fibronectin, fibrin, or collagen, from hierarchically structured fibres, that present a different topography than the standard 2D culture dish [444]–[446]. Advancements in the field of nanotechnology and micropatterning facilitate the development of more sophisticated 2D surfaces, characterized by a precisely controlled surface topography. Patterning the surfaces with nanoscale ridges induces cells to align themselves parallel to the ridges and migrate along them in a phenomenon called contact guidance [447], [448]. Moreover, cells possess the capability to discern variations in surface elevation in the order of a few nanometres [447], [449], [450]. Cells furthermore exhibit sensitivity to the spatial arrangement of adhesion islands, as exemplified by investigations employing organized islands of RGD-coated regions [451]–[453]. Nanotopography emerges as a potent design parameter in the realm of tissue engineering, such as in the case of nanotopographic features for dental implants, which were shown to enhance bone formation [454].

1.1.2.3 Tensile force of the extracellular matrix

Tensile force or stretching force, holds significant importance in various physiological processes such as atherogenesis, muscle and joint movement, cardiovascular modelling, and cell behaviours (e.g. proliferation) [455]–[457]. In the vascular wall, tensile force promotes remodelling and contraction [458]. The dynamic tension of the joint can affect the final behaviours of muscles [459]. In the cardiovascular system, tensile force generated by blood flow elicits responses from principal effector cells including endothelial cells, cardiac myocytes, and smooth muscle cell [460]. Tensile force can induce cardiomyocyte hypertrophy though the activation of nuclear factor-like2 (Nrf2) and interferon-regulated transcription factors. Furthermore, tensile force plays a role in urothelium proliferation through the focal adhesion kinase (FAK) signalling pathway [461]. It contributes to the development of animal neurons by regulating gene transcription [462], [463]. The magnitude, frequency and duration of tensile force can exert multifaceted effects on cellular processes such as apoptosis, proliferation, migration, differentiation, and alignment [429].

1.2 Methods for mechanical evaluation of cells and tissues

Two methods will be discussed that have been used to evaluate the mechanical properties of cells and tissues in literature. The first method being atomic force microscopy, which represents a non-invasive approach to assessing the topography and the elasticity of a specimen. Secondly, Förster resonance energy transfer biosensors will be discussed, where cells are transfected and imaged using confocal microscopy both in live and in fixed conditions.

1.2.1 FRET-based tension sensors

1.2.1.1 Basic principles of FRET

The Förster resonance energy transfer (FRET) technique was named after German scientist Theodor Förster [464], [465]. This technique is based on the energy transfer between two light-sensitive molecules, such as green fluorescent (GFP) and red fluorescent protein (RFP). Herein, GFP is excited at its specific fluorescence excitation wavelength, with this energy being transferred to RFP and GFP returning to the ground state.

The FRET efficiency (E) depends on a variety of factors such as i) the physical distance between the donor and the acceptor, ii) the spectral overlap between the donor emission spectrum and the acceptor excitation spectrum, iii) the relative orientation of the donor emission dipole moment, and the acceptor adsorption dipole moment [466]. For a single pare of fluorophores, E is inversely proportional to the distance between donor and acceptor [466].

1.2.1.2 Fluorescent pairs for FRET experiments

Four different fluorescent pair categories will be discussed as an example of potential pairs for relevant applications [467]. Their disadvantages and advantages are briefly highlighted.

CFP-YFP FRET Pairs

The evolution of FRET pairs began with enhanced blue fluorescent protein (EBFP) and enhanced green fluorescent protein (EGFP) combinations, but limitations in photostability and susceptibility to near-ultraviolet excitation hindered their utility [468]. Cyan fluorescent protein (CFP) and yellow fluorescent protein pairs (YFP) pairs (CFP-YFP) addressed these issues with improved quantum yields and stability [468]–[470].

However, challenges persisted within CFP-YFP pairs, including phototoxicity from violet donor excitation, rapid YFP photobleaching, and spectral crosstalk [471].

GFP-RFP FRET Pairs

Green-red FRET pairs offer advantages over cyan-yellow pairs, mitigating issues related to autofluorescence, phototoxicity, and spectral overlap. Although historically plagued by dim red fluorescent protein brightness, recent advancements have addressed this limitation. For instance, the EGFP-mCherry pair demonstrates a decent dynamic range in FLIM-FRET imaging due to EGFP's relatively long fluorescence lifetime and substantial spectral overlap [472].

Multicolour FRET Pairs

A plethora of fluorescent proteins has expanded FRET pairs to allow multicolour imaging, granting the possibility of simultaneous observation of numerous cellular processes. They are categorized by the number of pairs and excitations: two pairs/two excitations, two pairs/single excitation, and three pairs [473].

DsRed, a red fluorescent protein, has a spectral overlay with CFP and YFP, leading it to be a suitable acceptor to those fluorescent proteins. However, DsRed suffers from interactions between CFP-DsRed and YFP-DsRed, which could underestimate the FRET efficiency. Monomeric FPs like mOrange2-mCherry, TagRFP-mPlum, and mTagBFP-sfGFP offer improved spectral separation for dual imaging. Large Stokes Shift (LSS) fluorescent proteins reduce the spectral crosstalk between donor and acceptor to enable ratiometric imaging by providing a larger FRET change. LSS fluorescent proteins enable excitation of spectrally distinct fluorescent proteins with a single excitation wavelength. Examples like mAmetrine and LSSmOrange enable simultaneous imaging in various sensors [474]–[476].

To surpass two-protein interaction limits, 3-FRET and 3sFRET techniques emerged. 3sFRET uses three fused fluorophores, like mTFP, mVenus, and tdTomato, to study cellular component interactions. N-Way FRET extends this, allowing multiple fluorophore interaction analysis. These advancements facilitate comprehensive, simultaneous cellular dynamics study beyond traditional two-pair FRET setups [477], [478].

Homo-FRET Pairs

In addition to FRET between different fluorescent proteins (hetero-FRET), homo-FRET transfers energy between proteins tagged with the same fluorophore. Homo-FRET, using a single fluorophore, is valuable for investigating homo-oligomerization due to its sensitivity in detecting acceptor-acceptor and donor-donor interactions, aiding multi-colour prFRET imaging alongside distinct fluorescent proteins [479].

For homo-FRET, a small Stokes shift fluorophore with significant excitation-emission overlap is essential. Techniques like anisotropy-FLIM and fluorescence anisotropy combined with microscopy measure clustering details, determining distances between fluorophores, cluster size, and orientation [480]. Methods like Bader *et al.*'s system quantify protein clustering and the average fluorophores per cluster, crucially used in studying GPI-anchored proteins [479].

1.2.1.3 FRET-based biosensors

To measure intracellular forces without disrupting the cells, FRET-based tension sensors have been developed. In 2008, Meng *et al.* developed the first FRET force

sensor, which was named stretch-sensitive FRET (stFRET) [481]. A next generation spectrin stFRET (sstFRET) was designed to improve the sensitivity of the original stFRET sensor [482]. In the novel design, the α-helix was replaced with a spectrin repeat and used to visualise time-course tension changes around focal adhesions.

A relevant example of further optimized FRET-based biosensor was designed by Wang *et al.* in 2016 [483]. They have designed a new FRET module based on the sstFRET basis, and a GFP and RFP pair (sstFRET-GR). Subsequently, the structure was inserted into the actin filament crosslinking protein α-actinin for the production of Actinin-sstFRET-GR. α-Actinin is an actin binding protein, that is sensitive to stretch, and results in low FRET when the actin filaments are under high tension and high FRET when the filaments are under low tension [484], as visualised on Figure 46.

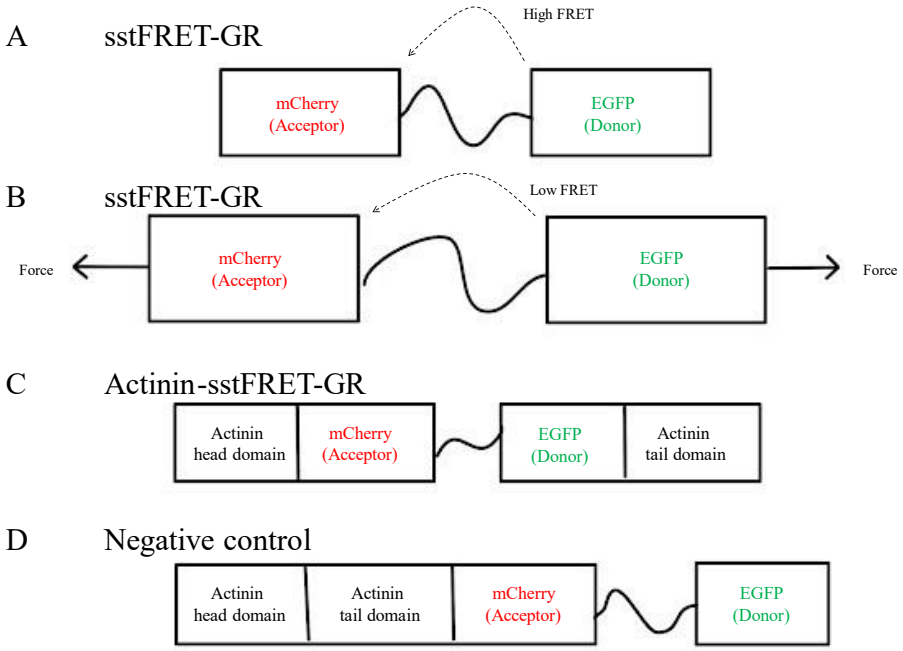

Figure 46: Working principle of the Actinin-sstFRET-GR biosensor.
A. A typical example of the working principle of a sstFRET-GR probe under low tension and experiencing high FRET. B. An example of the sstFRET-GR probe under high tension, experiencing low FRET. C. Implementation of the sstFRET-GR probe in the Actinin domain. D. Implementation of the sstFRET-GR probe in the Actinin domain as a negative control, insensitive to tension. Diagram based on [484].

The Wang group evaluated the tension as being inversely related to the FRET ratio. This parameter was calculated by acquiring the donor channel using the

donor-specific excitation wavelength (488 nm) and recording emission in the 505-525 nm range. They measured the acceptor channel using an excitation wavelength of either between 505-525 nm or 488 nm, with emission in the 560-660 nm range [483], [484]. Using these two channels, the FRET ratio was defined as the ratio of acceptor to donor signal using the intensity of the raw images.

1.2.1.4 Acquisition of FRET for cell biology applications

In general, there are a various different ways to acquire a FRET signal using commercially available microscope components. Five different methods (Sensitized emission, acceptor photobleaching, Fluorescence lifetime imaging microscopy, spectral imaging, and polarization anisotropy imaging) will be briefly discussed, as well as their advantages and disadvantages.

Sensitized emission is the simplest method of imaging FRET and is also referred to as two-colour ratio imaging [468]. In this set-up, the donor is excited by a specific wavelength and the signal is collected with specific emission filters for both donor and acceptor [485]. This method is sensitive to the crosstalk between the two fluorophores, causing more noise, which leads to extensive control experiments [485], [486]. Moreover, this method requires more effort for situations where the ratio between donor and acceptor is not 1:1 and the FRET changes are smaller [468]. However, for biosensors such as the Actinin-sstFRET-GR, this ratio is 1:1 and thus the sensitized emission could be considered since the FRET changes are rather large [487]. Therefore, sensitized emission acquisition is favourable in the case of dynamic studies in the interaction of proteins [488].

Acceptor photobleaching is another straightforward way of measuring the FRET efficiency, however, the method is destructive and therefore limited to a single measurement [489]. The principle is based on the donor fluorescence being quenched by the FRET, as some of the donor energy will go towards the acceptor fluorescence. By bleaching the acceptor fluorophore, this quenching will be released, and the donor fluorescence increases [490]. In these experiments, however, it is crucial that the donor is not degraded by the bleaching [468]. The method provides a straightforward way to calculate FRET efficiency by subtracting the donor intensity in presence of the acceptor fluorescence, from the donor intensity after photobleaching [488], [490]. The method damages the sample and is thus less suited for dynamic or live experiments [468].

Fluorescence lifetime imaging microscopy (FLIM) uses the exponential decay in fluorescence on a nanosecond timescale and is highly sensitive to the molecular environment and changes in molecular conformation [491]. For FRET related purposes, the principle is similar to that of acceptor photobleaching: the donor fluorescence is quenched due to the presence of FRET. Therefore, the amount of

quenching can be discovered using the decrease in the fluorescence decay time of the donor in the presence of FRET [468]. FLIM-FRET can even be applied to non-fluorescent acceptor fluorophores, and is less sensitive to acceptor artefacts as it only requires direct excitation of the donor [491]. The measurements are more complicated than for the two aforementioned methods since the nanosecond lifetime measurements require more expensive instrumentation. Because of the high sensitivity to external factors, FLIM-FRET is also less straightforward in the scenario of live cell measurements [468]. Compared to intensity-based FRET, in FLIM-FRET it is necessary to carefully measure the reference lifetime value for the donor alone, without any acceptor fluorophore present [491].

A fourth technique to evaluate FRET is called spectral imaging, which is a variation of sensitised emission. In this case the complete emission spectrum containing both the donor and the acceptor fluorescence is collected on excitation of the donor [492]. Using the whole fluorescence spectrum, the overlapping spectra should be able to be separated by using the peak and distinct shapes of the spectral tails [493].

Another way to measure FRET is reliant on the fact that polarized light excitation selects a population of fluorescent molecules that are aligned parallel to the excitation polarization. This technique is called polarization anisotropy imaging [494]. Immediately after the excitation, the fluorescence will be anisotropic in terms of polarization, due to the majority of the fluorescence being polarized parallel to the excitation [468]. For fluorescent pairs with FRET, the fluorescence will come out at a slightly different angle thanks to misaligned fluorophores. The technique is well suited for the detection of the presence of FRET, but it is less applicable when differentiating between strong and weak signals [468].

All these methods are good at assessing the effectiveness of the fluorescent pairs, and at quantifying the FRET signal when required. For a tension sensitive biosensor, with a ratio of 1:1 of the donor and the acceptor molecules present, it is possible to use the FRET ratio to determine the tension the sensor is undergoing. The FRET ratio in this case is simply defined as being the intensity of the acceptor channel when excited using the donor excitation wavelength, over the intensity measured in the donor channel [484].

1.2.2 Atomic force microscopy

The second method used to evaluate the mechanical identity of the cells, is atomic force microscopy to evaluate cell elasticity. The technique has been used in Chapter I for material evaluation, but has applications in biological research as well, relevant for the mechanical identity evaluation of cells. The following

paragraphs briefly clarify the working principles and its use in life sciences for both tissues and single cells.

1.2.2.1 Introduction to atomic force microscopy

Atomic force microscopy (AFM) enables the visualisation and manipulation of matter at the atomic, molecular, and cellular scale. The technique was first introduced in 1986 and has since become a vital tool in various fields of research such as materials science, nanotechnology, and biology [495], [496]. AFM can analyse a variety of substrates, independent of their surface properties (e.g., conductivity, stiffness) and can be performed in both air and aqueous environments, at physiological temperatures [495], [497], [498].

Working principle of atomic force microscopy

For AFM imaging and sample analysis, piezoelectric positioners allow the technique to obtain high-precision maps by moving the probe with sub-nanometre precision. The technique uses a micrometre sized cantilever with a nanometre size probe at the end to trace the topography or, for instance, explore forces between the probe and sample with high sensitivity. The probes typically consist of a silicon oxide, silicon nitride, or silicon tip and have different shapes depending on the application [495], [498]. AFM measures the forces between the atoms of the probe, and those of the sample, while an optical detector detects deflections of the cantilever caused by the probe-sample interaction [499]. The basic principles of AFM are demonstrated in Figure 47 to visualise the mechanism.

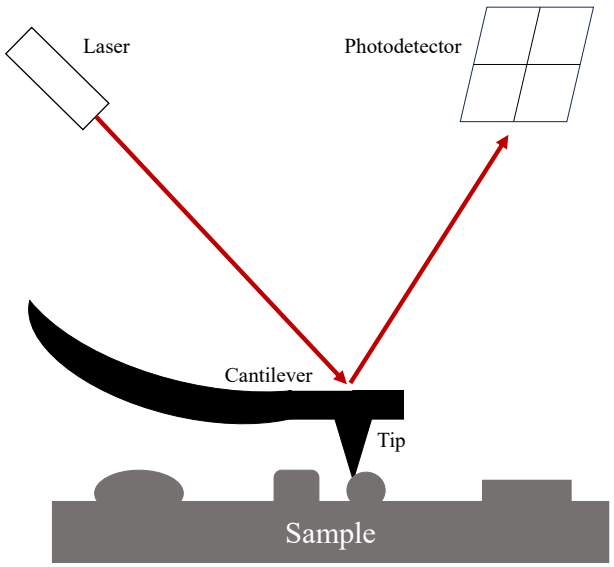

Figure 47: Working principle of AFM.

Operating modes of AFM

Modes of operating for the AFM include Contact mode, Tapping mode, Lateral Force and Force-Distance [59].

In the operational mode termed "contact mode", the AFM tip remains consistently engaged with the specimen throughout the experimentation [500]. Upon the tip's interaction with a morphological attribute larger than the current scan plane, the cantilever structure undergoes deflection, inducing an increased force upon the specimen [497]. To rectify this, a deliberate increase in the tip-to-surface distance is implemented. Conversely, analogous adjustments transpire upon encountering a lower feature. These corrective measures result in the rendered depiction of the specimen's surface topography [497].

In tapping mode, also called intermittent contact mode, the tip oscillates at its resonance frequency. In this set-up, contact is only made at the lower part of the oscillation. The difference between the applied oscillation and the actual oscillation leads to information about the mechanical properties of the surface, as well as the force interactions between the tip and the specimen [497].

In lateral force mode, the torsional movement of the cantilever is recorded using the horizontal movement of the laser beam on the detector. Contrast emerges as a result of the fluctuations in friction. More specific interactions are detected when modifying the chemistry of the tip, leading to this set-up being described as chemical force microscopy [497], [501].

Since the cantilever behaves like a small spring, it lends itself naturally to the quantification of forces between the probing tip and the sample surface. The force applied, denoted as F, exhibits proportionality to the deflection, d, undergone by the cantilever: $F = k \times d$. The coefficient of proportionality is the spring constant, k, empirically determinable, thus enabling quantitative analyses [497].

AFM furthermore offers the possibility to measure the phase shift of the oscillating cantilever relative to the driving signal. That shift is then correlated with material specific properties that exert an influence on the tip/specimen interactions. This method allows to differentiate elasticity, viscosity, adhesion, and friction on different areas of a sample [501].

During the process of the tip approaching the surface, it experiences intricate force interactions. At a distance of approximately 50 nm from the surface, repulsive electrostatic forces come into effect, causing the tip to bend away from the surface. At a distance of a few nanometres from the surface, a distinct transformation occurs, wherein attractive van der Waals forces draw the tip into contact with the surface [497].

Advantages and limitations of AFM

AFM offers the possibility to measure nano-structural details and biomechanical properties of biological samples. It can measure changes in mechanical properties of cells such as the stiffness and viscoelasticity [502]. A principal advantage of AFM is that the technique allows for these measures to be carried out in the cell's natural environment, in both medium or buffers, without the need for fixation or sample preparation [503], [504]. Moreover, there is the possibility to detect molecular forces on the surface of living cells [501].

Currently, conventional AFMs present some limitations in the field of biomedical research. The speed is relatively low, because of the sequential mechanical scanning method used by the cantilever probe. AFM also requires more complicated calibration and parameter selection to avoid damaging fragile biological samples [505].

1.2.2.2 Topographical analysis of samples using AFM

One of the primary applications of AFM is the characterisation of the surface topography. While scanning across the surface, AFM can generate three-dimensional high-resolution images of the encountered topography. The technique is used for metals, polymers, and biological samples and to obtain information about the surface roughness, particle size, or defects [506]. In the following sections some examples of studies are provided in which AFM was used to determine key aspects of the topography of cells and tissues, as an illustration of its use in cell and tissue biology.

Topographical analysis of living cells

The surface of biological samples can be evaluated at the nanometre, imaging dynamics of proteins and lipids [507]. One example includes endothelial cells, where the cells were kept in their growth medium to assure cell viability [508]. A dynamic force microscopy protocol can be used for the visualisation of the general topography, and the filaments on flat parts of the cell, presuming to be cytoskeleton features below the cell membrane. The resolution of the living cells is partially hindered by the flexibility of the membrane. Fixing the cells allowed for higher resolution in the nuclear area of structural details [509].

Combinations of AFM with different types of optical microscopy techniques have been designed in the past as well. Examples of this are simultaneous differential interference contrast microscopy with AFM and fluorescent microscopy with AFM, reviewed in [510], [511]. Combining these techniques leads to, for instance, better visualisation of cell organelles or visualisation of selectively labelled compartments within the cell.

Topographical analysis of tissues and tissue constructs

The topographical mapping analysis is not limited to materials and individual cells but has been proven applicable in tissue and ECM analysis as well [512]. The surface topography of decellularized extracellular matrices provides information about the orientation of protein fibres, the diameter of those fibres and the spacing [513]. Combining this with a fluorescent microscopy technique further enables the study of which protein presents that orientation or spacing [514].

A second example to demonstrate the importance of AFM in previous research, is a study which compared hydrated and dehydrated conditions in cartilage tissues [515]. The nanostructure of the cartilage could be characterized by describing the collagen fibril spacing, the diameter and the surface roughness in both conditions. The results showed that collagen in the dehydrated condition had a more heterogeneous fibre distribution when compared to the homogeneous fibre distribution in the hydrated condition. Furthermore, loss of water in cartilage lead to a rougher structure [515].

Smolyakov *et al.* used AFM for topographical analysis of thin sections of murine frontal cortex tissue. They proved that maturing sections had a lower roughness compared to younger tissue slices [516]. This decrease in surface roughness corresponds to critical timeframes for the ECM deposition. Their study concluded that AFM could be a useful tool to evaluate the cytoarchitecture of brain tissues, with hopes of identifying morphometric markers in neurodegenerative pathologies [516].

1.2.2.3 Mechanical evaluation of biological samples using AFM

Apart from visualising structures and imaging topography, AFM allows the investigation of the mechanical properties of living cells. Using a controlled force, the AFM probe can indent the cells, providing insights in the mechanical properties of a sample, including the Young's modulus of cellular areas, viscoelastic properties of cells and cell adhesion, for instance.

Force mapping is not only useful for single cells and cellular compartments but can also be used when characterising the mechanical and structural properties of *in vitro* created tissues and tissue constructs. The mechanical integrity can be assessed, as well as the Young's Modulus of the tissues to measure the tissue stiffness. The following section explains how the force mapping and data acquisition work in an *in vitro* setting, followed by examples of the use of AFM for mechanical properties of cells and tissues.

Elasticity fit of samples analysed with AFM and tip selection

The Young's Modulus is an elastic property of a material that is defined as the stress of a material divided by the strain, leading to a normalised measure of the

compressibility of the sample [517]. The higher the Young's Modulus is, the stiffer the sample will be [518].

In a homogeneous compression, the Young's Modulus calculation is straightforward, however, when using AFM tips, the indentation geometry is more intricate [519]. The surface in this case, is locally indented with a tip of a particular size and shape. For this type of scenario, fitting is generally required and in standard situations done using the Hertz model [520]. The model, however, does make important assumptions about the specimen to be indented, such as the sample being infinitely thick, homogenous, and purely elastic. Currently, the Hertz model refers to a family of different methods that were adapted to different sample indentation geometries.

An interesting geometry for this work, is the four-sided pyramid, as it can be used to measure the Young's modulus of cells [521]. In this set-up, the Bilodeau formula is used [522]:

$$F = 0.7453 \frac{E}{1-\nu^2} \delta^2 \tan(\alpha)$$

Where F is the force exerted on the sample, E is the Young's Modulus to be determined, ν is the Poisson's Ratio, δ is the indentation and α is the face angle of a pyramid.

Mechanical evaluation of living cells

AFM has been used to measure the local elastic response of cell membranes and the underlying cytoskeleton by fitting force-indentation curves to contact models such as those of Hertz and Sneddon [523]. Apparent stiffness of mammalian cells, as measured with AFM, typically ranges between 1 and 100's of kPa [524]. This value indicates the stiffness in a particular point of indentation into the cell and can change depending on where in the cell the tip makes contact and on what is below the surface of the tip [525].

The initial point of indentation between the AFM probe and the cell is the glycocalyx, enveloping the cell. This region possesses a thickness ranging from approximately 40 to 400 nm, along with a stiffness within the range of 200 to 400 Pa [526]. Upon further indentation, the AFM tip proceeds to engage and deform the thin and soft cell membrane [527], which measures between 5 to 8 nm in thickness and is interconnected with the actomyosin cortex. The actomyosin cortex, has a thickness of around 100 to 1000 nm and displays significantly greater Young's moduli compared to preceding components, ranging between 10 to 100 kPa [528]. Furthermore, as the indentation progresses through the cytoskeletal structure, the probe pushes into the cytoplasm [529] until encountering more rigid

filamentous structures such as actin or microtubules (with stiffness of 0.1 to 1 kPa) or the nucleus (with stiffness of 1 to 10 kPa) [498], [530]–[533]. Unfortunately, this mechanical anisotropy of mammalian cellular components presents some challenges when captured by contact models based on assumptions of an infinitely extended, smooth, and uniformly consistent surface [498].

The Young's modulus of a cell does not only depend on the cellular region measured, but also on the cell type. Comparison of different cell types indicates the large variety of Young's moduli that cells can demonstrate in similar cellular regions. For instance, C2C12 cells have demonstrated values between 11 and 45 kPa [532], [534], [535], before differentiation and values around 8 to 17 kPa after differentiation into myotubes [534], [535]. Myofibrils demonstrate moduli of 12 kPa in healthy models and 16 kPa in injured models [534], [536]. Skeletal muscle tissue generally is considered to have Young's Modulus of 12 kPa [537]. Fibroblasts have shown values between 1 and 27 kPa [538], and osteoblasts demonstrated ranges between 0.3 and 20 kPa [539], [540]. Measurements on erythrocytes showed values between 14 and 110 kPa [541] and cardiac myocytes exhibited Young's moduli around 100 kPa [542], [543].

Even though AFM can be applied to cells in their native environment and in a physiologically relevant medium, sometimes it can be more convenient to analyse the cells after fixation. This due to the set-up of the cells, or the lack of facilities for temperature and CO_2 control. However, in the case of the mechanical properties of the cells, studies carried out using fibroblasts saw a significant difference between living and fixed cells of different cell lines. For example, 3T3 cells had a Young's modulus of around 5.2 kPa when measured alive but compared to 82 kPa when measured after fixation [544]. This finding was consistent in SW13 cells too, leading to a factor of 14 – 16 multiplications between the Young's Modulus of live and fixed cells [544]. This conclusion was similarly made for cardiomyocytes, which show a factor of 16 between live and fixed cells and for erythrocytes with a factor of 10 [545], [546].

Furthermore, cells from a healthy or diseased phenotype can exhibit different apparent stiffness values. Examples of this principle are erythrocytes isolated from elderly patients with Diabetes type 2, which were shown to be significantly less deformable compared to cells isolated from healthy elderly people and healthy younger people [547]. In comparisons of normal prostate or breast derived cells and their cancerous counterpart, the Young's Moduli of the healthy versus cancerous cells have presented altered values in research. This indicates that also in cancer, healthy versus cancerous cells can present different stiffnesses, measured using AFM [548]. This type of research has not only been carried out for prostate and breast cancer, but also in ovarian cancer for instance, where the

cells are softer when compared to healthy cells [549]. In cancer diagnostics, cell elasticity could allow for detection of cancerous cells in tissue slices [548], [550]. In skeletal muscle cells, an example of a similar distinction is when the cells lack functional dystrophin, causing a decrease in cortical stiffness of the cells. For instance, in Duchenne muscular dystrophy, the dystrophin protein is absent in the cells, leading to a reduction of myotube stiffness and vulnerable cells [551].

Another possibility for the use of AFM in mammalian cell culture research is by stimulating the cells and reading out their real-stime response using fluorescent constructs able to report, for instance, the calcium flux across a membrane [552]. Ossola *et al.* measured voltage-gated channels while mechanically stimulating beating cardiac cells using a combination of AFM and the patch clamp technique [498], [553].

Young's modulus of tissues and tissue constructs

Whilst AFM is regularly used for investigating molecules and cells, there has been less emphasis on the assessment of mechanical characteristics of tissues and organisms. It has been proven that the stiffness of a substrate can influence the differentiation of stem cells into different tissue types [360], [554]. AFM measurements have, furthermore, shown that the stiffness of differentiated cells correlates to that of the underlying substrate. This suggests that the physical properties of the environment influence the mechanical attributes of the cell [555]. For instance, neurons have the ability to detect and respond to the stiffness of their surroundings [556]. A combination of AFM-based force mapping and fluorescence microscopy revealed that axons tend to grow preferentially into brain regions with specific stiffness values. Furthermore, localized injury to the neocortex resulted in a substantial softening of the adjacent brain tissue, serving as a signal to restrict neuronal regeneration in the area [557].

Changes in the stiffness of cells and tissues are indications of cancer too, however, less straightforward is how this tissue stiffening relates to the development of tumours. Experiments have revealed that tumour tissues are far more stiff than individual tumour cells, highlighting the potential of AFM for the examination of mechanical properties in diseased phenotypes [558]–[561].

In aging skeletal muscle, the tissue is characterised by a lower regenerative potential, which can be linked to an increase in the stiffness of the myofibre microenvironment. These findings have been shown using myofibres and myoblasts derived from primary cultures, and stiffness tuneable hydrogels. Skeletal muscle tissue slices from aged samples were determined with AFM to be stiffer than those of adult samples. The increase in the stiffness of aged damaged myofibres reduced the proliferative capabilities of myogenic progenitor cells

[562]–[564]. Other studies have compared isolated intact myofibres with collapsed myofibres to represent a damaged tissue model, and found that the Young's modulus of increased four times when the myofibre collapsed [565].

1.3 Migration of cells on the nanogrooved substrates

As indicated in previous chapters, the extracellular environment influences processes such as cell adhesion, proliferation and migration. In this section some migratory behaviours of cells are discussed to understand the mechanisms in 2D and 3D, in single cell migration and in collective cell migration, to introduce the topic of cellular migration on the artificial niche.

1.3.1 Single cell migration

Generally, two types of cell migration behaviour are distinguished for single cells: mesenchymal and amoeboid cell migration. Mesenchymal migration is characterised by a leading and trailing edge and strong stress fibres [566]. Amoeboid migration is marked by blebbing and weak adhesions, seen, for instance, in 3D environments for leukocytes and primordial germ cells.

In 2D mesenchymal migration, the mechanisms of force transmission include initial symmetry breaking, as a result of various internal and external signalling cues, particularly through G protein-coupled receptors. This leads to polarization of secondary messengers and subsequent non-isotropic distribution of Rho GTPase activity [567]. Actin dynamics at the leading edge, which are characterized by the actin polymerization rates and retrograde actin flow, together with integrin-mediated force transmission are drivers of cell propulsion [568]. Integrins transmit forces from the cytoskeleton to the ECM, thereby facilitating cell migration, and participate in bidirectional signalling. The force asymmetry along the planar axis of the cells results in forward propulsion, enhanced by the detachment of FAs at the trailing edge of the cell [569]. The leading edge of the cells is not a constant structure. It adapts through cycles of extension, adhesion and contraction [567], [570].

Motion patterns in 2D occur through a stochastic self-organizing process, where the cells transition between different phases of random and directed motion, alike strategies seen in bacterial swimming for sparse target detection [567]. Interestingly, these motions are modulated by substrate properties such as adhesiveness, rigidity, and topography. These properties influence the direction and efficiency of cell migration. An example is haptotaxis, where cells migrate towards the regions of higher adhesiveness, of durotaxis, where cells migrate depending on a stiffness gradient [571], [572].

This behaviour is not only observed in 2D settings but in 3D environments as well. Where cells were shown to move to a higher substrate stiffness and haptotactic

behaviour was observed [573], [574]. However, compared to 2D, 3D environments demonstrate additional parameters such as the size of the pores of the ECM through which the cells are migrating and the cells are able to engage with all directions [567]. The local ECM is altered by migrating cells, both by pulling of the cells on the fibres, and by ECM secretion of the migrating cells [575], [576].

Mesenchymal migration relies on integrin-mediated force transmission, while amoeboid migration uses protrusive or contractile forces, which lead to membrane protrusions mediated by actin polymerization or hydrostatic pressure due to the contractility of the actin cytoskeleton. The combination of these parameters determines amoeboid migration, and is cell specific [577]. While mesenchymal migration is associated with remodelling of the ECM, amoeboid cells leave a smaller mark on their environment [567].

Moreover, the diversity in cell migration modes extends to adaptability between these modes based on various environmental cues. These modes thus reflect a continuum rather than distinct categories. The relevance of these different modes varies based on cellular function, suggesting a nuanced interplay between cell type, microenvironment, and migration strategy [567].

During skeletal muscle regeneration, the resident stem cells (satellite cells) start dividing upon anti-inflammatory cues. This activation is not limited to cells in the immediate vicinity of the injury, but includes also cells at further distances that migrate towards the site of injury [578]. During muscle development, growth and regeneration, myoblasts are able to cross the basal lamina and migrate from one fibre to another [579]. Satellite cells demonstrate high levels of α7- and β1-Integrins, essential for migration and interactions with the ECM [119], [580].

1.3.2 Collective cell migration

In contrast to single cell migration, collective cell migration is defined as the ability of a group of cells to move together, while also affecting the behaviour of the cells, trough stable or temporary cell-cell interactions [581]. Global ordering of the cell migration, for instance, due to chemical gradients present, is not collective migration as it is controlled by the interaction of individual cells with global stimulation [582]. Collective cell migration requires cooperation between the migrating cells.

Collection migration events can involve collective movements of epithelial sheets where cells retain stable adherence junctions, or transient adherence junctions as is the case in mesenchymal layers. In both types of events, the cells are mechanically linked to each other, and the cell layers interact with the extracellular environment during migration [581], [583], [584] .

To some extent, the collective migration behaviour can be compared to single cell migration, as the cells in the front of the group form protrusions, similar to the leading edge in single cell migration [581]. In the branch formation of blood vessels, the cells in leader position migrate more actively than the follower cells, which focus on proliferation or intercalation, for instance. In mesenchymal collective migration, such as for the neural crest, the whole group of cells is migratory [581].

In muscle cultures *in vitro*, C2C12 cells presented a sort of collective pattern when seeded on fibronectin, which was not present when seeded on laminin or gelatine. The authors described an increase in collective migration on the fibronectin coated substrates, forming streams of cells, resembling the collective cell migration in neural crest cells [179]. Other studies reported a decrease in migration when using fibronectin coating instead [178].

2. MATERIALS AND METHODS

2.1 FRET biosensor

In these experiments, the FRET biosensor was first validated using C2C12 cells cultured on glass for optimal visualisation. The cells received Blebbistatin treatment to induce a weaker cytoskeleton, to quantify differences between cells with and without the treatment as a way to calibrate the probe. After these experiments, the C2C12 were seeded on polydimethylsiloxane (PDMS) substrates for a characterisation of tension in cells on flat or nanopatterned PDMS substrates.

2.1.1 Material fabrication of substrates for transfection experiments

Substrates were fabricated for transfection experiments using a spin coater (WS-650Mz-23NPPB, Laurell). 1 mL of either 5:1 PDMS or 10:1 PDMS was added to polycarbonate (PC) masters, which were then spun at 1200 rpm for one minute. After the spin coating procedure, the PDMS was cured at 80°C for 1 hour. The resulting PDMS films were between 50 µm and 100 µm thickness, to minimize the noise caused by the PDMS. In experiments comparing different samples, the PDMS layer was always taken from the same batch of spin coated substrates, to minimise the difference in thickness between different samples. A difference of < 2 µm was deemed acceptable. Culture dishes used in this case were Ibidi Glass and polymer bottom dishes with a 35 mm diameter (Ibidi, Cat. N° 81156).

2.1.2 Transfection of C2C12

C2C12 cells at a low passage (P < 6) were replated in a high seeding density (12 500 cells/cm²) in a 35 mm culture dish (Corning), 24 hours before the start of the transfection protocol. Ten minutes before starting the transfection, the cultures were washed twice with PBS and incubated in OptiMem™ Reduced Serum Medium (Thermo Fisher Scientific). Cells were then transfected using 3.75 µL of Lipofectamine LTX and 3.5 µL P3000 Reagent (Thermo Fisher Scientific), with 0.7 µg of Actinin-sstFRET-GR DNA (Tetsuya Kitaguchi, Addgene plasmid # 83416; RRID: Addgene_83416) and incubated in the OptiMem™ medium for 6 hours, before replacing the medium with normal growth medium.

2.1.3 Cell culture of transfected C2C12

Cells were seeded using the same procedure as for the formation of tissue constructs in Chapter II. The surfaces of PDMS or glass were treated with oxygen plasma at 50 W for 3 minutes (Pfeiffer Vacuum Single Gauge – Cesar RF Power Generator) before coating them in 10 µg/mL Fibronectin (F0895, Sigma Aldrich) solution for 1 hour at room temperature. Excess coating solution was taken off and the cells were seeded in the same density as for the skeletal muscle tissue experiments, meaning 3100 cells/cm².

For experiments comparing the different types of ECM coating, a comparison was made between fibronectin, laminin and growth medium coating. Fibronectin was coated using a 10 µg/mL concentration for 1 hour at room temperature, while laminin coatings (L2020, Sigma Aldrich) were incubated for 2 hours at 37°C according to the manufacturer's recommendations. Growth medium coatings were carried out by incubating the substrates overnight at 37°C after oxygen plasma treatment.

After 24 hours in culture, cells were either fixed using 4% paraformaldehyde (Electron Microscopy Sciences) for 20 minutes or imaged live.

2.1.4 Visualisation after transfection

Transfected cells were visualised both in live and in fixed conditions using a confocal microscope (LEICA TCS SP5 II with Coherent multiphoton laser module) and the 488 nm argon laser line for excitation of both donor and acceptor. Visualisation in the microscope took place for live cells at 5 hours after seeding and 24 hours after cell seeding. At the 24 hours after seeding time mark, the cells were fixed for further characterisation of the fluorescence signal. Glass comparison samples were included, where one sample was treated in the same way as the PDMS samples, meaning, after seeding only visualisation and fixation, while one set of samples was treated with 4 mM Blebbistatin for two hours.

2.1.5 Evaluation of the tension

Images are acquired with confocal microscope (LEICA TCS SP5 II with Coherent multiphoton laser module) and were split in the respective donor (EGFP) and acceptor (mCherry) signal. The donor signal was defined as the fluorescence in the 505 – 525 nm emission band, upon excitation using the 488 nm Argon laser, while the acceptor FRET signal was defined using the 560 – 660 nm emission band upon excitation of the 488 nm Argon laser.

The tension within transfected cells was evaluated by using the ratio of the donor fluorescence intensity and the acceptor fluorescence intensity. The FRET ratio can be found in this way and is defined as [484]:

$$FRET = \frac{Intensity\ of\ the\ acceptor}{Intensity\ of\ the\ donor}$$

As the FRET ratio is inversely correlated to the tension within cells, as defined by Wang et al 2019 [484], this ratio can also be transformed to a tension ratio given by:

$$Tension = \frac{Intensity\ of\ the\ donor}{Intensity\ of\ the\ acceptor}$$

These ratios can be used to evaluate changes in tension within the cells. If the distance between the fluorophores is high, and thus the tension is high, and the actin is stretched, the donor signal will increase while the acceptor signal will decrease. This leads to a decrease in the FRET ratio but an increase in the tension ratio.

Images containing the donor and the acceptor fluorescence were imported in ImageJ, where a region of interest was isolated, and the background was removed [585]. A second region of interest (ROI) was defined as the background signal for both the donor and acceptor signals. The two ROIs with each a donor and acceptor image were imported in MATLAB for further calculations. The background ROI was used to calculate an average background value, which was later subtracted from the signal of the donor and acceptor of the cells. Next, the tension calculations were carried out pixel by pixel of acquired images in MATLAB by determining the tension ratio given previously. A second type of evaluation was used in the calibration experiments where the tension ratio was also evaluated using a median filter, that averages 3x3 pixels. The average tension of a cell was determined as the average ratio of all the pixels within a cell.

2.2 Atomic force microscopy evaluation of cellular elasticity

2.2.1 Cell culture for atomic force microscopy

Cells were seeded using the same procedure as for the formation of tissue constructs and for the FRET biosensor experiments. The surfaces of glass or PDMS were treated with oxygen plasma before coating them with (i) 10 µg/mL fibronectin solution for 1 hour at room temperature (ii) 10 µg/mL laminin solution for 2 hours at 37°C or (iii) 1 mL growth medium, overnight at 37°C. Excess coating solution was taken off and the cells were seeded in the same density as for the other experiments, meaning 3100 cells/cm².

2.2.2 Atomic force microscopy of cells

Young's moduli of cells were evaluated using AFM (JPK NanoWizardII) with silicon nitride cantilevers. The tips used had a square pyramid tip incorporated at their free end (PNP-DB, Nanoworld) and a spring constant of 0.06 N/m. The spring constants of the cantilevers were also measured independently for every experiment by calibrating the tips on a glass substrate. The AFM was mounted on a Zeiss LSM 700 confocal microscope to align the AFM tips with the cells or tissue constructs. The force curves were recorded at a scan rate equal to 1 Hz and correspond to a maximal loading rate of 1 nN/s with a maximum force of 1 nN. An area of 20 x 20 µm was scanned in 64 force curves with an indentation speed of 1 µm/s. The measurement of cells on different substrates was carried out in live culture conditions at 24h after seeding. For each substrate at least 10 cells/areas

were evaluated in growth medium at 37°C. The Young's modulus of individual cells was determined by fitting the force-indentation curve using the Hertzian model for linearly elastic materials.

2.2.3 Data collection of AFM results

Force curves and Young's moduli were analysed and evaluated using the JPK-data processing software. Force curves were first recalibrated using the determined values for sensitivity and the spring constant during the calibration process of the tip. Next, data was smoothened using the Gaussian method with a smoothing width of 3.00. The baseline offset was subtracted, and the contact adjusted. The height was corrected for the bending of the cantilever to calculate the vertical tip position and lastly, the Young's Modulus is determined by fitting indentation data with the Hertzian model for linearly elastic materials. The corresponding values were evaluated and imported into MATLAB (version R2022a) for further statistical analysis.

2.3 Cell migration evaluation

Timelapses were taken of cells seeded according to the procedures 2.2.1, on flat and patterned substrates. A Zeiss LSM 700 microscope was used to image the cells every 30 minutes for 4 to 48 hours, at or 7 to 14 days after seeding. Particle image velocimetry (PIV) analysis was performed to analyse the vector angle of sequential images of timelapse experiments and a mean migration angle was determined. The PIV analysis was performed using a MATLAB (MathWorks) plugin: PIVlab by William Thielicke [586].

2.4 Statistical analysis

All statistical analyses were carried out in MATLAB (version R2022a) using either Wilcoxon rank-sum test or Kruskal Wallis test, with post hoc Dunn's tests. Statistical relevant differences were defined as having a p-value below 0.05.

3. RESULTS

3.1 Cellular tension can be measured using a FRET-biosensor

The optimal transfection protocol for C2C12 cells was found by using a concentration of 1.64 µL/mL lipofectamine and 0.7 µg/mL DNA to transfect the cells for 6 hours. These concentrations lead to the least amount of cell death and while still transfecting the cells. To test the efficacy of the FRET-biosensor, transfected cells were grown on glass dishes for optimal imaging. In a second phase, thin PDMS membranes were used to evaluate the tension within the cells on flat and nanogrooved substrates. Lastly, on a patterned substrate, different types of protein coating were tested to evaluate whether the tension was affected by the composition of the artificial niche.

3.1.1 Determination of the FRET and TENSION ratio in MATLAB

The tension within a cell was evaluated by evaluating the energy transfer from donor to acceptor in the transfected cells. If the cells are under low tension, the donor and acceptor fluorophores are in close proximity, leading to a higher energy transfer from donor to acceptor signal. Close proximity will cause the donor signal to decrease, while increasing the acceptor signal when excited using the 488 nm laser, leading to an increase in FRET ratio and a decrease in the TENSION ratio. Vice versa is also true for high tension situations where there is less energy transfer from the donor to the acceptor fluorophore, leading to a higher FRET ratio and a lower TENSION ratio.

These images were imported in ImageJ (Fiji) software for initial processing. These processing steps include splitting the image in two channels, followed by the removal of background signal. The background was removed by evaluating only the cellular signals minus the average value of the whole background signal, to correct for noise (Figure 48A).

The resulting split images were imported into MATLAB using the *imread()* function to transform 1024x1024 pixel images into a matrix of 1024x1024 intensity values. A value of 0 refers to a completely black pixel, whereas a value of 255 refers to a fully white pixel. Using these matrices, the FRET values and TENSION values could be calculated per pixel for each image, as can be seen in Figure 48 panels B and C. FRET and TENSION values can then be used to reconstruct the images with a colourmap indicating the areas within a cell with higher or lower FRET or TENSION values.

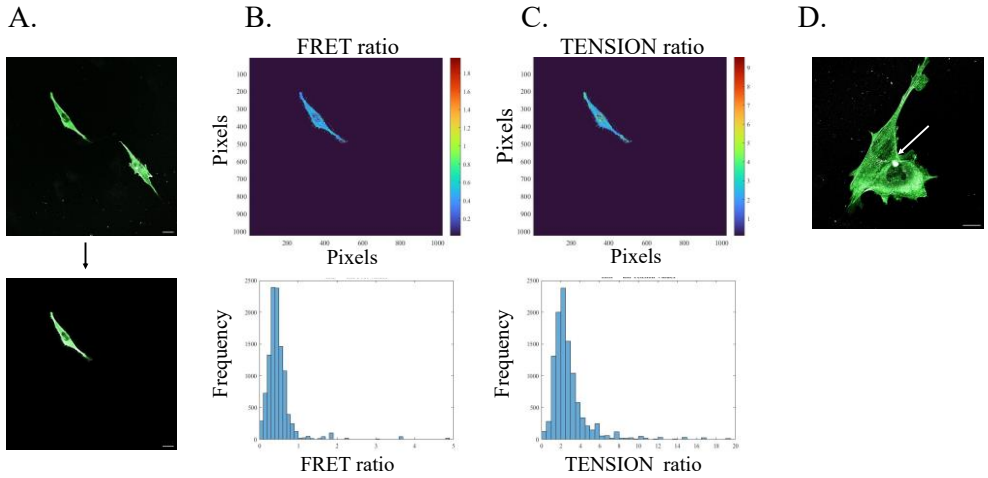

Figure 48: Transformation of microscopy data to FRET ratios and tension values in MATLAB
A. C2C12 cells transfected using the EGFP-mCherry actinin FRET biosensor. Green indicates the donor fluorophores while white indicates the energy transferred from the donor to the acceptor fluorophores. The second image indicates the cell after background removal and how the image was imported into MATLAB. B. The FRET ratio of the cell seen in panel A, determined by the ratio of acceptor intensity and donor intensity. This histogram indicates the frequency of the FRET frequency values for this cell. C. The TENSION ratio of the cell seen in panel A determined by the ratio of donor intensity and acceptor intensity. The histogram indicates the TENSION frequency values for this cell. Graphs and colourmaps determined using MATLAB. D. Example of cells with noise caused by impurities or the material, and of cells with cytoskeletal overlap. This type of images was excluded from the TENSION analyses. All scalebars indicate 20 µm.

These values were then used to compare cells in different conditions for their overall cellular tension. It is important to consider the cell-to-cell contact/overlap and the background noise. Therefore, cells with a cytoskeletal overlap were not considered for these experiments as the tension of one cell could not be calculated without either subtracting a significant part of the cell or calculating the ratio of the overlap. Bright spots, caused by the material under the cells were also removed from the analysis as they alter the tension ratios without signifying an altered cellular tension. An example of an excluded instance is shown in Figure 48D.

Furthermore, the transfected cells survived and proliferated until confluence. Upon verifying the fluorescence of the cells after a few days, a trend could be seen where the donor fluorescence disappeared completely and noise in the 560 – 660 nm emission channel became more prominent. This fluorescence is not related to the actin and thus only experiments in the initial phase after seeding were considered. Figure 49 shows the progression of transfected cells, at different timepoints after seeding them at low density on a coated glass plate.

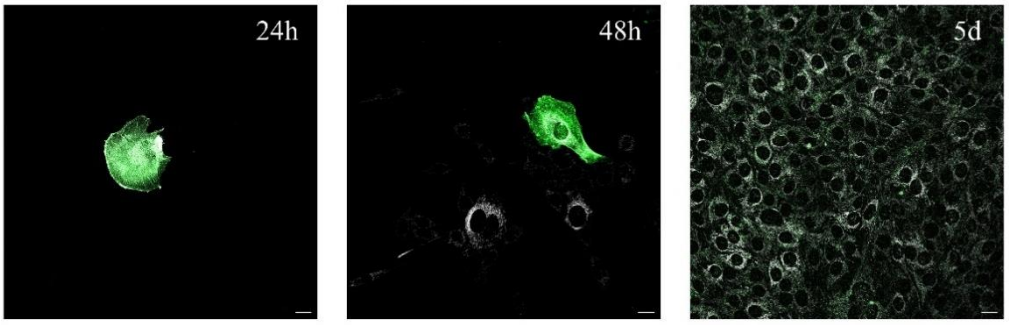

Figure 49: Fluorescence of transfected C2C12 cells at different points in time.
Three representative images of C2C12 cells at 24 hours, 48 hours, and 5 days after seeding. Green represents donor signal in the 505 – 525 nm emission band and white represents the acceptor signal in the 560 – 660 nm emission band, both upon excitation with the 488 nm Argon laser. Scalebars = 100 µm.

Acquisitions further in time showed an increase in noise and nonspecific fluorescence, which was unrelated to the actin tension of the cells.

3.1.2 Calibration experiments using Blebbistatin

To validate the acquisition protocol and FRET or tension ratio determination, an experiment using C2C12 cells on glass culture dishes with or without Blebbistatin treatment was set up. The cells were seeded on fibronectin coated glass culture dishes and in the case of the Blebbistatin samples, treated for 2 hours with 4 mM of Blebbistatin, after 22 hours in culture. At 24 hours after seeding all cells were fixed for image analysis. Figure 50A shows a representative example of a non-treated cell, with its tension ratio determined pixel by pixel and by applying a median filter to reduce possible noise. Figure 50B contains this same data but for a Blebbistatin treated sample. In Figure 50C the pixel-by-pixel tension values were compared and it was found that the tension within Blebbistatin treated cells was significantly lower than in non-treated cells. This is in line with expectations and literature as the Blebbistatin causes a softening of the actin cytoskeleton [587].

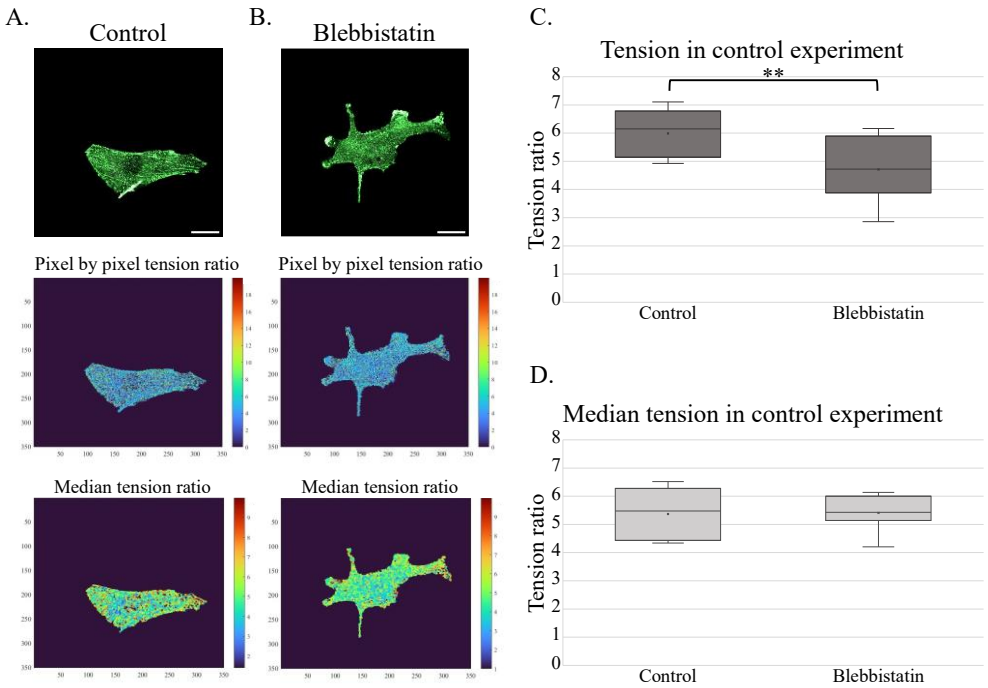

Figure 50: Tension in calibration experiments using Blebbistatin treated C2C12 cells for decreasing intracellular tension.

A – B. Control experiments of C2C12 cells seeded on glass dishes, fixed after 24 hours in culture either without or with Blebbistatin treatment, respectively. On fluorescent images, green represents donor emission in the 505 - 525 nm emission band and white represents the acceptor emission in the 560 - 660 nm emission band. For each sample, a corresponding pixel by pixel tension ratio is shown and a median filtered tension ratio. Scalebars represent 20 µm. C. Boxplot indicating the difference in pixel by pixel determined tension for control samples and samples with Blebbistatin treatment. ** $p < 0.01$ and n equals 10. D. Boxplot indicating the difference in median filtered tension rations for control samples and samples with Blebbistatin treatment. n equals 10.

Figure 50D contains the boxplot overview of these same samples, but in the case of applying a median filter to the tension maps. While the median filter proves itself to be useful when highlighting different areas under tension within a cell, it deletes some important information in some cases on more specific and finer filaments.

In these calibration experiments, Z-stacks of the cells were also considered to get an average tension value of the whole cell, and not solely of one plane. Figure 51 illustrates these experiments using the full body of a cell. Representative cells are shown of the control and Blebbistatin group, with their corresponding cross-sections.

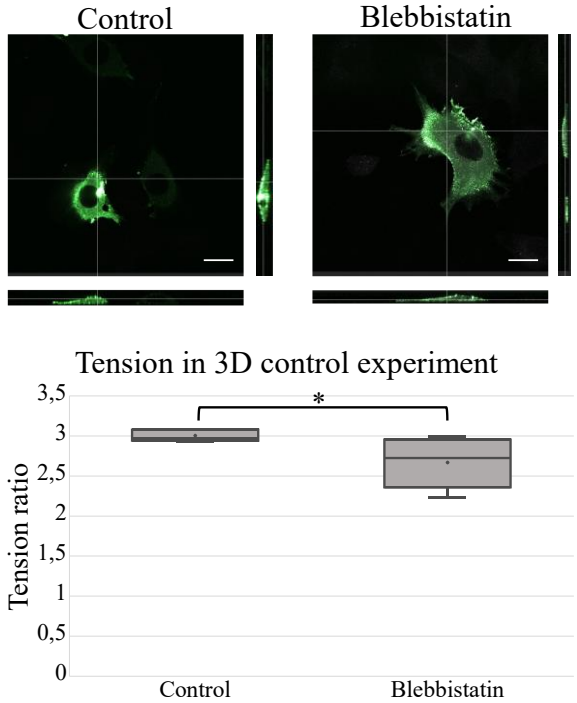

Figure 51: Z-stack analysis of tension in calibration experiments using Blebbistatin treated C2C12 cells for decreasing intracellular tension.
Example of control Z-stack experiments of C2C12 cells seeded on glass dishes, fixed after 24 hours in culture either without or with Blebbistatin treatment, respectively. On fluorescent images, green represents donor emission in the 505 - 525 nm emission band and white represents the acceptor emission in the 560 - 660 nm emission band. Images were stacked and sectioned in ImageJ software. Scalebar = 20 µm. The boxplot indicates the difference in pixel by pixel determined tension for control samples and samples with Blebbistatin treatment. * $p < 0.05$ and $n = 5$.

To calculate these tension ratios for stacked images, a 3D matrix per cell was calculated containing the tension ratios for every pixel of the stack. For comparison, average tension values were taking from this stack to find a single mean value per cell. These observations demonstrate that using Z-stacks is an effective way to analyse the tension as measured by the Actinin-sstFRET-GR biosensor.

3.1.3 Transfection of cells on flat and patterned substrates

To determine the tension of cells seeded on flat and patterned substrates in the context of future muscle tissue formation, the cells were seeded according the same procedure as in Chapter II. The difference here is that the cells are seeded on glass and polymer bottom dishes using a thin 50-100 µm membrane of PDMS for optimal visualisation of the actin.

The cells on the PDMS substrates were imaged after 24 hours in culture, either after a fixation step or live using an incubator chamber at 37°C. Representative images of the cells on the four categories of substrates are shown in Figure 52A, B, C, D. Their corresponding tension map is shown in the picture as well. The fixed cells showed that cells cultured on medium-hard, flat PDMS experienced a significantly lower intracellular tension when compared to cells on a patterned surface with the same stiffness. Furthermore, cells on the hard, patterned PDMS experienced less tension than cells on the medium hard, patterned PDMS (Figure 52E). This last comparison was not significant when comparing solely the averages per cell, but an interesting trend was observed, nevertheless.

For each condition, 23 images were collected and selected based upon their suitability to the criteria discussed in III.3.1.1. For statistical analysis, 22 representative cells were compared. Comparisons were made between materials of the same stiffness to evaluate the effect of the topography on cells seeded on that particular material elasticity. The opposite was also true, in the presence of the same topographical cues, the comparison was made between the material elasticities to understand the effect of solely varying the stiffness on the tension within a cell.

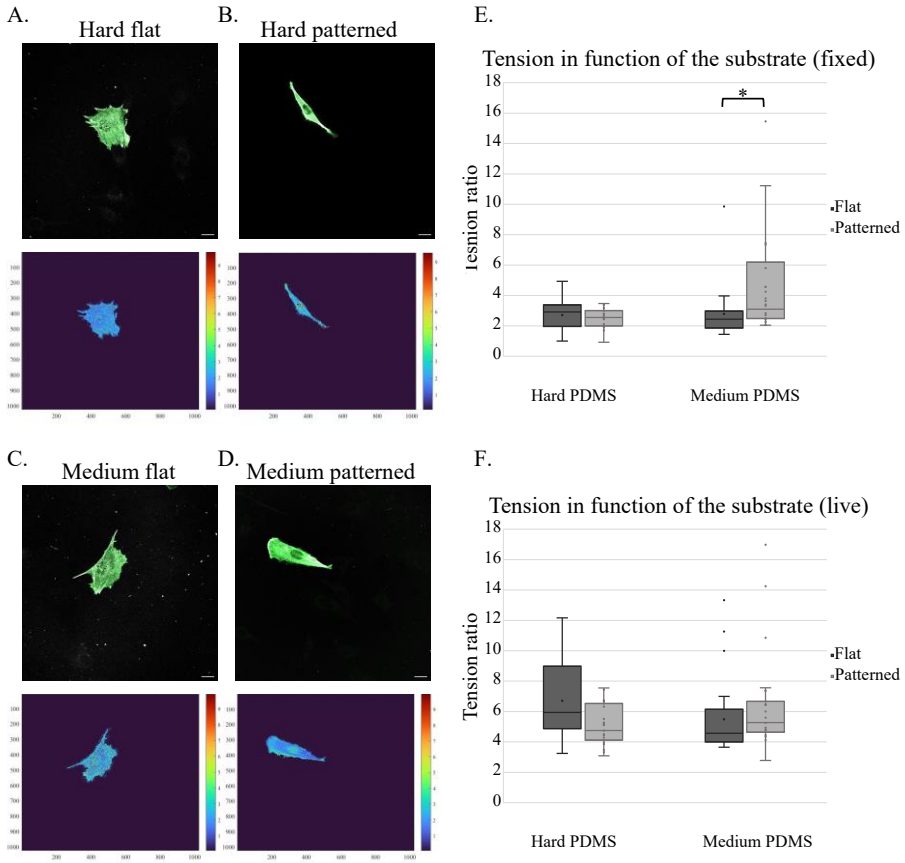

Figure 52: Cellular tension compared in function of the topography and stiffness of the substrates.
A. – D. C2C12 cells cultured on their respective substrates with green representing donor emission in the 505 - 525 nm emission band and white representing the acceptor emission in the 560 - 660 nm emission band. Samples were excited with the 488 nm laser. Corresponding MATLAB created tension images where red indicates high tension and blue indicates low tension. Scalebar = 20 µm. C. Comparison of tension values for cells cultured on the different substrates, while imaged after fixation, n equals 22. F. Comparison of tension values for cells cultured on the different substrates. Images acquired during live imaging; n equals 23. * $p < 0.05$.

In the case of imaging living cells, a similar phenomenon was observed for the medium-hard substrates with and without pattern. The cells on patterned substrates experienced higher intracellular stiffness when compared to cells on flat substrates, although not significant for average values. For stiffer PDMS, the live experiment demonstrated the inverse effect, where cells on a hard, flat substrate experience higher tension than cells on a medium-hard, flat substrate. In the case of live experiments, 23 representative cells, which met the selection criteria, were compared for statistical analysis.

3.1.4 Transfection of cells on surfaces coated with different proteins

Different types of protein coating were compared to see their effect on the tension experienced within cells adhering to the coating. To this aim, fibronectin, laminin, and medium were considered suitable coatings given their relevance and use in Chapter II.

For these three coating procedures, cells were imaged live, and the tension ratios were calculated and compared from two experiments with each 32 images per condition (Figure 53).

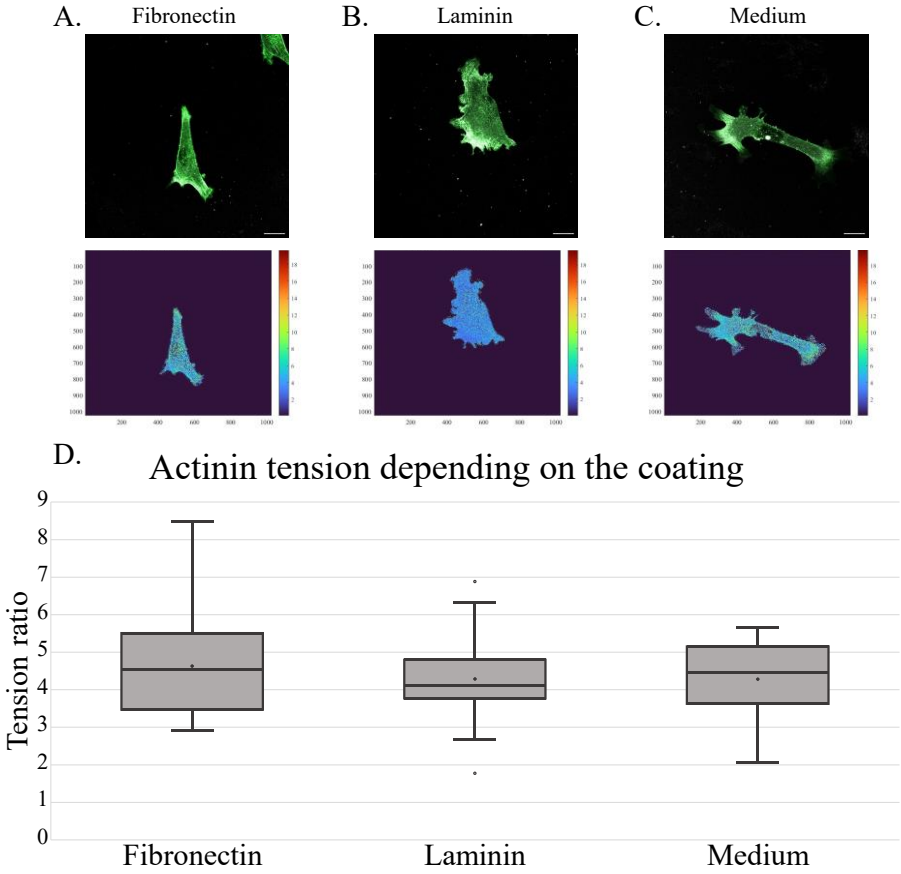

Figure 53: Tension evaluated on different protein coatings.
A. C2C12 cells seeded on PDMS with 10 µg/mL fibronectin coating for one hour at room temperature and visualised after 24 hours in culture. B. C2C12 cells seeded on PDMS with 10 µg/mL laminin coating for two hours at 37°C and visualised after 24 hours in culture. C. C2C12 seeded on overnight medium coated PDMS and visualised after 24 hours in culture. A, B, C, green represents donor emission and white represents acceptor emission when excited with the 488 nm laser. The resulting MATLAB tension maps are created using a colour code where red signifies high tension and blue signifies low tension. D. Overview of average tension values for C2C12 cells on different coatings with n equalling 32. Tension is determined as a ratio of two fluorescent intensities and is a dimensionless number.

The tension profiles found were considered not significantly differing after Kruskal-Wallis and post hoc Dunn's testing, indicating no significant trend in the tension profile, caused by the type of protein on the surface.

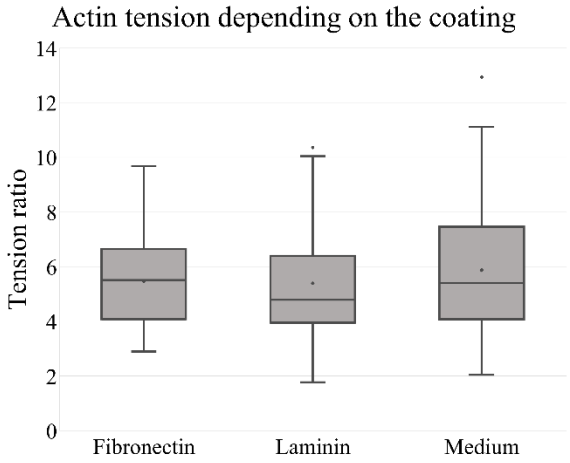

Figure 54: Extend repeat experiment of protein coated substrates.
Extended tension comparison of cells on substrates with fibronectin coating, laminin coating and medium coating in a first experiment.

Extending the experiment with a duplicate and pooling the results, resulted in an altered comparison, where no differences between the coating were observed, pooling all 62 tension averages (Figure 54). The second experiment was a biological replicate of the experiment demonstrated in Figure 53, with the sole difference that there might be slight variations in the thickness of the PDMS (a few µm) or the environmental conditions as it was done in an independent setting.

In both cases, the cells showed no significant difference when comparing laminin coated substrates with fibronectin or medium coated substrates, leading to the conclusion that this factor does not influence the actin cytoskeletal tension.

3.2 The Young's modulus of single cells on PDMS substrates as measured with AFM

The Young's Modulus of the cytoskeleton was determined in single cell measurements using AFM. The cantilever was placed on a portion of the cell, and a 20 x 20 µm force map was scanned to quantify the elasticity of the cells. On later time points, a force map was made of confluent areas, to compare the difference between confluent cells on different substrates. The following sections demonstrate these results for different setups. Every force map was reduced to an average Young's Modulus in this section, instead of using all 320 to 640 individual values. Comparisons using all the values instead are highlighted in the supplementary materials, as they were a way to compare if trends observed using

average values, were consistent. Using such a large number of values though, leads to incredibly small p values, which should be taken into consideration when comparing both types of analysis. Nevertheless, using both types of measurements confirmed that the values and trends observed were robust.

3.2.1 The Young's Modulus of C2C12 cells in function of substrate topography and stiffness

To evaluate the elasticity of cells cultured on different substrates, AFM indentation was used to determine the Young's Modulus. A Pyrex-Nitride Probe with Diving Board AFM Cantilever and quadratic pyramid tip was used to create a force map of single cells. Attention was paid to not indent the cells on the nucleus but in a zone of the cell body for every force map. The Young's modulus of individual cells was determined by fitting the force-indentation curve using the Hertzian model for linearly elastic materials.

All substrates were treated in the same manner with oxygen plasma, followed by one hour of fibronectin coating, before seeding the cells at low density.

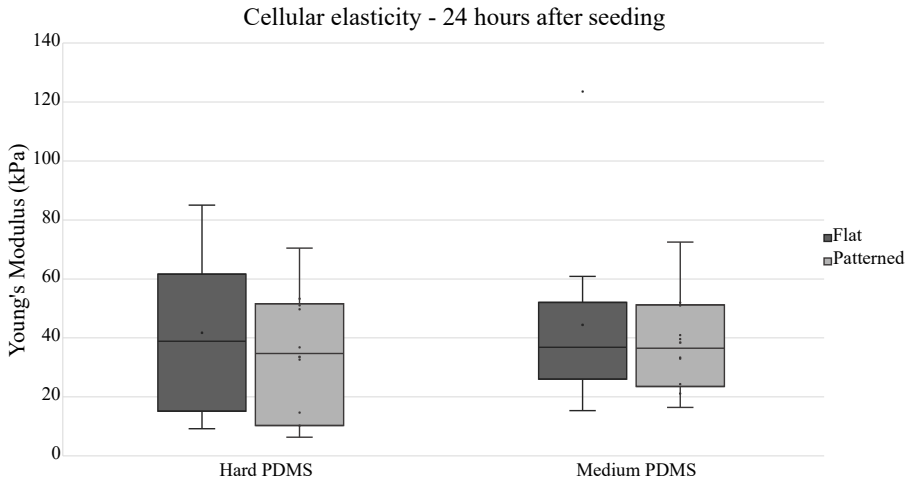

Figure 55: Young's Modulus of C2C12 cells on flat and patterned substrates, 24 hours after seeding. Boxplots comparing the average Young's Modulus of C2C12 cells seeded on different substrates, measured in live conditions, 24 hours after seeding. n equals 10.

Indentation of C2C12 on different substrates 24 hours after seeding did not demonstrate any difference in Young's Modulus of the cells, in function of their substrate, as can be seen in the boxplots of Figure 55. The average Young's Modulus of cells cultured on the substrates was in line with previous evaluations of the elasticity in C2C12 where they found values between 11 and 45 kPa [542]. Average measured values for the C2C12 in this case, were found to be between 33.5 and 44.5 kPa.

Since the AFM does not result in a timeframe issue, as the transfection did, it was possible to continue measuring the elasticity of the cells at different points in the cell culture process. Figure 56 shows the results of measurements at day 4 and 7 for cells on the different substrates, to evaluate their progression in time and the Young's Modulus of confluent cell layers.

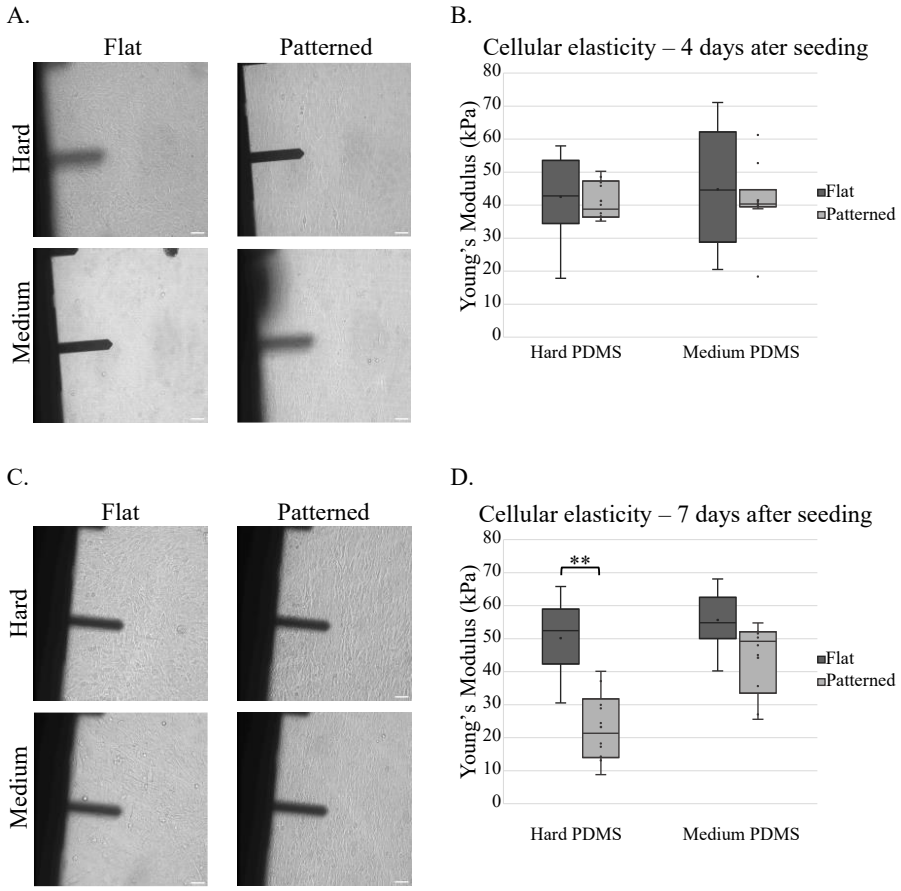

Figure 56: Young's Modulus of C2C12 cells on flat and patterned substrates at four and seven days after seeding.

A. C2C12 confluent layer after four days in culture, during AFM acquisition. Different substrate patterns and stiffnesses are shown. B. Boxplot overview of the Young's Moduli from the different experimental set-ups after four days in culture. C. C2C12 confluent layer on different substrates after seven days in culture, during AFM acquisition. D. Boxplot overview of the Young's Moduli from the different experimental set-ups after seven days in culture. Scalebars on the brightfield images represent 50 µm. n is larger than 5 for all experiments. * $p < 0.05$, ** $p < 0.01$, *** $p < 0.001$

As shown in Figure 56B, the Young's Moduli of confluent cell layers do not differ depending on the type of substrate on day 4 in culture, when taking into account solely the average value per force map. The layers on day 4 show average Young's Moduli between 41 and 44 kPa. A trend is observed where the distribution of

values on patterned substrates is smaller compared to those on flat substrates and the Young's Moduli are slight lower.

Interestingly, the average Young's Modulus for patterned samples drops at day 7, showing a significantly lower average for both hard, patterned PDMS when compared to the flat counterpart (Figure 56D). On medium hard PDMS substrates, this difference was observed as well, but using average values to evaluate the force of the confluent layers did not indicate this trend to be significantly different.

These experiments were continued to evaluate the Young's Modulus of cell layers on day 11 and day 14 after seeding (Figure 57). The softening of the cellular layer between flat and patterned substrates for hard and medium hard PDMS was seen on day 11 in culture as well. Longer culture times proved to be difficult for flat samples, with cellular detachment on surfaces placed in the AFM. Measurement at fourteen days in culture are therefore solely carried out on patterned substrates for both hard and medium PDMS. As seen on the two-week mark, the layers formed on hard PDMS were softer than layers formed on medium hard PDMS.

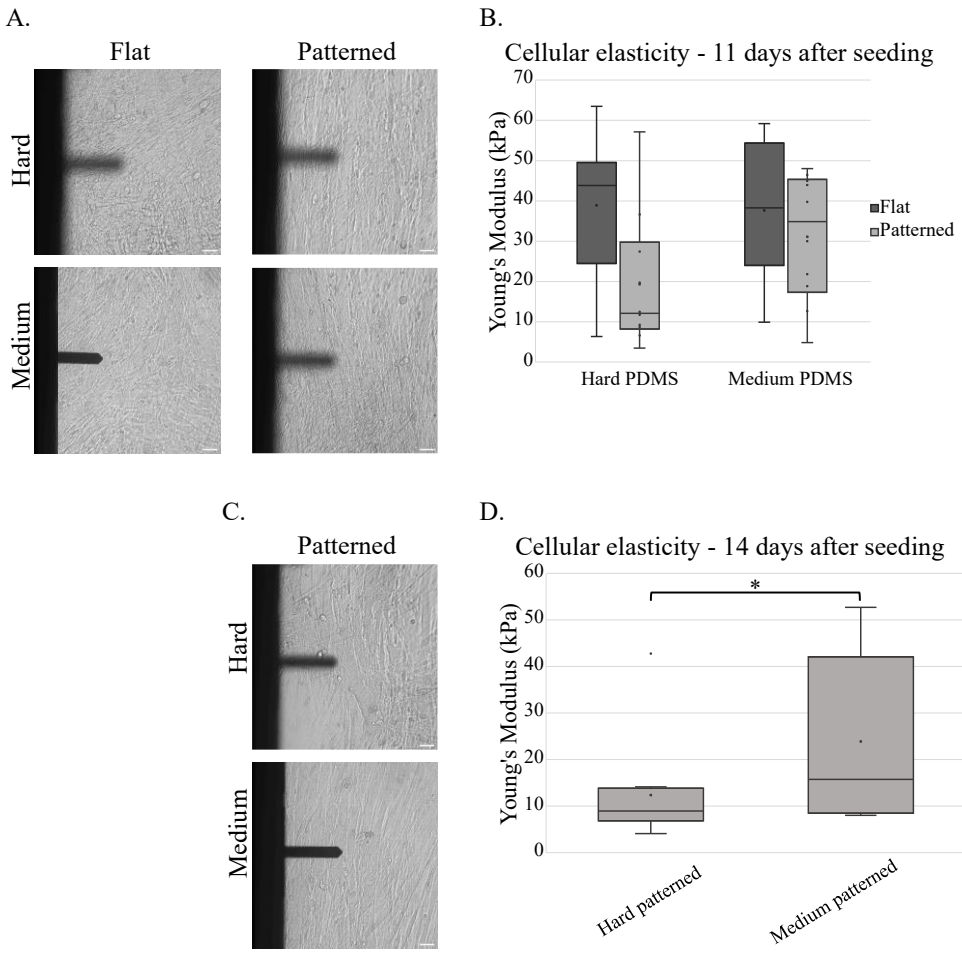

Figure 57: Young's Modulus of C2C12 cells on flat and patterned substrates at eleven and fourteen days after seeding.
A. C2C12 confluent layer after eleven days in culture, during AFM acquisition. Different substrate patterns and stiffnesses are shown. B. Boxplot overview of the Young's Moduli from the different experimental set-ups after eleven days in culture. C. C2C12 confluent layer on different substrates after fourteen days in culture, during AFM acquisition. Different substrate stiffnesses are shown for grooved surfaces. D. Boxplot overview of the Young's Moduli from the different experimental set-ups after fourteen days in culture. Scalebars on the brightfield images represent 50 µm. n is larger than 10 for all experiments. * $p < 0.05$.

As stated, these figures and statistics were obtained using average values per force map instead of all the individual measurements of a force map. In the supplementary materials document, attention is paid to this difference. Comparisons between average values and all values were used as a method to evaluate the robustness of the experiments. All these values were measured using a pyramidical tip as stated in the materials and methods section, leading to an increase in the variability of all individual force curves. Using average Young's

Moduli as a method for comparisons, was considered to reduce this variability caused by the tip shape.

3.2.2 The Young's Modulus of C2C12 cells in function of the protein coating of substrates

A similar evaluation as in III.3.1.4 was carried out for substrates with different types of protein coating, to compare the effects of coating proteins on the mechanical identity of the cells. To this end, substrates were coated either with 10 µg/mL of fibronectin for one hour at room temperature, 10 µg/mL laminin for two hours at 37°C or overnight with complete growth medium. Cells on all three substrates were then compared using AFM at 24 hours after seeding, at 4 days, 7 days and at 15 days after seeding. Resulting images and Young's Modulus values for cells 24 hours in culture are shown in Figure 58.

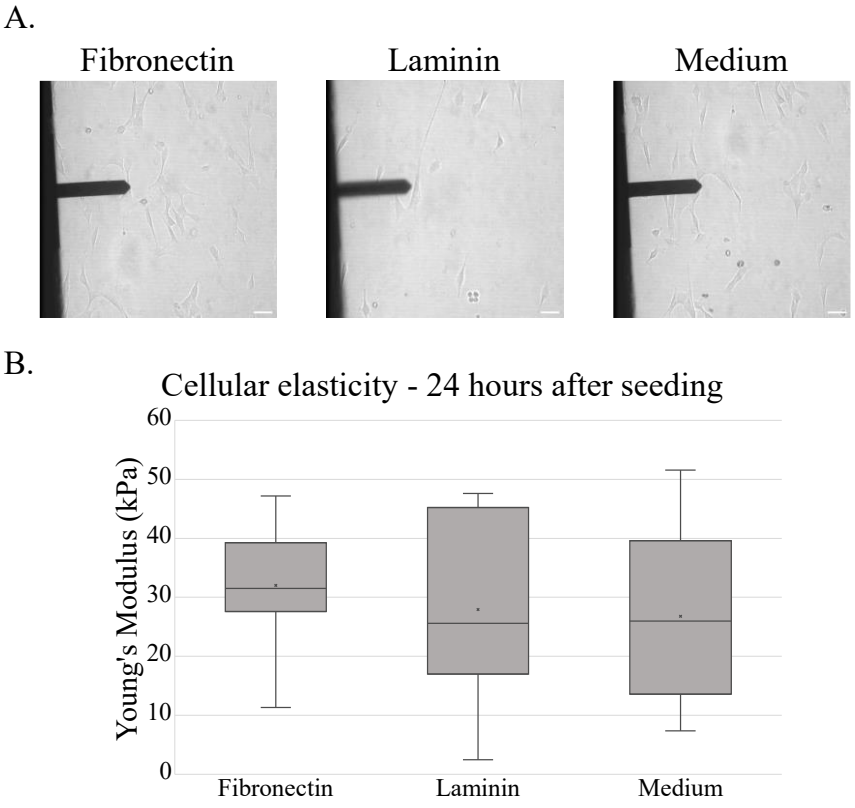

Figure 58: Young's Modulus of C2C12 cells on protein coated substrates at 24 hours after seeding.
A. C2C12 single cells after 24 hours in culture, during AFM acquisition. Different types of coating for the substrates are shown. B. Boxplot overview of the Young's Moduli from the different experimental set-ups after 24 hours in culture. Scalebars on the brightfield images represent 50 µm. n is 10 for all experiments.

Figure 58A contains three representative images of the three compared substrates, with cells that were seeded 24 hours prior to image acquisition and AFM Young's Moduli determination. The average values between the three substrates were 32.00 ± 10.04 kPa for cells on fibronectin, 27.94 ± 15.38 kPa for the laminin substrates and 26.77 ± 14.86 kPa for the growth medium coated substrates. The boxplots in Figure 58B demonstrate the range of average values for each substrate.

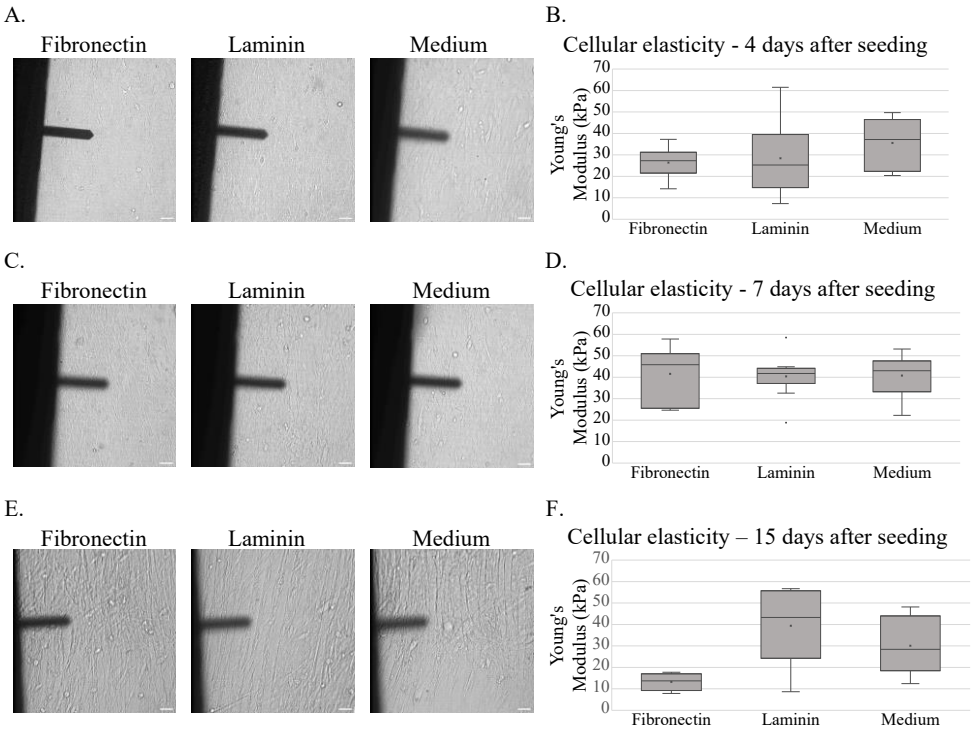

Figure 59: Young's Modulus of C2C12 cells on protein coated substrates at 4, 7 and 15 days after seeding.

A. C2C12 single cells after four days in culture, during AFM acquisition. Different types of coating for the substrates are shown. B. Boxplot overview of the Young's Moduli from the different experimental set-ups after four days in culture. C. C2C12 single cells after seven days in culture, during AFM acquisition. Different types of coating for the substrates are shown. D. Boxplot overview of the Young's Moduli from the different experimental set-ups after seven days in culture. E. C2C12 single cells after fifteen days in culture, during AFM acquisition. Different types of coating for the substrates are shown. F. Boxplot overview of the Young's Moduli from the different experimental set-ups after fifteen days in culture. Scalebars on the brightfield images represent 50 µm. n = 10 for experiments on day 4 and 7, and n = 5 for experiments on day 15.

Figure 59 shows the evolution of Young's Moduli in time for the different coating types. While on days 4 and 7 in culture (panels A, B, C, D) no noticeable difference is observed when comparing different coating types, at day 15 in culture, cells seeded on fibronectin demonstrate a decreasing trend in Young's Modulus compared to Laminin and medium coated substrates (Panels E, F).

Cellular layers on fibronectin showed an average Young's Modulus of 13.24 ± 4.05 kPa, compared to 39.45 ± 19.39 kPa and 30.07 ± 13.35 kPa for Laminin and Medium coated substrates respectively.

3.2.3 Young's Modulus of skeletal muscle tissue constructs

Applying the same measurement method to skeletal muscle tissue constructs revealed information about the mechanical characteristics of the constructs formed in Chapter II. Two separate constructs were analysed with one presenting a normal construct geometry in the culture dish, while the second one additionally showed contraction during the measurement. Real-time videos of this contraction are presented in the supplementary data.

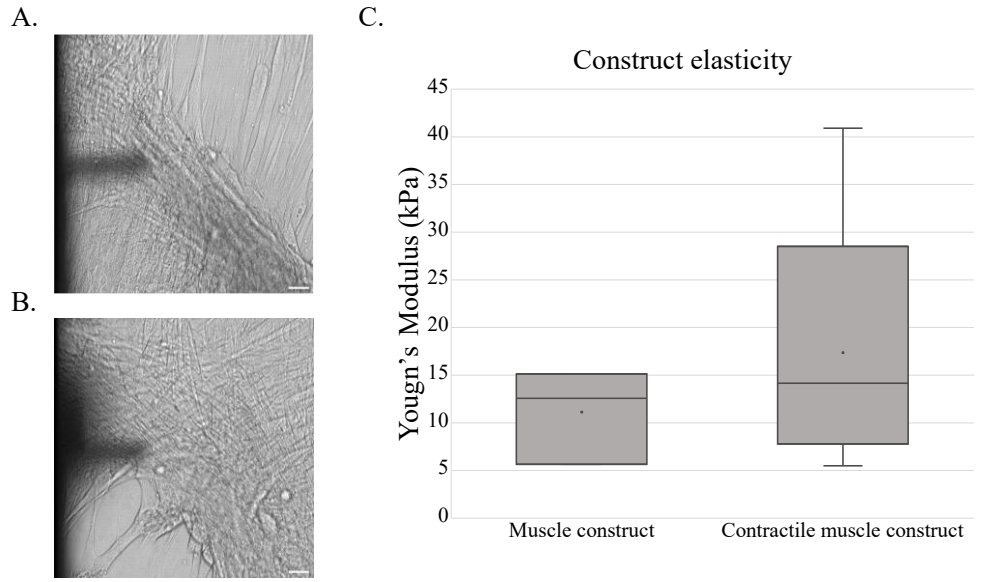

Figure 60: Young's Modulus of skeletal muscle tissue constructs after fourteen days after seeding.
A. Skeletal muscle tissue construct after fourteen days in culture, during AFM acquisition B. Contractile skeletal muscle tissue construct after fourteen days in culture, during AFM acquisition. The construct was contracting during the measurement and extremely large values (E > 300 kPa) were filtered out based on previous results. C. Boxplot overview of the Young's Moduli measured on the demonstrated muscle constructs. Scalebars on the brightfield images represent 50 µm.

For the muscle construct, 174 force curves were fitted and used for E determination, while for the contractile construct 250 force curves were fitted, divided over 3 and 5 regions of interest respectively. The resulting observations are shown in Figure 60, for the average Young's Modulus per region of interest. Using instead all values of all the force curves, resulted in a similar trend and are given in supplementary materials section. The non-contractile construct demonstrated a Young's Modulus of around 11.12 kPa, similar to that of native skeletal muscle tissues, which were found to have a Young's Modulus of 12 kPa [537]. The contracting muscle construct on the other hand presented slightly

higher values resulting in an average Young's Modulus of 17.35 kPa. These values indicate the relevance of the formed muscle constructs, that self-assemble into a mechanically relevant muscle construct.

3.3 Migratory behaviour of C2C12 cells on the PDMS substrates

The PIVlab MATLAB plugin was used to give an estimation of the direction of cell migration on the PDMS substrates of brightfield timelapses. In this type of setup, the velocity field of an entire region within a flow is measured simultaneously [588], instead of following the behaviour of single cells. The advantage of the plugin was that this technique could effectively and quickly provide information about the direction of the cell migration on the substrates from high contrast brightfield timelapses directly. The technique and analysis can be optimized by using nanoparticles or fluorescent trackers but for the construct formation and muscle cell culture, these extensions interfered with the proper behaviour of the cells on the substrates. The PIVlab data is included to extend observations of the global cellular behaviour on different substrates, and construct formation seen in Chapter II.

In the early stages of cell culture, the surfaces did not present a confluent cell layer, and PIVlab observations did not seem to match with the reality. Hence solely from day 8, this method is considered of interest for the direction of the migration of cells, illustrated in Figure 61.

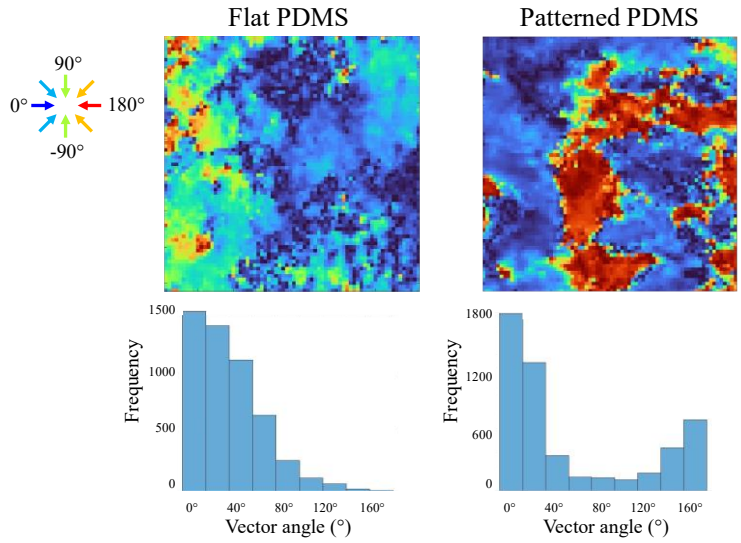

Figure 61: PIVlab vector angle results for flat and patterned surfaces from eight days in culture to ten days in culture.

Overview of a flat and patterned substrate, where the legend on the left indicates the direction of movement represented by coloured arrows. Samples considered here were confluent layers in culture, with no particular construct formation. The groove pattern is aligned horizontally for the patterned substrate.

At later timepoint in culture the skeletal muscle constructs start forming, as seen in Chapter II, so timelapses of this construct formation were analysed as well using the PIVlab plugin. These observations shed light on the direction of the cellular movement around the tissue construct formation and indicated a type of colliding movement, shown in Figure 62.

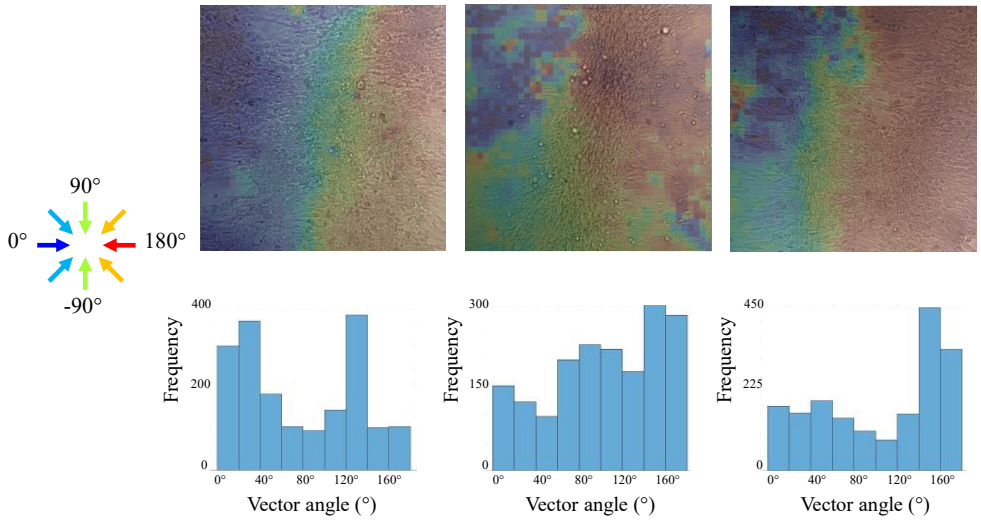

Figure 62: PIVlab vector angle results for patterned surfaces from nine to ten days in culture.
Overview of three different patterned substrates with construct formation, where the legend on the left indicates the direction of movement represented by coloured arrows. The groove pattern is aligned horizontally in all these images. Scalebars = 100µm.

Early construct formation was thus characterized by colliding migration patterns for cells during long term timelapses. An independent setup with pillars on the substrates, demonstrated similar findings, by indicating a type of colliding pattern around the muscle tissue construct, illustrated in Figure 63. At later timepoints, both in Figure 62 and Figure 63, the distribution of angles between 0° and 180° as indicated in the legend presents a variation in the vector angles. This might be due to the collision and resulting migration direction observed close to muscle tissue constructs.

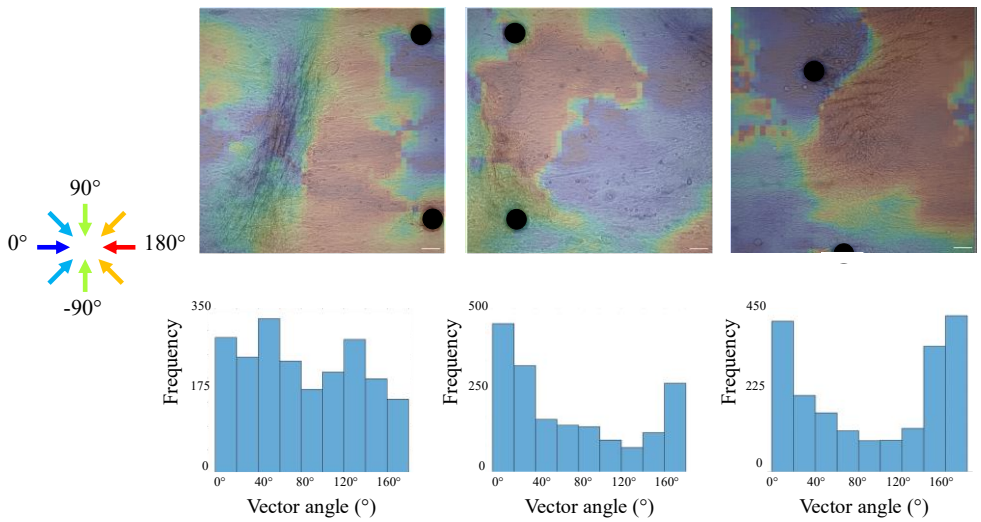

Figure 63: PIVlab vector angle results for patterned surfaces from eleven to fourteen days in culture. Overview of three different patterned substrates with construct formation, where the legend on the left indicates the direction of movement represented by coloured arrows. The groove pattern is aligned horizontally in all these images. Scalebars = 100µm.

Inclusion of pillars on the substrates resulted in similar vector angle profiles around the formation of constructs. As can be observed in Figure 63 on the left, the large construct formed presents vector angles from left to right on the left on the construct (given in blue), while on the right of the construct, the cells migrate from right to left (given in red). Both these global cell movements collide at the location of the structure formation. An interesting hypothesis forms by observing these global cell movements, relating to the fact that global cell migration forces on the substrates might aid and improve the construct formation seen on PDMS patterned substrates.

4. DISCUSSION AND CONCLUSIONS

The extracellular microenvironment proved to be an important regulator of cellular mechanics, which in turn regulate different aspects of cell behaviour [429], [589], [590]. Along these lines, the composition of the ECM along with its 3D organisation can all cell adhesion to the substrates, thus impacting cellular stiffness, which plays an important role during differentiation and commitment processes. *In vitro* artificial models have been used to recreate the niche by including biophysical features, such as topography or stiffness, to study cell functions like migration and differentiation [591], [592]. To evaluate the impact of nanopatterned surfaces on the cellular mechanical identity, two sets of experimental campaigns were carried out, each focusing on a different part of cellular mechanical identity. The two parts of the mechanical identity were defined as the tension within a cell, evaluated by actin stretching and the elasticity of a cell, evaluated by measuring the indentation Young's Modulus with AFM.

4.1 Actinin-FRET biosensor as a tool to evaluate intracellular tension

Skeletal muscle is a dynamic tissue experiencing tension and stress to allow contraction and movement [593]. Its flexibility is known to protect tendons, cartilage, and bones from disproportionate stress. C2C12 cells, and muscle cells in general, are highly mechanosensitive [594]. Increases in pulsed ultrasound can enhance the proliferation of C2C12 [595], flow induced shear stress has been demonstrated to lead to an increase in cytosolic calcium, due to mechanosensitive TRPV2 channels [596] and mechanical loading of the cells has resulted in upregulation of myogenic and anabolic factors [597].

Changing thus the type of substrate on which cells are cultured, could result in an effective strategy to alter mechanical cues that the cells can experience. These adapted cues are suggested to influence the behaviour and mechanical identity of the cell [598].

Actinin has been proposed as a tension sensor of actin bundles within cells, due to its flexible cross-linking and anchoring [599]. Therefore, in order to evaluate the effect of surface stiffness along with the impact of topography in form of nanogrooves on cellular mechanical identity, a protocol was optimised for the transfection of C2C12 cells with an Actinin-sstFRET-GR biosensor as an indicator for cytoskeletal tension. The FRET probe is able to indicate a higher tension of the actin cytoskeleton, as demonstrated by a lower energy transfer from donor to acceptor fluorophore. A custom MATLAB script was developed for this specific biosensor and acquisition method, according to the information given by Wang et al, when designing the probe [483]. Close attention was paid to analyse one cell per image and remove the background and artifacts before evaluating both the FRET ratio and the tension ratio given by the equations in 2.1.5. The values for

the tension are not expressed as a quantitative unit of force, but rather as a ratio, indicating the inverse of the FRET ratio.

Unfortunately, this probe was only effective in measuring cell stress within the first 48 hours after transfection, with a large increase in acceptor noise from 72 hours after transfecting the cells (thus 48 hours after cell seeding). In both fixed and live samples, C2C12 cells seeded on substrates possessing the same stiffness but different topographic cues presented an altered average intracellular tension. As cellular fixation can mitigate the actin cytoskeleton [600] mechanical properties, more attention was paid to the cells visualised in live conditions. Moreover, the tension biosensor results with this current acquisition method, in a unitless indication of the tension in the whole cell or part of the cells. It is imperative to note that this ratio is not a measurement of tension expressed in stretched distance or force. Expanding the current method, by instead of considering the whole cell, selecting the individual stress fibres as regions of interest, could improve the specificity of the method.

Another study approached the FRET measured tension by culturing Human Embryonic Kidney cells on fibronectin stripes coated surfaces, where adhesive islands confided the cell shape [601]. During their analysis, instead of taking the whole cell FRET ratio, they divided the cells into regions attached to the pattern, and bridged regions over the non-adhesive glass [601]. They indicated that cells adhering to the fibronectin T-shaped pattern possessed lower tension values at their adhesive areas, in contrast to a higher tension on the bridged regions over the non-adhesive surface. On long adhesive stripes and round patterns, the differences were negligible.

On flat substrates, increased tension of actinin is linked with, for instance, the development of focal adhesions. α-Actinin sustains increased tension during adhesion formation in migrating cells. In stable adhesive cells, the tension is then decreased to a comparable value to the surrounding cellular areas. Actinin stress, furthermore, has been shown to increase in the minutes preceding FA complex growth, and during the enlargement of FAs [602]. Increases in tension of cells cultured on medium hard, patterned substrates compared to medium hard, flat substrates could therefore be related to the adhesion of cells on both substrates.

Using this approach, cellular tension could be described using actinin tension after 24 hours of culture. A medium stiff PDMS demonstrated that for fixed cells, the presence of a pattern alters the tension within C2C12 cells. Stiffer PDMS did not demonstrate this effect and samples on both flat and patterned substrates experienced a similar tension. Since these measurements took into account the whole cell instead of regions of stress fibres, the experiments at this stage are

considered inconclusive as to the cytoskeletal tension of cells on the different substrates. The inability of this method to consider longer experiments, lead to the decision to not further refine this particular set-up at this stage.

4.2 AFM as a tool to evaluate cell elasticity

Muscle stiffness is an important parameter in diseases such as Duchenne muscular dystrophy, where an increase in muscle stiffness is observed [603], [604]. Moreover, in regenerated muscle after injury an increase of stiffness is distinguished [309], indicating a role of the stiffness profile of muscles for health and diseases or injuries. During the regeneration process, the muscle softens immediately after injury, and then it stiffens due to collagen deposition. These variations indicate a diverse elasticity profile for muscle tissues. Muscle stem cells, for instance, respond to an increase in stiffness by increasing their proliferation, but other cells react differently to changes in substrate stiffness and topography [309], [605].

Furthermore, the goal was to further evaluate the mechanical response of C2C12 cells on the engineered substrates, to assess the elasticity of the cells at different timepoints, by means of AFM.

Initial experiments showed that cells maintained a similar elasticity on flat, patterned, stiff and ECM coated substrates, within the first four days of culture. After a week in culture, C2C12 cultured on patterned substrates drastically decreased their Young's Modulus indicating a softer cellular layer on substrates with nanogrooves compared to flat substrates. Eleven days after seeding these layers on stiff patterned substrates were still softer than their flat counterpart. However, further measurements were not possible as the cells on the flat substrate detached upon placement in the AFM. Fourteen days after seeding, the anisotropic cellular layers on hard substrates showed a reduction in Young's Modulus compared to similar layers on medium PDMS.

Moreover, a subset of experiments was carried out in order to assess the contribution of surface coating with different ECM proteins (fibronectin, laminin, serum) in modulating cellular stiffness. However, these experiments demonstrated no influence of the coating type on the stiffness of cells and the confluent cellular layers stiffness, until fifteen days after seeding. Around two weeks in culture, the cellular layers formed on Fibronectin coated substrates showed a significant reduction in Young's Modulus compared to layers on Laminin coated substrates and Medium coated substrates.

This decrease in the Young's Modulus of organised layers is interesting as C2C12 cells have been shown to have a relatively varied Young's Modulus between 2 and 45 kPa when visualised as single cells. In contrast to the stiffness of muscle [537]

tissues which falls within the more concise range of 10 to 17 kPa, which the organised layers approximate. The designed skeletal muscle tissue constructs were evaluated as well, for their mechanical relevance to native muscle tissue, and Young's Modulus values were found to be in this suggested range too. This finding indicates that the niche designed in chapter II, has the capacity to form a mechanically relevant skeletal muscle tissue *in vitro*, by allowing the cells to self-assemble into a tissue construct.

A recent study demonstrated that the Young's Modulus of cells in earlier stages is regulated by individual cell proliferation and cell-matrix interactions [605]. Epithelial cells then demonstrated a shift to the influence of cell-cell interactions mediated by E-cadherin on the Young's Modulus, which was not observed for mesenchymal stem cells, for instance. These findings could be interesting to relate to the shift in cellular mechanics, found on the patterned surfaces, where the tight knit organised network can affect the Young's Modulus of the layer compared to the chaotic layers on flat substrates. Further research into the molecular pathways involved in the reaction of the cells on the nanogrooves, could shed light on such a mechanism mediated by either cell-cell interactions, or newly formed matrix interactions.

4.3 Global cell migration on patterned substrates

In the previous chapters, methods were developed to study skeletal muscle cell behaviour *in vitro*, using substrate interactions and environmental cues. These parameters not solely effect the growth and proliferation of the cells, but the migration as well. During these evaluations in previous chapters, migration patterns were observed as demonstrated in this chapter, to gain knowledge on how these cells move in the artificial niche. On flat substrates, fibronectin has been shown in the past to cause some sort of global cell alignment and migration, unique to the specific coating. Using laminin or gelatine, for instance, did not lead to these observations [179].

To investigate the movement of cells, close to muscle construct formation, PIVlab was used as a tool to evaluate global cell migration rather than individual cell migration. Moving fields of two opposite horizontal global migrations, seem to collide at the region of construct formation, paving a way for migration being a driving force behind tissue construct formation. These PIVlab observations are just scratching the surface of tissue construct formation and extensive timelapses at different points in time, could improve the understanding of these processes. Do the migrating cellular fields cause the structure formation? Or does the formed structure attract its neighbouring cells to migrate towards the muscle, after initial formation? Based on the previous work carried out on fibronectin versus laminin flat coated substrates [179] observing a collective cell migration on fibronectin

substrates, the role of the fibronectin coating in the *in vitro* muscle construct formation might be extended. The fibronectin coating present influences not solely the initial cell attachment but also the migration patterns of the cells, an effect contributing to the formation of these global cellular movements.

4.4 Conclusion and future perspectives

Both the FRET tension biosensor and the AFM measurement were effective techniques able to detect variations of C2C12 cell mechanical properties caused by substrate topography and stiffness. This work demonstrated that altering these two biophysical cues resulted in an adapted tension profile, whereas at the same timepoints, the Young's Modulus of the cells remained constant. Longer culture times on different layers then demonstrated a decrease in the Young's Modulus of cell when the layers formed were organised, indicating a softer and more elastic cellular layer.

These findings are interesting to relate to the tissue formation of skeletal muscle constructs on nanogrooved patterns, discussed in Chapter II. As described extensively, the muscle tissue constructs are formed using only cues given in the beginning of the cell culture. Tissue formation occurred spontaneously upon optimisation of said cues. Describing the mechanical identity using tension and elasticity, brings the project closer to deciphering the reason behind tissue formation on the patterned substrates.

Further perspectives of the model, include mostly approaches to improve measurements of each specific parameter. Given that the field of FRET based microscopy is incredibly wide, as demonstrated in the introduction, comparing different methods using, for instance, FLIM imaging, could ameliorate the robustness of this value for tension within muscle cells.

Furthermore, the current model discusses the average tension of a whole cell, instead of that of individual fibres. Since the tension sensor is connected to Actinin; dorsal, ventral and transverse actin stress fibre types will have been visualised in a single image. It could be interesting to expand the current model in a way that a clear difference between the stress fibres is visualised. Such alterations to the model could indicate and expand on the tension those stress fibres experience individually on flat/patterned/stiff substrates.

A limitation of tension experiments was that the focus lies solely on PDMS films, and different materials were excluded. It was not the goal of these experiments to create equally thin films for PC and for FlexDym™ by designing completely different fabrication methods. Future experiments could focus on the influence of the material surface on the tension within cells, however, improved fabrication

methods for FlexDym™ are necessary in order to visualize the FRET signal with the least amount of noise possible.

On the other hand, AFM experiments into the cell mechanics suffer from large standard deviations and the possibility to lose the laser alignment between measurements. Special attention to these effects is certainly paid during experimental campaigns, but systems as the PIUMA from OPTICS11 could provide a fixed solution for the measurement multicellular layers. Their system does not rely on manual laser calibration but comes equipped with micro-machined fibre-optic sensors and pre-calibrated glass spherical tips.

Further interesting experiments on the mechanical identity of cells on the patterned substrates would include settings were signalling pathways relevant to mechanosensitive are targeted. The mechanosensitive Hippo signalling pathway [595], [606], which is responsible for the displacement of YAP transcription factor form the cytoplasm to the nucleus, is one of the interesting pathways for skeletal muscle. Increased stiffness leads to nuclear localisation of YAP [606]. Displacement of YAP in skeletal muscle is associated with conditions such as muscular dystrophy [140], whereas an upregulation of YAP is linked to muscle hypertrophy [141]. YAP promotes, for instance, the proliferation of satellite cells, while simultaneously blocking differentiation [142]–[145] and influences satellite cell migration, crucial for the regeneration process [140].

The Hippo signalling pathway is just one example of a mechanosensitive pathway that would provide an interesting addition to the presented tension/elasticity models for skeletal muscle on different substrates.

The shift in elasticity of the cells on different substrates presents an interesting pathway from an *in vitro* model type of perspective. The presence of altered tension ratios depending on the substrate, highlights a role of the designed pattern and stiffness in altering actin tension within cells. Further research into what signalling pathway shift causes could aide in the design of more effective *in vitro* models for 3D muscle culture.

IV. CONCLUSION

The microenvironment plays an important regulatory role on skeletal muscle behaviour, culture and morphology *in vitro* and in vivo, as has been demonstrated in the past chapters. In the field of tissue engineering, the interactions between single cells and biochemical/biophysical signals holds the potential to establish innovative platforms for the engineering of functional materials to guide tissue formation. Specifically for *in vitro* models, the cell-material interactions can be used to guide the cells towards controlled cellular behaviour and, in the case of skeletal muscle, towards the formation of an *in vitro* organised skeletal muscle tissue.

The events occurring when a single cell engages with a material surface that possesses customized attributes such as topography, biochemistry and specific surface stiffness, were of interest specifically for skeletal muscle tissue engineering within this work. In this thesis, substrates with biophysical cues were designed for the formation of an *in vitro* artificial microenvironment for skeletal muscle cells. Both the cellular growth into supracellular structures and the individual cell mechanics on the designed substrates were evaluated to shed light on the interaction of muscle cells with the artificial microenvironment.

The substrates used were characterised in Chapter I by assessing their topographical cues, indentation stiffness on the surface and adhesive properties. Different types of materials were considered, to evaluate specific material characteristics important for the muscle cell cultures. Polydimethylsiloxane (PDMS) and FlexDym™ were able to replicate the nanogrooved pattern of a polycarbonate (PC) master, and all three materials were used to evaluate skeletal muscle cell culture. To improve the cell adhesion to the surface, extra hydrophilizing steps were considered, and their effect on surface stiffness was monitored using atomic force microscopy techniques. The surface treatment to hydrophilize the substrates affected the Young's Modulus of the surface layer in a quite dramatic way, with increases larger than 36x in stiffness after treatment. Even though all materials evaluated were suitable for skeletal muscle cell culture but solely on PDMS supracellular structures, organised in skeletal muscle constructs were found.

Chapter II tackled the characterisation and improvement of skeletal muscle tissue constructs. PDMS substrates with a nanogrooved topography and fibronectin coating guided the cells from a confluent monolayer, towards the formation of a three-dimensional tissue construct. Starting from a layer of cells parallel to the groove direction provided, using the right combinations of initial biophysical cues, muscle constructs were formed in an orthogonal direction to the grooves. These

constructs consisted of remodelled extracellular matrix and myotubes, to form a 3D, orthogonal muscle construct with contractility and mechanical relevance, as measured using atomic force microscopy. As seen in images over time of construct formation, these constructs start forming thanks to a sort of disruption and splitting of the confluent monolayer of cells around 10 days in culture. Both pillars and millipatterns provided additional initial signals for cells to start preferring the orthogonal construct formation and were demonstrated to improve the localisation and formation of the muscle tissue constructs. The fibronectin coating used for the initial adherence on the substrates, was observed to be remodelled by the cells, on PDMS substrates, and to a lesser extent on PC and FlexDym™ substrates, where the construct formation was not discerned. Primary cells provided some initial information on the application of the engineered substrates in this type of culture, but further research into their use is necessary as they imply different cell sizes and a decrease in reproducibility.

In Chapter III, the influence of the material on three specific parameters for cell culture was discussed, including cytoskeletal tension, elasticity and global migration of the C2C12 cells. Cells seeded on medium-hard patterned substrates experienced a different type of intracellular tension, compared to cells on their flat counterpart substrates. This indicates a specific role of the nanotopography in cytoskeletal forces and tension profiles, relevant for cell mechanics and behaviour. Furthermore, at increased culture times, the pattern caused confluent cell layers to exhibit a lower Young's Modulus compared to the isotropic layers formed on flat substrates, indicating an increased elastic behaviour thanks to the presence of topographical cues. The native skeletal muscle environment is far from flat, with long and elongated fibres spanning across the tissue. Replicating this type of behaviour *in vitro*, paves the way for closer mimics of the native skeletal muscle niche, compared to standard culture practices. The elasticity of the formed skeletal muscle constructs was evaluated and compared to the Young's modulus of native skeletal muscle tissue. Striking similarities were found, indicating that the skeletal muscle structure formed, has a strong mechanical relevance. The formation of this construct was, furthermore, shown in Chapter III to be accompanied by migration of cells towards the tissue in a migration pattern parallel to the grooves. These parallel migration patterns collided close the formed muscle tissue constructs, indicating a role for global cell migration in the formation or maintenance of the skeletal muscle tissue constructs.

The combination of the adhered fibronectin, the global cell migration, the anisotropic surface topography and the stiffness and surface energy of the PDMS substrates provides all the initial cues necessary to form a skeletal muscle tissue construct.

In the work of this thesis, a novel skeletal muscle tissue fabrication method was described, based on the self-assembly of a tissue *in vitro*, without the need for external forces or manipulations to create 3D muscle tissue constructs. By providing a set of initial cues, the cells self-assembled into forming a tissue construct, highlighting the role of the cell-material interactions in tissue engineering approaches.

BIBLIOGRAPHY

[1] A. Qureshi *et al.*, 'Surface modification of polycarbonate by plasma treatment', *J. Phys. Conf. Ser.*, vol. 208, p. 012108, Feb. 2010, doi: 10.1088/1742-6596/208/1/012108.

[2] S. G. Gizer, V. R. Bhethanabotla, R. S. Ayyala, and N. Sahiner, 'Low-pressure plasma treated polycarbonate and polymethyl methacrylate (PMMA) sheets with different surface patterns to change their surface properties', *Surf. Interfaces*, vol. 37, p. 102646, Apr. 2023, doi: 10.1016/j.surfin.2023.102646.

[3] G. Kalita *et al.*, 'Fluorination of multi-walled carbon nanotubes (MWNTs) via surface wave microwave (SW-MW) plasma treatment', *Phys. E Low-Dimens. Syst. Nanostructures*, vol. 41, no. 2, pp. 299–303, Dec. 2008, doi: 10.1016/j.physe.2008.07.015.

[4] D. R. Monteiro, L. F. Gorup, A. S. Takamiya, A. C. Ruvollo-Filho, E. R. de Camargo, and D. B. Barbosa, 'The growing importance of materials that prevent microbial adhesion: antimicrobial effect of medical devices containing silver', *Int. J. Antimicrob. Agents*, vol. 34, no. 2, pp. 103–110, Aug. 2009, doi: 10.1016/j.ijantimicag.2009.01.017.

[5] T. Krausz, D. A. serban, R. M. Negru, A. G. Radu, and L. Marsavina, 'The effect of strain rate and temperature on the mechanical properties of polycarbonate composites', *Mater. Today Proc.*, vol. 45, pp. 4211–4215, Jan. 2021, doi: 10.1016/j.matpr.2020.12.121.

[6] N. Connor, 'Polycarbonate | Properties, Price & Application', Material Properties. Accessed: Dec. 20, 2023. [Online]. Available: https://material-properties.org/polycarbonate-properties-application-price/

[7] 'Refractive Index of Polycarbonate, Lexan, Makrolon, PC for Thin Film Thickness Measurement'. Accessed: Dec. 20, 2023. [Online]. Available: https://www.filmetrics.com/refractive-index-database/Polycarbonate/Lexan-Makrolon-PC

[8] S. A. Hafad *et al.*, 'Mechanical properties study of polycarbonate and other thermoplastic polymers', *J. Phys. Conf. Ser.*, vol. 1973, no. 1, p. 012001, Aug. 2021, doi: 10.1088/1742-6596/1973/1/012001.

[9] G. Gómez-Gras, M. D. Abad, and M. A. Pérez, 'Mechanical Performance of 3D-Printed Biocompatible Polycarbonate for Biomechanical Applications', *Polymers*, vol. 13, no. 21, p. 3669, Oct. 2021, doi: 10.3390/polym13213669.

[10] W. S. Higley, P. A. Cantor, and B. S. Fisher, 'Thin polycarbonate membranes for use in hemodialysis', CA1093240A, Jan. 06, 1981 Accessed: Dec. 20, 2023. [Online]. Available: https://patents.google.com/patent/CA1093240A/en

[11] L. Czuba, 'Application of Plastics in Medical Devices and Equipment', *Handb. Polym. Appl. Med. Med. Devices*, pp. 9–19, 2014, doi: 10.1016/B978-0-323-22805-3.00002-5.

[12] Y. J. Yun *et al.*, 'Highly Elastic Graphene-Based Electronics Toward Electronic Skin', *Adv. Funct. Mater.*, vol. 27, no. 33, Sep. 2017, doi: 10.1002/adfm.201701513.

[13] D. Pinho, B. N. Muñoz-Sánchez, C. F. Anes, E. J. Vega, and R. Lima, 'Flexible PDMS microparticles to mimic RBCs in blood particulate analogue fluids', *Mech. Res. Commun.*, vol. 100, p. 103399, Sep. 2019, doi: 10.1016/j.mechrescom.2019.103399.

[14] M. P. Wolf, G. B. Salieb-Beugelaar, and P. Hunziker, 'PDMS with designer functionalities—Properties, modifications strategies, and applications', *Prog. Polym. Sci.*, vol. 83, pp. 97–134, Aug. 2018, doi: 10.1016/j.progpolymsci.2018.06.001.

[15] J. C. McDonald and G. M. Whitesides, 'Poly(dimethylsiloxane) as a Material for Fabricating Microfluidic Devices', *Acc. Chem. Res.*, vol. 35, no. 7, pp. 491–499, Jul. 2002, doi: 10.1021/ar010110q.

[16] I. Teixeira *et al.*, 'Polydimethylsiloxane mechanical properties: A systematic review', *AIMS Mater. Sci.*, vol. 8, no. 6, Art. no. matersci-08-06-058, 2021, doi: 10.3934/matersci.2021058.

[17] D. J. Campbell *et al.*, 'Replication and Compression of Bulk Surface Structures with Polydimethylsiloxane Elastomer', *J. Chem. Educ*, no. 76, p. 537, 1999.

[18] J. Iturri, J. Miholich, S. Zemljic, A. Andorfer-Sarr, R. Benitez, and J. L. Toca-Herrera, 'The stiffness of elastomeric surfaces influences the mechanical properties of endothelial cells', arXiv.org. Accessed: Dec. 20, 2023. [Online]. Available: https://arxiv.org/abs/2210.15038v1

[19] I. D. Johnston, D. K. McCluskey, C. K. L. Tan, and M. C. Tracey, 'Mechanical characterization of bulk Sylgard 184 for microfluidics and microengineering', *J. Micromechanics Microengineering*, vol. 24, no. 3, p. 035017, Mar. 2014, doi: 10.1088/0960-1317/24/3/035017.
[20] H. Hillborg, J. F. Ankner, U. W. Gedde, G. D. Smith, H. K. Yasuda, and K. Wikström, 'Crosslinked polydimethylsiloxane exposed to oxygen plasma studied by neutron reflectometry and other surface specific techniques', *Polymer*, vol. 41, no. 18, pp. 6851–6863, Aug. 2000, doi: 10.1016/S0032-3861(00)00039-2.
[21] S. H. Tan, N.-T. Nguyen, Y. C. Chua, and T. G. Kang, 'Oxygen plasma treatment for reducing hydrophobicity of a sealed polydimethylsiloxane microchannel', *Biomicrofluidics*, vol. 4, no. 3, p. 032204, Sep. 2010, doi: 10.1063/1.3466882.
[22] B. Ruben *et al.*, 'Oxygen plasma treatments of polydimethylsiloxane surfaces: effect of the atomic oxygen on capillary flow in the microchannels', *Micro Nano Lett.*, vol. 12, no. 10, pp. 754–757, 2017, doi: 10.1049/mnl.2017.0230.
[23] K. Efimenko, W. E. Wallace, and J. Genzer, 'Surface Modification of Sylgard-184 Poly(dimethyl siloxane) Networks by Ultraviolet and Ultraviolet/Ozone Treatment', *J. Colloid Interface Sci.*, vol. 254, no. 2, pp. 306–315, Oct. 2002, doi: 10.1006/jcis.2002.8594.
[24] K. Fateh-Alavi and U. W. Gedde, 'Effect of stabilizers on surface oxidation of silicone rubber by corona discharge', *Polym. Degrad. Stab.*, vol. 84, no. 3, pp. 469–474, Jun. 2004, doi: 10.1016/j.polymdegradstab.2004.01.005.
[25] J. R. Hollahan and G. L. Carlson, 'Hydroxylation of polymethylsiloxane surfaces by oxidizing plasmas', *J. Appl. Polym. Sci.*, vol. 14, no. 10, pp. 2499–2508, 1970, doi: 10.1002/app.1970.070141006.
[26] J. Song *et al.*, 'Surface Ionization State and Nanoscale Chemical Composition of UV-Irradiated Poly(dimethylsiloxane) Probed by Chemical Force Microscopy, Force Titration, and Electrokinetic Measurements', *Langmuir*, vol. 23, no. 10, pp. 5430–5438, May 2007, doi: 10.1021/la063168s.
[27] J. Roth *et al.*, 'Surface Functionalization of Silicone Rubber for Permanent Adhesion Improvement', *Langmuir*, vol. 24, no. 21, pp. 12603–12611, Nov. 2008, doi: 10.1021/la801970s.
[28] K. Duangkanya, A. Kopwitthaya, S. Chanhorm, and Y. Infahsaeng, 'Oxygen plasma treatment time induced hydrophilicity of polydimethylsiloxane (PDMS) thin films for liquid lenses application', *Mater. Today Proc.*, vol. 65, pp. 2442–2445, Jan. 2022, doi: 10.1016/j.matpr.2022.06.121.
[29] M. Morra, E. Occhiello, R. Marola, F. Garbassi, P. Humphrey, and D. Johnson, 'On the aging of oxygen plasma-treated polydimethylsiloxane surfaces', *J. Colloid Interface Sci.*, vol. 137, no. 1, pp. 11–24, Jun. 1990, doi: 10.1016/0021-9797(90)90038-P.
[30] D. Bodas and C. Khan-Malek, 'Hydrophilization and hydrophobic recovery of PDMS by oxygen plasma and chemical treatment—An SEM investigation', *Sens. Actuators B Chem.*, vol. 123, no. 1, pp. 368–373, Apr. 2007, doi: 10.1016/j.snb.2006.08.037.
[31] A. Tóth, I. Bertóti, M. Blazsó, G. Bánhegyi, A. Bognar, and P. Szaplonczay, 'Oxidative damage and recovery of silicone rubber surfaces. I. X-ray photoelectron spectroscopic study', *J. Appl. Polym. Sci.*, vol. 52, no. 9, pp. 1293–1307, 1994, doi: 10.1002/app.1994.070520914.
[32] J. Kim, M. K. Chaudhury, M. J. Owen, and T. Orbeck, 'The Mechanisms of Hydrophobic Recovery of Polydimethylsiloxane Elastomers Exposed to Partial Electrical Discharges', *J. Colloid Interface Sci.*, vol. 244, no. 1, pp. 200–207, Dec. 2001, doi: 10.1006/jcis.2001.7909.
[33] D. T. Eddington, J. P. Puccinelli, and D. J. Beebe, 'Thermal aging and reduced hydrophobic recovery of polydimethylsiloxane', *Sens. Actuators B Chem.*, vol. 114, no. 1, pp. 170–172, Mar. 2006, doi: 10.1016/j.snb.2005.04.037.
[34] X. Zhu *et al.*, 'Fabrication of reconfigurable protein matrices by cracking', *Nat. Mater.*, vol. 4, no. 5, Art. no. 5, May 2005, doi: 10.1038/nmat1365.
[35] M. Kim, B.-U. Moon, and C. H. Hidrovo, 'Enhancement of the thermo-mechanical properties of PDMS molds for the hot embossing of PMMA microfluidic devices', *J. Micromechanics Microengineering*, vol. 23, no. 9, p. 095024, Aug. 2013, doi: 10.1088/0960-1317/23/9/095024.
[36] G. Tifui, M. Dobromir, and L. Sirghi, 'Stiffening of polydimethylsiloxane surface as result of exposure to low-pressure argon discharge plasma', *Plasma Process. Polym.*, vol. 20, no. 8, p. 2300014, 2023, doi: 10.1002/ppap.202300014.
[37] J. Song, D. Tranchida, and G. J. Vancso, 'Contact Mechanics of UV/Ozone-Treated PDMS by AFM and JKR Testing: Mechanical Performance from Nano- to Micrometer Length Scales', *Macromolecules*, vol. 41, no. 18, pp. 6757–6762, Sep. 2008, doi: 10.1021/ma800536y.

[38] F. C. P. Sales, R. M. Ariati, V. T. Noronha, and J. E. Ribeiro, 'Mechanical Characterization of PDMS with Different Mixing Ratios', *Procedia Struct. Integr.*, vol. 37, pp. 383–388, Jan. 2022, doi: 10.1016/j.prostr.2022.01.099.
[39] G. Zhang, Y. Sun, B. Qian, H. Gao, and D. Zuo, 'Experimental study on mechanical performance of polydimethylsiloxane (PDMS) at various temperatures', *Polym. Test.*, vol. 90, p. 106670, Oct. 2020, doi: 10.1016/j.polymertesting.2020.106670.
[40] F. Sales *et al.*, 'Composite Material of PDMS with Interchangeable Transmittance: Study of Optical, Mechanical Properties and Wettability', *J. Compos. Sci.*, vol. 5, no. 4, Art. no. 4, Apr. 2021, doi: 10.3390/jcs5040110.
[41] 'SYLGARD™ 184 Silicone Elastomer Kit'. Accessed: Dec. 20, 2023. [Online]. Available: https://www.dow.com/en-us/pdp.sylgard-184-silicone-elastomer-kit.01064291z.html
[42] F. Schneider, J. Draheim, R. Kamberger, and U. Wallrabe, 'Process and material properties of polydimethylsiloxane (PDMS) for Optical MEMS', *Sens. Actuators Phys.*, vol. 151, no. 2, pp. 95–99, Apr. 2009, doi: 10.1016/j.sna.2009.01.026.
[43] J. Hong, J. Lee, C. K. Hong, and S. E. Shim, 'Effect of dispersion state of carbon nanotube on the thermal conductivity of poly(dimethyl siloxane) composites', *Curr. Appl. Phys.*, vol. 10, no. 1, pp. 359–363, Jan. 2010, doi: 10.1016/j.cap.2009.06.028.
[44] S. P. Forry, D. R. Reyes, M. Gaitan, and L. E. Locascio, 'Facilitating the Culture of Mammalian Nerve Cells with Polyelectrolyte Multilayers', *Langmuir*, vol. 22, no. 13, pp. 5770–5775, Jun. 2006, doi: 10.1021/la053244b.
[45] S. Kuddannaya, J. Bao, and Y. Zhang, 'Enhanced In Vitro Biocompatibility of Chemically Modified Poly(dimethylsiloxane) Surfaces for Stable Adhesion and Long-term Investigation of Brain Cerebral Cortex Cells', *ACS Appl. Mater. Interfaces*, vol. 7, no. 45, pp. 25529–25538, Nov. 2015, doi: 10.1021/acsami.5b09032.
[46] J. N. Lee, X. Jiang, D. Ryan, and G. M. Whitesides, 'Compatibility of Mammalian Cells on Surfaces of Poly(dimethylsiloxane)', *Langmuir*, vol. 20, no. 26, pp. 11684–11691, Dec. 2004, doi: 10.1021/la048562+.
[47] K. M. F. Rossi de Aguiar *et al.*, 'Urethanes PDMS-based: Functional hybrid coatings for metallic dental implants', *Appl. Surf. Sci.*, vol. 484, pp. 1128–1140, Aug. 2019, doi: 10.1016/j.apsusc.2019.04.058.
[48] I. Miranda *et al.*, 'Properties and Applications of PDMS for Biomedical Engineering: A Review', *J. Funct. Biomater.*, vol. 13, no. 1, p. 2, Dec. 2021, doi: 10.3390/jfb13010002.
[49] N. Hijón, M. Manzano, A. J. Salinas, and M. Vallet-Regí, 'Bioactive CaO−SiO2−PDMS Coatings on Ti6Al4V Substrates', *Chem. Mater.*, vol. 17, no. 6, pp. 1591–1596, Mar. 2005, doi: 10.1021/cm048755i.
[50] P. A. Tran, K. Fox, and N. Tran, 'Novel hierarchical tantalum oxide-PDMS hybrid coating for medical implants: One pot synthesis, characterization and modulation of fibroblast proliferation', *J. Colloid Interface Sci.*, vol. 485, pp. 106–115, Jan. 2017, doi: 10.1016/j.jcis.2016.06.048.
[51] J. Barthes *et al.*, 'Biofunctionalization of 3D-printed silicone implants with immunomodulatory hydrogels for controlling the innate immune response: An in vivo model of tracheal defect repair', *Biomaterials*, vol. 268, p. 120549, Jan. 2021, doi: 10.1016/j.biomaterials.2020.120549.
[52] S. Tavakoli, S. Nemati, M. Kharaziha, and S. Akbari-Alavijeh, 'Embedding CuO Nanoparticles in PDMS-SiO2 Coating to Improve Antibacterial Characteristic and Corrosion Resistance', *Colloid Interface Sci. Commun.*, vol. 28, pp. 20–28, Jan. 2019, doi: 10.1016/j.colcom.2018.11.002.
[53] D. S. Lee *et al.*, 'Biocompatibility of a PDMS-coated micro-device: Bladder volume monitoring sensor', *Chin. J. Polym. Sci.*, vol. 30, no. 2, pp. 242–249, Mar. 2012, doi: 10.1007/s10118-012-1119-1.
[54] 'Flexdym Starter Pack - Alternative to PDMS', Eden Tech. Accessed: Nov. 03, 2022. [Online]. Available: https://eden-microfluidics.com/eden-materials/flexdym-pack-alternative-to-pdms/
[55] J. Lachaux *et al.*, 'Thermoplastic elastomer with advanced hydrophilization and bonding performances for rapid (30 s) and easy molding of microfluidic devices', *Lab. Chip*, vol. 17, no. 15, pp. 2581–2594, Jul. 2017, doi: 10.1039/C7LC00488E.
[56] A. H. McMillan, E. K. Thomée, A. Dellaquila, H. Nassman, T. Segura, and S. C. Lesher-Pérez, 'Rapid Fabrication of Membrane-Integrated Thermoplastic Elastomer Microfluidic Devices', *Micromachines*, vol. 11, no. 8, Art. no. 8, Aug. 2020, doi: 10.3390/mi11080731.

[57] J. Lachaux *et al.*, 'Soft Thermoplastic Elastomer for Easy and Rapid Spin-Coating Fabrication of Microfluidic Devices with High Hydrophilization and Bonding Performances', *Adv. Mater. Technol.*, vol. 4, no. 2, p. 1800308, 2019, doi: 10.1002/admt.201800308.
[58] C. F. Natale *et al.*, 'Topographic Cues Impact on Embryonic Stem Cell Zscan4-Metastate', *Front. Bioeng. Biotechnol.*, vol. 8, p. 178, Mar. 2020, doi: 10.3389/fbioe.2020.00178.
[59] 'Nanowizard 3 User Manual'. JPK Instruments, 2012. [Online]. Available: https://www.nanophys.kth.se/nanolab/afm/jpk/manuf-manuals/usermanual.4.2.pdf
[60] R. Ariati, F. Sales, A. Souza, R. A. Lima, and J. Ribeiro, 'Polydimethylsiloxane Composites Characterization and Its Applications: A Review', *Polymers*, vol. 13, no. 23, p. 4258, Dec. 2021, doi: 10.3390/polym13234258.
[61] R. Suriano, C. Credi, M. Levi, and S. Turri, 'AFM nanoscale indentation in air of polymeric and hybrid materials with highly different stiffness', *Appl. Surf. Sci.*, vol. 311, pp. 558–566, Aug. 2014, doi: 10.1016/j.apsusc.2014.05.108.
[62] A. Oláh, H. Hillborg, and G. J. Vancso, 'Hydrophobic recovery of UV/ozone treated poly(dimethylsiloxane): adhesion studies by contact mechanics and mechanism of surface modification', *Appl. Surf. Sci.*, vol. 239, no. 3, pp. 410–423, Jan. 2005, doi: 10.1016/j.apsusc.2004.06.005.
[63] C.-S. Han, S. H. R. Sanei, and F. Alisafaei, 'On the origin of indentation size effects and depth dependent mechanical properties of elastic polymers', *J. Polym. Eng.*, vol. 36, no. 1, pp. 103–111, Jan. 2016, doi: 10.1515/polyeng-2015-0030.
[64] A. Buxboim, K. Rajagopal, A. E. X. Brown, and D. E. Discher, 'How deeply cells feel: methods for thin gels', *J. Phys. Condens. Matter Inst. Phys. J.*, vol. 22, no. 19, p. 194116, May 2010, doi: 10.1088/0953-8984/22/19/194116.
[65] G. K. Toworfe, R. J. Composto, C. S. Adams, I. M. Shapiro, and P. Ducheyne, 'Fibronectin adsorption on surface-activated poly(dimethylsiloxane) and its effect on cellular function', *J. Biomed. Mater. Res. A*, vol. 71A, no. 3, pp. 449–461, 2004, doi: 10.1002/jbm.a.30164.
[66] L. Wang, B. Sun, K. S. Ziemer, G. A. Barabino, and R. L. Carrier, 'Chemical and physical modifications to poly(dimethylsiloxane) surfaces affect adhesion of Caco-2 cells', *J. Biomed. Mater. Res. A*, vol. 93A, no. 4, pp. 1260–1271, 2010, doi: 10.1002/jbm.a.32621.
[67] A. J. García, M. D. Vega, and D. Boettiger, 'Modulation of Cell Proliferation and Differentiation through Substrate-dependent Changes in Fibronectin Conformation', *Mol. Biol. Cell*, vol. 10, no. 3, pp. 785–798, Mar. 1999.
[68] P. Rico, M. Cantini, G. Altankov, and M. Salmerón-Sánchez, 'Matrix Protein Interactions with Synthetic Surfaces', in *Polymers in Regenerative Medicine*, John Wiley & Sons, Ltd, 2014, pp. 91–146. doi: 10.1002/9781118356692.ch3.
[69] M. Ferrari, F. Cirisano, and M. C. Morán, 'Mammalian Cell Behavior on Hydrophobic Substrates: Influence of Surface Properties', *Colloids Interfaces*, vol. 3, no. 2, Art. no. 2, Jun. 2019, doi: 10.3390/colloids3020048.
[70] S. M. Kang and I. S. Choi, 'Control of Cell Adhesion on a Superhydrophobic Surface by Polydopamine Coating', *Bull. Korean Chem. Soc.*, vol. 34, no. 8, pp. 2525–2527, 2013, doi: 10.5012/bkcs.2013.34.8.2525.
[71] G. Altankov, F. Grinnell, and T. Groth, 'Studies on the biocompatibility of materials: Fibroblast reorganization of substratum-bound fibronectin on surfaces varying in wettability', *J. Biomed. Mater. Res.*, vol. 30, no. 3, pp. 385–391, 1996, doi: 10.1002/(SICI)1097-4636(199603)30:3<385::AID-JBM13>3.0.CO;2-J.
[72] A. T. Nguyen, S. R. Sathe, and E. K. F. Yim, 'From nano to micro: topographical scale and its impact on cell adhesion, morphology and contact guidance', *J. Phys. Condens. Matter*, vol. 28, no. 18, p. 183001, Apr. 2016, doi: 10.1088/0953-8984/28/18/183001.
[73] R. G. Flemming, C. J. Murphy, G. A. Abrams, S. L. Goodman, and P. F. Nealey, 'Effects of synthetic micro- and nano-structured surfaces on cell behavior', *Biomaterials*, vol. 20, no. 6, pp. 573–588, Mar. 1999, doi: 10.1016/S0142-9612(98)00209-9.
[74] W. A. Loesberg *et al.*, 'The threshold at which substrate nanogroove dimensions may influence fibroblast alignment and adhesion', *Biomaterials*, vol. 28, no. 27, pp. 3944–3951, Sep. 2007, doi: 10.1016/j.biomaterials.2007.05.030.

[75] B. K. K. Teo *et al.*, ‘Nanotopography Modulates Mechanotransduction of Stem Cells and Induces Differentiation through Focal Adhesion Kinase’, *ACS Nano*, vol. 7, no. 6, pp. 4785–4798, Jun. 2013, doi: 10.1021/nn304966z.
[76] Y. Liu, Y. Ji, K. Ghosh, R. A. F. Clark, L. Huang, and M. H. Rafailovich, ‘Effects of fiber orientation and diameter on the behavior of human dermal fibroblasts on electrospun PMMA scaffolds’, *J. Biomed. Mater. Res. A*, vol. 90A, no. 4, pp. 1092–1106, 2009, doi: 10.1002/jbm.a.32165.
[77] E. Rebollar *et al.*, ‘Proliferation of aligned mammalian cells on laser-nanostructured polystyrene’, *Biomaterials*, vol. 29, no. 12, pp. 1796–1806, Apr. 2008, doi: 10.1016/j.biomaterials.2007.12.039.
[78] L. Ricotti *et al.*, ‘Proliferation and skeletal myotube formation capability of C2C12 and H9c2 cells on isotropic and anisotropic electrospun nanofibrous PHB scaffolds’, *Biomed. Mater.*, vol. 7, no. 3, p. 035010, Apr. 2012, doi: 10.1088/1748-6041/7/3/035010.
[79] C. G. Anene-Nzelu *et al.*, ‘Scalable cell alignment on optical media substrates’, *Biomaterials*, vol. 34, no. 21, pp. 5078–5087, Jul. 2013, doi: 10.1016/j.biomaterials.2013.03.070.
[80] C. Wu *et al.*, ‘Rapid nanomolding of nanotopography on flexible substrates to control muscle cell growth with enhanced maturation’, *Microsyst. Nanoeng.*, vol. 7, p. 89, Nov. 2021, doi: 10.1038/s41378-021-00316-4.
[81] W. Boron and E. L. Boulpaep, *Medical physiology 3rd edition*. Elsevier, 2016. [Online]. Available: https://bookshelf.health.elsevier.com/books/9780323391580
[82] R. L. Lieber and J. Fridén, ‘Functional and clinical significance of skeletal muscle architecture’, *Muscle Nerve*, vol. 23, no. 11, pp. 1647–1666, 2000, doi: 10.1002/1097-4598(200011)23:11<1647::AID-MUS1>3.0.CO;2-M.
[83] D. A. Sleboda, K. K. Stover, and T. J. Roberts, ‘Diversity of extracellular matrix morphology in vertebrate skeletal muscle’, *J. Morphol.*, vol. 281, no. 2, pp. 160–169, Feb. 2020, doi: 10.1002/jmor.21088.
[84] J. R. Sanes, ‘The Basement Membrane/Basal Lamina of Skeletal Muscle *’, *J. Biol. Chem.*, vol. 278, no. 15, pp. 12601–12604, Apr. 2003, doi: 10.1074/jbc.R200027200.
[85] F. Rahimov and L. M. Kunkel, ‘Cellular and molecular mechanisms underlying muscular dystrophy’, *J. Cell Biol.*, vol. 201, no. 4, pp. 499–510, May 2013, doi: 10.1083/jcb.201212142.
[86] H. L. Sweeney and D. W. Hammers, ‘Muscle Contraction’, *Cold Spring Harb. Perspect. Biol.*, vol. 10, no. 2, p. a023200, Feb. 2018, doi: 10.1101/cshperspect.a023200.
[87] E. N. Marieb, ‘The muscular system’, in *Essentials of human anatomy and physiology 11th ed.*, Pearson, 2015, pp. 205–248.
[88] M. Murphy and G. Kardon, ‘Origin of Vertebrate Limb Muscle: The Role of Progenitor and Myoblast Populations’, *Curr. Top. Dev. Biol.*, vol. 96, pp. 1–32, 2011, doi: 10.1016/B978-0-12-385940-2.00001-2.
[89] J. Chal and O. Pourquié, ‘Making muscle: skeletal myogenesis in vivo and in vitro’, *Development*, vol. 144, no. 12, pp. 2104–2122, Jun. 2017, doi: 10.1242/dev.151035.
[90] G. E. Lyons, M. E. Buckingham, and H. G. Mannherz, ‘α-actin proteins and gene transcripts are colocalized in embryonic mouse muscle’, *Development*, vol. 111, no. 2, pp. 451–454, Feb. 1991, doi: 10.1242/dev.111.2.451.
[91] D. A. Sassoon, I. Garner, and M. Buckingham, ‘Transcripts of α-cardiac and α-skeletal actins are early markers for myogenesis in the mouse embryo’, *Development*, vol. 104, no. 1, pp. 155–164, Sep. 1988, doi: 10.1242/dev.104.1.155.
[92] G. E. Lyons, M. Ontell, R. Cox, D. Sassoon, and M. Buckingham, ‘The expression of myosin genes in developing skeletal muscle in the mouse embryo.’, *J. Cell Biol.*, vol. 111, no. 4, pp. 1465–1476, Oct. 1990, doi: 10.1083/jcb.111.4.1465.
[93] F. Babai, J. Musevi-Aghdam, W. Schurch, A. Royal, and G. Gabbiani, ‘Coexpression of α-sarcomeric actin, α-smooth muscle actin and desmin during myogenesis in rat and mouse embryos I. Skeletal muscle’, *Differentiation*, vol. 44, no. 2, pp. 132–142, Aug. 1990, doi: 10.1111/j.1432-0436.1990.tb00546.x.
[94] D. Sieiro-Mosti, M. De La Celle, M. Pelé, and C. Marcelle, ‘A dynamic analysis of muscle fusion in the chick embryo’, *Development*, vol. 141, no. 18, pp. 3605–3611, Sep. 2014, doi: 10.1242/dev.114546.

[95] R. B. White, A.-S. Biérinx, V. F. Gnocchi, and P. S. Zammit, 'Dynamics of muscle fibre growth during postnatal mouse development', *BMC Dev. Biol.*, vol. 10, no. 1, p. 21, Feb. 2010, doi: 10.1186/1471-213X-10-21.
[96] J. Gros, M. Manceau, V. Thomé, and C. Marcelle, 'A common somitic origin for embryonic muscle progenitors and satellite cells', *Nature*, vol. 435, no. 7044, pp. 954–958, Jun. 2005, doi: 10.1038/nature03572.
[97] L. Kassar-Duchossoy, E. Giacone, B. Gayraud-Morel, A. Jory, D. Gomès, and S. Tajbakhsh, 'Pax3/Pax7 mark a novel population of primitive myogenic cells during development', *Genes Dev.*, vol. 19, no. 12, pp. 1426–1431, Jun. 2005, doi: 10.1101/gad.345505.
[98] F. Relaix, D. Rocancourt, A. Mansouri, and M. Buckingham, 'A Pax3/Pax7-dependent population of skeletal muscle progenitor cells', *Nature*, vol. 435, no. 7044, Art. no. 7044, Jun. 2005, doi: 10.1038/nature03594.
[99] K. Shilagardi *et al.*, 'Actin-propelled invasive membrane protrusions promote fusogenic protein engagement during cell-cell fusion', *Science*, vol. 340, no. 6130, pp. 359–363, Apr. 2013, doi: 10.1126/science.1234781.
[100] K. L. Sens *et al.*, 'An invasive podosome-like structure promotes fusion pore formation during myoblast fusion', *J. Cell Biol.*, vol. 191, no. 5, pp. 1013–1027, Nov. 2010, doi: 10.1083/jcb.201006006.
[101] J. H. Kim *et al.*, 'Mechanical Tension Drives Cell Membrane Fusion', *Dev. Cell*, vol. 32, no. 5, pp. 561–573, Mar. 2015, doi: 10.1016/j.devcel.2015.01.005.
[102] J. H. Kim, P. Jin, R. Duan, and E. H. Chen, 'Mechanisms of myoblast fusion during muscle development', *Curr. Opin. Genet. Dev.*, vol. 32, pp. 162–170, Jun. 2015, doi: 10.1016/j.gde.2015.03.006.
[103] S. M. Abmayr and G. K. Pavlath, 'Myoblast fusion: lessons from flies and mice', *Dev. Camb. Engl.*, vol. 139, no. 4, pp. 641–656, Feb. 2012, doi: 10.1242/dev.068353.
[104] S. C. Sampath, S. C. Sampath, and D. P. Millay, 'Myoblast fusion confusion: the resolution begins', *Skelet. Muscle*, vol. 8, p. 3, Jan. 2018, doi: 10.1186/s13395-017-0149-3.
[105] K. Rochlin, S. Yu, S. Roy, and M. K. Baylies, 'Myoblast fusion: When it takes more to make one', *Dev. Biol.*, vol. 341, no. 1, pp. 66–83, May 2010, doi: 10.1016/j.ydbio.2009.10.024.
[106] M. Laurin, N. Fradet, A. Blangy, A. Hall, K. Vuori, and J.-F. Côté, 'The atypical Rac activator Dock180 (Dock1) regulates myoblast fusion in vivo', *Proc. Natl. Acad. Sci. U. S. A.*, vol. 105, no. 40, pp. 15446–15451, Oct. 2008, doi: 10.1073/pnas.0805546105.
[107] P. Seale, L. A. Sabourin, A. Girgis-Gabardo, A. Mansouri, P. Gruss, and M. A. Rudnicki, 'Pax7 Is Required for the Specification of Myogenic Satellite Cells', *Cell*, vol. 102, no. 6, pp. 777–786, Sep. 2000, doi: 10.1016/S0092-8674(00)00066-0.
[108] C. Lepper and C.-M. Fan, 'Inducible lineage tracing of Pax7-descendant cells reveals embryonic origin of adult satellite cells', *Genes. N. Y. N 2000*, vol. 48, no. 7, pp. 424–436, Jul. 2010, doi: 10.1002/dvg.20630.
[109] E. Vasyutina, D. C. Lenhard, and C. Birchmeier, 'Notch function in myogenesis', *Cell Cycle Georget. Tex*, vol. 6, no. 12, pp. 1451–1454, Jun. 2007.
[110] J. Rohwedel *et al.*, 'Formation of postsynaptic-like membranes during differentiation of embryonic stem cells in vitro', *Exp. Cell Res.*, vol. 239, no. 2, pp. 214–225, Mar. 1998, doi: 10.1006/excr.1997.3903.
[111] E. Hirsch, L. Lohikangas, D. Gullberg, S. Johansson, and R. Fässler, 'Mouse myoblasts can fuse and form a normal sarcomere in the absence of beta1 integrin expression', *J. Cell Sci.*, vol. 111 (Pt 16), pp. 2397–2409, Aug. 1998, doi: 10.1242/jcs.111.16.2397.
[112] G. Skoglund, J. Lainé, R. Darabi, E. Fournier, R. Perlingeiro, and N. Tabti, 'Physiological and ultrastructural features of human induced pluripotent and embryonic stem cell-derived skeletal myocytes in vitro', *Proc. Natl. Acad. Sci.*, vol. 111, no. 22, pp. 8275–8280, Jun. 2014, doi: 10.1073/pnas.1322258111.
[113] J. Chal *et al.*, 'Differentiation of pluripotent stem cells to muscle fiber to model Duchenne muscular dystrophy', *Nat. Biotechnol.*, vol. 33, no. 9, Art. no. 9, Sep. 2015, doi: 10.1038/nbt.3297.
[114] S. Schiaffino and C. Reggiani, 'Fiber Types in Mammalian Skeletal Muscles', *Physiol. Rev.*, vol. 91, no. 4, pp. 1447–1531, Oct. 2011, doi: 10.1152/physrev.00031.2010.
[115] S. Ciciliot and S. Schiaffino, 'Regeneration of Mammalian Skeletal Muscle: Basic Mechanisms and Clinical Implications', *Curr. Pharm. Des.*, vol. 16, no. 8, pp. 906–914.

[116] J. G. Tidball, ‘Regulation of muscle growth and regeneration by the immune system’, *Nat. Rev. Immunol.*, vol. 17, no. 3, Art. no. 3, Mar. 2017, doi: 10.1038/nri.2016.150.
[117] E. W. Li, O. C. McKee-Muir, and P. M. Gilbert, ‘Cellular Biomechanics in Skeletal Muscle Regeneration’, *Curr. Top. Dev. Biol.*, vol. 126, pp. 125–176, 2018, doi: 10.1016/bs.ctdb.2017.08.007.
[118] A. Dellavalle *et al.*, ‘Pericytes of human skeletal muscle are myogenic precursors distinct from satellite cells’, *Nat. Cell Biol.*, vol. 9, no. 3, Art. no. 3, Mar. 2007, doi: 10.1038/ncb1542.
[119] M. Schmidt, S. C. Schüler, S. S. Hüttner, B. von Eyss, and J. von Maltzahn, ‘Adult stem cells at work: regenerating skeletal muscle’, *Cell. Mol. Life Sci. CMLS*, vol. 76, no. 13, pp. 2559–2570, Jul. 2019, doi: 10.1007/s00018-019-03093-6.
[120] S. A. Villalta, H. X. Nguyen, B. Deng, T. Gotoh, and J. G. Tidball, ‘Shifts in macrophage phenotypes and macrophage competition for arginine metabolism affect the severity of muscle pathology in muscular dystrophy’, *Hum. Mol. Genet.*, vol. 18, no. 3, pp. 482–496, Feb. 2009, doi: 10.1093/hmg/ddn376.
[121] D. M. D’Souza *et al.*, ‘Diet-induced obesity impairs muscle satellite cell activation and muscle repair through alterations in hepatocyte growth factor signaling’, *Physiol. Rep.*, vol. 3, no. 8, p. e12506, Aug. 2015, doi: 10.14814/phy2.12506.
[122] Y. Wang, M. Wehling-Henricks, G. Samengo, and J. G. Tidball, ‘Increases of M2a macrophages and fibrosis in aging muscle are influenced by bone marrow aging and negatively regulated by muscle-derived nitric oxide’, *Aging Cell*, vol. 14, no. 4, pp. 678–688, Aug. 2015, doi: 10.1111/acel.12350.
[123] C. Lepper, T. A. Partridge, and C.-M. Fan, ‘An absolute requirement for Pax7-positive satellite cells in acute injury-induced skeletal muscle regeneration’, *Dev. Camb. Engl.*, vol. 138, no. 17, pp. 3639–3646, Sep. 2011, doi: 10.1242/dev.067595.
[124] F. Relaix *et al.*, ‘Perspectives on skeletal muscle stem cells’, *Nat. Commun.*, vol. 12, no. 1, Art. no. 1, Jan. 2021, doi: 10.1038/s41467-020-20760-6.
[125] C. Bonnans, J. Chou, and Z. Werb, ‘Remodelling the extracellular matrix in development and disease’, *Nat. Rev. Mol. Cell Biol.*, vol. 15, no. 12, pp. 786–801, Dec. 2014, doi: 10.1038/nrm3904.
[126] T. M. Mirzoev, ‘Mechanotransduction for Muscle Protein Synthesis via Mechanically Activated Ion Channels’, *Life*, vol. 13, no. 2, Art. no. 2, Feb. 2023, doi: 10.3390/life13020341.
[127] G. R. Marcotte, D. W. D. West, and K. Baar, ‘The Molecular Basis for Load-Induced Skeletal Muscle Hypertrophy’, *Calcif. Tissue Int.*, vol. 96, no. 3, pp. 196–210, Mar. 2015, doi: 10.1007/s00223-014-9925-9.
[128] C. A. Goodman, ‘The role of mTORC1 in regulating protein synthesis and skeletal muscle mass in response to various mechanical stimuli’, *Rev. Physiol. Biochem. Pharmacol.*, vol. 166, pp. 43–95, 2014, doi: 10.1007/112_2013_17.
[129] G. R. Adams and M. M. Bamman, ‘Characterization and regulation of mechanical loading-induced compensatory muscle hypertrophy’, *Compr. Physiol.*, vol. 2, no. 4, pp. 2829–2870, Oct. 2012, doi: 10.1002/cphy.c110066.
[130] T. A. Hornberger, D. D. Armstrong, T. J. Koh, T. J. Burkholder, and K. A. Esser, ‘Intracellular signaling specificity in response to uniaxial vs. multiaxial stretch: implications for mechanotransduction’, *Am. J. Physiol. Cell Physiol.*, vol. 288, no. 1, pp. C185-194, Jan. 2005, doi: 10.1152/ajpcell.00207.2004.
[131] Q. Zhang *et al.*, ‘Nesprin-1 and -2 are involved in the pathogenesis of Emery–Dreifuss muscular dystrophy and are critical for nuclear envelope integrity’, *Hum. Mol. Genet.*, vol. 16, no. 23, pp. 2816–2833, Dec. 2007, doi: 10.1093/hmg/ddm238.
[132] M. J. Stroud *et al.*, ‘Nesprin 1α2 is essential for mouse postnatal viability and nuclear positioning in skeletal muscle’, *J. Cell Biol.*, vol. 216, no. 7, pp. 1915–1924, Jul. 2017, doi: 10.1083/jcb.201612128.
[133] M. J. Puckelwartz *et al.*, ‘Disruption of nesprin-1 produces an Emery Dreifuss muscular dystrophy-like phenotype in mice’, *Hum. Mol. Genet.*, vol. 18, no. 4, pp. 607–620, Feb. 2009, doi: 10.1093/hmg/ddn386.
[134] P. Gimpel *et al.*, ‘Nesprin-1α-Dependent Microtubule Nucleation from the Nuclear Envelope via Akap450 Is Necessary for Nuclear Positioning in Muscle Cells’, *Curr. Biol.*, vol. 27, no. 19, pp. 2999-3009.e9, Oct. 2017, doi: 10.1016/j.cub.2017.08.031.

[135] A. Brull, B. Morales Rodriguez, G. Bonne, A. Muchir, and A. T. Bertrand, 'The Pathogenesis and Therapies of Striated Muscle Laminopathies', *Front. Physiol.*, vol. 9, 2018, Accessed: Dec. 21, 2023. [Online]. Available: https://www.frontiersin.org/articles/10.3389/fphys.2018.01533
[136] S. Jabre, W. Hleihel, and C. Coirault, 'Nuclear Mechanotransduction in Skeletal Muscle', *Cells*, vol. 10, no. 2, p. 318, Feb. 2021, doi: 10.3390/cells10020318.
[137] F. Donnaloja, F. Carnevali, E. Jacchetti, and M. T. Raimondi, 'Lamin A/C Mechanotransduction in Laminopathies', *Cells*, vol. 9, no. 5, Art. no. 5, May 2020, doi: 10.3390/cells9051306.
[138] A. Janin and V. Gache, 'Nesprins and Lamins in Health and Diseases of Cardiac and Skeletal Muscles', *Front. Physiol.*, vol. 9, 2018, Accessed: Dec. 21, 2023. [Online]. Available: https://www.frontiersin.org/articles/10.3389/fphys.2018.01277
[139] D. J. Owens *et al.*, 'Lamin Mutations Cause Increased YAP Nuclear Entry in Muscle Stem Cells', *Cells*, vol. 9, no. 4, Art. no. 4, Apr. 2020, doi: 10.3390/cells9040816.
[140] M. Fischer, P. Rikeit, P. Knaus, and C. Coirault, 'YAP-Mediated Mechanotransduction in Skeletal Muscle', *Front. Physiol.*, vol. 7, 2016, Accessed: Nov. 15, 2022. [Online]. Available: https://www.frontiersin.org/articles/10.3389/fphys.2016.00041
[141] C. A. Goodman, J. M. Dietz, B. L. Jacobs, R. M. McNally, J.-S. You, and T. A. Hornberger, 'Yes-Associated Protein is up-regulated by mechanical overload and is sufficient to induce skeletal muscle hypertrophy', *FEBS Lett.*, vol. 589, no. 13, pp. 1491–1497, Jun. 2015, doi: 10.1016/j.febslet.2015.04.047.
[142] K. Schlegelmilch *et al.*, 'Yap1 acts downstream of α-catenin to control epidermal proliferation', *Cell*, vol. 144, no. 5, pp. 782–795, Mar. 2011, doi: 10.1016/j.cell.2011.02.031.
[143] K. I. Watt *et al.*, 'Yap is a novel regulator of C2C12 myogenesis', *Biochem. Biophys. Res. Commun.*, vol. 393, no. 4, pp. 619–624, Mar. 2010, doi: 10.1016/j.bbrc.2010.02.034.
[144] X. Cao, S. L. Pfaff, and F. H. Gage, 'YAP regulates neural progenitor cell number via the TEA domain transcription factor', *Genes Dev.*, vol. 22, no. 23, pp. 3320–3334, Dec. 2008, doi: 10.1101/gad.1726608.
[145] F. D. Camargo *et al.*, 'YAP1 increases organ size and expands undifferentiated progenitor cells', *Curr. Biol. CB*, vol. 17, no. 23, pp. 2054–2060, Dec. 2007, doi: 10.1016/j.cub.2007.10.039.
[146] N. Ibata and E. M. Terentjev, 'Why exercise builds muscles: titin mechanosensing controls skeletal muscle growth under load', *Biophys. J.*, vol. 120, no. 17, pp. 3649–3663, Sep. 2021, doi: 10.1016/j.bpj.2021.07.023.
[147] S. M. Pang, S. Le, and J. Yan, 'Mechanical responses of the mechanosensitive unstructured domains in cardiac titin', *Biol. Cell*, vol. 110, no. 3, pp. 65–76, 2018, doi: 10.1111/boc.201700061.
[148] J. Bogomolovas, A. Gasch, F. Simkovic, D. J. Rigden, S. Labeit, and O. Mayans, 'Titin kinase is an inactive pseudokinase scaffold that supports MuRF1 recruitment to the sarcomeric M-line', *Open Biol.*, vol. 4, no. 5, p. 140041, May 2014, doi: 10.1098/rsob.140041.
[149] T. Benavides Damm and M. Egli, 'Calcium's Role in Mechanotransduction during Muscle Development', *Cell. Physiol. Biochem.*, vol. 33, no. 2, pp. 249–272, Jan. 2014, doi: 10.1159/000356667.
[150] S. Lange *et al.*, 'The kinase domain of titin controls muscle gene expression and protein turnover', *Science*, vol. 308, no. 5728, pp. 1599–1603, Jun. 2005, doi: 10.1126/science.1110463.
[151] E. W. Yeung and D. G. Allen, 'Stretch-Activated Channels in Stretch-Induced Muscle Damage: Role in Muscular Dystrophy', *Clin. Exp. Pharmacol. Physiol.*, vol. 31, no. 8, pp. 551–556, 2004, doi: 10.1111/j.1440-1681.2004.04027.x.
[152] Y. Hirata *et al.*, 'A Piezo1/KLF15/IL-6 axis mediates immobilization-induced muscle atrophy', *J. Clin. Invest.*, vol. 132, no. 10, May 2022, doi: 10.1172/JCI154611.
[153] A. Mauro, 'SATELLITE CELL OF SKELETAL MUSCLE FIBERS', *J. Biophys. Biochem. Cytol.*, vol. 9, no. 2, pp. 493–495, Feb. 1961.
[154] C. A. Collins *et al.*, 'Stem cell function, self-renewal, and behavioral heterogeneity of cells from the adult muscle satellite cell niche', *Cell*, vol. 122, no. 2, pp. 289–301, Jul. 2005, doi: 10.1016/j.cell.2005.05.010.
[155] D. J. Burkin and S. J. Kaufman, 'The alpha7beta1 integrin in muscle development and disease', *Cell Tissue Res.*, vol. 296, no. 1, pp. 183–190, Apr. 1999, doi: 10.1007/s004410051279.
[156] V. Carmignac and M. Durbeej, 'Cell–matrix interactions in muscle disease', *J. Pathol.*, vol. 226, no. 2, pp. 200–218, 2012, doi: 10.1002/path.3020.

[157] P. Kannus *et al.*, 'Location and distribution of non-collagenous matrix proteins in musculoskeletal tissues of rat', *Histochem. J.*, vol. 30, no. 11, pp. 799–810, Nov. 1998, doi: 10.1023/a:1003448106673.
[158] D. Hantaï, J. Labat-Robert, J. A. Grimaud, and M. Fardeau, 'Fibronectin, laminin, type I, III and IV collagens in Duchenne's muscular dystrophy, congenital muscular dystrophies and congenital myopathies: an immunocytochemical study', *Connect. Tissue Res.*, vol. 13, no. 4, pp. 273–281, 1985, doi: 10.3109/03008208509152408.
[159] T. Nishimura, E. Futami, A. Taneichi, T. Mori, and A. Hattori, 'Decorin expression during development of bovine skeletal muscle and its role in morphogenesis of the intramuscular connective tissue', *Cells Tissues Organs*, vol. 171, no. 2–3, pp. 199–214, 2002, doi: 10.1159/000063713.
[160] W. Zhang, Y. Liu, and H. Zhang, 'Extracellular matrix: an important regulator of cell functions and skeletal muscle development', *Cell Biosci.*, vol. 11, no. 1, p. 65, Mar. 2021, doi: 10.1186/s13578-021-00579-4.
[161] S. Yamada, N. Buffinger, J. DiMario, and R. C. Strohman, 'Fibroblast growth factor is stored in fiber extracellular matrix and plays a role in regulating muscle hypertrophy', *Med. Sci. Sports Exerc.*, vol. 21, no. 5 Suppl, pp. S173-180, Oct. 1989.
[162] J. DiMario, N. Buffinger, S. Yamada, and R. C. Strohman, 'Fibroblast growth factor in the extracellular matrix of dystrophic (mdx) mouse muscle', *Science*, vol. 244, no. 4905, pp. 688–690, May 1989, doi: 10.1126/science.2717945.
[163] P. T. Martin, A. J. Ettinger, and J. R. Sanes, 'A synaptic localization domain in the synaptic cleft protein laminin beta 2 (s-laminin)', *Science*, vol. 269, no. 5222, pp. 413–416, Jul. 1995, doi: 10.1126/science.7618109.
[164] E. W. Godfrey and K. S. Gradall, 'Basal lamina molecules are concentrated in myogenic regions of the mouse limb bud', *Anat. Embryol. (Berl.)*, vol. 198, no. 6, pp. 481–486, Dec. 1998, doi: 10.1007/s004290050198.
[165] T. Nishimura, K. Ojima, A. Hattori, and K. Takahashi, 'Developmental expression of extracellular matrix components in intramuscular connective tissue of bovine semitendinosus muscle', *Histochem. Cell Biol.*, vol. 107, no. 3, pp. 215–221, Mar. 1997, doi: 10.1007/s004180050106.
[166] M. A. Chapman, K. Mukund, S. Subramaniam, D. Brenner, and R. L. Lieber, 'Three distinct cell populations express extracellular matrix proteins and increase in number during skeletal muscle fibrosis', *Am. J. Physiol. Cell Physiol.*, vol. 312, no. 2, pp. C131–C143, Feb. 2017, doi: 10.1152/ajpcell.00226.2016.
[167] M. C. Salimena, J. Lagrota-Candido, and T. Quírico-Santos, 'Gender dimorphism influences extracellular matrix expression and regeneration of muscular tissue in mdx dystrophic mice', *Histochem. Cell Biol.*, vol. 122, no. 5, pp. 435–444, Nov. 2004, doi: 10.1007/s00418-004-0707-8.
[168] C. Alexakis, T. Partridge, and G. Bou-Gharios, 'Implication of the satellite cell in dystrophic muscle fibrosis: a self-perpetuating mechanism of collagen overproduction', *Am. J. Physiol.-Cell Physiol.*, vol. 293, no. 2, pp. C661–C669, Aug. 2007, doi: 10.1152/ajpcell.00061.2007.
[169] X. Liu *et al.*, 'Type I collagen promotes the migration and myogenic differentiation of C2C12 myoblasts via the release of interleukin-6 mediated by FAK/NF-κB p65 activation', *Food Funct.*, vol. 11, no. 1, pp. 328–338, Jan. 2020, doi: 10.1039/c9fo01346f.
[170] K. P. Goetsch, K. Kallmeyer, and C. U. Niesler, 'Decorin modulates collagen I-stimulated, but not fibronectin-stimulated, migration of C2C12 myoblasts', *Matrix Biol. J. Int. Soc. Matrix Biol.*, vol. 30, no. 2, pp. 109–117, Mar. 2011, doi: 10.1016/j.matbio.2010.10.009.
[171] A. Ito, M. Yamamoto, K. Ikeda, M. Sato, Y. Kawabe, and M. Kamihira, 'Effects of type IV collagen on myogenic characteristics of IGF-I gene-engineered myoblasts', *J. Biosci. Bioeng.*, vol. 119, no. 5, pp. 596–603, May 2015, doi: 10.1016/j.jbiosc.2014.10.008.
[172] N. Petäjäniemi *et al.*, 'Localization of laminin alpha4-chain in developing and adult human tissues', *J. Histochem. Cytochem. Off. J. Histochem. Soc.*, vol. 50, no. 8, pp. 1113–1130, Aug. 2002, doi: 10.1177/002215540205000813.
[173] K. J. Wilschut, H. P. Haagsman, and B. A. J. Roelen, 'Extracellular matrix components direct porcine muscle stem cell behavior', *Exp. Cell Res.*, vol. 316, no. 3, pp. 341–352, Feb. 2010, doi: 10.1016/j.yexcr.2009.10.014.

[174] J. H. Miner and P. D. Yurchenco, ‘Laminin functions in tissue morphogenesis’, *Annu. Rev. Cell Dev. Biol.*, vol. 20, pp. 255–284, 2004, doi: 10.1146/annurev.cellbio.20.010403.094555.
[175] J. E. Rooney, P. B. Gurpur, and D. J. Burkin, ‘Laminin-111 protein therapy prevents muscle disease in the mdx mouse model for Duchenne muscular dystrophy’, *Proc. Natl. Acad. Sci.*, vol. 106, no. 19, pp. 7991–7996, May 2009, doi: 10.1073/pnas.0811599106.
[176] S. S. Rayagiri *et al.*, ‘Basal lamina remodeling at the skeletal muscle stem cell niche mediates stem cell self-renewal’, *Nat. Commun.*, vol. 9, no. 1, Art. no. 1, Mar. 2018, doi: 10.1038/s41467-018-03425-3.
[177] W. Roman, J. P. Martins, and E. R. Gomes, ‘Local Arrangement of Fibronectin by Myofibroblasts Governs Peripheral Nuclear Positioning in Muscle Cells’, *Dev. Cell*, vol. 46, no. 1, pp. 102-111.e6, Jul. 2018, doi: 10.1016/j.devcel.2018.05.031.
[178] S. Calve and H.-G. Simon, ‘Biochemical and mechanical environment cooperatively regulate skeletal muscle regeneration’, *FASEB J.*, vol. 26, no. 6, pp. 2538–2545, 2012, doi: 10.1096/fj.11-200162.
[179] R. Vaz, G. G. Martins, S. Thorsteinsdóttir, and G. Rodrigues, ‘Fibronectin promotes migration, alignment and fusion in an in vitro myoblast cell model’, *Cell Tissue Res.*, vol. 348, no. 3, pp. 569–578, Jun. 2012, doi: 10.1007/s00441-012-1364-1.
[180] I. Dinulovic, R. Furrer, M. Beer, A. Ferry, B. Cardel, and C. Handschin, ‘Muscle PGC-1α modulates satellite cell number and proliferation by remodeling the stem cell niche’, *Skelet. Muscle*, vol. 6, no. 1, p. 39, Dec. 2016, doi: 10.1186/s13395-016-0111-9.
[181] L. Lukjanenko *et al.*, ‘Loss of fibronectin from the aged stem cell niche affects the regenerative capacity of skeletal muscle in mice’, *Nat. Med.*, vol. 22, no. 8, pp. 897–905, Aug. 2016, doi: 10.1038/nm.4126.
[182] U. R. Goessler, K. Hormann, and F. Riedel, ‘Tissue engineering with adult stem cells in reconstructive surgery (review)’, *Int. J. Mol. Med.*, vol. 15, no. 6, pp. 899–905, Jun. 2005.
[183] B. P. Chan and K. W. Leong, ‘Scaffolding in tissue engineering: general approaches and tissue-specific considerations’, *Eur. Spine J.*, vol. 17, no. Suppl 4, pp. 467–479, Dec. 2008, doi: 10.1007/s00586-008-0745-3.
[184] J. W. Nichol and A. Khademhosseini, ‘Modular Tissue Engineering: Engineering Biological Tissues from the Bottom Up’, *Soft Matter*, vol. 5, no. 7, pp. 1312–1319, 2009, doi: 10.1039/b814285h.
[185] A. Aazmi *et al.*, ‘Biofabrication methods for reconstructing extracellular matrix mimetics’, *Bioact. Mater.*, vol. 31, pp. 475–496, Jan. 2024, doi: 10.1016/j.bioactmat.2023.08.018.
[186] A. R. Namjoo, F. N. Abrbekoh, S. Saghati, H. Amini, M. A. E. Saadatlou, and R. Rahbarghazi, ‘Tissue engineering modalities in skeletal muscles: focus on angiogenesis and immunomodulation properties’, *Stem Cell Res. Ther.*, vol. 14, no. 1, p. 90, Apr. 2023, doi: 10.1186/s13287-023-03310-x.
[187] B. Langridge, M. Griffin, and P. E. Butler, ‘Regenerative medicine for skeletal muscle loss: a review of current tissue engineering approaches’, *J. Mater. Sci. Mater. Med.*, vol. 32, no. 1, p. 15, 2021, doi: 10.1007/s10856-020-06476-5.
[188] S. Mantha *et al.*, ‘Smart Hydrogels in Tissue Engineering and Regenerative Medicine’, *Materials*, vol. 12, no. 20, p. 3323, Oct. 2019, doi: 10.3390/ma12203323.
[189] M. C. Catoira, L. Fusaro, D. Di Francesco, M. Ramella, and F. Boccafoschi, ‘Overview of natural hydrogels for regenerative medicine applications’, *J. Mater. Sci. Mater. Med.*, vol. 30, no. 10, p. 115, Oct. 2019, doi: 10.1007/s10856-019-6318-7.
[190] M. B. Evangelista *et al.*, ‘Upregulation of bone cell differentiation through immobilization within a synthetic extracellular matrix’, *Biomaterials*, vol. 28, no. 25, pp. 3644–3655, Sep. 2007, doi: 10.1016/j.biomaterials.2007.04.028.
[191] Q. T. Nguyen, Y. Hwang, A. C. Chen, S. Varghese, and R. L. Sah, ‘Cartilage-like mechanical properties of poly (ethylene glycol)-diacrylate hydrogels’, *Biomaterials*, vol. 33, no. 28, pp. 6682–6690, Oct. 2012, doi: 10.1016/j.biomaterials.2012.06.005.
[192] J. Comelles, V. Fernández-Majada, N. Berlanga-Navarro, V. Acevedo, K. Paszkowska, and E. Martínez, ‘Microfabrication of poly(acrylamide) hydrogels with independently controlled topography and stiffness’, *Biofabrication*, vol. 12, no. 2, p. 025023, Mar. 2020, doi: 10.1088/1758-5090/ab7552.

[193] L. Vannozzi, I. C. Yasa, H. Ceylan, A. Menciassi, L. Ricotti, and M. Sitti, 'Self-Folded Hydrogel Tubes for Implantable Muscular Tissue Scaffolds', *Macromol. Biosci.*, vol. 18, no. 4, p. 1700377, 2018, doi: 10.1002/mabi.201700377.
[194] D. P. Browe *et al.*, 'Characterization and optimization of actuating poly(ethylene glycol) diacrylate/acrylic acid hydrogels as artificial muscles', *Polymer*, vol. 117, pp. 331–341, May 2017, doi: 10.1016/j.polymer.2017.04.044.
[195] D. Boso *et al.*, 'Porcine Decellularized Diaphragm Hydrogel: A New Option for Skeletal Muscle Malformations', *Biomedicines*, vol. 9, no. 7, p. 709, Jun. 2021, doi: 10.3390/biomedicines9070709.
[196] J. H. Jensen *et al.*, 'Large-scale spontaneous self-organization and maturation of skeletal muscle tissues on ultra-compliant gelatin hydrogel substrates', *Sci. Rep.*, vol. 10, no. 1, Art. no. 1, Aug. 2020, doi: 10.1038/s41598-020-69936-6.
[197] D. Boso, E. Maghin, E. Carraro, M. Giagante, P. Pavan, and M. Piccoli, 'Extracellular Matrix-Derived Hydrogels as Biomaterial for Different Skeletal Muscle Tissue Replacements', *Materials*, vol. 13, no. 11, p. 2483, May 2020, doi: 10.3390/ma13112483.
[198] B. E. Pollot, C. R. Rathbone, J. C. Wenke, and T. Guda, 'Natural polymeric hydrogel evaluation for skeletal muscle tissue engineering', *J. Biomed. Mater. Res. B Appl. Biomater.*, vol. 106, no. 2, pp. 672–679, 2018, doi: 10.1002/jbm.b.33859.
[199] P. Heher *et al.*, 'A novel bioreactor for the generation of highly aligned 3D skeletal muscle-like constructs through orientation of fibrin via application of static strain', *Acta Biomater.*, vol. 24, pp. 251–265, Sep. 2015, doi: 10.1016/j.actbio.2015.06.033.
[200] D. Neal, M. S. Sakar, L.-L. S. Ong, and H. Harry Asada, 'Formation of elongated fascicle-inspired 3D tissues consisting of high-density, aligned cells using sacrificial outer molding', *Lab. Chip*, vol. 14, no. 11, pp. 1907–1916, Jun. 2014, doi: 10.1039/c4lc00023d.
[201] N. Matthias *et al.*, 'Volumetric muscle loss injury repair using in situ fibrin gel cast seeded with muscle-derived stem cells (MDSCs)', *Stem Cell Res.*, vol. 27, pp. 65–73, Mar. 2018, doi: 10.1016/j.scr.2018.01.008.
[202] M. Marcinczyk, H. Elmashhady, M. Talovic, A. Dunn, F. Bugis, and K. Garg, 'Laminin-111 enriched fibrin hydrogels for skeletal muscle regeneration', *Biomaterials*, vol. 141, pp. 233–242, Oct. 2017, doi: 10.1016/j.biomaterials.2017.07.003.
[203] E. Alarcin *et al.*, 'Current Strategies for the Regeneration of Skeletal Muscle Tissue', *Int. J. Mol. Sci.*, vol. 22, no. 11, Art. no. 11, Jan. 2021, doi: 10.3390/ijms22115929.
[204] W. M. Han, M. Mohiuddin, S. E. Anderson, A. J. García, and Y. C. Jang, 'Co-delivery of Wnt7a and muscle stem cells using synthetic bioadhesive hydrogel enhances murine muscle regeneration and cell migration during engraftment', *Acta Biomater.*, vol. 94, pp. 243–252, Aug. 2019, doi: 10.1016/j.actbio.2019.06.025.
[205] A. García-Lizarribar, X. Fernández-Garibay, F. Velasco-Mallorquí, A. G. Castaño, J. Samitier, and J. Ramon-Azcon, 'Composite Biomaterials as Long-Lasting Scaffolds for 3D Bioprinting of Highly Aligned Muscle Tissue', *Macromol. Biosci.*, vol. 18, no. 10, p. 1800167, 2018, doi: 10.1002/mabi.201800167.
[206] A. Fallahi *et al.*, 'Customizable Composite Fibers for Engineering Skeletal Muscle Models', *ACS Biomater. Sci. Eng.*, vol. 6, no. 2, pp. 1112–1123, Feb. 2020, doi: 10.1021/acsbiomaterials.9b00992.
[207] C. Fuoco *et al.*, '3D hydrogel environment rejuvenates aged pericytes for skeletal muscle tissue engineering', *Front. Physiol.*, vol. 5, p. 203, 2014, doi: 10.3389/fphys.2014.00203.
[208] W. Mulyasasmita *et al.*, 'Avidity-controlled hydrogels for injectable co-delivery of induced pluripotent stem cell-derived endothelial cells and growth factors', *J. Control. Release Off. J. Control. Release Soc.*, vol. 191, pp. 71–81, Oct. 2014, doi: 10.1016/j.jconrel.2014.05.015.
[209] S. V. Murphy and A. Atala, '3D bioprinting of tissues and organs', *Nat. Biotechnol.*, vol. 32, no. 8, Art. no. 8, Aug. 2014, doi: 10.1038/nbt.2958.
[210] F. Xu, J. Celli, I. Rizvi, S. Moon, T. Hasan, and U. Demirci, 'A three-dimensional in vitro ovarian cancer coculture model using a high-throughput cell patterning platform', *Biotechnol. J.*, vol. 6, no. 2, pp. 204–212, Feb. 2011, doi: 10.1002/biot.201000340.
[211] V. Mironov, T. Boland, T. Trusk, G. Forgacs, and R. R. Markwald, 'Organ printing: computer-aided jet-based 3D tissue engineering', *Trends Biotechnol.*, vol. 21, no. 4, pp. 157–161, Apr. 2003, doi: 10.1016/S0167-7799(03)00033-7.

[212] X. Zhang and Y. Zhang, 'Tissue Engineering Applications of Three-Dimensional Bioprinting', *Cell Biochem. Biophys.*, vol. 72, no. 3, pp. 777–782, Jul. 2015, doi: 10.1007/s12013-015-0531-x.
[213] S. Derakhshanfar, R. Mbeleck, K. Xu, X. Zhang, W. Zhong, and M. Xing, '3D bioprinting for biomedical devices and tissue engineering: A review of recent trends and advances', *Bioact. Mater.*, vol. 3, no. 2, pp. 144–156, Jun. 2018, doi: 10.1016/j.bioactmat.2017.11.008.
[214] K. K. Thakur, R. Lekurwale, S. Bansode, and R. Pansare, '3D Bioprinting: A Systematic Review for Future Research Direction', *Indian J. Orthop.*, vol. 57, no. 12, pp. 1949–1967, Dec. 2023, doi: 10.1007/s43465-023-01000-7.
[215] W. Lin, H. Shen, J. Fu, and S. Wu, 'Online quality monitoring in material extrusion additive manufacturing processes based on laser scanning technology', *Precis. Eng.*, vol. 60, pp. 76–84, Nov. 2019, doi: 10.1016/j.precisioneng.2019.06.004.
[216] N. Hong, G.-H. Yang, J. Lee, and G. Kim, '3D bioprinting and its in vivo applications', *J. Biomed. Mater. Res. B Appl. Biomater.*, vol. 106, no. 1, pp. 444–459, Jan. 2018, doi: 10.1002/jbm.b.33826.
[217] H. Ma *et al.*, 'Integrated design and fabrication strategies based on bioprinting for skeletal muscle regeneration: Current status and future perspectives', *Mater. Des.*, vol. 225, p. 111591, Jan. 2023, doi: 10.1016/j.matdes.2023.111591.
[218] P. Mozetic, S. M. Giannitelli, M. Gori, M. Trombetta, and A. Rainer, 'Engineering muscle cell alignment through 3D bioprinting', *J. Biomed. Mater. Res. A*, vol. 105, no. 9, pp. 2582–2588, 2017, doi: 10.1002/jbm.a.36117.
[219] M. Costantini *et al.*, 'Microfluidic-enhanced 3D bioprinting of aligned myoblast-laden hydrogels leads to functionally organized myofibers in vitro and in vivo', *Biomaterials*, vol. 131, pp. 98–110, Jul. 2017, doi: 10.1016/j.biomaterials.2017.03.026.
[220] O. Alheib, L. P. da Silva, Y. H. Youn, I. K. Kwon, R. L. Reis, and V. M. Correlo, '3D bioprinting of gellan gum-based hydrogels tethered with laminin-derived peptides for improved cellular behavior', *J. Biomed. Mater. Res. A*, vol. 110, no. 10, pp. 1655–1668, 2022, doi: 10.1002/jbm.a.37415.
[221] L. Ouyang, C. B. Highley, W. Sun, and J. A. Burdick, 'A Generalizable Strategy for the 3D Bioprinting of Hydrogels from Nonviscous Photo-crosslinkable Inks', *Adv. Mater.*, vol. 29, no. 8, p. 1604983, 2017, doi: 10.1002/adma.201604983.
[222] T. Distler, A. A. Solisito, D. Schneidereit, O. Friedrich, R. Detsch, and A. R. Boccaccini, '3D printed oxidized alginate-gelatin bioink provides guidance for C2C12 muscle precursor cell orientation and differentiation via shear stress during bioprinting', *Biofabrication*, vol. 12, no. 4, p. 045005, Jul. 2020, doi: 10.1088/1758-5090/ab98e4.
[223] K. Fakhruddin, M. S. A. Hamzah, and S. I. A. Razak, 'Effects of extrusion pressure and printing speed of 3D bioprinted construct on the fibroblast cells viability', *IOP Conf. Ser. Mater. Sci. Eng.*, vol. 440, no. 1, p. 012042, Oct. 2018, doi: 10.1088/1757-899X/440/1/012042.
[224] W. Kim and G. Kim, '3D bioprinting of functional cell-laden bioinks and its application for cell-alignment and maturation', *Appl. Mater. Today*, vol. 19, p. 100588, Jun. 2020, doi: 10.1016/j.apmt.2020.100588.
[225] W. Arab, S. Rauf, O. Al-Harbi, and C. A. E. Hauser, 'Novel ultrashort self-assembling peptide bioinks for 3D culture of muscle myoblast cells', *Int. J. Bioprinting*, vol. 4, no. 2, p. 129, Jul. 2018, doi: 10.18063/IJB.v4i2.129.
[226] C. Tomasina, T. Bodet, C. Mota, L. Moroni, and S. Camarero-Espinosa, 'Bioprinting Vasculature: Materials, Cells and Emergent Techniques', *Materials*, vol. 12, no. 17, Art. no. 17, Jan. 2019, doi: 10.3390/ma12172701.
[227] Y.-J. Choi *et al.*, 'A 3D cell printed muscle construct with tissue-derived bioink for the treatment of volumetric muscle loss', *Biomaterials*, vol. 206, pp. 160–169, Jun. 2019, doi: 10.1016/j.biomaterials.2019.03.036.
[228] B. Sanz *et al.*, 'Light Cross-Linkable Marine Collagen for Coaxial Printing of a 3D Model of Neuromuscular Junction Formation', *Biomedicines*, vol. 9, no. 1, Art. no. 1, Jan. 2021, doi: 10.3390/biomedicines9010016.
[229] J. H. Kim *et al.*, 'Pd27-10 accelerated innervation of 3d bioprinted muscle construct with pre-fabricated neuromuscular junctions and neurotrophic factor release system', *J. Urol.*, vol. 206, no. Supplement 3, pp. e447–e447, Sep. 2021, doi: 10.1097/JU.0000000000002020.10.

[230] G. H. Yang, W. Kim, J. Kim, and G. Kim, 'A skeleton muscle model using GelMA-based cell-aligned bioink processed with an electric-field assisted 3D/4D bioprinting', *Theranostics*, vol. 11, no. 1, pp. 48–63, Jan. 2021, doi: 10.7150/thno.50794.
[231] M. C. Koetting, J. T. Peters, S. D. Steichen, and N. A. Peppas, 'Stimulus-responsive hydrogels: Theory, modern advances, and applications', *Mater. Sci. Eng. R Rep.*, vol. 93, pp. 1–49, Jul. 2015, doi: 10.1016/j.mser.2015.04.001.
[232] Y.-J. Choi *et al.*, '3D Cell Printing of Functional Skeletal Muscle Constructs Using Skeletal Muscle-Derived Bioink', *Adv. Healthc. Mater.*, vol. 5, no. 20, pp. 2636–2645, 2016, doi: 10.1002/adhm.201600483.
[233] R. Wang, J. Ozsvar, B. Aghaei-Ghareh-Bolagh, M. A. Hiob, S. M. Mithieux, and A. S. Weiss, 'Freestanding hierarchical vascular structures engineered from ice', *Biomaterials*, vol. 192, pp. 334–345, Feb. 2019, doi: 10.1016/j.biomaterials.2018.11.011.
[234] G. Huang *et al.*, 'Functional and Biomimetic Materials for Engineering of the Three-Dimensional Cell Microenvironment', *Chem. Rev.*, vol. 117, no. 20, pp. 12764–12850, Oct. 2017, doi: 10.1021/acs.chemrev.7b00094.
[235] G. Bhattacharjee *et al.*, 'Exploring the potential of microfluidics for next-generation drug delivery systems', *OpenNano*, vol. 12, p. 100150, Jul. 2023, doi: 10.1016/j.onano.2023.100150.
[236] D. G. Rackus, I. H. Riedel-Kruse, and N. Pamme, '"Learning on a chip:" Microfluidics for formal and informal science education', *Biomicrofluidics*, vol. 13, no. 4, p. 041501, Jul. 2019, doi: 10.1063/1.5096030.
[237] W. Sun *et al.*, 'Organ-on-a-Chip for Cancer and Immune Organs Modeling', *Adv. Healthc. Mater.*, vol. 8, no. 4, p. e1801363, Feb. 2019, doi: 10.1002/adhm.201801363.
[238] L. Yin *et al.*, 'Efficient Drug Screening and Nephrotoxicity Assessment on Co-culture Microfluidic Kidney Chip', *Sci. Rep.*, vol. 10, no. 1, Art. no. 1, Apr. 2020, doi: 10.1038/s41598-020-63096-3.
[239] M. Baydoun *et al.*, 'An Interphase Microfluidic Culture System for the Study of Ex Vivo Intestinal Tissue', *Micromachines*, vol. 11, no. 2, p. 150, Jan. 2020, doi: 10.3390/mi11020150.
[240] E. Moradi, S. Jalili-Firoozinezhad, and M. Solati-Hashjin, 'Microfluidic organ-on-a-chip models of human liver tissue', *Acta Biomater.*, vol. 116, pp. 67–83, Oct. 2020, doi: 10.1016/j.actbio.2020.08.041.
[241] T. Leelasattarathkul, S. Liawruangrath, M. Rayanakorn, B. Liawruangrath, W. Oungpipat, and N. Youngvises, 'Greener analytical method for the determination of copper(II) in wastewater by micro flow system with optical sensor', *Talanta*, vol. 72, no. 1, pp. 126–131, Apr. 2007, doi: 10.1016/j.talanta.2006.10.007.
[242] Q. Liu, X. Zhang, Y. Yao, W. Jing, S. Liu, and G. Sui, 'A novel microfluidic module for rapid detection of airborne and waterborne pathogens', *Sens. Actuators B Chem.*, vol. 258, pp. 1138–1145, Apr. 2018, doi: 10.1016/j.snb.2017.11.113.
[243] J. Saez, R. Catalan-Carrio, R. M. Owens, L. Basabe-Desmonts, and F. Benito-Lopez, 'Microfluidics and materials for smart water monitoring: A review', *Anal. Chim. Acta*, vol. 1186, p. 338392, Nov. 2021, doi: 10.1016/j.aca.2021.338392.
[244] I. Oita, H. Halewyck, B. Thys, B. Rombaut, Y. Vander Heyden, and D. Mangelings, 'Microfluidics in macro-biomolecules analysis: macro inside in a nano world', *Anal. Bioanal. Chem.*, vol. 398, no. 1, pp. 239–264, Sep. 2010, doi: 10.1007/s00216-010-3857-7.
[245] O. G. Chavez-Pineda, R. Rodriguez-Moncayo, D. F. Cedillo-Alcantar, P. E. Guevara-Pantoja, J. U. Amador-Hernandez, and J. L. Garcia-Cordero, 'Microfluidic systems for the analysis of blood-derived molecular biomarkers', *ELECTROPHORESIS*, vol. 43, no. 16–17, pp. 1667–1700, 2022, doi: 10.1002/elps.202200067.
[246] Q. Ramadan, M. Alberti, M. Dufva, and Y.-C. Tung, 'Editorial: Medical and Industrial Applications of Microfluidic-Based Cell/Tissue Culture and Organs-on-a-Chip', *Front. Bioeng. Biotechnol.*, vol. 7, p. 151, Jun. 2019, doi: 10.3389/fbioe.2019.00151.
[247] J. P. Martins, G. Torrieri, and H. A. Santos, 'The importance of microfluidics for the preparation of nanoparticles as advanced drug delivery systems', *Expert Opin. Drug Deliv.*, vol. 15, no. 5, pp. 469–479, May 2018, doi: 10.1080/17425247.2018.1446936.
[248] S. T. Sanjay *et al.*, 'Recent advances of controlled drug delivery using microfluidic platforms', *Adv. Drug Deliv. Rev.*, vol. 128, pp. 3–28, Mar. 2018, doi: 10.1016/j.addr.2017.09.013.

[249] T. Rademakers, J. M. Horvath, C. A. van Blitterswijk, and V. L. S. LaPointe, ‘Oxygen and nutrient delivery in tissue engineering: Approaches to graft vascularization’, *J. Tissue Eng. Regen. Med.*, vol. 13, no. 10, pp. 1815–1829, Oct. 2019, doi: 10.1002/term.2932.
[250] V. van Duinen, S. J. Trietsch, J. Joore, P. Vulto, and T. Hankemeier, ‘Microfluidic 3D cell culture: from tools to tissue models’, *Curr. Opin. Biotechnol.*, vol. 35, pp. 118–126, Dec. 2015, doi: 10.1016/j.copbio.2015.05.002.
[251] I. Francis, J. Shrestha, K. R. Paudel, P. M. Hansbro, M. E. Warkiani, and S. C. Saha, ‘Recent advances in lung-on-a-chip models’, *Drug Discov. Today*, vol. 27, no. 9, pp. 2593–2602, Sep. 2022, doi: 10.1016/j.drudis.2022.06.004.
[252] I. Risueño, L. Valencia, J. L. Jorcano, and D. Velasco, ‘Skin-on-a-chip models: General overview and future perspectives’, *APL Bioeng.*, vol. 5, no. 3, p. 030901, Jul. 2021, doi: 10.1063/5.0046376.
[253] L. Amirifar *et al.*, ‘Brain-on-a-chip: Recent advances in design and techniques for microfluidic models of the brain in health and disease’, *Biomaterials*, vol. 285, p. 121531, Jun. 2022, doi: 10.1016/j.biomaterials.2022.121531.
[254] A. Mansoorifar, R. Gordon, R. Bergan, and L. E. Bertassoni, ‘Bone-on-a-chip: microfluidic technologies and microphysiologic models of bone tissue’, *Adv. Funct. Mater.*, vol. 31, no. 6, p. 2006796, Feb. 2021, doi: 10.1002/adfm.202006796.
[255] Z. Peng, L. Zhou, J. K. W. Wong, and Y. K. Chan, ‘Eye-on-a-chip (EOC) models and their role in the future of ophthalmic drug discovery’, *Expert Rev. Ophthalmol.*, vol. 15, no. 5, pp. 259–261, Sep. 2020, doi: 10.1080/17469899.2020.1788388.
[256] M. Abulaiti *et al.*, ‘Establishment of a heart-on-a-chip microdevice based on human iPS cells for the evaluation of human heart tissue function’, *Sci. Rep.*, vol. 10, no. 1, Art. no. 1, Nov. 2020, doi: 10.1038/s41598-020-76062-w.
[257] M. M. Smoak, H. A. Pearce, and A. G. Mikos, ‘Microfluidic Devices for Disease Modeling in Muscle Tissue’, *Biomaterials*, vol. 198, pp. 250–258, Apr. 2019, doi: 10.1016/j.biomaterials.2018.08.059.
[258] F. Akther, P. Little, Z. Li, N.-T. Nguyen, and H. T. Ta, ‘Hydrogels as artificial matrices for cell seeding in microfluidic devices’, *RSC Adv.*, vol. 10, no. 71, pp. 43682–43703, 2020, doi: 10.1039/D0RA08566A.
[259] D.-H. Lee, C. Y. Bae, S. Kwon, and J.-K. Park, ‘User-friendly 3D bioassays with cell-containing hydrogel modules: narrowing the gap between microfluidic bioassays and clinical end-users’ needs’, *Lab. Chip*, vol. 15, no. 11, pp. 2379–2387, Jun. 2015, doi: 10.1039/c5lc00239g.
[260] M. Filippi, T. Buchner, O. Yasa, S. Weirich, and R. K. Katzschmann, ‘Microfluidic Tissue Engineering and Bio-Actuation’, *Adv. Mater.*, vol. 34, no. 23, p. 2108427, 2022, doi: 10.1002/adma.202108427.
[261] R. de Jongh, X. M. Spijkers, S. Pasteuning-Vuhman, P. Vulto, and R. J. Pasterkamp, ‘Neuromuscular junction-on-a-chip: ALS disease modeling and read-out development in microfluidic devices’, *J. Neurochem.*, vol. 157, no. 3, pp. 393–412, 2021, doi: 10.1111/jnc.15289.
[262] R. Visone, M. Gilardi, A. Marsano, M. Rasponi, S. Bersini, and M. Moretti, ‘Cardiac Meets Skeletal: What’s New in Microfluidic Models for Muscle Tissue Engineering’, *Molecules*, vol. 21, no. 9, p. 1128, Aug. 2016, doi: 10.3390/molecules21091128.
[263] R. Atmaramani *et al.*, ‘The Effect of Microfluidic Geometry on Myoblast Migration’, *Micromachines*, vol. 10, no. 2, p. 143, Feb. 2019, doi: 10.3390/mi10020143.
[264] Z. Roveimiab, F. Lin, and J. Anderson, ‘“Microfluidics Studies of the Regulation of Myoblast Migration and Differentiation Behaviour – Possible Application in Wound Healing”’, *FASEB J.*, vol. 35, no. S1, 2021, doi: 10.1096/fasebj.2021.35.S1.03710.
[265] H. N. Roman, D. Juncker, and A.-M. Lauzon, ‘A microfluidic chamber to study the dynamics of muscle-contraction-specific molecular interactions’, *Anal. Chem.*, vol. 87, no. 5, pp. 2582–2587, Mar. 2015, doi: 10.1021/ac503963r.
[266] M. M. Ferreira, R. E. Dewi, and S. C. Heilshorn, ‘Microfluidic analysis of extracellular matrix-bFGF crosstalk on primary human myoblast chemoproliferation, chemokinesis, and chemotaxis’, *Integr. Biol. Quant. Biosci. Nano Macro*, vol. 7, no. 5, pp. 569–579, May 2015, doi: 10.1039/c5ib00060b.
[267] H. Onoe *et al.*, ‘Metre-long cell-laden microfibres exhibit tissue morphologies and functions’, *Nat. Mater.*, vol. 12, no. 6, Art. no. 6, Jun. 2013, doi: 10.1038/nmat3606.

[268] K. Shimizu, H. Araki, K. Sakata, W. Tonomura, M. Hashida, and S. Konishi, 'Microfluidic devices for construction of contractile skeletal muscle microtissues', *J. Biosci. Bioeng.*, vol. 119, no. 2, pp. 212–216, Feb. 2015, doi: 10.1016/j.jbiosc.2014.07.003.
[269] A. Ionescu, E. E. Zahavi, T. Gradus, K. Ben-Yaakov, and E. Perlson, 'Compartmental microfluidic system for studying muscle–neuron communication and neuromuscular junction maintenance', *Eur. J. Cell Biol.*, vol. 95, no. 2, pp. 69–88, Feb. 2016, doi: 10.1016/j.ejcb.2015.11.004.
[270] Y.-T. Li *et al.*, 'Real-time Monitoring of Discrete Synaptic Release Events and Excitatory Potentials within Self-reconstructed Neuromuscular Junctions', *Angew. Chem. Int. Ed.*, vol. 54, no. 32, pp. 9313–9318, 2015, doi: 10.1002/anie.201503801.
[271] J. M. Fernández-Costa, A. Tejedera-Vilafranca, X. Fernández-Garibay, and J. Ramón-Azcón, 'Muscle-on-a-chip devices: a new era for in vitro modelling of muscular dystrophies', *Dis. Model. Mech.*, vol. 16, no. 6, p. dmm050107, Jun. 2023, doi: 10.1242/dmm.050107.
[272] X. Gao, C. Xu, N. Asada, and P. S. Frenette, 'The hematopoietic stem cell niche: from embryo to adult', *Development*, vol. 145, no. 2, p. dev139691, Jan. 2018, doi: 10.1242/dev.139691.
[273] C. A. Chacón-Martínez, J. Koester, and S. A. Wickström, 'Signaling in the stem cell niche: regulating cell fate, function and plasticity', *Development*, vol. 145, no. 15, p. dev165399, Aug. 2018, doi: 10.1242/dev.165399.
[274] A. Raspa and F. Gelain, 'Mimicking Extracellular Matrix via Engineered Nanostructured Biomaterials for Neural Repair', *Curr. Neuropharmacol.*, vol. 19, no. 12, pp. 2110–2124, Dec. 2021, doi: 10.2174/1570159X18666201111111102.
[275] P. Simmons, T. McElroy, and A. R. Allen, 'A Bibliometric Review of Artificial Extracellular Matrices Based on Tissue Engineering Technology Literature: 1990 through 2019', *Materials*, vol. 13, no. 13, p. 2891, Jun. 2020, doi: 10.3390/ma13132891.
[276] J. Nicolas, S. Magli, L. Rabbachin, S. Sampaolesi, F. Nicotra, and L. Russo, '3D Extracellular Matrix Mimics: Fundamental Concepts and Role of Materials Chemistry to Influence Stem Cell Fate', *Biomacromolecules*, vol. 21, no. 6, pp. 1968–1994, Jun. 2020, doi: 10.1021/acs.biomac.0c00045.
[277] F. Z. Volpato, T. Führmann, C. Migliaresi, D. W. Hutmacher, and P. D. Dalton, 'Using extracellular matrix for regenerative medicine in the spinal cord', *Biomaterials*, vol. 34, no. 21, pp. 4945–4955, Jul. 2013, doi: 10.1016/j.biomaterials.2013.03.057.
[278] L. N. Novikova, L. N. Novikov, and J.-O. Kellerth, 'Biopolymers and biodegradable smart implants for tissue regeneration after spinal cord injury', *Curr. Opin. Neurol.*, vol. 16, no. 6, pp. 711–715, Dec. 2003, doi: 10.1097/01.wco.0000102620.38669.3e.
[279] L. A. Struzyna, J. P. Harris, K. S. Katiyar, H. I. Chen, and D. K. Cullen, 'Restoring nervous system structure and function using tissue engineered living scaffolds', *Neural Regen. Res.*, vol. 10, no. 5, pp. 679–685, May 2015, doi: 10.4103/1673-5374.156943.
[280] V. Hidalgo-Alvarez, H. S. Dhowre, O. A. Kingston, C. M. Sheridan, and H. J. Levis, 'Biofabrication of Artificial Stem Cell Niches in the Anterior Ocular Segment', *Bioengineering*, vol. 8, no. 10, Art. no. 10, Oct. 2021, doi: 10.3390/bioengineering8100135.
[281] C. E. Ghezzi, J. Rnjak-Kovacina, and D. L. Kaplan, 'Corneal tissue engineering: recent advances and future perspectives', *Tissue Eng. Part B Rev.*, vol. 21, no. 3, pp. 278–287, Jun. 2015, doi: 10.1089/ten.TEB.2014.0397.
[282] K. Chakrabarty, R. Shetty, and A. Ghosh, 'Corneal cell therapy: with iPSCs, it is no more a far-sight', *Stem Cell Res. Ther.*, vol. 9, no. 1, p. 287, Oct. 2018, doi: 10.1186/s13287-018-1036-5.
[283] C. Matellan and A. E. del Río Hernández, 'Engineering the cellular mechanical microenvironment – from bulk mechanics to the nanoscale', *J. Cell Sci.*, vol. 132, no. 9, p. jcs229013, Apr. 2019, doi: 10.1242/jcs.229013.
[284] S.-Y. Tee, J. Fu, C. S. Chen, and P. A. Janmey, 'Cell Shape and Substrate Rigidity Both Regulate Cell Stiffness', *Biophys. J.*, vol. 100, no. 5, pp. L25–L27, Mar. 2011, doi: 10.1016/j.bpj.2010.12.3744.
[285] P. Tseng and D. Di Carlo, 'Substrates with Patterned Extracellular Matrix and Subcellular Stiffness Gradients Reveal Local Biomechanical Responses', *Adv. Mater.*, vol. 26, no. 8, pp. 1242–1247, 2014, doi: 10.1002/adma.201304607.

[286] M. Quarta *et al.*, 'A bioengineered niche preserves the quiescence of muscle stem cells and enhances their therapeutic efficacy', *Nat. Biotechnol.*, vol. 34, no. 7, pp. 752–759, Jul. 2016, doi: 10.1038/nbt.3576.
[287] M. Pumberger *et al.*, 'Synthetic niche to modulate regenerative potential of MSCs and enhance skeletal muscle regeneration', *Biomaterials*, vol. 99, pp. 95–108, Aug. 2016, doi: 10.1016/j.biomaterials.2016.05.009.
[288] C. McCuller, R. Jessu, and A. L. Callahan, 'Physiology, Skeletal Muscle', in *StatPearls*, Treasure Island (FL): StatPearls Publishing, 2023. Accessed: Dec. 21, 2023. [Online]. Available: http://www.ncbi.nlm.nih.gov/books/NBK537139/
[289] J. Xie, M. R. MacEwan, W. Z. Ray, W. Liu, D. Y. Siewe, and Y. Xia, 'Radially Aligned, Electrospun Nanofibers as Dural Substitutes for Wound Closure and Tissue Regeneration Applications', *ACS Nano*, vol. 4, no. 9, pp. 5027–5036, Sep. 2010, doi: 10.1021/nn101554u.
[290] X. Li *et al.*, 'Effects of aligned and random fibers with different diameter on cell behaviors', *Colloids Surf. B Biointerfaces*, vol. 171, pp. 461–467, Nov. 2018, doi: 10.1016/j.colsurfb.2018.07.045.
[291] J. Xie *et al.*, '"Aligned-to-random" nanofiber scaffolds for mimicking the structure of the tendon-to-bone insertion site', *Nanoscale*, vol. 2, no. 6, pp. 923–926, Jun. 2010, doi: 10.1039/C0NR00192A.
[292] Z. X. Meng, Y. S. Wang, C. Ma, W. Zheng, L. Li, and Y. F. Zheng, 'Electrospinning of PLGA/gelatin randomly-oriented and aligned nanofibers as potential scaffold in tissue engineering', *Mater. Sci. Eng. C*, vol. 30, no. 8, pp. 1204–1210, Oct. 2010, doi: 10.1016/j.msec.2010.06.018.
[293] D. Gupta *et al.*, 'Aligned and random nanofibrous substrate for the in vitro culture of Schwann cells for neural tissue engineering', *Acta Biomater.*, vol. 5, no. 7, pp. 2560–2569, Sep. 2009, doi: 10.1016/j.actbio.2009.01.039.
[294] G. C. Reilly and A. J. Engler, 'Intrinsic extracellular matrix properties regulate stem cell differentiation', *J. Biomech.*, vol. 43, no. 1, pp. 55–62, Jan. 2010, doi: 10.1016/j.jbiomech.2009.09.009.
[295] C. S. Chen, 'Mechanotransduction – a field pulling together?', *J. Cell Sci.*, vol. 121, no. 20, pp. 3285–3292, Oct. 2008, doi: 10.1242/jcs.023507.
[296] S. Gerecht, C. J. Bettinger, Z. Zhang, J. T. Borenstein, G. Vunjak-Novakovic, and R. Langer, 'The effect of actin disrupting agents on contact guidance of human embryonic stem cells', *Biomaterials*, vol. 28, no. 28, pp. 4068–4077, Oct. 2007, doi: 10.1016/j.biomaterials.2007.05.027.
[297] S. H. Lim, X. Y. Liu, H. Song, K. J. Yarema, and H.-Q. Mao, 'The effect of nanofiber-guided cell alignment on the preferential differentiation of neural stem cells', *Biomaterials*, vol. 31, no. 34, pp. 9031–9039, Dec. 2010, doi: 10.1016/j.biomaterials.2010.08.021.
[298] Y. Zhao, H. Zeng, J. Nam, and S. Agarwal, 'Fabrication of Skeletal Muscle Constructs by Topographic Activation of Cell Alignment', *Biotechnol. Bioeng.*, vol. 102, no. 2, p. 10.1002/bit.22080, Feb. 2009, doi: 10.1002/bit.22080.
[299] E. Ko *et al.*, 'Matrix Topography Regulates Synaptic Transmission at the Neuromuscular Junction', *Adv. Sci.*, vol. 6, no. 6, p. 1801521, 2019, doi: 10.1002/advs.201801521.
[300] K. Shimizu, H. Fujita, and E. Nagamori, 'Alignment of skeletal muscle myoblasts and myotubes using linear micropatterned surfaces ground with abrasives', *Biotechnol. Bioeng.*, vol. 103, no. 3, pp. 631–638, 2009, doi: 10.1002/bit.22268.
[301] M. T. Lam, S. Sim, X. Zhu, and S. Takayama, 'The effect of continuous wavy micropatterns on silicone substrates on the alignment of skeletal muscle myoblasts and myotubes', *Biomaterials*, vol. 27, no. 24, pp. 4340–4347, Aug. 2006, doi: 10.1016/j.biomaterials.2006.04.012.
[302] N. F. Huang *et al.*, 'Myotube Assembly on Nanofibrous and Micropatterned Polymers', *Nano Lett.*, vol. 6, no. 3, pp. 537–542, Mar. 2006, doi: 10.1021/nl060060o.
[303] Y.-W. Cheng, D. J. Shiwarski, R. L. Ball, K. A. Whitehead, and A. W. Feinberg, 'Engineering Aligned Skeletal Muscle Tissue Using Decellularized Plant-Derived Scaffolds', *ACS Biomater. Sci. Eng.*, vol. 6, no. 5, pp. 3046–3054, May 2020, doi: 10.1021/acsbiomaterials.0c00058.
[304] C. P. Pennisi, C. G. Olesen, M. de Zee, J. Rasmussen, and V. Zachar, 'Uniaxial cyclic strain drives assembly and differentiation of skeletal myocytes', *Tissue Eng. Part A*, vol. 17, no. 19–20, pp. 2543–2550, Oct. 2011, doi: 10.1089/ten.TEA.2011.0089.

[305] R. Chandran, T. J. Knobloch, M. Anghelina, and S. Agarwal, 'Biomechanical signals upregulate myogenic gene induction in the presence or absence of inflammation', *Am. J. Physiol. Cell Physiol.*, vol. 293, no. 1, pp. C267-276, Jul. 2007, doi: 10.1152/ajpcell.00594.2006.
[306] K. J. M. Boonen, M. L. P. Langelaan, R. B. Polak, D. W. J. van der Schaft, F. P. T. Baaijens, and M. J. Post, 'Effects of a combined mechanical stimulation protocol: Value for skeletal muscle tissue engineering', *J. Biomech.*, vol. 43, no. 8, pp. 1514–1521, May 2010, doi: 10.1016/j.jbiomech.2010.01.039.
[307] P. M. Gilbert *et al.*, 'Substrate elasticity regulates skeletal muscle stem cell self-renewal in culture', *Science*, vol. 329, no. 5995, pp. 1078–1081, Aug. 2010, doi: 10.1126/science.1191035.
[308] H. Safaee *et al.*, 'Tethered Jagged-1 Synergizes with Culture Substrate Stiffness to Modulate Notch-Induced Myogenic Progenitor Differentiation', *Cell. Mol. Bioeng.*, vol. 10, no. 5, pp. 501–513, Oct. 2017, doi: 10.1007/s12195-017-0506-7.
[309] J. S. Silver *et al.*, 'Injury-mediated stiffening persistently activates muscle stem cells through YAP and TAZ mechanotransduction', *Sci. Adv.*, vol. 7, no. 11, p. eabe4501, Mar. 2021, doi: 10.1126/sciadv.abe4501.
[310] L. R. Smith *et al.*, 'Contribution of extracellular matrix components to the stiffness of skeletal muscle contractures in patients with cerebral palsy', *Connect. Tissue Res.*, vol. 62, no. 3, pp. 287–298, May 2021, doi: 10.1080/03008207.2019.1694011.
[311] J. K. Lee, J. M. Link, J. C. Y. Hu, and K. A. Athanasiou, 'The Self-Assembling Process and Applications in Tissue Engineering', *Cold Spring Harb. Perspect. Med.*, vol. 7, no. 11, p. a025668, Nov. 2017, doi: 10.1101/cshperspect.a025668.
[312] G. D. DuRaine, W. E. Brown, J. C. Hu, and K. A. Athanasiou, 'Emergence of Scaffold-free Approaches for Tissue Engineering Musculoskeletal Cartilages', *Ann. Biomed. Eng.*, vol. 43, no. 3, pp. 543–554, Mar. 2015, doi: 10.1007/s10439-014-1161-y.
[313] U. A. Gurkan, V. Kishore, K. W. Condon, T. M. Bellido, and O. Akkus, 'A scaffold-free multicellular three-dimensional in vitro model of osteogenesis', *Calcif. Tissue Int.*, vol. 88, no. 5, pp. 388–401, May 2011, doi: 10.1007/s00223-011-9467-3.
[314] S. Bhumiratana, R. E. Eton, S. R. Oungoulian, L. Q. Wan, G. A. Ateshian, and G. Vunjak-Novakovic, 'Large, stratified, and mechanically functional human cartilage grown in vitro by mesenchymal condensation', *Proc. Natl. Acad. Sci. U. S. A.*, vol. 111, no. 19, p. 6940, May 2014, doi: 10.1073/pnas.1324050111.
[315] K. Nishida *et al.*, 'Functional bioengineered corneal epithelial sheet grafts from corneal stem cells expanded ex vivo on a temperature-responsive cell culture surface', *Transplantation*, vol. 77, no. 3, pp. 379–385, Feb. 2004, doi: 10.1097/01.TP.0000110320.45678.30.
[316] J. C. Hu and K. A. Athanasiou, 'A self-assembling process in articular cartilage tissue engineering', *Tissue Eng.*, vol. 12, no. 4, pp. 969–979, Apr. 2006, doi: 10.1089/ten.2006.12.969.
[317] T. A. Gwyther, J. Z. Hu, K. L. Billiar, and M. W. Rolle, 'Directed Cellular Self-Assembly to Fabricate Cell-Derived Tissue Rings for Biomechanical Analysis and Tissue Engineering', *J. Vis. Exp. JoVE*, no. 57, p. 3366, Nov. 2011, doi: 10.3791/3366.
[318] D. Raghothaman *et al.*, 'Engineering cell matrix interactions in assembled polyelectrolyte fiber hydrogels for mesenchymal stem cell chondrogenesis', *Biomaterials*, vol. 35, no. 9, pp. 2607–2616, Mar. 2014, doi: 10.1016/j.biomaterials.2013.12.008.
[319] G. Ofek, C. M. Revell, J. C. Hu, D. D. Allison, K. J. Grande-Allen, and K. A. Athanasiou, 'Matrix Development in Self-Assembly of Articular Cartilage', *PLOS ONE*, vol. 3, no. 7, p. e2795, Jul. 2008, doi: 10.1371/journal.pone.0002795.
[320] M. L. Manning, R. A. Foty, M. S. Steinberg, and E.-M. Schoetz, 'Coaction of intercellular adhesion and cortical tension specifies tissue surface tension', *Proc. Natl. Acad. Sci.*, vol. 107, no. 28, pp. 12517–12522, Jul. 2010, doi: 10.1073/pnas.1003743107.
[321] R. C. Strohman, E. Bayne, D. Spector, T. Obinata, J. Micou-Eastwood, and A. Maniotis, 'Myogenesis and histogenesis of skeletal muscle on flexible membranes in vitro', *Vitro Cell. Dev. Biol. J. Tissue Cult. Assoc.*, vol. 26, no. 2, pp. 201–208, Feb. 1990, doi: 10.1007/BF02624113.
[322] P. E. Kosnik, J. A. Faulkner, and R. G. Dennis, 'Functional Development of Engineered Skeletal Muscle from Adult and Neonatal Rats', *Tissue Eng.*, vol. 7, no. 5, pp. 573–584, Oct. 2001, doi: 10.1089/107632701753213192.

[323] R. G. Dennis, P. E. Kosnik, M. E. Gilbert, and J. A. Faulkner, ‘Excitability and contractility of skeletal muscle engineered from primary cultures and cell lines’, *Am. J. Physiol.-Cell Physiol.*, vol. 280, no. 2, pp. C288–C295, Feb. 2001, doi: 10.1152/ajpcell.2001.280.2.C288.
[324] M. T. Lam, Y.-C. Huang, R. K. Birla, and S. Takayama, ‘Microfeature guided skeletal muscle tissue engineering for highly organized 3-dimensional free-standing constructs’, *Biomaterials*, vol. 30, no. 6, pp. 1150–1155, Feb. 2009, doi: 10.1016/j.biomaterials.2008.11.014.
[325] H. Takahashi and T. Okano, ‘Cell Sheet-Based Tissue Engineering for Organizing Anisotropic Tissue Constructs Produced Using Microfabricated Thermoresponsive Substrates’, *Adv. Healthc. Mater.*, vol. 4, no. 16, pp. 2388–2407, Nov. 2015, doi: 10.1002/adhm.201500194.
[326] H. Takahashi, T. Shimizu, and T. Okano, ‘Engineered Human Contractile Myofiber Sheets as a Platform for Studies of Skeletal Muscle Physiology’, *Sci. Rep.*, vol. 8, no. 1, Art. no. 1, Sep. 2018, doi: 10.1038/s41598-018-32163-1.
[327] H. Takahashi, T. Shimizu, M. Nakayama, M. Yamato, and T. Okano, ‘The use of anisotropic cell sheets to control orientation during the self-organization of 3D muscle tissue’, *Biomaterials*, vol. 34, no. 30, pp. 7372–7380, Oct. 2013, doi: 10.1016/j.biomaterials.2013.06.033.
[328] E. Nagamori *et al.*, ‘Network formation through active migration of human vascular endothelial cells in a multilayered skeletal myoblast sheet’, *Biomaterials*, vol. 34, no. 3, pp. 662–668, Jan. 2013, doi: 10.1016/j.biomaterials.2012.08.055.
[329] T. X. Ngo *et al.*, ‘Endothelial cell behavior inside myoblast sheets with different thickness’, *Biotechnol. Lett.*, vol. 35, no. 7, pp. 1001–1008, Jul. 2013, doi: 10.1007/s10529-013-1174-x.
[330] M. E. Afshar *et al.*, ‘A 96-well culture platform enables longitudinal analyses of engineered human skeletal muscle microtissue strength’, *Sci. Rep.*, vol. 10, p. 6918, Apr. 2020, doi: 10.1038/s41598-020-62837-8.
[331] M. Ebrahimi *et al.*, ‘De novo revertant fiber formation and therapy testing in a 3D culture model of Duchenne muscular dystrophy skeletal muscle’, *Acta Biomater.*, vol. 132, pp. 227–244, Sep. 2021, doi: 10.1016/j.actbio.2021.05.020.
[332] A. Khodabukus, ‘Tissue-Engineered Skeletal Muscle Models to Study Muscle Function, Plasticity, and Disease’, *Front. Physiol.*, vol. 12, 2021, Accessed: Oct. 20, 2022. [Online]. Available: https://www.frontiersin.org/articles/10.3389/fphys.2021.619710
[333] S. Saporito, C. F. Natale, C. Menna, P. A. Netti, and M. Ventre, ‘A role for nuclear stretching and NPCs changes in the cytoplasmic-nuclear trafficking of YAP: An experimental and numerical modelling approach’, *Mater. Today Bio*, vol. 15, p. 100335, Jun. 2022, doi: 10.1016/j.mtbio.2022.100335.
[334] X. Li *et al.*, ‘A nanostructure platform for live-cell manipulation of membrane curvature’, *Nat. Protoc.*, vol. 14, no. 6, Art. no. 6, Jun. 2019, doi: 10.1038/s41596-019-0161-7.
[335] M. Iannone, M. Ventre, L. Formisano, L. Casalino, E. J. Patriarca, and P. A. Netti, ‘Nanoengineered Surfaces for Focal Adhesion Guidance Trigger Mesenchymal Stem Cell Self-Organization and Tenogenesis’, *Nano Lett.*, vol. 15, no. 3, pp. 1517–1525, Mar. 2015, doi: 10.1021/nl503737k.
[336] V. Coppola, M. Ventre, C. F. Natale, F. Rescigno, and P. A. Netti, ‘On the influence of surface patterning on tissue self-assembly and mechanics’, *J. Tissue Eng. Regen. Med.*, vol. 12, no. 7, pp. 1621–1633, 2018, doi: 10.1002/term.2688.
[337] E. G. Hayman, M. D. Pierschbacher, S. Suzuki, and E. Ruoslahti, ‘Vitronectin—A major cell attachment-promoting protein in fetal bovine serum’, *Exp. Cell Res.*, vol. 160, no. 2, pp. 245–258, Oct. 1985, doi: 10.1016/0014-4827(85)90173-9.
[338] H. Noh and E. A. Vogler, ‘Volumetric Interpretation of Protein Adsorption: Competition from Mixtures and the Vroman Effect’, *Biomaterials*, vol. 28, no. 3, pp. 405–422, Jan. 2007, doi: 10.1016/j.biomaterials.2006.09.006.
[339] M. Volpi, A. Paradiso, M. Costantini, and W. Święszkowski, ‘Hydrogel-Based Fiber Biofabrication Techniques for Skeletal Muscle Tissue Engineering’, *ACS Biomater. Sci. Eng.*, vol. 8, no. 2, pp. 379–405, Feb. 2022, doi: 10.1021/acsbiomaterials.1c01145.
[340] A. M. Almonacid Suarez, M. G. L. Brinker, L. A. Brouwer, I. van der Ham, M. C. Harmsen, and P. van Rijn, ‘Topography-Mediated Myotube and Endothelial Alignment, Differentiation, and Extracellular Matrix Organization for Skeletal Muscle Engineering’, *Polymers*, vol. 12, no. 9, p. 1948, Aug. 2020, doi: 10.3390/polym12091948.

[341] T. Fujii, 'PDMS-based microfluidic devices for biomedical applications', *Microelectron. Eng.*, vol. 61–62, pp. 907–914, Jul. 2002, doi: 10.1016/S0167-9317(02)00494-X.
[342] M. Khabiry and N. Jalili, 'A Microfluidic Platform Containing Sidewall Microgrooves for Cell Positioning and Trapping', *Nanobiomedicine*, vol. 2, p. 4, Jan. 2015, doi: 10.5772/60562.
[343] B. G. Chung, A. Manbachi, and A. Khademhosseini, 'A microfluidic device with groove patterns for studying cellular behavior', *J. Vis. Exp. JoVE*, no. 7, p. 270, 2007, doi: 10.3791/270.
[344] M. M. Smoak and A. G. Mikos, 'Advances in biomaterials for skeletal muscle engineering and obstacles still to overcome', *Mater. Today Bio*, vol. 7, p. 100069, Jun. 2020, doi: 10.1016/j.mtbio.2020.100069.
[345] G. Agrawal, A. Aung, and S. Varghese, 'Skeletal muscle-on-a-chip: an in vitro model to evaluate tissue formation and injury', *Lab. Chip*, vol. 17, no. 20, pp. 3447–3461, Oct. 2017, doi: 10.1039/c7lc00512a.
[346] E. Jastrzebska *et al.*, 'Biological characterization of the modified poly(dimethylsiloxane) surfaces based on cell attachment and toxicity assays', *Biomicrofluidics*, vol. 12, no. 4, p. 044105, Jul. 2018, doi: 10.1063/1.5035176.
[347] J. J. Cunningham, J. Nikolovski, J. J. Linderman, and D. J. Mooney, 'Quantification of fibronectin adsorption to silicone-rubber cell culture substrates', *BioTechniques*, vol. 32, no. 4, pp. 876, 878, 880 passim, Apr. 2002, doi: 10.2144/02324rr05.
[348] Pakstis and Cicerone, 'Optimization of cellular response on flexible surfaces using chemically bound proteins', 2007, [Online]. Available: https://api.semanticscholar.org/CorpusID:55005136
[349] C. F. Natale, M. Ventre, and P. A. Netti, 'Tuning the material-cytoskeleton crosstalk via nanoconfinement of focal adhesions', *Biomaterials*, vol. 35, no. 9, pp. 2743–2751, Mar. 2014, doi: 10.1016/j.biomaterials.2013.12.023.
[350] F. Zampieri, M. Coen, and G. Gabbiani, 'The prehistory of the cytoskeleton concept', *Cytoskeleton*, vol. 71, no. 8, pp. 464–471, 2014, doi: 10.1002/cm.21177.
[351] K. A. Jansen, D. M. Donato, H. E. Balcioglu, T. Schmidt, E. H. J. Danen, and G. H. Koenderink, 'A guide to mechanobiology: Where biology and physics meet', *Biochim. Biophys. Acta BBA - Mol. Cell Res.*, vol. 1853, no. 11, Part B, pp. 3043–3052, Nov. 2015, doi: 10.1016/j.bbamcr.2015.05.007.
[352] M.-F. Carlier, 'Nucleotide hydrolysis regulates the dynamics of actin filaments and microtubules', 1992, doi: 10.1098/rstb.1992.0048.
[353] A. Robert, M. J. Rossow, C. Hookway, S. A. Adam, and V. I. Gelfand, 'Vimentin filament precursors exchange subunits in an ATP-dependent manner', *Proc. Natl. Acad. Sci. U. S. A.*, vol. 112, no. 27, pp. E3505–E3514, Jul. 2015, doi: 10.1073/pnas.1505303112.
[354] G. Ofek, D. C. Wiltz, and K. A. Athanasiou, 'Contribution of the Cytoskeleton to the Compressive Properties and Recovery Behavior of Single Cells', *Biophys. J.*, vol. 97, no. 7, pp. 1873–1882, Oct. 2009, doi: 10.1016/j.bpj.2009.07.050.
[355] C. P. Brangwynne *et al.*, 'Microtubules can bear enhanced compressive loads in living cells because of lateral reinforcement', *J. Cell Biol.*, vol. 173, no. 5, pp. 733–741, Jun. 2006, doi: 10.1083/jcb.200601060.
[356] Y. Li *et al.*, 'Compressive forces stabilize microtubules in living cells', *Nat. Mater.*, vol. 22, no. 7, pp. 913–924, Jul. 2023, doi: 10.1038/s41563-023-01578-1.
[357] P. A. Janmey, U. Euteneuer, P. Traub, and M. Schliwa, 'Viscoelastic properties of vimentin compared with other filamentous biopolymer networks', *J. Cell Biol.*, vol. 113, no. 1, pp. 155–160, Apr. 1991, doi: 10.1083/jcb.113.1.155.
[358] M. Schopferer *et al.*, 'Desmin and Vimentin Intermediate Filament Networks: Their Viscoelastic Properties Investigated by Mechanical Rheometry', *J. Mol. Biol.*, vol. 388, no. 1, pp. 133–143, Apr. 2009, doi: 10.1016/j.jmb.2009.03.005.
[359] C. Storm, J. J. Pastore, F. C. MacKintosh, T. C. Lubensky, and P. A. Janmey, 'Nonlinear elasticity in biological gels', *Nature*, vol. 435, no. 7039, Art. no. 7039, May 2005, doi: 10.1038/nature03521.
[360] A. J. Engler, S. Sen, H. L. Sweeney, and D. E. Discher, 'Matrix Elasticity Directs Stem Cell Lineage Specification', *Cell*, vol. 126, no. 4, pp. 677–689, Aug. 2006, doi: 10.1016/j.cell.2006.06.044.

[361] K. Burridge and E. S. Wittchen, ‘The tension mounts: Stress fibers as force-generating mechanotransducers’, *J. Cell Biol.*, vol. 200, no. 1, pp. 9–19, Jan. 2013, doi: 10.1083/jcb.201210090.
[362] S. Tojkander, G. Gateva, and P. Lappalainen, ‘Actin stress fibers – assembly, dynamics and biological roles’, *J. Cell Sci.*, vol. 125, no. 8, pp. 1855–1864, Apr. 2012, doi: 10.1242/jcs.098087.
[363] D.-H. Kim, A. B. Chambliss, and D. Wirtz, ‘The multi-faceted role of the actin cap in cellular mechanosensation and mechanotransduction’, *Soft Matter*, vol. 9, no. 23, pp. 5516–5523, Jun. 2013, doi: 10.1039/C3SM50798J.
[364] P. Naumanen, P. Lappalainen, and P. Hotulainen, ‘Mechanisms of actin stress fibre assembly’, *J. Microsc.*, vol. 231, no. 3, pp. 446–454, 2008, doi: 10.1111/j.1365-2818.2008.02057.x.
[365] E. Kassianidou and S. Kumar, ‘A biomechanical perspective on stress fiber structure and function’, *Biochim. Biophys. Acta*, vol. 1853, no. 11 0 0, pp. 3065–3074, Nov. 2015, doi: 10.1016/j.bbamcr.2015.04.006.
[366] B. Kovac, J. L. Teo, T. P. Mäkelä, and T. Vallenius, ‘Assembly of non-contractile dorsal stress fibers requires α-actinin-1 and Rac1 in migrating and spreading cells’, *J. Cell Sci.*, vol. 126, no. Pt 1, pp. 263–273, Jan. 2013, doi: 10.1242/jcs.115063.
[367] U. S. Schwarz and M. L. Gardel, ‘United we stand: integrating the actin cytoskeleton and cell-matrix adhesions in cellular mechanotransduction’, *J. Cell Sci.*, vol. 125, no. Pt 13, pp. 3051–3060, Jul. 2012, doi: 10.1242/jcs.093716.
[368] C. Ciobanasu, B. Faivre, and C. Le Clainche, ‘Actomyosin-dependent formation of the mechanosensitive talin–vinculin complex reinforces actin anchoring’, *Nat. Commun.*, vol. 5, no. 1, Art. no. 1, Jan. 2014, doi: 10.1038/ncomms4095.
[369] C. K. Choi, M. Vicente-Manzanares, J. Zareno, L. A. Whitmore, A. Mogilner, and A. R. Horwitz, ‘Actin and α-actinin orchestrate the assembly and maturation of nascent adhesions in a myosin II motor-independent manner’, *Nat. Cell Biol.*, vol. 10, no. 9, pp. 1039–1050, Sep. 2008.
[370] S. Lee and S. Kumar, ‘Actomyosin stress fiber mechanosensing in 2D and 3D’, *F1000Research*, vol. 5, p. F1000 Faculty Rev-2261, Sep. 2016, doi: 10.12688/f1000research.8800.1.
[371] M. Ochsner, M. Textor, V. Vogel, and M. L. Smith, ‘Dimensionality Controls Cytoskeleton Assembly and Metabolism of Fibroblast Cells in Response to Rigidity and Shape’, *PLoS ONE*, vol. 5, no. 3, p. e9445, Mar. 2010, doi: 10.1371/journal.pone.0009445.
[372] F. Rehfeldt *et al.*, ‘Hyaluronic acid matrices show matrix stiffness in 2D and 3D dictates cytoskeletal order and myosin-II phosphorylation within stem cells’, *Integr. Biol. Quant. Biosci. Nano Macro*, vol. 4, no. 4, pp. 422–430, Apr. 2012, doi: 10.1039/c2ib00150k.
[373] F. C. Ho, W. Zhang, Y. Y. Li, and B. P. Chan, ‘Mechanoresponsive, omni-directional and local matrix-degrading actin protrusions in human mesenchymal stem cells microencapsulated in a 3D collagen matrix’, *Biomaterials*, vol. 53, pp. 392–405, Jun. 2015, doi: 10.1016/j.biomaterials.2015.02.102.
[374] J. C. Effler, Y.-S. Kee, J. M. Berk, M. N. Tran, P. A. Iglesias, and D. N. Robinson, ‘Mitosis-Specific Mechanosensing and Contractile Protein Redistribution Control Cell Shape’, *Curr. Biol. CB*, vol. 16, no. 19, pp. 1962–1967, Oct. 2006, doi: 10.1016/j.cub.2006.08.027.
[375] R. Fernandez-Gonzalez, S. de M. Simoes, J.-C. Röper, S. Eaton, and J. A. Zallen, ‘Myosin II dynamics are regulated by tension in intercalating cells’, *Dev. Cell*, vol. 17, no. 5, pp. 736–743, Nov. 2009, doi: 10.1016/j.devcel.2009.09.003.
[376] T. Luo, K. Mohan, P. A. Iglesias, and D. N. Robinson, ‘Molecular mechanisms of cellular mechanosensing’, *Nat. Mater.*, vol. 12, no. 11, pp. 1064–1071, Nov. 2013, doi: 10.1038/nmat3772.
[377] Y. Ren *et al.*, ‘Mechanosensing through cooperative interactions between myosin II and the actin crosslinker cortexillin I’, *Curr. Biol. CB*, vol. 19, no. 17, pp. 1421–1428, Sep. 2009, doi: 10.1016/j.cub.2009.07.018.
[378] C. A. Henderson, C. G. Gomez, S. M. Novak, L. Mi-Mi, and C. C. Gregorio, ‘Overview of the Muscle Cytoskeleton’, *Compr. Physiol.*, vol. 7, no. 3, pp. 891–944, Jun. 2017, doi: 10.1002/cphy.c160033.
[379] H. R. Bergen, K. Ajtai, T. P. Burghardt, A. I. Nepomuceno, and D. C. Muddiman, ‘Mass spectral determination of skeletal/cardiac actin isoform ratios in cardiac muscle’, *Rapid Commun. Mass Spectrom. RCM*, vol. 17, no. 13, pp. 1467–1471, 2003, doi: 10.1002/rcm.1075.

[380] K. Crawford *et al.*, 'Mice Lacking Skeletal Muscle Actin Show Reduced Muscle Strength and Growth Deficits and Die during the Neonatal Period', *Mol. Cell. Biol.*, vol. 22, no. 16, pp. 5887–5896, Aug. 2002, doi: 10.1128/MCB.22.16.5887-5896.2002.
[381] T. C. Hoock, P. M. Newcomb, and I. M. Herman, 'Beta actin and its mRNA are localized at the plasma membrane and the regions of moving cytoplasm during the cellular response to injury.', *J. Cell Biol.*, vol. 112, no. 4, pp. 653–664, Feb. 1991, doi: 10.1083/jcb.112.4.653.
[382] P. Vedula and A. Kashina, 'The makings of the 'actin code': regulation of actin's biological function at the amino acid and nucleotide level', *J. Cell Sci.*, vol. 131, no. 9, p. jcs215509, May 2018, doi: 10.1242/jcs.215509.
[383] T. M. Bunnell, B. J. Burbach, Y. Shimizu, and J. M. Ervasti, 'β-Actin specifically controls cell growth, migration, and the G-actin pool', *Mol. Biol. Cell*, vol. 22, no. 21, pp. 4047–4058, Nov. 2011, doi: 10.1091/mbc.e11-06-0582.
[384] A. R. O'Rourke *et al.*, 'Impaired muscle relaxation and mitochondrial fission associated with genetic ablation of cytoplasmic actin isoforms', *FEBS J.*, vol. 285, no. 3, pp. 481–500, Feb. 2018, doi: 10.1111/febs.14367.
[385] A. K. Peter, H. Cheng, R. S. Ross, K. U. Knowlton, and J. Chen, 'The costamere bridges sarcomeres to the sarcolemma in striated muscle', *Prog. Pediatr. Cardiol.*, vol. 31, no. 2, pp. 83–88, May 2011, doi: 10.1016/j.ppedcard.2011.02.003.
[386] A. Akhmanova and L. C. Kapitein, 'Mechanisms of microtubule organization in differentiated animal cells', *Nat. Rev. Mol. Cell Biol.*, vol. 23, no. 8, Art. no. 8, Aug. 2022, doi: 10.1038/s41580-022-00473-y.
[387] S. Rhee, H. Jiang, C.-H. Ho, and F. Grinnell, 'Microtubule function in fibroblast spreading is modulated according to the tension state of cell–matrix interactions', *Proc. Natl. Acad. Sci. U. S. A.*, vol. 104, no. 13, pp. 5425–5430, Mar. 2007, doi: 10.1073/pnas.0608030104.
[388] A. M. Malek and S. Izumo, 'Mechanism of endothelial cell shape change and cytoskeletal remodeling in response to fluid shear stress', *J. Cell Sci.*, vol. 109 (Pt 4), pp. 713–726, Apr. 1996, doi: 10.1242/jcs.109.4.713.
[389] R. Zhu, S. Antoku, and G. G. Gundersen, 'Centrifugal Displacement of Nuclei Reveals Multiple LINC Complex Mechanisms for Homeostatic Nuclear Positioning', *Curr. Biol. CB*, vol. 27, no. 20, pp. 3097-3110.e5, Oct. 2017, doi: 10.1016/j.cub.2017.08.073.
[390] J. C. Gonçalves, S. Quintremil, J. Yi, and R. B. Vallee, 'Nesprin-2 Recruitment of BicD2 to the Nuclear Envelope Controls Dynein/Kinesin-Mediated Neuronal Migration In Vivo', *Curr. Biol. CB*, vol. 30, no. 16, pp. 3116-3129.e4, Aug. 2020, doi: 10.1016/j.cub.2020.05.091.
[391] S. Taiber *et al.*, 'A Nesprin-4/kinesin-1 cargo model for nuclear positioning in cochlear outer hair cells', *Front. Cell Dev. Biol.*, vol. 10, 2022, Accessed: Dec. 22, 2023. [Online]. Available: https://www.frontiersin.org/articles/10.3389/fcell.2022.974168
[392] M. H. Wilson and E. L. F. Holzbaur, 'Nesprins anchor kinesin-1 motors to the nucleus to drive nuclear distribution in muscle cells', *Development*, vol. 142, no. 1, pp. 218–228, Jan. 2015, doi: 10.1242/dev.114769.
[393] I. Holt *et al.*, 'Nesprin-1-alpha2 associates with kinesin at myotube outer nuclear membranes, but is restricted to neuromuscular junction nuclei in adult muscle', *Sci. Rep.*, vol. 9, no. 1, Art. no. 1, Oct. 2019, doi: 10.1038/s41598-019-50728-6.
[394] M. Mavrakis and M. A. Juanes, 'The compass to follow: Focal adhesion turnover', *Curr. Opin. Cell Biol.*, vol. 80, p. 102152, Feb. 2023, doi: 10.1016/j.ceb.2023.102152.
[395] B. Bance, S. Seetharaman, C. Leduc, B. Boëda, and S. Etienne-Manneville, 'Microtubule acetylation but not detyrosination promotes focal adhesion dynamics and astrocyte migration', *J. Cell Sci.*, vol. 132, no. 7, p. jcs225805, Apr. 2019, doi: 10.1242/jcs.225805.
[396] R. Becker, M. Leone, and F. B. Engel, 'Microtubule Organization in Striated Muscle Cells', *Cells*, vol. 9, no. 6, Art. no. 6, Jun. 2020, doi: 10.3390/cells9061395.
[397] L. Lucas and T. A. Cooper, 'Insights into Cell-Specific Functions of Microtubules in Skeletal Muscle Development and Homeostasis', *Int. J. Mol. Sci.*, vol. 24, no. 3, p. 2903, Feb. 2023, doi: 10.3390/ijms24032903.
[398] M. Azevedo and M. K. Baylies, 'Getting into Position: Nuclear Movement in Muscle Cells', *Trends Cell Biol.*, vol. 30, no. 4, pp. 303–316, Apr. 2020, doi: 10.1016/j.tcb.2020.01.002.
[399] E. Mercuri, C. G. Bönnemann, and F. Muntoni, 'Muscular dystrophies', *Lancet Lond. Engl.*, vol. 394, no. 10213, pp. 2025–2038, Nov. 2019, doi: 10.1016/S0140-6736(19)32910-1.

[400] A. A. Minin and M. V. Moldaver, ‘Intermediate vimentin filaments and their role in intracellular organelle distribution’, *Biochem. Biokhimiia*, vol. 73, no. 13, pp. 1453–1466, Dec. 2008, doi: 10.1134/s0006297908130063.
[401] K. T. Sapra and O. Medalia, ‘Bend, Push, Stretch: Remarkable Structure and Mechanics of Single Intermediate Filaments and Meshworks’, *Cells*, vol. 10, no. 8, p. 1960, Aug. 2021, doi: 10.3390/cells10081960.
[402] J. Block *et al.*, ‘Nonlinear Loading-Rate-Dependent Force Response of Individual Vimentin Intermediate Filaments to Applied Strain’, *Phys. Rev. Lett.*, vol. 118, no. 4, p. 048101, Jan. 2017, doi: 10.1103/PhysRevLett.118.048101.
[403] K. Seltmann, A. W. Fritsch, J. A. Käs, and T. M. Magin, ‘Keratins significantly contribute to cell stiffness and impact invasive behavior’, *Proc. Natl. Acad. Sci. U. S. A.*, vol. 110, no. 46, pp. 18507–18512, Nov. 2013, doi: 10.1073/pnas.1310493110.
[404] L. Ramms *et al.*, ‘Keratins as the main component for the mechanical integrity of keratinocytes’, *Proc. Natl. Acad. Sci. U. S. A.*, vol. 110, no. 46, pp. 18513–18518, Nov. 2013, doi: 10.1073/pnas.1313491110.
[405] E. E. Charrier *et al.*, ‘The desmin network is a determinant of the cytoplasmic stiffness of myoblasts’, *Biol. Cell*, vol. 110, no. 4, pp. 77–90, 2018, doi: 10.1111/boc.201700040.
[406] E. Infante and S. Etienne-Manneville, ‘Intermediate filaments: Integration of cell mechanical properties during migration’, *Front. Cell Dev. Biol.*, vol. 10, 2022, Accessed: Dec. 22, 2023. [Online]. Available: https://www.frontiersin.org/articles/10.3389/fcell.2022.951816
[407] C. De Pascalis *et al.*, ‘Intermediate filaments control collective migration by restricting traction forces and sustaining cell-cell contacts’, *J. Cell Biol.*, vol. 217, no. 9, pp. 3031–3044, Sep. 2018, doi: 10.1083/jcb.201801162.
[408] A.-B. Ndiaye, G. H. Koenderink, and M. Shemesh, ‘Intermediate Filaments in Cellular Mechanoresponsiveness: Mediating Cytoskeletal Crosstalk From Membrane to Nucleus and Back’, *Front. Cell Dev. Biol.*, vol. 10, 2022, Accessed: Dec. 22, 2023. [Online]. Available: https://www.frontiersin.org/articles/10.3389/fcell.2022.882037
[409] M. G. Palmisano *et al.*, ‘Skeletal muscle intermediate filaments form a stress-transmitting and stress-signaling network’, *J. Cell Sci.*, vol. 128, no. 2, pp. 219–224, Jan. 2015, doi: 10.1242/jcs.142463.
[410] K. Wang and R. Ramirez-Mitchell, ‘A network of transverse and longitudinal intermediate filaments is associated with sarcomeres of adult vertebrate skeletal muscle’, *J. Cell Biol.*, vol. 96, no. 2, pp. 562–570, Feb. 1983, doi: 10.1083/jcb.96.2.562.
[411] D. J. Milner, M. Mavroidis, N. Weisleder, and Y. Capetanaki, ‘Desmin Cytoskeleton Linked to Muscle Mitochondrial Distribution and Respiratory Function’, *J. Cell Biol.*, vol. 150, no. 6, pp. 1283–1298, Sep. 2000.
[412] K. Mado, V. Chekulayev, I. Shevchuk, M. Puurand, K. Tepp, and T. Kaambre, ‘On the role of tubulin, plectin, desmin, and vimentin in the regulation of mitochondrial energy fluxes in muscle cells’, *Am. J. Physiol.-Cell Physiol.*, vol. 316, no. 5, pp. C657–C667, May 2019, doi: 10.1152/ajpcell.00303.2018.
[413] M. Hu, Z. Ling, and X. Ren, ‘Extracellular matrix dynamics: tracking in biological systems and their implications’, *J. Biol. Eng.*, vol. 16, no. 1, p. 13, May 2022, doi: 10.1186/s13036-022-00292-x.
[414] B. Yue, ‘Biology of the Extracellular Matrix: An Overview’, *J. Glaucoma*, pp. S20–S23, 2014, doi: 10.1097/IJG.0000000000000108.
[415] A. D. Theocharis, S. S. Skandalis, C. Gialeli, and N. K. Karamanos, ‘Extracellular matrix structure’, *Adv. Drug Deliv. Rev.*, vol. 97, pp. 4–27, Feb. 2016, doi: 10.1016/j.addr.2015.11.001.
[416] C. Frantz, K. M. Stewart, and V. M. Weaver, ‘The extracellular matrix at a glance’, *J. Cell Sci.*, vol. 123, no. 24, pp. 4195–4200, Dec. 2010, doi: 10.1242/jcs.023820.
[417] N. Wight, G. Kinsella, and E. E. QwarnstrGm, ‘The role of proteoglycans in cell adhesion, migration and proliferation’, *Cell Biol.*, pp. 793–801, 1992.
[418] L. Salvatore, N. Gallo, M. L. Natali, A. Terzi, A. Sannino, and M. Madaghiele, ‘Mimicking the Hierarchical Organization of Natural Collagen: Toward the Development of Ideal Scaffolding Material for Tissue Regeneration’, *Front. Bioeng. Biotechnol.*, vol. 9, 2021, Accessed: Dec. 22, 2023. [Online]. Available: https://www.frontiersin.org/articles/10.3389/fbioe.2021.644595

[419] W. Halfter *et al.*, 'The Bi-Functional Organization of Human Basement Membranes', *PLOS ONE*, vol. 8, no. 7, p. e67660, Jul. 2013, doi: 10.1371/journal.pone.0067660.
[420] J. H. Miner, 'The Glomerular Basement Membrane', *Exp. Cell Res.*, vol. 318, no. 9, pp. 973–978, May 2012, doi: 10.1016/j.yexcr.2012.02.031.
[421] P. D. Yurchenco, 'Basement Membranes: Cell Scaffoldings and Signaling Platforms', *Cold Spring Harb. Perspect. Biol.*, vol. 3, no. 2, p. a004911, Feb. 2011, doi: 10.1101/cshperspect.a004911.
[422] K. P. Campbell and J. T. Stull, 'Skeletal Muscle Basement Membrane-Sarcolemma-Cytoskeleton Interaction Minireview Series', *J. Biol. Chem.*, vol. 278, no. 15, pp. 12599–12600, Apr. 2003, doi: 10.1074/jbc.R300005200.
[423] J. E. Murphy-Ullrich and E. H. Sage, 'Revisiting the matricellular concept', *Matrix Biol. J. Int. Soc. Matrix Biol.*, vol. 37, pp. 1–14, Jul. 2014, doi: 10.1016/j.matbio.2014.07.005.
[424] B. Li, C. Moshfegh, Z. Lin, J. Albuschies, and V. Vogel, 'Mesenchymal Stem Cells Exploit Extracellular Matrix as Mechanotransducer', *Sci. Rep.*, vol. 3, no. 1, Art. no. 1, Aug. 2013, doi: 10.1038/srep02425.
[425] R. A. F. Clark, J. M. Lanigan, P. DellaPelle, E. Manseau, H. F. Dvorak, and R. B. Colvin, 'Fibronectin and Fibrin Provide a Provisional Matrix for Epidermal Cell Migration During Wound Reepithelialization', *J. Invest. Dermatol.*, vol. 79, no. 5, pp. 264–269, Nov. 1982, doi: 10.1111/1523-1747.ep12500075.
[426] T. Guo, C. He, A. Venado, and Y. Zhou, 'Extracellular Matrix Stiffness in Lung Health and Disease', *Compr. Physiol.*, vol. 12, no. 3, pp. 3523–3558, Jun. 2022, doi: 10.1002/cphy.c210032.
[427] K. R. Levental *et al.*, 'Matrix Crosslinking Forces Tumor Progression by Enhancing Integrin signaling', *Cell*, vol. 139, no. 5, pp. 891–906, Nov. 2009, doi: 10.1016/j.cell.2009.10.027.
[428] O. Chaudhuri *et al.*, 'Extracellular matrix stiffness and composition jointly regulate the induction of malignant phenotypes in mammary epithelium', *Nat. Mater.*, vol. 13, no. 10, Art. no. 10, Oct. 2014, doi: 10.1038/nmat4009.
[429] X. Di *et al.*, 'Cellular mechanotransduction in health and diseases: from molecular mechanism to therapeutic targets', *Signal Transduct. Target. Ther.*, vol. 8, p. 282, Jul. 2023, doi: 10.1038/s41392-023-01501-9.
[430] J. H. Wang and B. Li, 'Mechanics rules cell biology', *BMC Sports Sci. Med. Rehabil.*, vol. 2, no. 1, p. 16, Jul. 2010, doi: 10.1186/1758-2555-2-16.
[431] V. Gensbittel, M. Kräter, S. Harlepp, I. Busnelli, J. Guck, and J. G. Goetz, 'Mechanical Adaptability of Tumor Cells in Metastasis', *Dev. Cell*, vol. 56, no. 2, pp. 164–179, Jan. 2021, doi: 10.1016/j.devcel.2020.10.011.
[432] B. Piersma, M.-K. Hayward, and V. M. Weaver, 'Fibrosis and cancer: A strained relationship', *Biochim. Biophys. Acta Rev. Cancer*, vol. 1873, no. 2, p. 188356, Apr. 2020, doi: 10.1016/j.bbcan.2020.188356.
[433] W. Zhang, S. Zhang, W. Zhang, Y. Yue, W. Qian, and Z. Wang, 'Matrix stiffness and its influence on pancreatic diseases', *Biochim. Biophys. Acta Rev. Cancer*, vol. 1876, no. 1, p. 188583, Aug. 2021, doi: 10.1016/j.bbcan.2021.188583.
[434] S. van Putten, Y. Shafieyan, and B. Hinz, 'Mechanical control of cardiac myofibroblasts', *J. Mol. Cell. Cardiol.*, vol. 93, pp. 133–142, Apr. 2016, doi: 10.1016/j.yjmcc.2015.11.025.
[435] C. Júnior *et al.*, 'Baseline Stiffness Modulates the Non-Linear Response to Stretch of the Extracellular Matrix in Pulmonary Fibrosis', *Int. J. Mol. Sci.*, vol. 22, no. 23, p. 12928, Nov. 2021, doi: 10.3390/ijms222312928.
[436] W. S. Leong *et al.*, 'Thickness sensing of hMSCs on collagen gel directs stem cell fate', *Biochem. Biophys. Res. Commun.*, vol. 401, no. 2, pp. 287–292, Oct. 2010, doi: 10.1016/j.bbrc.2010.09.052.
[437] J. P. Winer, S. Oake, and P. A. Janmey, 'Non-Linear Elasticity of Extracellular Matrices Enables Contractile Cells to Communicate Local Position and Orientation', *PLOS ONE*, vol. 4, no. 7, p. e6382, Jul. 2009, doi: 10.1371/journal.pone.0006382.
[438] X. Ma *et al.*, 'Fibers in the Extracellular Matrix Enable Long-Range Stress Transmission between Cells', *Biophys. J.*, vol. 104, no. 7, pp. 1410–1418, Apr. 2013, doi: 10.1016/j.bpj.2013.02.017.
[439] Q. Wen and P. A. Janmey, 'Effects of nonlinearity on cell-ECM interactions', *Exp. Cell Res.*, vol. 319, no. 16, pp. 2481–2489, Oct. 2013, doi: 10.1016/j.yexcr.2013.05.017.

[440] I. K. Piechocka, R. G. Bacabac, M. Potters, F. C. MacKintosh, and G. H. Koenderink, 'Structural Hierarchy Governs Fibrin Gel Mechanics', *Biophys. J.*, vol. 98, no. 10, pp. 2281–2289, May 2010, doi: 10.1016/j.bpj.2010.01.040.
[441] K. A. Jansen, R. G. Bacabac, I. K. Piechocka, and G. H. Koenderink, 'Cells actively stiffen fibrin networks by generating contractile stress', *Biophys. J.*, vol. 105, no. 10, pp. 2240–2251, Nov. 2013, doi: 10.1016/j.bpj.2013.10.008.
[442] F. Grinnell, 'Fibroblast biology in three-dimensional collagen matrices', *Trends Cell Biol.*, vol. 13, no. 5, pp. 264–269, May 2003, doi: 10.1016/S0962-8924(03)00057-6.
[443] A. K. Yip *et al.*, 'Cellular response to substrate rigidity is governed by either stress or strain', *Biophys. J.*, vol. 104, no. 1, pp. 19–29, Jan. 2013, doi: 10.1016/j.bpj.2012.11.3805.
[444] V. Ottani, D. Martini, M. Franchi, A. Ruggeri, and M. Raspanti, 'Hierarchical structures in fibrillar collagens', *Micron Oxf. Engl. 1993*, vol. 33, no. 7–8, pp. 587–596, 2002, doi: 10.1016/s0968-4328(02)00033-1.
[445] Z. Yang, I. Mochalkin, and R. F. Doolittle, 'A model of fibrin formation based on crystal structures of fibrinogen and fibrin fragments complexed with synthetic peptides', *Proc. Natl. Acad. Sci.*, vol. 97, no. 26, pp. 14156–14161, Dec. 2000, doi: 10.1073/pnas.97.26.14156.
[446] E. Klotzsch *et al.*, 'Fibronectin forms the most extensible biological fibers displaying switchable force-exposed cryptic binding sites', *Proc. Natl. Acad. Sci.*, vol. 106, no. 43, pp. 18267–18272, Oct. 2009, doi: 10.1073/pnas.0907518106.
[447] J. Sun *et al.*, 'Exploring Cellular Contact Guidance Using Gradient Nanogratings', *Biomacromolecules*, vol. 11, no. 11, pp. 3067–3072, Nov. 2010, doi: 10.1021/bm100883m.
[448] I. A. Janson and A. J. Putnam, 'Extracellular matrix elasticity and topography: material-based cues that affect cell function via conserved mechanisms', *J. Biomed. Mater. Res. A*, vol. 103, no. 3, pp. 1246–1258, Mar. 2015, doi: 10.1002/jbm.a.35254.
[449] V. Brunetti *et al.*, 'Neurons sense nanoscale roughness with nanometer sensitivity', *Proc. Natl. Acad. Sci.*, vol. 107, no. 14, pp. 6264–6269, Apr. 2010, doi: 10.1073/pnas.0914456107.
[450] W. Chen, Y. Sun, and J. Fu, 'Microfabricated Nanotopological Surfaces for Study of Adhesion-dependent Cell mechanosensitivity**', *Small Weinh. Bergstr. Ger.*, vol. 9, no. 1, pp. 81–89, Jan. 2013, doi: 10.1002/smll.201201098.
[451] M. J. Dalby *et al.*, 'The control of human mesenchymal cell differentiation using nanoscale symmetry and disorder', *Nat. Mater.*, vol. 6, no. 12, Art. no. 12, Dec. 2007, doi: 10.1038/nmat2013.
[452] M. Arnold *et al.*, 'Activation of integrin function by nanopatterned adhesive interfaces', *Chemphyschem Eur. J. Chem. Phys. Phys. Chem.*, vol. 5, no. 3, pp. 383–388, Mar. 2004, doi: 10.1002/cphc.200301014.
[453] E. A. Cavalcanti-Adam, T. Volberg, A. Micoulet, H. Kessler, B. Geiger, and J. P. Spatz, 'Cell Spreading and Focal Adhesion Dynamics Are Regulated by Spacing of Integrin Ligands', *Biophys. J.*, vol. 92, no. 8, pp. 2964–2974, Apr. 2007, doi: 10.1529/biophysj.106.089730.
[454] A. Ballo, H. Agheli, J. Lausmaa, P. Thomsen, and S. Petronis, 'Nanostructured model implants for in vivo studies: influence of well-defined nanotopography on de novo bone formation on titanium implants', *Int. J. Nanomedicine*, vol. 6, pp. 3415–3428, 2011, doi: 10.2147/IJN.S25867.
[455] C. A. Lemarié, P.-L. Tharaux, and S. Lehoux, 'Extracellular matrix alterations in hypertensive vascular remodeling', *J. Mol. Cell. Cardiol.*, vol. 48, no. 3, pp. 433–439, Mar. 2010, doi: 10.1016/j.yjmcc.2009.09.018.
[456] A. Leychenko, E. Konorev, M. Jijiwa, and M. L. Matter, 'Stretch-Induced Hypertrophy Activates NFkB-Mediated VEGF Secretion in Adult Cardiomyocytes', *PLOS ONE*, vol. 6, no. 12, p. e29055, Dec. 2011, doi: 10.1371/journal.pone.0029055.
[457] A. Tijore *et al.*, 'Selective killing of transformed cells by mechanical stretch', *Biomaterials*, vol. 275, p. 120866, Aug. 2021, doi: 10.1016/j.biomaterials.2021.120866.
[458] S. Albinsson, A. Bhattachariya, and P. Hellstrand, 'Stretch-dependent smooth muscle differentiation in the portal vein-role of actin polymerization, calcium signaling, and microRNAs', *Microcirc. N. Y. N 1994*, vol. 21, no. 3, pp. 230–238, Apr. 2014, doi: 10.1111/micc.12106.
[459] J. Opplert and N. Babault, 'Acute Effects of Dynamic Stretching on Muscle Flexibility and Performance: An Analysis of the Current Literature', *Sports Med. Auckl. NZ*, vol. 48, no. 2, pp. 299–325, Feb. 2018, doi: 10.1007/s40279-017-0797-9.

[460] J. Rysä, H. Tokola, and H. Ruskoaho, ‘Mechanical stretch induced transcriptomic profiles in cardiac myocytes’, *Sci. Rep.*, vol. 8, no. 1, Art. no. 1, Mar. 2018, doi: 10.1038/s41598-018-23042-w.
[461] X. Gao *et al.*, ‘Physiological stretch induced proliferation of human urothelial cells via integrin α6-FAK signaling pathway’, *Neurourol. Urodyn.*, vol. 37, no. 7, pp. 2114–2120, Sep. 2018, doi: 10.1002/nau.23572.
[462] P. K. Purohit and D. H. Smith, ‘A model for stretch growth of neurons’, *J. Biomech.*, vol. 49, no. 16, pp. 3934–3942, Dec. 2016, doi: 10.1016/j.jbiomech.2016.11.045.
[463] J. R. Loverde, R. E. Tolentino, P. Soteropoulos, and B. J. Pfister, ‘Biomechanical Forces Regulate Gene Transcription During Stretch-Mediated Growth of Mammalian Neurons’, *Front. Neurosci.*, vol. 14, p. 600136, Dec. 2020, doi: 10.3389/fnins.2020.600136.
[464] Th. Förster, ‘Zwischenmolekulare Energiewanderung und Fluoreszenz’, *Ann. Phys.*, vol. 437, no. 1–2, pp. 55–75, 1948, doi: 10.1002/andp.19484370105.
[465] Th. Forster, ‘Energiewanderung und Fluoreszenz’, *Naturwissenschaften*, vol. 33, no. 6, pp. 166–175, Jun. 1946, doi: 10.1007/BF00585226.
[466] X. Zhang *et al.*, ‘FÖrster resonance energy transfer (FRET)-based biosensors for biological applications’, *Biosens. Bioelectron.*, vol. 138, p. 111314, Aug. 2019, doi: 10.1016/j.bios.2019.05.019.
[467] B. T. Bajar, E. S. Wang, S. Zhang, M. Z. Lin, and J. Chu, ‘A Guide to Fluorescent Protein FRET Pairs’, *Sensors*, vol. 16, no. 9, p. 1488, Sep. 2016, doi: 10.3390/s16091488.
[468] D. W. Piston and G.-J. Kremers, ‘Fluorescent protein FRET: the good, the bad and the ugly’, *Trends Biochem. Sci.*, vol. 32, no. 9, pp. 407–414, Sep. 2007, doi: 10.1016/j.tibs.2007.08.003.
[469] J. S. Lindsey, M. Taniguchi, D. F. Bocian, and D. Holten, ‘The fluorescence quantum yield parameter in Förster resonance energy transfer (FRET)—Meaning, misperception, and molecular design’, *Chem. Phys. Rev.*, vol. 2, no. 1, p. 011302, Mar. 2021, doi: 10.1063/5.0041132.
[470] R. Heim and R. Y. Tsien, ‘Engineering green fluorescent protein for improved brightness, longer wavelengths and fluorescence resonance energy transfer’, *Curr. Biol. CB*, vol. 6, no. 2, pp. 178–182, Feb. 1996, doi: 10.1016/s0960-9822(02)00450-5.
[471] A. J. Lam *et al.*, ‘Improving FRET dynamic range with bright green and red fluorescent proteins’, *Nat. Methods*, vol. 9, no. 10, pp. 1005–1012, Oct. 2012, doi: 10.1038/nmeth.2171.
[472] H. Tsutsui, S. Karasawa, Y. Okamura, and A. Miyawaki, ‘Improving membrane voltage measurements using FRET with new fluorescent proteins’, *Nat. Methods*, vol. 5, no. 8, pp. 683–685, Aug. 2008, doi: 10.1038/nmeth.1235.
[473] H. Kawai *et al.*, ‘Simultaneous real-time detection of initiator- and effector-caspase activation by double fluorescence resonance energy transfer analysis’, *J. Pharmacol. Sci.*, vol. 97, no. 3, pp. 361–368, Mar. 2005, doi: 10.1254/jphs.fp0040592.
[474] B. George Abraham, K. S. Sarkisyan, A. S. Mishin, V. Santala, N. V. Tkachenko, and M. Karp, ‘Fluorescent Protein Based FRET Pairs with Improved Dynamic Range for Fluorescence Lifetime Measurements’, *PLoS ONE*, vol. 10, no. 8, p. e0134436, Aug. 2015, doi: 10.1371/journal.pone.0134436.
[475] M. Ouyang *et al.*, ‘Simultaneous visualization of protumorigenic Src and MT1-MMP activities with fluorescence resonance energy transfer’, *Cancer Res.*, vol. 70, no. 6, pp. 2204–2212, Mar. 2010, doi: 10.1158/0008-5472.CAN-09-3698.
[476] D. M. Grant *et al.*, ‘Multiplexed FRET to image multiple signaling events in live cells’, *Biophys. J.*, vol. 95, no. 10, pp. L69-71, Nov. 2008, doi: 10.1529/biophysj.108.139204.
[477] Y. Sun, H. Wallrabe, C. F. Booker, R. N. Day, and A. Periasamy, ‘Three-Color Spectral FRET Microscopy Localizes Three Interacting Proteins in Living Cells’, *Biophys. J.*, vol. 99, no. 4, pp. 1274–1283, Aug. 2010, doi: 10.1016/j.bpj.2010.06.004.
[478] A. D. Hoppe, B. L. Scott, T. P. Welliver, S. W. Straight, and J. A. Swanson, ‘N-way FRET microscopy of multiple protein-protein interactions in live cells’, *PloS One*, vol. 8, no. 6, p. e64760, 2013, doi: 10.1371/journal.pone.0064760.
[479] A. N. Bader, E. G. Hofman, J. Voortman, P. M. P. van B. en Henegouwen, and H. C. Gerritsen, ‘Homo-FRET imaging enables quantification of protein cluster sizes with subcellular resolution’, *Biophys. J.*, vol. 97, no. 9, pp. 2613–2622, Nov. 2009, doi: 10.1016/j.bpj.2009.07.059.

[480] A. Pietraszewska-Bogiel and T. W. J. Gadella, ‘FRET microscopy: from principle to routine technology in cell biology’, *J. Microsc.*, vol. 241, no. 2, pp. 111–118, Feb. 2011, doi: 10.1111/j.1365-2818.2010.03437.x.
[481] F. Meng, T. M. Suchyna, and F. Sachs, ‘A fluorescence energy transfer-based mechanical stress sensor for specific proteins in situ’, *FEBS J.*, vol. 275, no. 12, pp. 3072–3087, Jun. 2008, doi: 10.1111/j.1742-4658.2008.06461.x.
[482] F. Meng and F. Sachs, ‘Visualizing dynamic cytoplasmic forces with a compliance-matched FRET sensor’, *J. Cell Sci.*, vol. 124, no. 2, pp. 261–269, Jan. 2011, doi: 10.1242/jcs.071928.
[483] J. Wang *et al.*, ‘Observations of intracellular tension dynamics of MC3T3-E1 cells during substrate adhesion using a FRET-based actinin tension sensor’, *J. Biomech. Sci. Eng.*, vol. 11, no. 4, pp. 16-00504-16–00504, 2016, doi: 10.1299/jbse.16-00504.
[484] J. Wang, S. Sugita, T. Michiue, T. Tsuboi, T. Kitaguchi, and T. Matsumoto, ‘A novel FRET analysis method for tension dynamics in a single actin stress fiber: Application to MC3T3-E1 cells during movement on a substrate’, *J. Biorheol.*, vol. 33, no. 1, pp. 21–26, 2019, doi: 10.17106/jbr.33.21.
[485] D. C. Youvan, C. M. Silva, E. J. Bylina, W. J. Coleman, M. R. Dilworth, and M. M. Yang, ‘Calibration of fluorescence resonance energy transfer in microscopy’, US6661909B2, Dec. 09, 2003 Accessed: Dec. 22, 2023. [Online]. Available: https://patents.google.com/patent/US6661909B2/en
[486] J. van Rheenen, M. Langeslag, and K. Jalink, ‘Correcting Confocal Acquisition to Optimize Imaging of Fluorescence Resonance Energy Transfer by Sensitized Emission’, *Biophys. J.*, vol. 86, no. 4, pp. 2517–2529, Apr. 2004.
[487] L. Tyas, V. A. Brophy, A. Pope, A. J. Rivett, and J. M. Tavaré, ‘Rapid caspase-3 activation during apoptosis revealed using fluorescence-resonance energy transfer’, *EMBO Rep.*, vol. 1, no. 3, pp. 266–270, Sep. 2000, doi: 10.1093/embo-reports/kvd050.
[488] J. QIAN, B. YAO, and C. WU, ‘Fluorescence resonance energy transfer detection methods: Sensitized emission and acceptor bleaching’, *Exp. Ther. Med.*, vol. 8, no. 5, pp. 1375–1380, Nov. 2014, doi: 10.3892/etm.2014.1928.
[489] E. L. Snapp and R. S. Hegde, ‘Rational Design and Evaluation of FRET Experiments to Measure Protein Proximities in Cells’, *Curr. Protoc. Cell Biol. Editor. Board Juan Bonifacino Al*, vol. CHAPTER, p. Unit-17.9, Oct. 2006, doi: 10.1002/0471143030.cb1709s32.
[490] T. Zal and N. R. J. Gascoigne, ‘Photobleaching-Corrected FRET Efficiency Imaging of Live Cells’, *Biophys. J.*, vol. 86, no. 6, pp. 3923–3939, Jun. 2004, doi: 10.1529/biophysj.103.022087.
[491] R. Datta, T. M. Heaster, J. T. Sharick, A. A. Gillette, and M. C. Skala, ‘Fluorescence lifetime imaging microscopy: fundamentals and advances in instrumentation, analysis, and applications’, *J. Biomed. Opt.*, vol. 25, no. 7, p. 071203, Jul. 2020, doi: 10.1117/1.JBO.25.7.071203.
[492] Y. Chen, J. P. Mauldin, R. N. Day, and A. Periasamy, ‘Characterization of spectral FRET imaging microscopy for monitoring nuclear protein interactions’, *J. Microsc.*, vol. 228, no. Pt 2, pp. 139–152, Nov. 2007, doi: 10.1111/j.1365-2818.2007.01838.x.
[493] H. Chen, H. L. Puhl, S. V. Koushik, S. S. Vogel, and S. R. Ikeda, ‘Measurement of FRET Efficiency and Ratio of Donor to Acceptor Concentration in Living Cells’, *Biophys. J.*, vol. 91, no. 5, pp. L39–L41, Sep. 2006, doi: 10.1529/biophysj.106.088773.
[494] A. L. Mattheyses, A. D. Hoppe, and D. Axelrod, ‘Polarized Fluorescence Resonance Energy Transfer Microscopy’, *Biophys. J.*, vol. 87, no. 4, pp. 2787–2797, Oct. 2004, doi: 10.1529/biophysj.103.036194.
[495] A. N. Patel and C. Kranz, ‘(Multi)functional Atomic Force Microscopy Imaging’, *Annu. Rev. Anal. Chem.*, vol. 11, no. 1, pp. 329–350, 2018, doi: 10.1146/annurev-anchem-061417-125716.
[496] G. Binnig, C. F. Quate, and Ch. Gerber, ‘Atomic Force Microscope’, *Phys. Rev. Lett.*, vol. 56, no. 9, pp. 930–933, Mar. 1986, doi: 10.1103/PhysRevLett.56.930.
[497] N. Gadegaard, ‘Atomic force microscopy in biology: technology and techniques’, *Biotech. Histochem.*, vol. 81, no. 2–3, pp. 87–97, Jan. 2006, doi: 10.1080/10520290600783143.
[498] M. Krieg *et al.*, ‘Atomic force microscopy-based mechanobiology’, *Nat. Rev. Phys.*, vol. 1, no. 1, Art. no. 1, Jan. 2019, doi: 10.1038/s42254-018-0001-7.
[499] D. Fotiadis, S. Scheuring, S. A. Müller, A. Engel, and D. J. Müller, ‘Imaging and manipulation of biological structures with the AFM’, *Micron Oxf. Engl. 1993*, vol. 33, no. 4, pp. 385–397, 2002, doi: 10.1016/s0968-4328(01)00026-9.

[500] M. Marrese, V. Guarino, and L. Ambrosio, ‘Atomic Force Microscopy: A Powerful Tool to Address Scaffold Design in Tissue Engineering’, *J. Funct. Biomater.*, vol. 8, no. 1, Art. no. 1, Mar. 2017, doi: 10.3390/jfb8010007.
[501] S. Vahabi, B. Nazemi Salman, and A. Javanmard, ‘Atomic Force Microscopy Application in Biological Research: A Review Study’, *Iran. J. Med. Sci.*, vol. 38, no. 2, pp. 76–83, Jun. 2013.
[502] D. Kirmizis, ‘Atomic force microscopy probing in the measurement of cell mechanics’, *Int. J. Nanomedicine*, p. 137, Mar. 2010, doi: 10.2147/IJN.S5787.
[503] E. Lipiec, K. Sofińska, S. Seweryn, N. Wilkosz, and M. Szymonski, ‘Revealing DNA Structure at Liquid/Solid Interfaces by AFM-Based High-Resolution Imaging and Molecular Spectroscopy’, *Molecules*, vol. 26, no. 21, Art. no. 21, Jan. 2021, doi: 10.3390/molecules26216476.
[504] Y. F. Dufrêne, A. Viljoen, J. Mignolet, and M. Mathelié-Guinlet, ‘AFM in cellular and molecular microbiology’, *Cell. Microbiol.*, vol. 23, no. 7, p. e13324, 2021, doi: 10.1111/cmi.13324.
[505] F. Xia and K. Youcef-Toumi, ‘Review: Advanced Atomic Force Microscopy Modes for Biomedical Research’, *Biosensors*, vol. 12, no. 12, p. 1116, Dec. 2022, doi: 10.3390/bios12121116.
[506] J. Joshi, S. V. Homburg, and A. Ehrmann, ‘Atomic Force Microscopy (AFM) on Biopolymers and Hydrogels for Biotechnological Applications—Possibilities and Limits’, *Polymers*, vol. 14, no. 6, p. 1267, Mar. 2022, doi: 10.3390/polym14061267.
[507] G. Guan, Y. He, and L. Mei, ‘Atomic force microscopy: A nanobiotechnology for cellular research’, *Nano TransMed*, vol. 1, no. 1, p. e9130004, Mar. 2022, doi: 10.26599/NTM.2022.9130004.
[508] M. Sato, K. Nagayama, N. Kataoka, M. Sasaki, and K. Hane, ‘Local mechanical properties measured by atomic force microscopy for cultured bovine endothelial cells exposed to shear stress’, *J. Biomech.*, vol. 33, no. 1, pp. 127–135, Jan. 2000, doi: 10.1016/S0021-9290(99)00178-5.
[509] F. Kienberger *et al.*, ‘Dynamic force microscopy imaging of native membranes’, *Ultramicroscopy*, vol. 97, no. 1, pp. 229–237, Oct. 2003, doi: 10.1016/S0304-3991(03)00047-0.
[510] J. Madl *et al.*, ‘A combined optical and atomic force microscope for live cell investigations’, *Ultramicroscopy*, vol. 106, no. 8, pp. 645–651, Jun. 2006, doi: 10.1016/j.ultramic.2005.12.020.
[511] M. Cascione, V. de Matteis, R. Rinaldi, and S. Leporatti, ‘Atomic force microscopy combined with optical microscopy for cells investigation’, *Microsc. Res. Tech.*, vol. 80, no. 1, pp. 109–123, 2017, doi: 10.1002/jemt.22696.
[512] P. K. Viji Babu and M. Radmacher, ‘Mechanics of Brain Tissues Studied by Atomic Force Microscopy: A Perspective’, *Front. Neurosci.*, vol. 13, 2019, Accessed: Dec. 22, 2023. [Online]. Available: https://www.frontiersin.org/articles/10.3389/fnins.2019.00600
[513] P. K. Viji Babu, C. Rianna, U. Mirastschijski, and M. Radmacher, ‘Nano-mechanical mapping of interdependent cell and ECM mechanics by AFM force spectroscopy’, *Sci. Rep.*, vol. 9, no. 1, Art. no. 1, Aug. 2019, doi: 10.1038/s41598-019-48566-7.
[514] I. Jorba, J. J. Uriarte, N. Campillo, R. Farré, and D. Navajas, ‘Probing Micromechanical Properties of the Extracellular Matrix of Soft Tissues by Atomic Force Microscopy’, *J. Cell. Physiol.*, vol. 232, no. 1, pp. 19–26, 2017, doi: 10.1002/jcp.25420.
[515] P. Zhu and M. Fang, ‘Nano-Morphology of Cartilage in Hydrated and Dehydrated Conditions Revealed by Atomic Force Microscopy’, *J. Phys. Chem. Biophys.*, vol. 02, no. 01, 2012, doi: 10.4172/2161-0398.1000106.
[516] G. Smolyakov *et al.*, ‘Nanoscale structural mapping as a measure of maturation in the murine frontal cortex’, *Brain Struct. Funct.*, vol. 223, no. 1, pp. 255–265, Jan. 2018, doi: 10.1007/s00429-017-1486-z.
[517] C. T. McKee, J. A. Last, P. Russell, and C. J. Murphy, ‘Indentation Versus Tensile Measurements of Young’s Modulus for Soft Biological Tissues’, *Tissue Eng. Part B Rev.*, vol. 17, no. 3, pp. 155–164, Jun. 2011, doi: 10.1089/ten.teb.2010.0520.
[518] P. Sajeesh, A. Raj, M. Doble, and A. K. Sen, ‘Characterization and sorting of cells based on stiffness contrast in a microfluidic channel’, *RSC Adv.*, vol. 6, no. 78, pp. 74704–74714, Aug. 2016, doi: 10.1039/C6RA09099K.
[519] R. Ferencz, J. Sanchez, B. Blümich, and W. Herrmann, ‘AFM nanoindentation to determine Young’s modulus for different EPDM elastomers’, *Polym. Test.*, vol. 31, no. 3, pp. 425–432, May 2012, doi: 10.1016/j.polymertesting.2012.01.003.

[520] S. V. Kontomaris, A. Malamou, and A. Stylianou, 'The Hertzian theory in AFM nanoindentation experiments regarding biological samples: Overcoming limitations in data processing', *Micron*, vol. 155, p. 103228, Apr. 2022, doi: 10.1016/j.micron.2022.103228.
[521] C. Cimmino, P. A. Netti, and M. Ventre, 'A switchable light-responsive azopolymer conjugating protein micropatterns with topography for mechanobiological studies', *Front. Bioeng. Biotechnol.*, vol. 10, p. 933410, Jul. 2022, doi: 10.3389/fbioe.2022.933410.
[522] 'JPK DP Data processing software manual'. JPK Instruments, Oct. 2012. [Online]. Available: https://www.nanophys.kth.se/nanolab/afm/jpk/manuf-manuals/DPmanual.4.2.pdf
[523] I. N. Sneddon, 'The relation between load and penetration in the axisymmetric boussinesq problem for a punch of arbitrary profile', *Int. J. Eng. Sci.*, vol. 3, no. 1, pp. 47–57, May 1965, doi: 10.1016/0020-7225(65)90019-4.
[524] K. Haase and A. E. Pelling, 'Investigating cell mechanics with atomic force microscopy', *J. R. Soc. Interface*, vol. 12, no. 104, p. 20140970, Mar. 2015, doi: 10.1098/rsif.2014.0970.
[525] S. V. Kontomaris, A. Georgakopoulos, A. Malamou, and A. Stylianou, 'The average Young's modulus as a physical quantity for describing the depth-dependent mechanical properties of cells', *Mech. Mater.*, vol. 158, p. 103846, Jul. 2021, doi: 10.1016/j.mechmat.2021.103846.
[526] R. O'Callaghan, K. M. Job, R. O. Dull, and V. Hlady, 'Stiffness and heterogeneity of the pulmonary endothelial glycocalyx measured by atomic force microscopy', *Am. J. Physiol. - Lung Cell. Mol. Physiol.*, vol. 301, no. 3, pp. L353–L360, Sep. 2011, doi: 10.1152/ajplung.00342.2010.
[527] C. E. Morris and U. Homann, 'Cell Surface Area Regulation and Membrane Tension', *J. Membr. Biol.*, vol. 179, no. 2, pp. 79–102, Jan. 2001, doi: 10.1007/s002320010040.
[528] A. X. Cartagena-Rivera, J. S. Logue, C. M. Waterman, and R. S. Chadwick, 'Actomyosin Cortical Mechanical Properties in Nonadherent Cells Determined by Atomic Force Microscopy', *Biophys. J.*, vol. 110, no. 11, pp. 2528–2539, Jun. 2016, doi: 10.1016/j.bpj.2016.04.034.
[529] P. A. Janmey and D. A. Weitz, 'Dealing with mechanics: mechanisms of force transduction in cells', *Trends Biochem. Sci.*, vol. 29, no. 7, pp. 364–370, Jul. 2004, doi: 10.1016/j.tibs.2004.05.003.
[530] N. Caille, O. Thoumine, Y. Tardy, and J.-J. Meister, 'Contribution of the nucleus to the mechanical properties of endothelial cells', *J. Biomech.*, vol. 35, no. 2, pp. 177–187, Feb. 2002, doi: 10.1016/s0021-9290(01)00201-9.
[531] F. Guilak, J. R. Tedrow, and R. Burgkart, 'Viscoelastic properties of the cell nucleus', *Biochem. Biophys. Res. Commun.*, vol. 269, no. 3, pp. 781–786, Mar. 2000, doi: 10.1006/bbrc.2000.2360.
[532] A. B. Mathur, G. A. Truskey, and W. M. Reichert, 'Atomic force and total internal reflection fluorescence microscopy for the study of force transmission in endothelial cells.', *Biophys. J.*, vol. 78, no. 4, pp. 1725–1735, Apr. 2000.
[533] J. Lammerding, 'Mechanics of the Nucleus', *Compr. Physiol.*, vol. 1, no. 2, pp. 783–807, Apr. 2011, doi: 10.1002/cphy.c100038.
[534] A. M. Collinsworth, S. Zhang, W. E. Kraus, and G. A. Truskey, 'Apparent elastic modulus and hysteresis of skeletal muscle cells throughout differentiation', *Am. J. Physiol.-Cell Physiol.*, vol. 283, no. 4, pp. C1219–C1227, Oct. 2002, doi: 10.1152/ajpcell.00502.2001.
[535] J. S. Zhang, W. E. Kraus, and G. A. Truskey, 'Stretch-induced nitric oxide modulates mechanical properties of skeletal muscle cells', *Am. J. Physiol.-Cell Physiol.*, vol. 287, no. 2, pp. C292–C299, Aug. 2004, doi: 10.1152/ajpcell.00018.2004.
[536] A. Urciuolo *et al.*, 'Collagen VI regulates satellite cell self-renewal and muscle regeneration', *Nat. Commun.*, vol. 4, p. 1964, 2013, doi: 10.1038/ncomms2964.
[537] A. J. Engler, M. A. Griffin, S. Sen, C. G. Bönnemann, H. L. Sweeney, and D. E. Discher, 'Myotubes differentiate optimally on substrates with tissue-like stiffness', *J. Cell Biol.*, vol. 166, no. 6, pp. 877–887, Sep. 2004, doi: 10.1083/jcb.200405004.
[538] A. J. Ford and P. Rajagopalan, 'Measuring Cytoplasmic Stiffness of Fibroblasts as a Function of Location and Substrate Rigidity Using Atomic Force Microscopy', *ACS Biomater. Sci. Eng.*, vol. 4, no. 12, pp. 3974–3982, Dec. 2018, doi: 10.1021/acsbiomaterials.8b01019.
[539] A. Simon *et al.*, 'Characterization of dynamic cellular adhesion of osteoblasts using atomic force microscopy', *Cytometry A*, vol. 54A, no. 1, pp. 36–47, 2003, doi: 10.1002/cyto.a.10052.
[540] E. Takai, K. D. Costa, A. Shaheen, C. T. Hung, and X. E. Guo, 'Osteoblast Elastic Modulus Measured by Atomic Force Microscopy Is Substrate Dependent', *Ann. Biomed. Eng.*, vol. 33, no. 7, pp. 963–971, Jul. 2005, doi: 10.1007/s10439-005-3555-3.

[541] I. Dulińska *et al.*, ‘Stiffness of normal and pathological erythrocytes studied by means of atomic force microscopy’, *J. Biochem. Biophys. Methods*, vol. 66, no. 1, pp. 1–11, Mar. 2006, doi: 10.1016/j.jbbm.2005.11.003.
[542] T. G. Kuznetsova, M. N. Starodubtseva, N. I. Yegorenkov, S. A. Chizhik, and R. I. Zhdanov, ‘Atomic force microscopy probing of cell elasticity’, *Micron Oxf. Engl. 1993*, vol. 38, no. 8, pp. 824–833, 2007, doi: 10.1016/j.micron.2007.06.011.
[543] A. B. Mathur, A. M. Collinsworth, W. M. Reichert, W. E. Kraus, and G. A. Truskey, ‘Endothelial, cardiac muscle and skeletal muscle exhibit different viscous and elastic properties as determined by atomic force microscopy’, *J. Biomech.*, vol. 34, no. 12, pp. 1545–1553, Dec. 2001, doi: 10.1016/s0021-9290(01)00149-x.
[544] B. Codan, V. Martinelli, L. Mestroni, and O. Sbaizero, ‘Atomic force microscopy of 3T3 and SW-13 cell lines: An investigation of cell elasticity changes due to fixation’, *Mater. Sci. Eng. C*, vol. 33, no. 6, pp. 3303–3308, Aug. 2013, doi: 10.1016/j.msec.2013.04.009.
[545] S. G. Shroff, D. R. Saner, and R. Lal, ‘Dynamic micromechanical properties of cultured rat atrial myocytes measured by atomic force microscopy’, *Am. J. Physiol.-Cell Physiol.*, vol. 269, no. 1, pp. C286–C292, Jul. 1995, doi: 10.1152/ajpcell.1995.269.1.C286.
[546] A. A. Mozhanova, N. I. Nurgazizov, and A. A. Bukharaev, ‘Local elastic properties of biological materials studied by SFM’.
[547] H. Jin *et al.*, ‘Detection of erythrocytes influenced by aging and type 2 diabetes using atomic force microscope’, *Biochem. Biophys. Res. Commun.*, vol. 391, no. 4, pp. 1698–1702, Jan. 2010, doi: 10.1016/j.bbrc.2009.12.133.
[548] M. Lekka *et al.*, ‘Cancer cell detection in tissue sections using AFM’, *Arch. Biochem. Biophys.*, vol. 518, no. 2, pp. 151–156, Feb. 2012, doi: 10.1016/j.abb.2011.12.013.
[549] W. Xu, R. Mezencev, B. Kim, L. Wang, J. McDonald, and T. Sulchek, ‘Cell Stiffness Is a Biomarker of the Metastatic Potential of Ovarian Cancer Cells’, *PLOS ONE*, vol. 7, no. 10, p. e46609, Oct. 2012, doi: 10.1371/journal.pone.0046609.
[550] S. E. Cross, Y.-S. Jin, J. Rao, and J. K. Gimzewski, ‘Nanomechanical analysis of cells from cancer patients’, *Nat. Nanotechnol.*, vol. 2, no. 12, Art. no. 12, Dec. 2007, doi: 10.1038/nnano.2007.388.
[551] C. Pasternak, S. Wong, and E. L. Elson, ‘Mechanical function of dystrophin in muscle cells’, *J. Cell Biol.*, vol. 128, no. 3, pp. 355–361, Feb. 1995, doi: 10.1083/jcb.128.3.355.
[552] B. M. Gaub and D. J. Müller, ‘Mechanical Stimulation of Piezo1 Receptors Depends on Extracellular Matrix Proteins and Directionality of Force’, *Nano Lett.*, vol. 17, no. 3, pp. 2064–2072, Mar. 2017, doi: 10.1021/acs.nanolett.7b00177.
[553] D. Ossola, M.-Y. Amarouch, P. Behr, J. Vörös, H. Abriel, and T. Zambelli, ‘Force-Controlled Patch Clamp of Beating Cardiac Cells’, *Nano Lett.*, vol. 15, no. 3, pp. 1743–1750, Mar. 2015, doi: 10.1021/nl504438z.
[554] D. E. Discher, P. Janmey, and Y.-L. Wang, ‘Tissue cells feel and respond to the stiffness of their substrate’, *Science*, vol. 310, no. 5751, pp. 1139–1143, Nov. 2005, doi: 10.1126/science.1116995.
[555] A. J. Engler, F. Rehfeldt, S. Sen, and D. E. Discher, ‘Microtissue Elasticity: Measurements by Atomic Force Microscopy and Its Influence on Cell Differentiation’, in *Methods in Cell Biology*, vol. 83, in Cell Mechanics, vol. 83. , Academic Press, 2007, pp. 521–545. doi: 10.1016/S0091-679X(07)83022-6.
[556] D. E. Koser *et al.*, ‘Mechanosensing is critical for axon growth in the developing brain’, *Nat. Neurosci.*, vol. 19, no. 12, pp. 1592–1598, Dec. 2016, doi: 10.1038/nn.4394.
[557] E. Moeendarbary *et al.*, ‘The soft mechanical signature of glial scars in the central nervous system’, *Nat. Commun.*, vol. 8, no. 1, Art. no. 1, Mar. 2017, doi: 10.1038/ncomms14787.
[558] J. R. Staunton, B. L. Doss, S. Lindsay, and R. Ros, ‘Correlating confocal microscopy and atomic force indentation reveals metastatic cancer cells stiffen during invasion into collagen I matrices’, *Sci. Rep.*, vol. 6, p. 19686, Jan. 2016, doi: 10.1038/srep19686.
[559] S. Iyer, R. M. Gaikwad, V. Subba-Rao, C. D. Woodworth, and I. Sokolov, ‘AFM Detects Differences in the Surface Brush of Normal and Cancerous Cervical Cells’, *Nat. Nanotechnol.*, vol. 4, no. 6, pp. 389–393, Jun. 2009, doi: 10.1038/nnano.2009.77.
[560] M. Plodinec *et al.*, ‘The nanomechanical signature of breast cancer’, *Nat. Nanotechnol.*, vol. 7, no. 11, Art. no. 11, Nov. 2012, doi: 10.1038/nnano.2012.167.

[561] J. I. Lopez, I. Kang, W.-K. You, D. M. McDonald, and V. M. Weaver, ‘In situ force mapping of mammary gland transformation’, *Integr. Biol. Quant. Biosci. Nano Macro*, vol. 3, no. 9, pp. 910–921, Sep. 2011, doi: 10.1039/c1ib00043h.
[562] C. M. Madl, I. A. Flaig, C. A. Holbrook, Y. X. Wang, and H. M. Blau, ‘Biophysical matrix cues from the regenerating niche direct muscle stem cell fate in engineered microenvironments’, *Biomaterials*, vol. 275, p. 120973, Aug. 2021, doi: 10.1016/j.biomaterials.2021.120973.
[563] J. Etienne, C. Liu, C. M. Skinner, M. J. Conboy, and I. M. Conboy, ‘Skeletal muscle as an experimental model of choice to study tissue aging and rejuvenation’, *Skelet. Muscle*, vol. 10, no. 1, p. 4, Feb. 2020, doi: 10.1186/s13395-020-0222-1.
[564] G. Lacraz *et al.*, ‘Increased Stiffness in Aged Skeletal Muscle Impairs Muscle Progenitor Cell Proliferative Activity’, *PLOS ONE*, vol. 10, no. 8, p. e0136217, Aug. 2015, doi: 10.1371/journal.pone.0136217.
[565] F. Trensz *et al.*, ‘Increased microenvironment stiffness in damaged myofibers promotes myogenic progenitor cell proliferation’, *Skelet. Muscle*, vol. 5, no. 1, p. 5, Feb. 2015, doi: 10.1186/s13395-015-0030-1.
[566] M. Lintz, A. Muñoz, and C. A. Reinhart-King, ‘The Mechanics of Single Cell and Collective Migration of Tumor Cells’, *J. Biomech. Eng.*, vol. 139, no. 2, pp. 0210051–0210059, Feb. 2017, doi: 10.1115/1.4035121.
[567] A. Pawluchin and M. Galic, ‘Moving through a changing world: Single cell migration in 2D vs. 3D’, *Front. Cell Dev. Biol.*, vol. 10, 2022, Accessed: Dec. 22, 2023. [Online]. Available: https://www.frontiersin.org/articles/10.3389/fcell.2022.1080995
[568] M. L. Gardel, B. Sabass, L. Ji, G. Danuser, U. S. Schwarz, and C. M. Waterman, ‘Traction stress in focal adhesions correlates biphasically with actin retrograde flow speed’, *J. Cell Biol.*, vol. 183, no. 6, pp. 999–1005, Dec. 2008, doi: 10.1083/jcb.200810060.
[569] M. Abercrombie, ‘The Croonian Lecture, 1978: The Crawling Movement of Metazoan Cells’, *Proc. R. Soc. Lond. B Biol. Sci.*, vol. 207, no. 1167, pp. 129–147, 1980.
[570] J. Stock and A. Pauli, ‘Self-organized cell migration across scales – from single cell movement to tissue formation’, *Development*, vol. 148, no. 7, p. dev191767, Apr. 2021, doi: 10.1242/dev.191767.
[571] J. H. Wen *et al.*, ‘Haptotaxis is cell type specific and limited by substrate adhesiveness’, *Cell. Mol. Bioeng.*, vol. 8, no. 4, pp. 530–542, Dec. 2015, doi: 10.1007/s12195-015-0398-3.
[572] C.-M. Lo, H.-B. Wang, M. Dembo, and Y. Wang, ‘Cell Movement Is Guided by the Rigidity of the Substrate’, *Biophys. J.*, vol. 79, no. 1, pp. 144–152, Jul. 2000, doi: 10.1016/S0006-3495(00)76279-5.
[573] O. Moreno-Arotzena, C. Borau, N. Movilla, M. Vicente-Manzanares, and J. M. García-Aznar, ‘Fibroblast Migration in 3D is Controlled by Haptotaxis in a Non-muscle Myosin II-Dependent Manner’, *Ann. Biomed. Eng.*, vol. 43, no. 12, pp. 3025–3039, 2015, doi: 10.1007/s10439-015-1343-2.
[574] B. J. DuChez, A. D. Doyle, E. K. Dimitriadis, and K. M. Yamada, ‘Durotaxis by Human Cancer Cells’, *Biophys. J.*, vol. 116, no. 4, pp. 670–683, Feb. 2019, doi: 10.1016/j.bpj.2019.01.009.
[575] W. V. Ingman, J. Wyckoff, V. Gouon-Evans, J. Condeelis, and J. W. Pollard, ‘Macrophages promote collagen fibrillogenesis around terminal end buds of the developing mammary gland’, *Dev. Dyn. Off. Publ. Am. Assoc. Anat.*, vol. 235, no. 12, pp. 3222–3229, Dec. 2006, doi: 10.1002/dvdy.20972.
[576] C. A. Lemmon, C. S. Chen, and L. H. Romer, ‘Cell traction forces direct fibronectin matrix assembly’, *Biophys. J.*, vol. 96, no. 2, pp. 729–738, Jan. 2009, doi: 10.1016/j.bpj.2008.10.009.
[577] T. Lämmermann and M. Sixt, ‘Mechanical modes of “amoeboid” cell migration’, *Curr. Opin. Cell Biol.*, vol. 21, no. 5, pp. 636–644, Oct. 2009, doi: 10.1016/j.ceb.2009.05.003.
[578] A. Kaczmarek *et al.*, ‘The Role of Satellite Cells in Skeletal Muscle Regeneration—The Effect of Exercise and Age’, *Biology*, vol. 10, no. 10, p. 1056, Oct. 2021, doi: 10.3390/biology10101056.
[579] S. M. Hughes and H. M. Blau, ‘Migration of myoblasts across basal lamina during skeletal muscle development’, *Nature*, vol. 345, no. 6273, pp. 350–353, May 1990, doi: 10.1038/345350a0.
[580] P. Feige, C. E. Brun, M. Ritso, and M. A. Rudnicki, ‘Orienting Muscle Stem Cells for Regeneration in Homeostasis, Aging, and Disease’, *Cell Stem Cell*, vol. 23, no. 5, pp. 653–664, Nov. 2018, doi: 10.1016/j.stem.2018.10.006.

[581] E. Scarpa and R. Mayor, ‘Collective cell migration in development’, *J. Cell Biol.*, vol. 212, no. 2, pp. 143–155, Jan. 2016, doi: 10.1083/jcb.201508047.
[582] P. Friedl, J. Locker, E. Sahai, and J. E. Segall, ‘Classifying collective cancer cell invasion’, *Nat. Cell Biol.*, vol. 14, no. 8, Art. no. 8, Aug. 2012, doi: 10.1038/ncb2548.
[583] E. Theveneau *et al.*, ‘Collective chemotaxis requires contact-dependent cell polarity’, *Dev. Cell*, vol. 19, no. 1, pp. 39–53, Jul. 2010, doi: 10.1016/j.devcel.2010.06.012.
[584] E. Theveneau and R. Mayor, ‘Cadherins in collective cell migration of mesenchymal cells’, *Curr. Opin. Cell Biol.*, vol. 24, no. 5, pp. 677–684, Oct. 2012, doi: 10.1016/j.ceb.2012.08.002.
[585] D. Spiering, J. J. Bravo-Cordero, Y. Moshfegh, V. Miskolci, and L. Hodgson, ‘Quantitative Ratiometric Imaging of FRET-Biosensors in Living Cells’, *Methods Cell Biol.*, vol. 114, pp. 593–609, 2013, doi: 10.1016/B978-0-12-407761-4.00025-7.
[586] W. Thielicke and R. Sonntag, ‘Particle Image Velocimetry for MATLAB: Accuracy and enhanced algorithms in PIVlab’, vol. 9, no. 1, Art. no. 1, May 2021, doi: 10.5334/jors.334.
[587] J. C. Martens and M. Radmacher, ‘Softening of the actin cytoskeleton by inhibition of myosin II’, *Pflüg. Arch. - Eur. J. Physiol.*, vol. 456, no. 1, pp. 95–100, Apr. 2008, doi: 10.1007/s00424-007-0419-8.
[588] M. D. Atkins, ‘Chapter 5 - Velocity Field Measurement Using Particle Image Velocimetry (PIV)’, in *Application of Thermo-Fluidic Measurement Techniques*, T. Kim, T. J. Lu, and S. J. Song, Eds., Butterworth-Heinemann, 2016, pp. 125–166. doi: 10.1016/B978-0-12-809731-1.00005-8.
[589] K. C. Clause and T. H. Barker, ‘Extracellular Matrix Signaling in Morphogenesis and Repair’, *Curr. Opin. Biotechnol.*, vol. 24, no. 5, pp. 830–833, Oct. 2013, doi: 10.1016/j.copbio.2013.04.011.
[590] X. Liao, X. Li, and R. Liu, ‘Extracellular-matrix mechanics regulate cellular metabolism: A ninja warrior behind mechano-chemo signaling crosstalk’, *Rev. Endocr. Metab. Disord.*, vol. 24, no. 2, pp. 207–220, Apr. 2023, doi: 10.1007/s11154-022-09768-z.
[591] M. Ventre and P. A. Netti, ‘Controlling Cell Functions and Fate with Surfaces and Hydrogels: The Role of Material Features in Cell Adhesion and Signal Transduction’, *Gels Basel Switz.*, vol. 2, no. 1, p. 12, Mar. 2016, doi: 10.3390/gels2010012.
[592] B. Yi, Q. Xu, and W. Liu, ‘An overview of substrate stiffness guided cellular response and its applications in tissue regeneration’, *Bioact. Mater.*, vol. 15, pp. 82–102, Dec. 2021, doi: 10.1016/j.bioactmat.2021.12.005.
[593] M. J. Mueller and K. S. Maluf, ‘Tissue Adaptation to Physical Stress: A Proposed “Physical Stress Theory” to Guide Physical Therapist Practice, Education, and Research’, *Phys. Ther.*, vol. 82, no. 4, pp. 383–403, Apr. 2002, doi: 10.1093/ptj/82.4.383.
[594] L.-Y. Hu *et al.*, ‘Skeletal muscle progenitors are sensitive to collagen architectural features of fibril size and cross linking’, *Am. J. Physiol.-Cell Physiol.*, vol. 321, no. 2, pp. C330–C342, Aug. 2021, doi: 10.1152/ajpcell.00065.2021.
[595] R. Puts *et al.*, ‘Activation of Mechanosensitive Transcription Factors in Murine C2C12 Mesenchymal Precursors by Focused Low-Intensity Pulsed Ultrasound (FLIPUS)’, *IEEE Trans. Ultrason. Ferroelectr. Freq. Control*, vol. 63, no. 10, pp. 1505–1513, Oct. 2016, doi: 10.1109/TUFFC.2016.2586972.
[596] F. Kurth, A. Franco-Obregón, M. Casarosa, S. K. Küster, K. Wuertz-Kozak, and P. S. Dittrich, ‘Transient receptor potential vanilloid 2-mediated shear-stress responses in C2C12 myoblasts are regulated by serum and extracellular matrix’, *FASEB J.*, vol. 29, no. 11, pp. 4726–4737, 2015, doi: 10.1096/fj.15-275396.
[597] A. Moustogiannis *et al.*, ‘Effect of Mechanical Loading of Senescent Myoblasts on Their Myogenic Lineage Progression and Survival’, *Cells*, vol. 11, no. 24, Art. no. 24, Jan. 2022, doi: 10.3390/cells11243979.
[598] T. Luo, B. Tan, L. Zhu, Y. Wang, and J. Liao, ‘A Review on the Design of Hydrogels With Different Stiffness and Their Effects on Tissue Repair’, *Front. Bioeng. Biotechnol.*, vol. 10, 2022, Accessed: Dec. 22, 2023. [Online]. Available: https://www.frontiersin.org/articles/10.3389/fbioe.2022.817391
[599] C. M. Hampton, D. W. Taylor, and K. A. Taylor, ‘Novel Structures for α-Actinin:F-Actin Interactions and their Implications for Actin–Membrane Attachment and Tension Sensing in the Cytoskeleton’, *J. Mol. Biol.*, vol. 368, no. 1, pp. 92–104, Apr. 2007, doi: 10.1016/j.jmb.2007.01.071.

[600] P. M. Pereira *et al.*, ‘Fix Your Membrane Receptor Imaging: Actin Cytoskeleton and CD4 Membrane Organization Disruption by Chemical Fixation’, *Front. Immunol.*, vol. 10, 2019, Accessed: Dec. 22, 2023. [Online]. Available: https://www.frontiersin.org/articles/10.3389/fimmu.2019.00675

[601] K. Suffoletto, N. Ye, F. Meng, D. Verma, and S. Z. Hua, ‘Intracellular forces during guided cell growth on micropatterns using FRET measurement’, *J. Biomech.*, vol. 48, no. 4, pp. 627–635, Feb. 2015, doi: 10.1016/j.jbiomech.2014.12.051.

[602] N. Ye, D. Verma, F. Meng, M. W. Davidson, K. Suffoletto, and S. Z. Hua, ‘Direct observation of α-actinin tension and recruitment at focal adhesions during contact growth’, *Exp. Cell Res.*, vol. 327, no. 1, pp. 57–67, Sep. 2014, doi: 10.1016/j.yexcr.2014.07.026.

[603] C. Cornu, F. Goubel, and M. Fardeau, ‘Muscle and joint elastic properties during elbow flexion in Duchenne muscular dystrophy’, *J. Physiol.*, vol. 533, no. Pt 2, pp. 605–616, Jun. 2001, doi: 10.1111/j.1469-7793.2001.0605a.x.

[604] L. Lacourpaille *et al.*, ‘Non-invasive assessment of muscle stiffness in patients with Duchenne muscular dystrophy’, *Muscle Nerve*, vol. 51, no. 2, pp. 284–286, Feb. 2015, doi: 10.1002/mus.24445.

[605] A. Guo *et al.*, ‘Consistent apparent Young’s modulus of human embryonic stem cells and derived cell types stabilized by substrate stiffness regulation promotes lineage specificity maintenance’, *Cell Regen.*, vol. 9, p. 15, Sep. 2020, doi: 10.1186/s13619-020-00054-4.

[606] X. Cai, K.-C. Wang, and Z. Meng, ‘Mechanoregulation of YAP and TAZ in Cellular Homeostasis and Disease Progression’, *Front. Cell Dev. Biol.*, vol. 9, 2021, Accessed: Dec. 22, 2023. [Online]. Available: https://www.frontiersin.org/articles/10.3389/fcell.2021.673599

SUPPLEMENTARY MATERIALS

The supplementary materials are available online, using the following link:

Willems_Sarah_36_Supplementary_Materials.docx